UC Riverside

UC Riverside Electronic Theses and Dissertations

Title

3>2>1: Investigation of Single Particle Particle and Many Body Physics in Dual-Gated 1,2,3 Layers of Graphene

Permalink

https://escholarship.org/uc/item/8z2321gj

Author

Velasco, Jairo

Publication Date

2012

Peer reviewed|Thesis/dissertation

eScholarship.org Powered by the California Digital Library
University of California

UNIVERSITY OF CALIFORNIA
RIVERSIDE

3>2>1: Investigation of Single Particle and Many Body Physics in Dual-Gated 1,2,3 Layers of Graphene

A Dissertation submitted in partial satisfaction
of the requirements for the degree of

Doctor of Philosophy

in

Physics

by

Jairo Velasco

September 2012

Dissertation Committee:
Dr. Chun Ning(Jeanie) Lau, Chairperson
Dr. Marc Bockrath
Dr. Roland K. Kawakami

Copyright by
Jairo Velasco
2012

The Dissertation of Jairo Velasco is approved by:

____

____

____

Committee Chairperson

University of California, Riverside

Acknowledgements

The work presented in this thesis was the product of six very enjoyable years in the Jeanie Lau group, in which I was immersed in a stimulating, and fun environment that lead to my maturation from a student to an independent researcher. I was quite fortunate to have many wise mentors, insightful colleagues and simply pleasant people that enriched my life on a daily basis. Below I acknowledge these people that were so crucial to my growth at UCR as a PhD student and as a person.

First and foremost, I acknowledge my advisor Jeanie Lau who will always be a role model and benchmark for the type of scientist I will strive to be. Jeanie possesses a great intuition for unraveling physical phenomena at the nano-scale. As her student I benefited immensely from this ability, and with her guidance I was able to produce a large body of work that I am very proud of. I will never forget the riveting experience of working on a "hot" project with Jeanie, each day was equivalent to an unrestrained high-speed rollercoaster ride. I thank her for sharing her scientific insights with me, for exhibiting unbounded patience as my teacher, and most importantly for fostering a nurturing environment in her group that stimulates creativity. I wish Jeanie all the best with her ever-growing group, and look forward to reading the many great works to come.

As a second generation student in the group I benefited tremendously from the previous work of setting up the lab, equipments and development of fabrication recipes by Feng Miao, Yong Zhang, Gang Liu and Ulas Coskun. I especially want to acknowledge Gang Liu who taught me fabrication and low temperature electrical measurements. His innovative idea of the contact-less top gate was a great place to start

my thesis, and lead to my love for fabrication. I also want to acknowledge Feng Miao, who trail blazed the path for graphene research in our group and has always shared his wisdom with me.

In the subsequent generation of students I would like to acknowledge Wenzhong Bao. I thank him for his support with graphene flakes in the earlier part of my studies, and enjoyed our exciting collaborative efforts with suspended bilayer and trilayer graphene. On a more personal note, I thank Bao for being a great friend that continually motivated me whenever I met difficult times with my experiments. I will always cherish our time together as students in the Jeanie Lau group.

I also would like to acknowledge Lei Jing and Yongjin Lee and thank them for their help with my projects on dual gated bilayer and trilayer graphene. Because of their work ethic and friendly disposition we produced a lot of good works together in a timely fashion. With the same breath, I want to thank the undergraduate students that worked with me Philip Kratz and David Tran. They are masters in the art of graphene exfoliation, and provided many great flakes for our group to use.

I want to acknoweledge Zhao Zheng and Hang Zhang for their efforts with the *Nanotechnology* paper. It was a pleasure to work together. I also thank Fenglin Wang, Jhao-Wun Huang and Kevin Myhro for making the lab a stimulating and fun place to work during these recent years.

I especially want to acknowledge Dr. Dmitry Smirnov at the National High Magnetic Field Laboratory in Tallahassee for his valuable assistance during my visitations. Dr. Smirnov taught me a lot about operating cryostats, and together we

improved the current annealing recipe. I also thank him greatly for his advice on my career and foreign film. I thank his post-doc Jean Marie Poumirol for assistance with measurements when I visited.

During my studies I was very fortunate to interact and collaborate with several of the professors in the condensed matter groups at UCR. I acknowledge Professors Chandra Varma and Vivek Aji and their valuable theoretical support on the *Nature Nanotechnology* paper. I also thank them for stimulating discussions on follow up measurements. I would like to also acknowledge Professor Shi, and his student Zhyiong Wang for providing the bulk Bismuth Selenide studied in the *Nanotechnology* paper. I thank Professor Shan Wei Tsai for career advice and help with my CV. I acknowledge professor Marc Bockrath for his contributions to several of the works presented in the thesis, and for helping me trouble shoot the fridge. I thank Professor Kawakami for advice on my career, and for making me feel welcomed in his group outings. I also thank Ana Aldana and Sonia Godinez for their patience with me!

I acknowledge Professor Allan Macdonald, Dr. Fan Zhang and Dr. Jeil Jung for their theoretical support on the *Nature Nanotechnology* paper, which was my favorite project during my studies. I thank Fan Zhang again for his assistance with several of the unpublished works presented at the end of the thesis.

I thank my friends Raquel and Vincent Meligne and Gian Guzman and Silvia Masis for their friendship, which often helped me cope with my frustrations with my

experiments. And finally, I thank my mother, father and brother for their love and support from a distance as I pursued my dreams.

Dedicated to my parents
(Mami y Papi)

ABSTRACT OF THE DISSERTATION

3>2>1: Investigation of Single Particle and Many Body Physics in Dual-Gated 1,2,3 Layers of Graphene

by

Jairo Velasco

Doctor of Philosophy, Graduate Program in Physics
University of California, Riverside, September 2012
Dr. Chun Ning(Jeanie) Lau, Chairperson

Graphene, a two-dimensional honeycomb lattice of carbon atoms, has become the hottest platform for condensed matter physics and a promising next generation electronic material. The band structures of single-, bi- and tri-layer graphene differ dramatically, yet all host chiral charge carriers with competing symmetries (such as spin, valley and orbital) that may be broken spontaneously or by an external field. In this thesis we present comprehensive transport studies on double-gated single-, bi- and tri-layer graphene, which lead to further insight into single particle and many-body physics in this fascinating 2D system.

A prevailing motif in these studies was the use of suspended structures with the aim to eliminate extrinsic factors such as disorder, which obscure intrinsic physical phenomena. Our efforts were most successful with dual gated suspended bilayer graphene where an unprecedented sample quality was achieved. These studies are discussed in chapters six through nine.

First, we focus on the observation of a spontaneous zero conductance gap at the charge neutrality point with zero out of plane electric and magnetic fields. By applying fields, this gap can be closed with an electric field of either polarity, and grows monotonically with increasing magnetic field. These findings provide insight into the underlying symmetries of this correlated electron phenomena.

Secondly, we performed a systematic study using several devices of the minimum conductivity at charge neutrality. These devices fall into one group with finite, and another with zero minimum conductivity. Because the second group consists of only high quality samples we surmise this insulating state is intrinsic. By tuning temperature we found this gapped insulating state has a critical temperature suggesting a phase transition between insulating and conducting states. Additionally, the transition is tuned by disorder, out-of-plane electric field, or carrier density, suggesting a quantum phase transition.

Lastly, we study broken symmetry quantum Hall states at finite carrier density in the presence of zero and finite out of plane electric field. We find minute electric fields, which are commonly induced in single gated samples, significantly affect the broken symmetry states. Hence this study with zero electric field is the first genuine measurement of these states.

Table of Contents

Table of Contents xi

List of Figures xvii

List of Tables xxxvi

Chapter 1

Introduction 1

1.1 Dimensionality 6

1.2 An Electronic Flatland: Two dimensional electron gas systems (2DEGS) 9

1.3 Flatland has arrived: A brief history of Graphene 14

Conclusion 16

References 17

Chapter 2 Tight binding calculations of single (SLG) and bilayer (BLG) graphene

Introduction 19

2.1 Tight Binding Model 19

2.2 Crystal structure and energy spectrum of SLG 22

2.3 Low energy spectrum of SLG 30

2.4 Crystal Structure and energy spectrum of BLG 35

2.4.1 Low energy spectrum of BLG 38

2.4.2 Induced Band Gap in BLG 42

2.5 Quantum Hall effect (QHE) 45

2.6.1 Energy spectrum and QHE for SLG 47

2.6.2 Energy spectrum and QHE for BLG 50

Conclusion 52

References...54

Chapter 3 Fabrication

Introduction...56

3.1 Fabrication of contactless topgates.. 59

3.1.1 Conventional dual gated devices.. 59

3.1.2 A novel trick.. 61

3.1.3 Stronger top gates.. 65

3.1.4 Substrate supported SLG and dual gated devices...68

3.2 Suspension and Measurement of Graphene and Bi_2Se_3 Atomic Membranes.......................... 71

3.2.1 Fabricating in my dreams.. 71

3.2.2 Atomic membranes and special electrodes...72

3.2.3 The same novel trick but different order 73

3.2.4 Suspended graphene and superconducting electrodes..78

3.2.5 Suspended Bi_2Se_3 and superconducting electrodes...79

3.3 Fabrication of dual gates with suspended graphene...82

3.4 Post fabrication treatment of dual gates with suspended graphene 87

Conclusion 90

References...91

Chapter 4. : QHE in graphene *pnp* junctions

Introduction...94

4.1 Device Characterization.. 95

4.1.1 Sample improvement through annealing 95

4.1.2 Single gate quantum Hall (QH) response.. 97

4.2 SLG *pnp* junctions: *B*=0T.. 99

4.2.1 The *pnp* Conductance map.. 99

4.2.2 Fabry Pérot oscillations at a *pn* interface..100

4.3 SLG *pnp* junctions: *B*=8T.. 104

4.3.1 Equilibration of edge states in SLG *pnp* junctions.. 104

4.3.2 Aspect ratio and SLG QHE.. 107

4.4 Observation of Conductance Fluctuations (CF) on transitions between QH plateaus..........110

4.4.1 Coulomb-induced charging of electron or hole-doped localized states................116

4.4.2 Temperature dependence of CF..118

Conclusion 119

References..121

Chapter 5 QHE in Bilayer *pnp* junction

Introduction..123

5.1 Device Characterization 124

5.2 Comparison with suspended BLG devices.. 126

5.3 Two gates are better than one: *B*=0.. 129

5.4 Two gates are better than one: *B*=8T.. 135

5.4.1 Edge state equilibration in BLG *pnp* junctions: *B*=8T..135

5.4.2 Two insulating states in BLG *pnp* junctions..138

Conclusion 140

References..143

Chapter 6 BLG has an intrinsic gap at the Charge Neutrality Point (CNP)

Introduction..145

6.1 A second look at the band structure of BLG………………………………......................146

6.2 Device characterization – A tale of two device mobilities.. 148

6.3 Bias-dependent measurements... 151

6.3.1 Bias-dependent measurements at B=0T……………………………………………..151

6.3.2 Bias measurements at finite B……………………………………………………….153

6.4 Sensitive gap measurements………………………………………………………..155

6.5 Discussion.……………………………………………………………………………..158

6.6 Bias measurement of the ν=0 QH state………………………………………………..161

Conclusion ……………………………………………...164

References…..166

Chapter 7 Phase transitions in ultra clean BLG

Introduction..169

7.1 The different ground states of BLG...169

7.2 Device Characterization……………... 171

7.3 Bimodal distribution of devices.. 173

7.4 Temperature dependence of single gated devices.. 175

7.5 Suppressing the gap..177

7.5.1 Suppressing the gap by turning up the heat…...177

7.5.2 Suppressing the gap by reducing sample quality...178

7.5.3 Suppressing the gap by tuning n and $E_\perp$..179

7.6 Discussion ……………………………………………………………………………..180

Conclusion …………………………………………...182

References…...184

Chapter 8 The CNP in the QH regime

Introduction...187

8.1 The ν=0 QH state via a linear measurement... 188

8.2 Hysteresis at the ν=0 QH state…………………………….. 190

8.3 Discussion.…………………………………………………………………………..195

Conclusion …………………………………………...196

References…...198

Chapter 9 Bias spectroscopy at finite densities

Introduction...199

9.1. Broken Symmetry states in BLG...200

9.2. Bias spectroscopy measurements using a single gate... 201

9.3 Bias spectroscopy measurements using two gates.. 203

9.4 Model behind the measurement technique.. 205

9.5. Bias spectroscopy measurements of $\Delta_{\nu=\pm 4}$ 207

9.6 Bias spectroscopy measurements of the broken symmetry states…….................................. 209

9.7 Comparison between dual gated and single gated measurements and E_c............................. 211

Conclusion …………………………………………...214

References…...216

Chapter 10: Broken Symmetry States in dual gated ABA TLG

Introduction..........217

10.1 QHE in ABA TLG, sibling rivalry..........218

10.2 Device characterization..........219

10.3 The band structure of ABA TLG..........220

10.4 Single particle QH states in ABA TLG..........221

10.5 Interaction induced QH states in ABA TLG 224

10.5.1 QH states resolved with one gate 224

10.5.2 QH states resolved with dual gates, and the role of $E_{\perp}$..........226

Conclusion 229

References..........231

Chapter 11: Conclusion and Outlook

Conclusion..........234

11.1 Boron-nitride based graphene samples..........234

11.2 Outlook..........235

References..........238

Appendix 1: Janis fridge and magnet operation

Appendix 2 Exposure and development parameters

List of Figures

Fig 1.1: Flatland and Graphene lane a. Artistic rendition of Flatland by Edwin Abbott Abbott. b. Graphene lane an actual street in Tallahassee Fl...1

Fig 1.2: Graphene mother of all carbon allotropes. Graphene can be used to construct (left to right) C_{60} a carbon fullerene, a single wall nanotube and stacked to make graphite. 6

Fig 1.3: Anatomy of a Si-MOSFET. Grey region is the p-doped Si substrate, white regions are n-doped Si, and are beneath the metallic contacts (black) labeled source and drain. An insulating SiO_2 layer (beige) separates the top gate electrode (black) from the p-type Si. There is a gate electrode beneath the substrate. 9

Fig 1.4: Band bending. Left to right: semiconductor, oxide (gold) and metal. Grey region corresponds to Fermi energy and black line represents bands. 11

Fig 1.5: Band bending at a semiconductor heterostructure. Left to right: Gate (grey), n-doped AlGaAs, which is a wide band gap semiconductor, AlGaAs spacer, and GaAs a narrow band gap semiconductor. Band offset in AlGaAs causes bending in GaAs. AlGaAs is often used as a spacer at the interface to reduce momentum scattering from dopants. Image from http://en.wikipedia.org/wiki/File:HEMT-band_structure_scheme-en.svg 12

Fig 2.1: Crystal structure of SLG and Bravais lattice. (a) Honeycomb carbon lattice of graphene with *A* and *B* sublattices depicted as red and blue, respectively. Primitive lattice vectors a_1 and a_2 emanate from one unit cell. Shaded rhombus explicitly shows a unit cell comprised of both *A* and *B* atoms. (b) Hexagonal Bravais lattice comprised of *A* and *B* atomic basis. Primitive lattice vectors a_1 and a_2 allow for translational invariant motion along lattice.

....22

Fig 2.2: Reciprocal lattice. The reciprocal lattice is constructed from the primitive reciprocal lattice vectors b_1 and b_2. The shaded region is the Brillouin zone

....24

Fig 2.3: σ and π bonds. Three different types of bonds between adjacent carbon atoms. In plane, two sp^2 bonds form a σ bond. Out of plane, two p_z bonds form a π bond. Image copyright ThomsonBrooks Cole 2004

....25

Fig 2.4: Nearest neighbor hopping. Real space lattice depicting hopping from an *A* atom to surrounding *B* atoms. $\delta_{1\text{-}3}$ represents the hopping terms.

....27

Fig 2.5: Band structure of SLG. a. Full tight binding calculation for the band structure of SLG, with γ_o = 3.033eV, s_o=0.129. b. Cross section from a. at k_y=0, note *E* is degenerate at the K_+ and K_- points, and valence and conduction bands meet and touch at these points.

....29

Fig 2.6: First Brillouin zone. The first Brillouin zone is shown, and it has six corners. Reciprocal lattice vectors connect K_+ and K_- to corners above and below but not to each other. K_+ and K_- are inequivalent.

....30

Fig 2.7: Sublattice of SLG. The sublattice degree of freedom cast as pseudospin. In a. and b. occupation of only one sublattice corresponds to an up or down pseudospin state. In c. occupation of both sublattices is a superposition of both states.

....33

Fig 2.8: Pseudospin in SLG. The pseudospin is depicted as a green arrow and momentum as a black arrow. Chirality is the relation of the direction of pseudospin with the direction of the momentum. Due to pseudospin conservation backscattering is not permitted within a valley.

....34

Fig 2.9: BLG in real space. In a. the three dimensional view of BLG is rendered depicting A_1(red), B_1(blue) atoms on bottom layer and A_2(blue), B_2(green) atoms on top layer. In b. the top view of BLG is shown. Shaded region is the unit cell comprised of all four atomic orbitals.

....35

Fig 2.10: Band structure of BLG. Tight binding calculation for the band structure of BLG, with γ_o = 3.033eV, s_o=0.129, and γ_1 = 0.39eV at k_y=0. Note E is degenerate at the K_+ and K_- points, and valence and conduction bands meet and touch.

....38

Fig 2.11: Hopping. Hopping is depicted between nearest neighbor intralayer and interlayer atoms represented by γ_o and γ_1 respectively.

....38

Fig 2.12: Sublattice for BLG. The sublattice degree of freedom in BLG is cast as pseudospin. Note it can also be viewed as a layer degree of freedom. In a. and b. occupation of only one sublattice corresponds to an up or down pseudospin state. In c occupation of both sublattices is a superposition of both states.

....42

Fig 2.13: Band structure of gapped BLG. Tight binding calculation for the band structure of gapped BLG, with $\gamma_o = 3.033$eV, s_o=0.129, and $\Delta=\gamma_1 = 0.39$eV at k_y=0. Note Δ occurs at the K_+ and K_- points, image from.
....44

Fig 2.14: QHE in a conventional 2DEGS. a. Schematic of Hall and longitudinal voltage measurements for a conventional 2DEG in the presence of a perpendicular *B*. b. Hall voltage and longitudinal voltage plotted as a function of increasing *B* for a similar 2DEG. Notice plateau in Hall voltage and periodic behavior in the longitudinal voltage. c. Energy plotted as a function of density of states for a conventional 2DEGS as *B* increases. Note, energy becomes discrete as *B* is increased (Landau levels) images from wikipedia section on QHE.
....45

Fig 2.15: Hall conductance and energy plotted as a function of density in the QH regime for various 2DEG systems. a. The Hall *G* and energy spectrum as a function of density for a conventional 2DEG. Note, the equal spacing among states, and the absence of a state at zero density. b. The Hall *G* and energy spectrum as a function of density for SLG. Unique to SLG, a state is present at zero density, and it is shared between holes and electrons. Also, the spacing between states changes as a function of density. The Hall *G* and energy spectrum as a function of density for BLG, which contains characteristics from both a. and b. Finite density states are equally spaced apart, but the zero density state is shared by both holes and electrons, and possess twice the degeneracy of the lowest LL in SLG.
....47

Fig 3.1: Suspended structures. a. A suspended graphene sample held up by four contacting electrodes made by [1]. This method uses a PMMA mask to only remove the oxide beneath the graphene while leaving the surrounding oxide intact. b. A suspended BLG sample clamped on by two contacting electrodes made by [4]. This method employs exfoliation onto pre-deifned trenches to suspend graphene, and a shadow mask to selectively deposit metal onto graphene for electrodes. c. A suspended top gate straddles from above a substrate supported graphene flake, made by [6]. This method utilizes a multi-level lithography technique to fabricate contactless top gates. d. A suspended top gate straddles from above a suspended graphene flake made by [9]. This

method combines a variation on the technique from fig 3.1a and 3.1c(see ch. 3 for references).
....57

Fig 3.2: Dual gated graphene structures with. a. Substrate supported graphene sample is contacted by two metallic leads and a layer of PMMA rests on top of graphene supporting the metallic top gate. The PMMA is stiffened by a procedure called cross-linking, which is simply a large exposure of 30,000 Kv, image from[12]. b. Substrate supported graphene sample is contacted by two metallic leads, and a 20 nm layer of HSQ(a negative resist) and 15 nm of HfO_2 that rests on top of graphene supporting the metallic top gate. The HSQ was spun onto the chip while the HfO_2 was grown by atomic layer deposition, image from[13] c. Substrate supported graphene sample is contacted by two metallic leads, and a 15 nm layer of SiO_2 rests on top of graphene supporting the metallic top gate. The SiO_2 was deposited via electron beam evaporation, image from[19]. d. Substrate supported graphene sample is contacted by two metallic leads, and a NCFL (non-covalent functionalized layer) and a 30 nm layer of $Al_2\ O_3$ that rests on top of graphene supporting the metallic top gate. Both layers were grown by atomic layer deposition, image from[10].
....60

Fig 3.3: Schematics of fabrication process. a. LOR blue and PMMA brown are deposited onto the substrate and exposed to electron beams arrows. b. Developing in MIBK and MIF319 solutions opens windows for the electrodes. c. Lift-off in acetone removes PMMA but leaves LOR layer intact. d. MMA green and PMMA brown are deposited, and exposed to electron beam arrows. e. Developing in MIBK opens windows for the electrodes and the suspended structure. f. Metals are evaporated at 45° and −45° in directions indicated by arrows in e. In g. Resists are lifted off in PG remover, leaving an air bridge contacted to electrodes.
....62

Fig 3.4 Schematics of angle evaporation at 45˚ and -45˚. a. Front view of metal bracket (orange) with a sample (purple) secured onto it in the two evaporation orientations. b. Top view of a. In c-d bracket is secured on the top part of bell-jar (black line), which is in the evaporator (gray box) directly perpendicular to the metal source in the two different orientations.
....64

Fig 3.5: Finished top gates. SEM images of suspended air bridges with different spans, widths, and heights. Scale bars: 2 μm.
....65

Fig 3.6: Schematics of third step evaporation. a. SEM image of a completed top gate, using two-step method, showing thin sidewalls. b. Schematic representation of third step evaporation with red arrow symbolizing metallization. c. Schematic representation of sample mounted on bell jar in evaporator. d-e two step and three step evaporation results of top gates. Third step displays stronger joints.
....66

Fig 3.7 Top gate dried with critical point dryer. a. Angled SEM image of a titanium top gate ~50nm above the substrate. b. Aluminum top gates with a suspended portion that is between 15~30μm and a height of 300nm. c. Aluminum top gate with a height of 300nm and suspension length of 40 μm, record for Lau group.
....67

Fig 3.8: Graphene based dual gated device. a. Detailed schematic of a device, graphene (pink) resting on SiO_2 substrate(lavender) is coupled to Ti/Al electrodes(yellow), while titanium contactless top gate (grey) straddles graphene flake. b. SEM image similar to schematic.
....69

Fig 3.9: Angled top gate devices. a. Schematic of a chip (purple) containing a device (grey and not to drawn scale) mounted onto angled bracket(gold), which is seen from top view. Chip is tilted along dashed line, which aligns device with the dashed line. SEM images of an angled top gate device where the metallization was performed with procedure demonstrated in schematic. 70

Fig 3.10: SEM images of top gates under applied voltage. SEM images of a suspended top gate under applied voltages of 70, 100 and 110V,respectively. 70

Fig 3.11: Schematics of fabrication process. a. Thin Crystal (TC) is exfoliated onto LOR (yellow) which rests on SiO_2/Si substrate (purple). b. Bilayer MMA/PMMA (light gray) resists are deposited onto sample, and alignment cross marks are patterned by EBL. A second EBL is performed to expose regions indicated by the red arrows. c. Developing in MIBK and MF319 removes both LOR and MMA/PMMA bilayer in the exposed regions. The final EBL step is performed to expose regions indicated by the red arrows. d. Developing in MIBK removes only the MMA/PMMA resist bilayer in the exposed regions. e. Metal deposition is performed at +45°, - 45° and 0° using Ti/Al (dark gray). Samples are then immersed in warm PG remover and dried using a critical point dryer, leaving suspended electrodes that “hold” TC above the substrate. 74

Fig 3.12: SEM images and transport data of suspended graphene devices. a-d. SEM images of suspended graphene sheets with different widths and lengths. Scale bars: 1 μm. Inset: a 40-μm long graphene sheet suspended by several electrodes. e-f. Device conductance as a function of gate voltage for two different suspended graphene devices. Red and black traces are for as-fabricated and current-annealed devices, respectively.

....78

Fig 3.13: SEM images and transport data of a suspended Bi_2Se_3 device. a-b. Top and angled view of a suspended Bi_2Se_3 device. Scale bar: 1 μm. The images are false-colored. c. Current measured as a function of voltage bias at 300K (red) and 4K (blue).

....81

Fig 3.14: Schematics depicting the importance of undercut. a. Schematic overlaid on SEM image of a device. Yellow (dotted line border) and red polygon (solid line border) represents the windows opened in PMMA and MMA after exposure and development, respectively. Light purple regions depict resist that is intact and the brown rectangle is the already present top gate. Note it is of paramount importance that the red polygons are separated from the top gate by MMA. b-g. Schematic cross section view of already present top gate (brown), MMA (lavender) and PMMA (purple) resists. The group of schematics b,d,f and c,e,g, respectively, represent a possible arrangement for resists and top gate. Schematics b and c are each an arrangement before exposure and development. Schematics d,f and e,g are each distinct arrangements after exposure, and the white region with dotted line borders represent the removed resist after exposure and development. For the first and second case d and e, respectively, depicts the unwanted outcome where no resist surrounds the top gate, and solvent can enter and compromise the structure. For the first and second case f and g, respectively, depicts the desired outcome where resist surrounds the top gate, and solvent cannot enter, hence the structure remains in tact.

....84

Fig 3.15: SEM images and schematics of device fabrication. a. Graphene (pink) resting on SiO_2 substrate (lavender) is coupled with chrome/gold electrodes (yellow), while chrome contactless top gate (red) straddles graphene flake. b. Red arrow illustrates completed device in a, and is immersed in hydrofluoric acid and then dried with critical point dryer (not shown). c. Using the same color scheme as in a., graphene is freestanding and clamped at the ends by Cr/Au electrodes and remaining SiO_2 substrate, while the chrome contactless top gate straddles graphene flake.

....86

Fig 3.16: Current annealing. a. Voltage bias is applied on source-drain electrode, top gate is floated, V_{bg}=0 and current is monitored. b. $G(V_{bg})$ measurements after each current annealing session, black is before any annealing, red is after the first session and green is after the last attempt.

....88

Fig 3.17: Single gate transport data at B=0 and T=300mK a. Resistivity plotted as a function of charge carrier density that is modulated by V_{bg}. b. Resistivity plotted as a function of charge carrier density that is modulated by V_{tg}. Both exhibit minute CNP offset suggesting minimal charge impurity doping.

....89

Fig 4.1: Device schematic and characterization. a. Device schematic with each component labeled: graphene (blue honeycomb lattice), electrodes (gold), top gate (silver), SiO_2 (purple), Si (blue). b. Local heater anneal, blue line represents before annealing and red line after annealing. c. Transport measurements at 300mK, $G(V_{bg},B)$ with color scale denoting conductance. d. Line trace $G(V_{bg})$ from c. at 8T.

....96

Fig 4.2: SLG transport data at $B=0$. a. $R(V_{bg}, V_{tg})$ of a double-gated SLG device. b. Line traces of a. from purple to red, V_{tg}=-30, -20, -10, 0, 10, 20, 29.5V, respectively.

....99

Fig 4.3: Transport data in B=0T. a. Four-terminal device resistance as functions of V_{bg} and V_{tg}. The arrows indicate oscillations in the *npn* region. b. Same data as a, but plotted against n_2 and n_1. c. Line trace along the dotted line in b, showing resistance oscillation as a function of n_2. d. The peak spacing Δn_2 vs. $\sqrt{n_2}$. The line represents a linear fit to the data.

....102

Fig 4.4: Schematics of edge state propagation. Edge state transport in the quantum Hall regime for different values of ν_1 and ν_2. Region 1 denotes back gate controlled only and both V_{bg} and V_{tg} control region 2.

....104

Fig 4.5: Theory and experiment for QHE of graphene *pnp* junctions. a. G(ν_1,ν_2) theoretical map displaying conductance plateau for different combinations of ν_1 and ν_2^2. b. G(V_{bg},V_{tg}) experimental map depicting conductance plateau. Note data reproduces right quadrant of a. c. G(V_{tg}) line traces from b. Note several plateau reproduce those predicted from a.

....106

Fig 4.6: Transport data at B =8T. a. Two-terminal device conductance G versus n_1 and n_2. b. Line trace along the green dotted line ν_1 =2 in a. c. The solid red curve is a line trace taken along the magenta dotted line $n_2 = n_1$ in a. The dotted line is a theoretical curve calculated using the expressions in [20] (see ch. 4 for references), L/W=3.5 and of the longitudinal resistivity in density.

....107

Fig 4.7: High resolution scans between conductance plateau. a. $G(V_{bg},V_{tg})$ with high resolution in gate voltage. b. dG/dV_{tg}(V_{bg},V_{tg}) by differentiating data in a. c. red line trace along the dotted line in a. the blue curve taken with medium V_{tg} resolution and offset for clarity.

....110

Fig 4.8: Differentiated Fan Diagram. dG/dV_{bg}(V_{bg},B) taken from a fan diagram not shown. Smooth areas correspond to conductance plateau rough areas are the transitions between different plateau. Dotted lines indicate the trajectory of QH plateau: 2,6 and 10 e^2/h. There are Lines parallel to these plateau but they are lesser in magnitude than dG/dV_{tg}(V_{tg},B) scans.

....111

Fig 4.9: Conductance fluctuations (CF). a. dG/dVtg(V_{tg}, B) at V_{tg},=2.5, or ν_1= 2. b. dG/dVtg (V_{tg}, B) at V_{tg}, =14 or ν_1 =6. The dotted lines indicate the trajectory of the QH plateaus in the locally gated area.

....113

Fig 4.10: CF in the QH regime for Si-MOSFETS. a. $G(V_g)$ displays CF at transitions between plateaus, similar to fig 4.5 in SLG. a-b. $dG/dV_g(B,V_g)$ displays both rough and smooth regions similar to fig 4.7.

....114

Fig 4.11: Visualization of disorder potential and formation of quantum dots. a. The density profile $n(x,y)$ and electrostatic potential profile $\phi(x,y)$, calculated self-consistently within the Thomas-Fermi scheme, for an almost empty (I), half full(II) and almost full(III) Landau level see ch. 4 for reference. At high magnetic fields, the edge channels in a 2D electron system form compressible and incompressible strips, with contours that generally follow the local potential landscapes. b. Schematic representation of formation of a quantum dot in a SLG sample. When a incompressible strip surrounds a compressible region a quantum dot is formed. Charging of the quantum dot is independent of B since it arises from disorder potential.

....116

Fig 4.12: CF temperature dependence measurement. a. $G(V_{tg})$ for a transition between the ν_2=2 and ν_2=6 plateaus. From right to left, T=0.26, 0.31, 0.42, 0.53, 0.76, 0.95, 1.43, 1.61, 1.72, 2.35 and 3.8 K. The traces are offset for clarity. b. T-dependence of G_p (red squares) and G_d (blue dots). The green line is a fit using eq 4.3.

....118

Fig 5.1: Transport measurements with a single gate at B=0~8T. a. $G(V_{bg})$ for a bilayer graphene device at T=260 mK and B=0. b. $G(V_{bg})$ of the device at B=8T. c. LL fan diagram $G(V_{bg},B)$ of the device. d. $dG/dV_{bg}(V_{bg},B)$ from c.

....124

Fig 5.2: Transport measurements of a suspended BLG sample with one gate in finite B. a. $G(B,V_{bg})$ of the device. b. $G(V_{bg})$ from a. at B= 0.6, 1.2, 1.6T note single particle QH states are

visible. c. $G(V_{bg})$ from a. at B=4, 4.6, 5.4, 6.4, 11, 18T, note new integer QH states are seen not present in fig 5.1 126

Fig 5.3: Transport measurements with two gates at B=0T. a. $G(V_{bg},V_{tg})$ of the device at B=0. The junction polarities are indicated on the graph. b. Data in a. plotted in terms of E_2 and n_2. Note the logarithmic color scale. c. (Top to bottom) Line traces $G(n_2)$ at E_2=0.21, 0.49, 0.65 and 0.73 V/nm. d. $R(E_2)$ at n_2=0. The line is a fit of the data to the Variable Range Hopping model, $R=R_0 + A\exp[-((4\pi e)/(k_B)aV_2)^{1/3}]$
.... 129

Fig 5.4: Schematic for variable range hopping. Vertical axis is energy and horizontal axis is position. White and red rectangles represent empty conduction and filled valence bands, respectively. Blue region depicts energy gap between bands and white dots are charge trap sites. In the absence of charge traps a pure gap exists. When charge traps are present electrons from valence band can traverse the gap by hopping through charge traps. This hopping depends on the distance and energetic spacing between the charge traps. At small separations or energetic differences hopping is facilitated.
.... 133

Fig 5.5: Transport measurements with two gates at B=8T. a.$G(V_{bg},V_{tg})$ of the device at B=8T. b. Line trace at ν_1=4, i.e., along the red dotted line in a. c. Line traces $G(V_{tg})$ at ν_1=8 (yellow) and ν_1=12 (purple). d.$G(V_{bg})$ with V_{tg}=0(red) and V_{tg}= (blue). Latter measurement displays resolution of several plateaus that start to appear in first measurement.
.... 136

Fig 5.6: Insulating state induced by B. a. $G(V_{tg},B)$ at V_{bg}=19V. b. Data in a differentiated with respect to V_{tg}. c. Line trace $G(B)$ taken at V_{bg}=19V and V_{tg}=-27V. The blue line is a fit to an exponential function.
.... 138

Fig 5.7: Transport measurements of a suspended BLG sample in finite *B*. a. $G(B)$ of the device at CNP. b. $G(E,n)$ at B=1.3T c. $G(E,n=0)$ from a. note two distinct insulating states not seen in fig 5.5a...141

Fig 6.1: Spin-valley configurations of the electrons in BLG for several possible phases. Here red (blue) arrows indicate electrons from the *K* (*K'*) valley.
....146

Fig 6.2: Transport measurements in finite *B* and at 260mK. a. Differential conductance G=dI/dV vs. *B* and V_{bg} showing the Landau fan diagram. b. Line traces $G(V_{bg})$ along the dotted line in c. at B=1.3, 2.8 and 6T, respectively.
....148

Fig 6.3:Dual gate transport data at B=0 and T=300mK for two different devices. a. $G(n, E)$ and line traces $G(n)$ at E=85, 71, 57, 42, 28, 14, 0, -14, -28, -42, -57, -71, -85 mV/nm, respectively (left to right). The line traces are laterally offset for clarity. b. $G(n, E)$ and line traces $G(n)$ at E=-37.5, -25, -12.5, 0, 12.5, 25 and 37.5 mV/nm, respectively (left to right). The line traces are laterally offset for clarity.
....150

Fig 6.4: Bias measurement at B=0 and T=300mK with two gates. a-b. Large range $G(V, E_\perp)$ and line trace $G(E_\perp)$ at n=0. b. High resolution $G(V, E_\perp)$ for small bias range at n=0. d. Line traces $G(V)$ along the dotted lines in b at $E_\perp$ =0 and -15 mV/nm, respectively.
....151

Fig 6.5: Transport data in magnetic field at n=0 and $E_\perp$=0. a-b. $G(V,B)$ and line traces $G(V)$ at B=-0.4 (red), -0.2 (orange), 0 (green), 0.2 (blue) and 0.4 T (purple), respectively. c. Large range $G(V,B)$. The dotted line plots Eq. (6.2) with Δ_o=1 meV, and a=5.5 meV/T. d. Line traces $G(V)$ at B=2 (red), 3 (orange), 4 (green), 5(cyan) and 6T (blue). Inset : Current-voltage characteristics at B=8T.
....153

Fig 6.6: G (V_{bg}) with different measurement configurations. Red curve is at a sweeping rate of 0.1V/step in V_g before the correction of ~0.4 mV dc offset. Blue is after correcting for the offset but still at the same sweeping speed. Green is after dc-offset correction and with a sweeping rate of 0.03 V/step.
....155

Fig 6.7: Transport Data of BLG devices. a $G(V)$ for the device of the main text at $E_\perp$=0 (red), $E_\perp$=-5mV/nm (green) and $E_\perp$=-9mV/nm (blue), (b-c) $G(V)$ for two additional devices at CNP and $E_\perp$=0.
....157

Fig 6.8: Transport data at constant B. a. $G(n, E)$ at B=3.5T. b-c, Line traces $G(n)$ along the dotted lines in a at E =0 and -20 mV/nm.
....161

Fig 6.9: Bias measurements with applied fields. a-c. $G(V,E_\perp)$ at B=1.3T, 2.6T and 3.6T, respectively. d. Critical electric field $E^*_\perp$ vs. B. The blue line is a best-fit to data, with a slope of 12.7 mV/nm/T.
....162

Fig 6.10: $G(E_\perp,B)$ at 250mK. The diagonal green band is a conductive segment that separates the 2 insulating (blue) regions, with a slope of ~10.5 mV/nm/T.
....164

Fig 7.1: SEM images of devices and transport data. a. and b. false-color scanning electron micrograph of BLG device with and without top gate. Scale Bar: 2μm. c-d. main panels and insets: σ (V_g) and $G(V_{bg},B)$ for two BLG devices with and without insulating state at CNP (T=1.5K). Both samples are single gated.
....171

Fig 7.2: Characteristics of several substrate supported and suspended BLG devices. a. $\sigma_{min}(\mu)$ for 9 substrate supported BLG devices (square symbols) and 23 suspended BLG devices (triangular

symbols). b-c. $\mu(V_{CNP})$ and $\sigma_{min}(V_{CNP})$ for suspended BLG devices. The blue symbols denote devices in region II.

....173

Fig 7.3: Temperature dependence measurements at CNP. a. $\sigma_{min}(1/T)$ for insulating and noninsulating single gated BLG devices. Inset: $\sigma_{min}(T)$ of data set. The solid lines are fits to data T<5K to Eq. (1). b. T-dependence of $\sigma(V_{sd})$ at CNP for an insulating-BLG device.

....175

Fig 7.4: Suppression of gap by several parameters. a. $\sigma(V_{sd})$ for insulating and noninsulating-BLG devices at the CNP. b. $\sigma(V_{sd})$ at n=0 for a doubly gated BLG at $E_{\perp}$=0, -5, -7 and -15 mV/nm. c. $\sigma(V_{sd})$ at $E_{\perp}$=0 for a doubly gated BLG at different values of n. d. Magnitude of flavor gap vs. n calculated from MFT.

....178

Fig 7.5: Band structure calculation shows gap suppression by increasing $E_{\perp}$. a. Small finite $E_{\perp}$, increases gap in one valley while diminishing it in the other. b. Further increase of $E_{\perp}$ closes gap in one valley completely. c. Continued increase of $E_{\perp}$ induces a transition into a flavor-layer polarized state that is also gapped. Band structures calculated using MFT by Fan Zhang.

....182

Fig 8.1: ν=0 and gap Δ measurement. a. $G(V_{bg},B)$ fan diagram for suspended BLG device at T=260mK. b.$G(V_{bg})$ from a. at the CNP, device image inset. c. $G(V_{sd},B)$ at the CNP and at T=260mK. d. IV traces at finite B. The red line trace is an actual IV measurement at B=8T, while the orange line trace(8T), yellow line trace(7T), and green line trace (3T) are dI/dV measurements from c. that were numerically integrated.
....188

Fig 8.2: B induced switching between conducting and insulating state. a. $I(B)$ with the device at

CNP and at V corresponding to the conducting branch of IV profile in fig 8.1d. b. $I(B)$ with the device at CNP and at V corresponding to the insulating branch of IV profile in fig 8.1d. 190

Fig 8.3: Hysteresis loops with increasing B. a. $I(V)$ up and down sweeps at the CNP and at B=0T(red), B=1T(green) and B=8T(blue). At B>2T the hysteresis loops are visible. b. Plot of hystersis loop size as a function of increasing B, with loop size on log scale......................190

Fig 8.4: Suppression of Hysteresis loops with increasing $E_{\perp}$. $I(V)$ up and down sweeps at the CNP and at B=8T. Different line traces correspond to increasing $E_{\perp}$, with $E_{\perp}$=0(red), $E_{\perp}$~0.1mV/nm(green), and $E_{\perp}$~0.5mV/nm(blue). 192

Fig 8.5: Suppression of hysteresis loops with increasing T. a. $I(V)$ up and down sweeps at the CNP and at B=18T. Direction of sweeps and inflection points are labeled. Different traces correspond to different T, with T=260mK(red), T=20K(green), and T=60K(blue). c. Movement of V_r(blue) and V_c(red) with increasing T. 193

Fig 8.6: Distribution of V_r and V_c at 260mK. a. Distribution of V_r from 100 up and down sweeps performed in tandem at 260mK. b. Distribution of V_c from 100 up and down sweeps performed in tandem at 260mK. Sweeps are not exactly similar, which is suggests stochastic behavior. 194

Fig 8.7: Tilted washboard potential. a. Washboard potential and ball with V=0. Minima represents the insulating state in our measurement, while slopped region represents the conducting state. b. increasing V tilts the potential as shown, in this case $0<V<V_c$. c. $V_c<V$, hence ball moves freely. The double sided blue arrow represents thermal fluctuations, which modify V_c and V_r. 195

Fig 9.1: Measurement schematics and bias measurements with a single gate. a. Measurement schematic depicting suspended BLG(pink) clamped on at the ends by electrodes(gold), which are

supported by remaining SiO_2 substrate(purple), and V_{bg} applied by Si below BLG, and V_{tg} applied by chrome air bridge above BLG. Source is biased by an AC and DC voltage simultaneously. b. False colored SEM image of device: electrodes are green, top gate is purple and graphene is pink. c. $G(V,V_b)$ measured at 250mK and B=1.3T. d. Line trace from $G(V_{bg},B)$ of fig 6.1 in chapter six with plateau that align in V_{bg} with diamonds in c.
....201

Fig 9.2: Bias measurements with dual gates at $E_\perp$=0, and in the QH regime. a. $G(V,n)$ at $E_\perp$=0 and B=2.5T and T=260mK. b. $G(V,n)$ at $E_\perp$=0 and B=3.5T and T=260mK. c. Line trace $G(V=0, n)$ from a. and b. d. Vertical line traces from a. and b. at n=-2.4x10^{11} and 3.5x10^{11} cm^{-2},respectively. e. Vertical line traces from a. and b. at n=-1.8x10^{11} and 2.63x10^{11} cm^{-2}, respectively.
....203

Fig 9.3: Model for bias spectroscopy. a. Red lines correspond to discrete energy bands (LL) plotted as a function of position, and the rectangle with dashed lines are the electrodes, light blue region is the Fermi energy E_f. Modulation of gates adjusts $E_\perp$ and E_f. When BLG E_f is tuned to above a LL transport is dominated by edge states. Adjusting bias allows access to the next unfilled LL, hence at zero bias there will be a dip. On the other hand, when E_f in BLG is tuned to an empty LL the transport is dominated by the bulk. Adjusting bias detunes BLG from the bulk transport, and results in a peak at zero bias.
....205

Fig 9.4: $\Delta_{\nu=-4}(B)$ at $E_\perp$=0 and finite $E_\perp$. The $\Delta_{\nu=-4}$ was acquired from $G(V,n)$ maps at finite and zero $E_\perp$. The gap size is linear with increasing B and independent of $E_\perp$.
....207

Fig 9.5: Bias spectroscopy measurements of broken symmetry states. a. $G(V,n)$ at B=3.5T and $E_\perp$=-14.4 mV/nm. b.-c. $G(V)$ at ν=-2 and -1, respectively, from a. d. $\Delta_{\nu=-2}$ and $\Delta_{\nu=-1}$ plotted as a function of increasing B, and at finite and zero $E_\perp$.
....209

Fig 9.6: Dual gated transport measurements in the QH regime, and at 260mK. a. $G(E_\perp,n)$ at

B=1.3T. b. $G(n)$ at $E_{\perp}$=0(red), $E_{\perp}$=-8 mV/nm (green), and $E_{\perp}$=-14.4 mV/nm(dotted blue line). Note, ν=±2 states emerge at $E_{\perp}$=-8 mV/nm and are stabilized with increasing $E_{\perp}$.
....212

Fig 9.7: Dual gated transport measurements in the QH regime, and at 260mK. a. $G(E_{\perp},n)$ at B=6T. b-c. $G(E_{\perp})$ at ν=1(red) and ν=2(green). Note, ν=1 and 2 exhibit sharp transitions driven by $E_{\perp}$.
....214

Fig 10.1:Before and after current annealing. a-b. $G(V_{bg})$ and $G(V_{tg})$ before(blue) and after(red) current annealing.
....219

Fig 10.2: The band structure of ABA TLG. a. Low energy band structure of ABA-stacked TLG calculating (left panel) using only γ_0 and γ_1, (right panel) using $\gamma_0 - \gamma_5$. b. ABA-stacked TLG lattice with hopping parameters γ_1-γ_5.
....220

Fig 10.3: Transport measurements at 260mK and in the QH regime. a-b. $G(V_{bg},B)$ and dG/dV_{bg} of a TLG device. Numbers indicate filling factors. c. $G(V_{bg})$ and $G(n)$ at B=1.5, 2.2, 3.5 and 4.2 T, respectively. d. $G(V_{bg})$ and $G(n)$ at B=4.5, 6, 7, 8 and 10 T.
....221

Fig 10.4: Transport measurements at 260mK and in the QH regime. e. $G(V_{bg},B)$ and $G(n)$ at B=10, 12, 14, 16 and 18T.
....224

Fig 10.5: Transport measurements at 260mK, and in the QH regime with dual gates. a-c. $G(n,E_{\perp})$ at B=5.5, 14 and 8T. d. $G(E_{\perp})$ along the vertical line in c. at n=0. e. $G(n)$ along the horizontal lines in c. at $E_{\perp}$=0 (red), 43 (green dotted line) and 73 mV/nm (blue), respectively.
....226

Fig 10.6: Critical electric field E_c plotted as a function of increasing B. $E_{\perp c}(B)$ from 3 different devices. The black and orange lines correspond to linear and $B^{1/2}$ fits, respectively. 227

Fig 10.7: Transport measurements at 260mK, and in the QH regime with dual gates. a. $G(n,E_{\perp})$ at B=7T. b. $G(n)$ at $E_{\perp}$=0 (red solid line), -17 (green dotted line) and13.6 mV/nm (blue dashed line). 229

List of Tables

Table 6.1. Attributes of possible ordered states in BLG at $n=E_{\perp}=0$.

....146

Table 9.1: Measured gap sizes for ν=-2 and -1. Listed are gap sizes for ν=-2 and -1 from two previously reported single gated studies, and from our single and dual gated study. Our gap size measurement with intentional applied E is similar in value to the first reported single gated study. 211

Chapter 1: Introduction

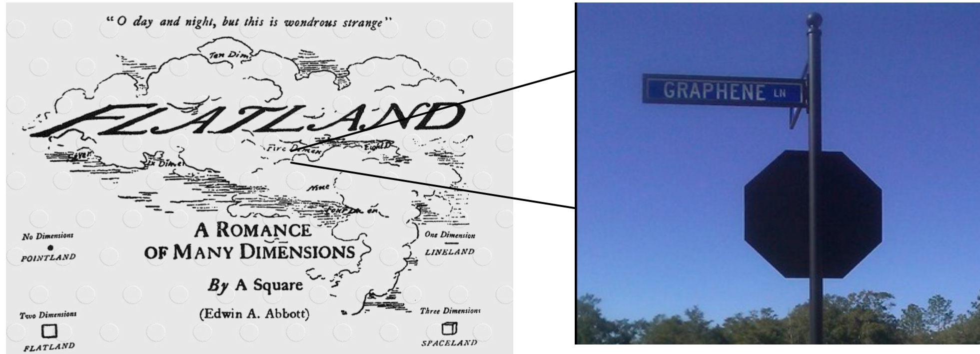

Fig 1.1: Flatland and Graphene lane: a. Artistic rendition of Flatland by Edwin Abbott Abbott. b. Graphene lane an actual street in Tallahassee Fl.

In 1884 Edwin Abbott Abbott wrote a fictional account about a four sided polygon named Square that is constrained to live in a two dimensional plane called Flatland[1]. The story is narrated from Square's point of view and details the social hierarchy and physical consequences of living in Flatland. As the novel progresses Square visits other lands of different spatial dimensions, such as Pointland, Lineland, and Spaceland. In his travels he learns about the physical consequences and differences between each realm. Astoundingly, this intellectual curiosity on the effect of dimensionality predates the major scientific revolutions, relativity and quantum mechanics, that provided the scientific framework for the actual exploration of low dimensional materials.

More than a century later researchers from many different disciplines are studying an actual two-dimensional plane called graphene[2]. Unlike Square's adventures,

these stories and adventures unraveling each day in the world's academic and industrial labs are not fictional, and represent a significant international effort. This thesis is a chronicle of my brief adventure with samples that I fabricated and then measured.

Chapter one begins with a short discussion on physical and electrical dimensionality followed by a brief overview of two-dimensional systems before the isolation of graphene. This knowledge provides a better appreciation of graphene and all of its wonderful electrical properties. Chapter two presents the theoretical background of SLG and BLG, focusing mainly on those based on tight binding calculations. Chapter three describes innovative techniques of fabricating high quality graphene devices with suspended structures, including dual gated graphene devices that are suspended or supported on substrates.

In chapter four we discuss conductance G measurements of substrate-supported single layer (SLG) *pnp* junctions, with suspended top gates, and in the QH regime. The devices display well-developed G plateaus at uniform charge density n, and in high magnetic fields B robust fractional valued plateaus at non-uniform densities are seen, which are in excellent agreement with a model based on equilibration of edge states. Interestingly, the same device types exhibit prominent conductance fluctuations on transitions between quantum Hall(QH) plateaus as the top gate voltage V_{tg} is varied. In the V_{tg}-B plane, the fluctuations form crisscrossing lines that are parallel to those of the adjacent plateaus, with different temperature dependences for the conductance peaks and valleys. These fluctuations arise from Coulomb-induced charging of electron-or hole-

doped localized states when the device bulk is delocalized, underscoring the importance of electronic interactions in graphene in the QH regime.

Chapters 5 through 9 focus on experiments on bilayer graphene (BLG). Chapter five extends our study of *pnp* junctions to BLG on substrate. These dual-gated structures offer *in situ* control of the n and type of different regions, as well as independent tuning of n_2 and applied electric field E_2 for the region under the top gate. In contrast to SLG, increasing E_2 drastically affects transport properties of BLG: at the CNP the device's conductance decreases exponentially as E_2 is increased. At large B, we observe quantum Hall conductance with fractional values, which arise from equilibration of edge states between the differentially doped regions. Additionally, we observe an insulating state that develops at filling factor ν=0, whose conductance is exponentially dependent on B. Hence, competing symmetries and insulating states in bilayer graphene can be tuned by E and B.

Chapter six continues our study of BLG using ultra-clean double-gated suspended samples. The unprecedented sample quality allows access to the electron-electron interaction effects that arise from the flat bands in BLG. Using source-drain bias as a spectroscopic tool we resolved an intrinsic gap of ~2 meV at the CNP; this gap can be closed by an electric field $E_\perp$ of either polarity, but increases monotonically with B, with an apparent particle-hole asymmetry above the gap. Our efforts are the first spectroscopic mapping of the spontaneous gap in the presence of both E and B, and provide insight into the underlying symmetries of this correlated electron phenomena.

In chapter seven we perform a systematic study of the minimum conductivity σ_{min} in a large number of single-gated and double-gated BLG samples, with a large range of different mobilities. We found a constant finite σ_{min} value for the majority of devices, independent of device mobility and the presence or absence of substrates. Interestingly, for the devices with highest mobility and smallest CNP offset an insulating state with an energy gap manifests. In these samples we found a transition between conducting and insulating states, which can be driven by disorder, temperature, n, and $E_{\perp}$. We attribute this observation to a phase transition tuned by T, and a quantum phase transition tuned by disorder, n and $E_{\perp}$.

In chapter eight we focus on current voltage (I-V) measurements at finite and zero $E_{\perp}$ in the QH regime. We found the IV profile is reminiscent to the VI profile of Josephson junctions. At the largest B, and at $E_{\perp}=0$, we find an intriguing hysteretic behavior in I, when V is swept up and down. This hysteresis can be quenched with increasing temperature T and $E_{\perp}$. To explain these observations we use a qualitative picture of a particle in a double-well potential, where V tilts the potential. This crude model explains most of the features seen in our data.

In chapter nine we discuss transport spectroscopy measurements of Landau level gaps in dual-gated suspended BLG at finite carrier densities. By plotting the device's two-terminal differential conductance $G=dI/dV$ as a function of V and n we observed a series of distinct diamonds. These diamonds arise from charge transport across graphene when the Fermi level is aligned to or detuned from Landau levels in the bulk of the device, and yield information on the bulk gap and edge channel transport. Using this

technique, and exploiting our additional gate, we measure the evolution of single particle and broken symmetry QH states with *B*(in the QH regime) in zero and finite $E_{\perp}$. We find the single particle states are independent of $E_{\perp}$ and in agreement with prior theoretical and experimental results. In contrast, the broken symmetry states are strongly $E_{\perp}$-dependent. Our results demonstrate a new simple and direct transport measurement of Landau level gaps, and provide valuable insight into the QH ferromagnetism in BLG.

In chapter ten we discuss transport measurements on dual-gated suspended ABA-trilayer graphene in the QH regime. We observe QH plateaus at filling factors in agreement with the full-parameter tight binding calculations. In high *B*, odd-integer plateaus are also resolved, indicating almost complete lifting of the 12-fold degeneracy of the lowest Landau levels (LL). These odd integer plateaus cannot be accounted for by any tight binding model, and their appearance at high *B* values in samples with high mobility strongly suggests symmetry breaking arising from electronic interactions. Under an out-of-plane electric field $E_{\perp}$, we observe degeneracy breaking and transitions between QH plateaus. Interestingly, depending on its direction, $E_{\perp}$ *selectively* breaks the LL degeneracies in the electron-doped or hole-doped regimes. Our results underscore the rich interaction-induced phenomena in ABA TLG.

Section 1.1: Dimensionality

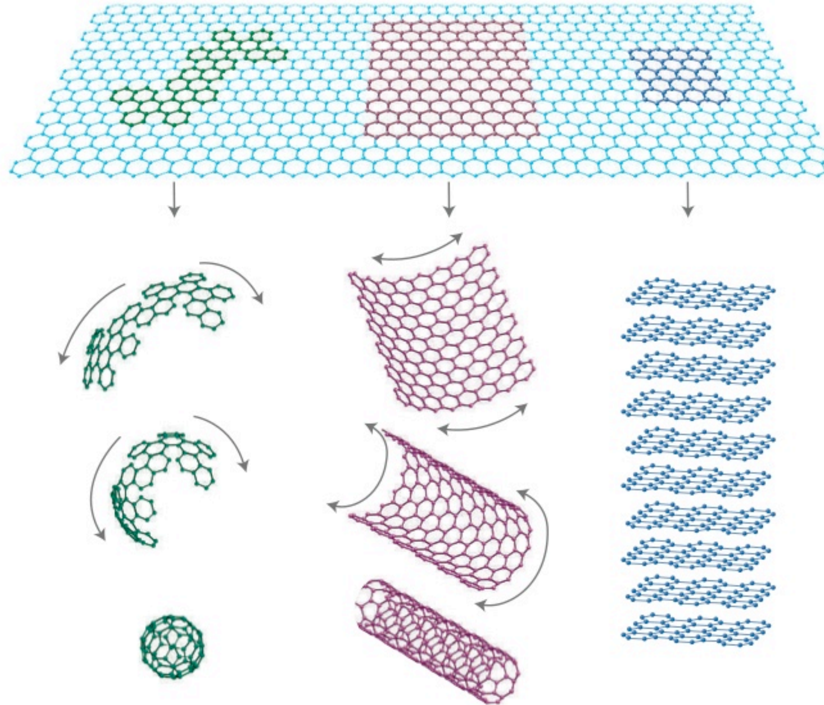

Fig 1.2: Graphene mother of all carbon allotropes. Graphene can be used to construct (left to right)C_{60} a carbon fullerene, a single wall nanotube and stacked to make graphite.

Physical dimensionality is illustrated by the various carbon systems shown in fig 1.2[3]. The first allotrope graphene, is constructed beginning with a basic unit of six carbon atoms arranged in a honeycomb that is then repeated to form a lattice. As a theoretical construct it is undoubtedly two-dimensional, in fact it is the quintessential physical Flatland since the out of plane dimension is atomic in scale.

Interestingly, graphene is the starting point for the other allotropes, both physically and electrically, and is a perfect analogue for the realms that Square visited in

his travels. For instance, Fullerenes are molecules comprised of carbon atoms that are arranged spherically, and hence, from a physical standpoint are zero-dimensional, similar to Pointland. Introducing pentagons in addition to hexagons in this structure, and using only 60 carbon atoms, leads to the well-known molecule C_{60} or the Buckeyball. This structure is reminiscent of the classic soccer ball design and the geodesic structures created by the architect Buckminster, hence the name Buckeyball. A single wall carbon nanotube is created when one end of the carbon sheet is rolled up along a specific direction and reconnected to the carbon atoms on the other end. Comprised of only hexagons this system is one-dimensional and similar to Lineland. Finally, stacking sheets of graphene on top of one another creates graphite a three-dimensional system similar to Spaceland.

How many sheets of stacked graphene make it three-dimensional? This question is answered by comparing the motion of electrons in a system to the width w of its confinement potential[4]. The relevant wavelength scale for electrons is the Fermi wavelength λ_f because electrons with larger wavelengths are buried within the Fermi sea and can not participate. To make the comparison of w with the sample I note $\lambda_f=2\pi/k_f$, where k_f is the Fermi wave vector, and depends on the carrier density n by $k_f=\sqrt{(4\pi n/\alpha)}$, and α simply denotes the degeneracies of the system. Thus, as long as $1/\sqrt{(4\pi n/\alpha)} >\sim w$ the system is electrically two-dimensional. In metals typical n values correspond to a $\lambda_f=0.3$ nm[4] roughly the interatomic spacing, but a metal thin film that consists of a single atomic layer is unstable. For graphene, on the other hand, this condition is easily satisfied because w=0.1~0.2nm is still meager compared to the smallest experimentally feasible λ_f

~1nm[4], and it is chemically stable due to the strong C-C covalent bond. In metal oxide silicon field effect transistors (Si-MOSFET) and aluminum gallium arsenisde-gallium arsenide heterostructures (AlGaAs-GaAs), where n is typically 10^9~10^{12}cm^{-2}, the 2-D dimensionality condition is satisfied when the fabricated sample w=5~50nm[4].

Electron transport phenomena in two-dimensions was extensively investigated in semiconductors before the appearance of graphene. A brief overview of these systems is presented in the subsequent section.

Section 1.2: An Electronic Flatland: Two dimensional electron gas systems (2DEGS)

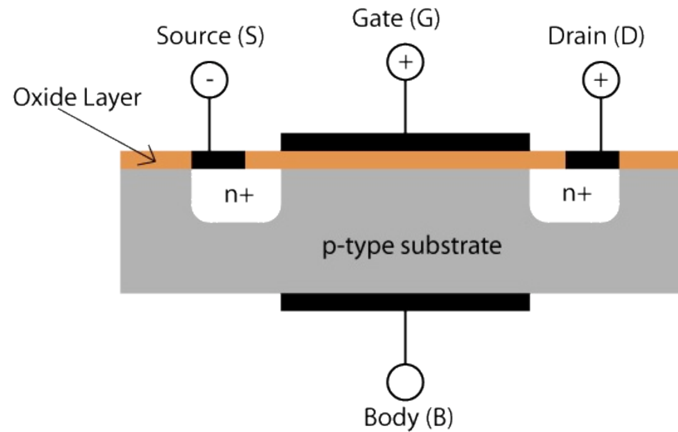

Fig 1.3: Anatomy of a Si-MOSFET. Grey region is the p-doped Si substrate, white regions are n-doped Si and are beneath the metallic contacts(black) labeled source and drain. An insulating SiO_2 layer(beige) separates the top gate electrode(black) from the p-type Si. There is also gate electrode beneath the substrate. Image taken from http://www.doitpoms.ac.uk/tlplib/semiconductors/mosfet.php.

The first two-dimensional electron gas was realized in the mid-1960's following several technological advances after the invention of the transistor at Bell Labs[5]. The device structure is shown in fig 1.3, and is comprised of a p-doped Si substrate, n-doped Si regions beneath the metallic contacts labeled source and drain, an insulating SiO_2 layer separating the top gate electrode from the p-type Si and a gate electrode beneath the substrate. The n-doped contacts in the Si are made by ion implantation followed by lateral diffusion and an annealing process[6]. Formation of the conduction channel that connects source and drain contacts is illustrated in fig 1.4a-c. Initially, at zero gate voltage the bands in the p-type Si are flat, but as the voltage is increased the resultant

electric field bend the bands. Because of the small thickness of the SiO_2 layer, large electric fields are possible in these structures. Further increasing the voltage repels the holes, and when the bands have bent sufficiently electrons begin to populate the conduction band. At this threshold voltage V_t a conduction channel emerges between source and drain. The carrier density henceforth is modulated by

$$n_s=\varepsilon_{ox}/ed_{ox}\,(V_g-V_t) \qquad (1.1)$$

where ε_{ox} is the oxide between the gate and the silicone, d_{ox} is thickness of the oxide and e is the charge of an electron. Due to the vertical confinement, the three-dimensional conduction is discretized into a series of two-dimensional subbands. Under typical device operating conditions, i.e $n_s \sim 10^{11}$-10^{12}, only a single two-dimensional band is occupied[6].

Modulation of the gate voltage V_g between zero and V_t renders the device as an electrical switch, which is a favorable capability from an applied electronics viewpoint. Moreover, this functionality is useful for logic architecture and memory because the gate tunable "on" and "off" state can form a binary system. Indeed, aided by scalable mass production and miniaturization, which allows for sophisticated logic integrated circuitry, the Si-MOSFET is a prevalent element in today's computers. Interestingly, this vital role in facilitating better technology led to massive efforts in improving the Si-SiO_2 interface. As society benefited with better performing digital electronics and greater information storage capability, physicists also reaped benefits because the improved material provided a suitable system for the exploration of quantum phenomena. As evident by the discovery of the quantum Hall effect in that same device architecture by Von Klitzing[7, 8].

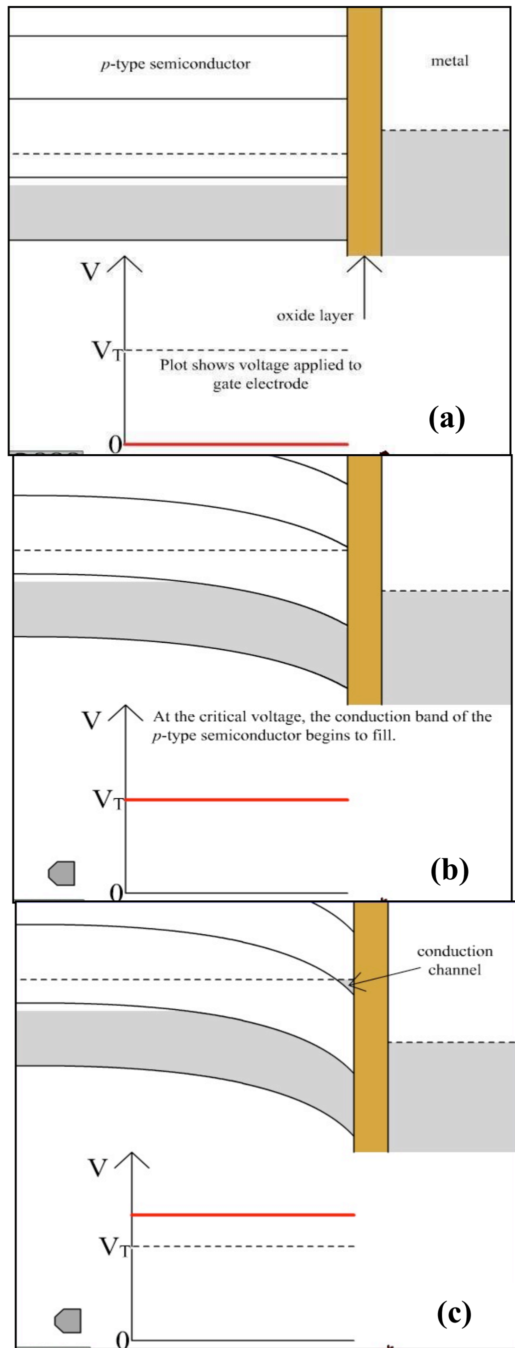

Fig 1.4: Band bending. Left to right: semiconductor, oxide (gold) and metal. Grey region corresponds to Fermi energy and black line represents bands. http://www.doitpoms.ac.uk/tlplib/semiconductors/mosfet.php

The Si-MOSFET has drawbacks related to its structure that obscure intrinsic 2D physical phenomena. Modulation-doped GaAs-AlGaAs heterostructures[8] address these shortcomings. These structures, which are shown in fig 1.5, consist of two semiconductors, AlGaAs a wide band gap material, and GaAs a narrow band gap material. Band bending, similar to that in Si-MOSFET, occurs because the AlGaAs is n-doped and has a conduction band offset, with respect to the adjacent GaAs, of ~3V[6]. At equilibrium the electrons are confined to the interface of the two semiconductors resulting in the emergence of 2D subbands.

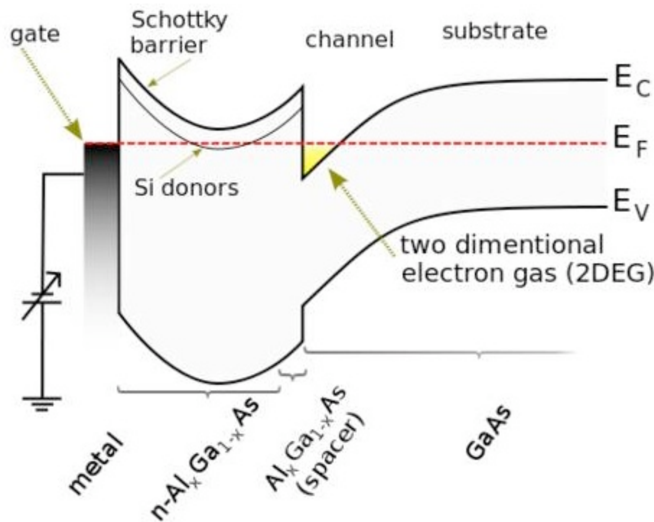

Fig 1.5: Band bending at a semiconductor heterostructure. Left to right: Gate (grey), n-doped AlGaAs, which is a wide band gap semiconductor, AlGaAs spacer, and GaAs a narrow band gap semiconductor. Band offset in AlGaAs causes bending in GaAs. AlGaAs is often used as a spacer at the interface to reduce momentum scattering from dopants. Image from http://en.wikipedia.org/wiki/File:HEMT-band_structure_scheme-en.svg

Importantly, dopants in the n-type AlGaAs can cause momentum scattering similar to the dopants in p-type Si-MOSFETs. To ameliorate this, a spacer, which is an

undoped AlGaAs region, is implemented at the interface, hence separating the dopants from the 2DEG[8]. Electron momentum scattering is further reduced by the absence of boundary scattering, which is ensured by the lattice match between the two different semiconductors. Another advantage in these structures over the Si-MOSFET is the smaller effective mass of the quasiparticles in GaAs, thus allowing higher mobility. Modulation doped AlGaAs-GaAs heterostructures provide physicists with a cleaner 2DEG, revealing new physics. This was demonstrated by the observation of a correlated electron effect called the fractional quantum Hall effect[9], which occurred a couple of years after the first observation of the integer quantum Hall effect.

Despite the many favorable properties of modulation doped AlGaAs-GaAs heterostructures they are not without drawbacks. Similar to the Si-MOSFET, and perhaps more crucial, the material growth and interface are vital for the device quality. This step in the device fabrication requires atomic control of the growth, which is achieved using a sophisticated technique called Molecular Beam Epitaxy (MBE). Gating, the experimental knob that conveniently tunes carrier density in Si-MOSFETS, is not so easily achieved in AlGaAs-GaAs heterostructures because the Schottky barier between AlGaAs and a metallic gate is low, thus it can short with the gate[10]. Unlike the Si-MOSFET devices, implementation of an oxide between the gate electrode and the AlGaAs has not been achieved due to the lack of a natural oxide. Also, any carrier modulation achieved is restricted to one carrier type due to the gap between the valence and conduction bands, and prevents in situ doping. Finally, surface probe methods such as optical or scanning

tunneling spectroscopy of the 2DEGS are precluded because in the heterostuctures and Si-MOSFETS "Flatland" is buried within some material.

Section 1.3: Flatland has arrived: A brief history of Graphene

The notion of graphene existed first as a toy model for the theoretical inquiry of electronic properties of other carbon systems. In 1947 P.R. Wallace published the first work of this nature[11], by using a tight binding calculation to calculate the band structure of single layer graphene, which will be discussed in more detail in chapter two. Subsequent efforts by McClure 1957 studied the interlayer effects between stacked monolayers, again with the aim of understanding graphite[12, 13]. Graphene was also used for the theoretical study of electronic properties of carbon nanotubes, which may be semiconducting or metallic depending on the rolling angle and tube radius[14].

Despite graphene's usefulness as a theoretical tool, researchers in the community still sought for its experimental realization, as is demonstrated by the several attempts to isolate graphene beginning in 1859 with the suspension of tiny crystals of graphene oxide [15]. Before 2004 several groups observed of graphene or graphene like materials through various imaging methods[16]. More relevant to the work of this thesis we focus on the pioneering works that appeared around 2004-2005[2, 17, 18].

The 2004 work by the Manchester group was seminal[2,16], as it was not only the first work that isolated and identified thin crystals of graphene, but also the first to report electrical transport measurements on graphene-based field effect transistors. The

scientific accomplishment is all the more amazing in view of the crude method of isolation, consisting of scotch tape peeling of a thin piece of bulk graphite and rubbing these flakes onto a SiO_2 substrate. This is in stark contrast to the advanced growth methods used in producing high quality SiMOSFET or modulation doped semiconducting heterostructures.

As shown by the Manchester group[2], graphene's amazing properties at room temperature measurements include: (1) high gate tunability with a strong ambipolar electric field effect that changed resisitivity by a factor ~100. At higher gate voltages (compared to charge neutrality point), which corresponds to $\sim 10^{13}cm^{-2}$ in charge carrier density, graphene behaves similar to a metal with low resistivity. While at low gate voltages (compared to charge neutrality point), which corresponds to $\sim 10^{11}cm^{-2}$ in charge carrier density, graphene behaves similar to a semiconductor with higher resistivity. Additionally, its carrier types are gate tunable, also unlike the conventional 2DEGS. Such tunability is unmatched by conventional 2DEGS discussed in the previous section. (2). 2) high electrical quality with charge carrier mobilities ~ 10,000 cm^2/Vs, which is an impressive feat considering the ambient measurement conditions and crude isolation method, and that this was the first transport study on graphene. Present day studies, which use different device schemes (discussed in chapters three and eleven), but the same exfoliated graphene, reach mobilities two orders of magnitude greater.

Several other works that appeared during 2004-2005 included measurements on exfoliated few layer graphene[19, 20] or graphene grown on silicone carbide[21], though these studies did not encompass all of the elements of the 2004 paper by the Manchester group.

In 2005 the back-to-back works by the Manchester[17] and Columbia[18] groups demonstrated the linear dispersion relation of the then nascent system of single atomic layer of carbon, by resolving the predicted anomalous half integer *G* spectrum for graphene[22], which is distinct from those in the conventional 2DEGS. Thus graphene is both electrically and physically 2D. I fortuitously joined the Jeanie Lau group the summer of 2006 when the group had recently obtained graphite flakes, and my colleague Feng Miao began the group's graphene efforts[23].

Conclusion

In summary, the notion of Flatland is an idea that captivated humanity's curiosity far before it was realized. Advances in technology in the 1960's allowed scientists to engineer an electronic equivalent of flatland where the characteristic length of the electron is much smaller than the confining out-of-plane potential. These systems exhibited QHE when in the presence of sufficiently high mobility, high magnetic fields and/or low temperatures. However, they require sophisticated growth techniques, and are embedded deep within oxides, thus limit surface based studies. Graphene, which was isolated and successfully electrically characterized in 2004[2] and 2005[17, 18], possess gate tunable carrier type and density, and exhibits high quality despite its crude isolation method; hence it is the quintessential 2DEG electrically and physically. We now proceed with a discussion on the origin of the electrical properties of graphene using tight binding calculation.

References

1. E. A. Abbott, *Flatland*. (Dover, 1884).

2. K. S. Novoselov, A. K. Geim, S. V. Morozov, D. Jiang, Y. Zhang, S. V. Dubonos, I. V. Grigorieva and A. A. Firsov, Science **306** (5296), 666-669 (2004).

3. A. K. Geim and K. S. Novoselov, Nat. Mater. **6** (3), 183-191 (2007).

4. S. Das Sarma, S. Adam, E. H. Hwang and E. Rossi, Rev. Mod. Phys. **83**, 407 (2011).

5. B. Jeckelmann and B. Jeanneret, Meas. Sci. Technol. **14** (8), 1229-1236 (2003).

6. T. Ando, A. B. Fowler and F. Stern, Reviews of Modern Physics **54** (2), 437-672 (1982).

7. K. von Klitzing, Physics of the Two-Dimensional Electron Gas. Proceedings of a NATO Advanced Study Institute, 1-2525 (1987).

8. H. L. Stormer, Surf. Sci. **132** (1-3), 519-526 (1983).

9. H. L. Stormer, A. Chang, D. C. Tsui, J. C. M. Hwang, A. C. Gossard and W. Wiegmann, Physical Review Letters **50** (24), 1953-1956 (1983).

10. C. W. J. Beenakker and H. van Houten, **- Volume 44**, - 228 (1991).

11. P. R. Wallace, Physical Review **71** (9), 622-634 (1947).

12. J. W. McClure, Phys. Rev. **104** (3), 666-671 (1956).

13. J. C. Slonczewski and P. R. Weiss, Physical Review **109** (2), 272-279 (1958).

14. R. Saito, M. Fujita, G. Dresselhaus and M. S. Dresselhaus, Appl. Phys. Lett. **60** (18), 2204-2206 (1992).

15. B. C. Brodie, Philosophical Transactions of the Royal Society of London **149**, 249-259 (1859).

16. A. K. Geim, Phys. Scr. **T146** (2012).

17. K. S. Novoselov, A. K. Geim, S. V. Morozov, D. Jiang, M. I. Katsnelson, I. V. Grigorieva, S. V. Dubonos and A. A. Firsov, Nature **438** (7065), 197-200 (2005).

18. Y. B. Zhang, Y. W. Tan, H. L. Stormer and P. Kim, Nature **438** (7065), 201-204 (2005).

19. J. S. Bunch, Y. Yaish, M. Brink, K. Bolotin and P. L. McEuen, Nano Lett. **5** (2), 287-290 (2005).

20. Y. Zhang, J. P. Small, M. E. S. Amori and P. Kim, Physical Review Letters **94** (17), 176803 (2005).

21. C. Berger, Z. M. Song, T. B. Li, X. B. Li, A. Y. Ogbazghi, R. Feng, Z. T. Dai, A. N. Marchenkov, E. H. Conrad, P. N. First and W. A. de Heer, Journal Of Physical Chemistry B **108** (52), 19912-19916 (2004).

22. G. W. Semenoff, Physical Review Letters **53** (26), 2449-2452 (1984).

23. F. Miao, S. Wijeratne, Y. Zhang, U. Coskun, W. Bao and C. N. Lau, Science **317**, 1530-1533 (2007).

Chapter 2: Tight binding calculations of single and bilayer graphene

Introduction:

In this chapter the tight binding method for single[1] and bilayer graphene[2] is discussed in detail. This approach has been very successful in predicting and explaining the dazzlingly single-particle phenomena expected and observed in both systems. First, the chapter begins with a brief introduction to the tight binding method and highlights the general procedure for calculating band structures for any system. Next, limiting ourselves to nearest neighbor hoping, the tight binding method is used to calculate the band structure of single layer graphene. Because the Fermi energy modulation achieved in electron transport measurements is small, we focus on the low energy region of the band structure. Using approximations and simple arguments in this low energy regime the resulting calculations provide insight into many of the wonderful properties of graphene. Section 2.4 covers the tight binding model of bilayer graphene in similar detail. Additional emphasis is given to the long wavelength portion of the energy spectrum.

On the other hand, though single particle phenomenon in both systems is adequately explained by the tight binding method, the effect of interactions is not. For a technical discussion on this topic the reader is referred to [3-7].

2.1 Tight Binding Model

The tight binding model is a standard method used for calculating the electronic band structure of materials. This method employs an approximate set of wave functions comprised of a superposition of Bloch functions for isolated atoms at each atomic site.

These Bloch wave functions, which represent the electrons, are tightly bound to the atom that they belong to and do not interact with one another. Although the tight binding model does not take electron interactions into account, it is very often used as a starting point for correlated systems and can provide valuable qualitative information.

In general, assuming translational invariance, a system with n atomic orbitals ϕ_j in a unit cell, where j denotes the unit cell, can be described by Bloch functions

$$\Phi_j(k,r) = \frac{1}{\sqrt{N}} \sum_{i=1}^{N} e^{ik \bullet R_{ji}} \phi_j(r - R_{ji}) \qquad (2.1)$$

where the sum is over the N different unit cells labeled by index i, and the R_{ji} specifies the position of the jth orbital in the ith unit cell.

More generally, an electronic wave function $\Psi_j(k,r)$ can be expanded into a linear superposition of n different Bloch functions,

$$\Psi_j(k,r) = \sum_{l=1}^{n} c_{jl}(k)\phi(k,r) \qquad (2.2)$$

The energy $E_j(k)$ is given by the inner product of the Schrödinger equation,

$$E_j(k) = \frac{\langle \psi_j | H | \psi_j \rangle}{\langle \psi_j | \psi_j \rangle} \qquad (2.3)$$

Substituting the expansion of the wave function into the expression for energy gives,

$$E_j(k) = \frac{\sum_{il}^{n} c^{*}_{ji} c_{jl} \langle \phi_i | H | \phi_i \rangle}{\sum_{il}^{n} c^{*}_{ji} c_{jl} \langle \phi_i | \phi_i \rangle} \qquad (2.4)$$

$$= \frac{\sum_{il}^{n} c^*_{ji} c_{jl} H_{il}}{\sum_{il}^{n} c^*_{ji} c_{jl} S_{il}} \qquad (2.5)$$

where the transfer integral and the matrix elements H_{il} and the overlap integral and matrix elements S_{il} are defined by,

$$H_{il} = \langle \phi_i | H | \phi_l \rangle, \quad S_{il} = \langle \phi_i | S | \phi_l \rangle \qquad (2.6)$$

We proceed in the standard fashion of minimizing E_j with respect to c^*_{jm},

$$\frac{\partial E_j}{\partial c^*_{jm}} = \frac{\sum_{l}^{n} H_{ml} c_{jl}}{\sum_{il}^{n} S_{il} c^*_{ji} c_{jl}} - \frac{\sum_{l}^{n} H_{ml} c^*_{ji} c_{jl} \sum_{l}^{n} S_{ml} c_{jl}}{(\sum_{il}^{n} S_{il} c^*_{ji} c_{jl})^2} = 0 \qquad (2.7)$$

Rearranging the above expression and using eqs. (4) and (5) produces,

$$\sum_{l=1}^{n} H_{ml} c_{jl} = E_j \sum_{l=1}^{n} S_{ml} c_{jl} \qquad (2.8)$$

We can define H as the transfer integral matrix, S the overlap integral matrix and ψ_j the column vector.

$$H = \begin{matrix} H_{11} & H_{12} & \ldots & H_{1n} \\ H_{21} & H_{22} & \cdots & H_{2n} \\ \vdots & \vdots & \ddots & \vdots \\ H_{n1} & H_{n2} & \cdots & H_{nn} \end{matrix}, \quad S = \begin{matrix} S_{11} & S_{12} & \ldots & S_{1n} \\ S_{21} & S_{22} & \cdots & S_{2n} \\ \vdots & \vdots & \ddots & \vdots \\ S_{n1} & S_{n2} & \cdots & S_{nn} \end{matrix}, \quad \psi_j = \begin{matrix} c_{j1} \\ \vdots \\ c_{jn} \end{matrix} \qquad (2.9)$$

With use of this matrix representation the E_j values are acquired by solving the secular equation,

$$\det (H - E_j S) = 0 \qquad (2.10)$$

where the number of solutions is determined by the number of different atomic orbitals for each unit cell. In the next section the crystal structure of graphene is discussed first and then the tight binding method shown here is applied.

2.2 Crystal structure and energy spectrum of single layer graphene (SLG)

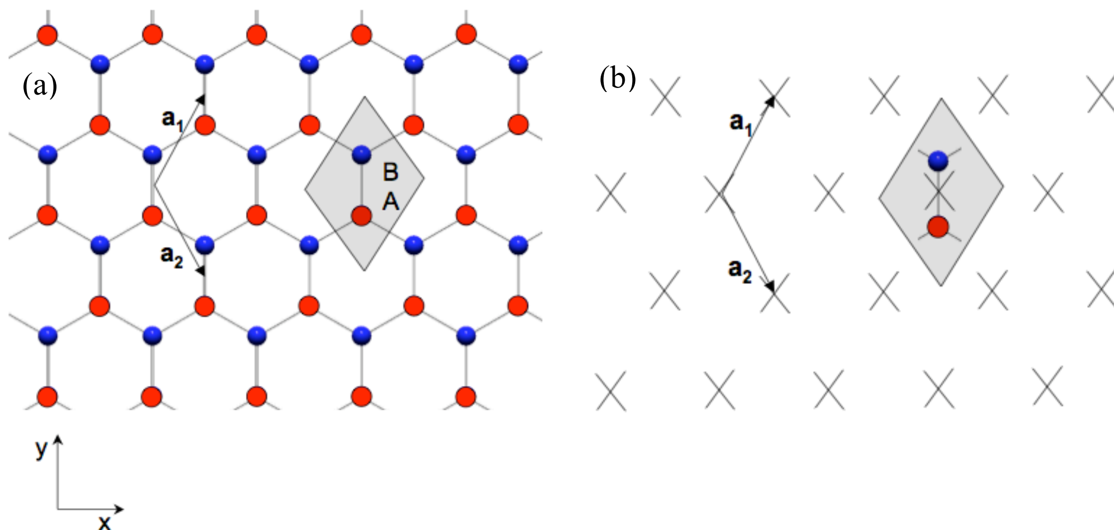

Fig 2.1: Crystal structure of SLG and Bravais lattice. (a) Honeycomb carbon lattice of graphene with A and B sublattices depicted as red and blue, respectively. Primitive lattice vectors a_1 and a_2 emanate from one unit cell. Shaded rhombus explicitly shows a unit cell comprised of both A and B atoms. (b) Hexagonal Bravais lattice comprised of A and B atomic basis. Primitive lattice vectors a_1 and a_2 allow for translational invariant motion along lattice.

The real space crystal structure of graphene is comprised of carbon atoms arranged in a honeycomb lattice that exists in the x-y plane shown in fig 2.1a. The atoms are differentiated as B (blue) and A (red), and with this distinction it is evident that this

structure is not a Bravais lattice, i.e. there is no translational invariance between the individual atoms. However, defining the *A-B* pair as the basis, with the shaded region representing the unit cell, the resultant lattice is indeed Bravais, which is shown in fig 2.1b with primitive lattice vectors,

$$a_1 = (\frac{a}{2}, \frac{\sqrt{3}a}{2}), \quad a_2 = (\frac{a}{2}, -\frac{\sqrt{3}a}{2}) \qquad (2.11)$$

where a= 2.46 A is distance between unit cells, and the carbon to carbon bond length of $a/\sqrt{3}$. Using the relations: $a_1 * b_1 = a_2 * b_2 = 2\pi$ and $a_1 * b_2 = a_2 * b_1 = 0$, the reciprocal lattice vectors are

$$b_1 = (\frac{2\pi}{a}, \frac{2\pi}{\sqrt{3}a}), \quad b_1 = (\frac{2\pi}{a}, -\frac{2\pi}{\sqrt{3}a}). \qquad (2.\ 12)$$

The reciprocal lattice vectors allow for construction of both the hexagonal Bravais lattice in *k*-space and the Brillouin zone (shaded region) indicated in fig. 2.2. The playground for the electrons in real and momentum space is defined, how do they behave in this flatland?

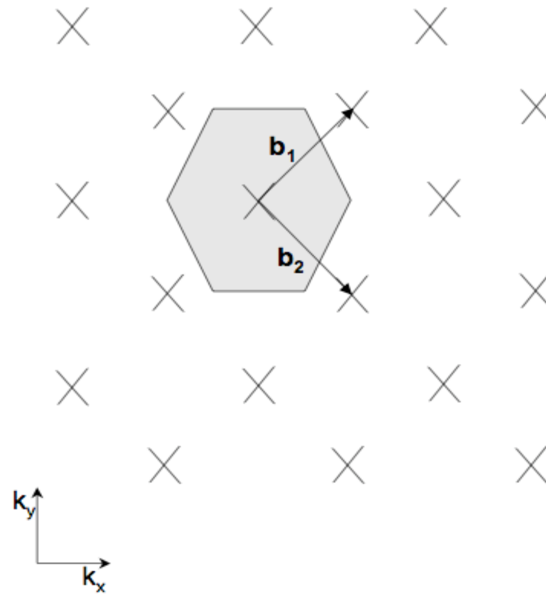

Fig 2.2: Reciprocoal lattice. The reciprocal lattice is constructed from the primitive reciprocal lattice vectors b_1 and b_2. The shaded region is the Brillouin zone

Before we resolve the behavior of the electrons in the graphene flatland we must first identify which electrons will participate in the fun. This is determined by considering carbon in detail; Carbon has six electrons, two are core electrons and four are valence electrons. The latter electrons are relevant for carbon's bonding, they reside in the $2s$, $2p_x$, $2p_y$, and $2p_z$ orbitals. Interestingly, in graphene the $2s$ and $2p$ orbitals are sp^2 hybridized, which simply means that two of the $2p$ orbitals mix with the one $2s$ orbital. In this planar, honeycomb array of carbon atoms, it is the $2p_x$ and $2p_y$ orbtials that mix with the $2s$ orbital to form robust σ bonds between the individual carbon atoms at 120°. These are represented as solid lines between the carbon atoms in the real space crystal structure, fig. 2.1a. The remaining $2p_z$ orbital from one carbon atom forms a π bond with

the $2p_z$ orbitals of the adjacent carbon atoms. Both σ and π bonds are illustrated in fig 2.3. It is the latter electrons that traverse the graphene flatland and it is their behavior that we will investigate next.

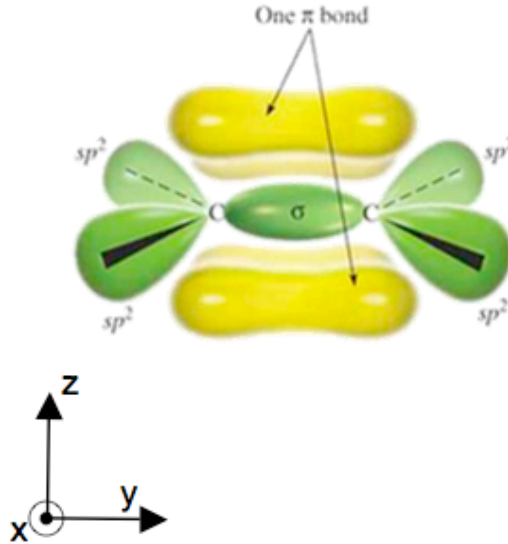

Fig 2.3: σ and π bonds. Three different types of bonds between adjacent carbon atoms. In plane, two sp^2 bonds form a σ bond. Out of plane, two p_z bonds form a π bond. Image copyright ThomsonBrooks Cole 2004

For the tight binding calculation of SLG the transfer *H* and overlap *S* matrices, and ψ column vector are constrained to two Bloch functions, because the unit cell is comprised of *A* and *B* atoms each with its own $2p_z$ orbital. The game plan is to determine each element of the matrices and then use this information to solve the secular equation.

By using the definition of a Bloch function eq. 2.2 the first diagonal term in the transfer matrix eq. 2.9 is,

$$H_{AA} = \frac{1}{N}\sum_{i=1}^{N}\sum_{j=1}^{N} e^{ik\cdot(R_{Aj}-R_{Ai})}\langle\phi_A(r-R_{Ai})|H|\phi_A(r-R_{Aj})\rangle \qquad (2.13)$$

where the double summation indicates contributions from all of the *A* sites of the lattice. Keeping only nearest neighbor contributions and noting that the matrix element H_{AA} is the same at each *A* site the above summation simplifies to

$$\begin{aligned} \varepsilon_{2p} &= \langle \phi_A(r - R_{Ai}) | H | \phi_A(r - R_{Ai}) \rangle \\ H_{AA} &\approx \frac{1}{N}\sum_{i=1}^{N} \varepsilon_{2p} = \varepsilon_{2p} \end{aligned} \tag{2.14}$$

Because *A* and B are both carbon atoms the diagonal element H_{BB} is similar in structure, hence $H_{AA} = H_{BB} \approx \varepsilon_{2p}$. In a similar fashion the nearest neighbor approximation will greatly simplify the diagonal overlap *S* matrix elements,

$$\begin{aligned} S_{AA} &= \frac{1}{N}\sum_{i=1}^{N}\sum_{j=1}^{N} e^{ik\cdot(R_{Aj} - R_{Ai})} \langle \phi_A(r - R_{Ai}) | \phi_A(r - R_{Aj}) \rangle \\ S_{AA} &= \frac{1}{N}\sum_{i=1}^{N} \langle \phi_A(r - R_{Ai}) | \phi_A(r - R_{Ai}) \rangle \end{aligned} \tag{2.15}$$

which reduces to unity $S_{AA} = S_{BB} \approx 1$.

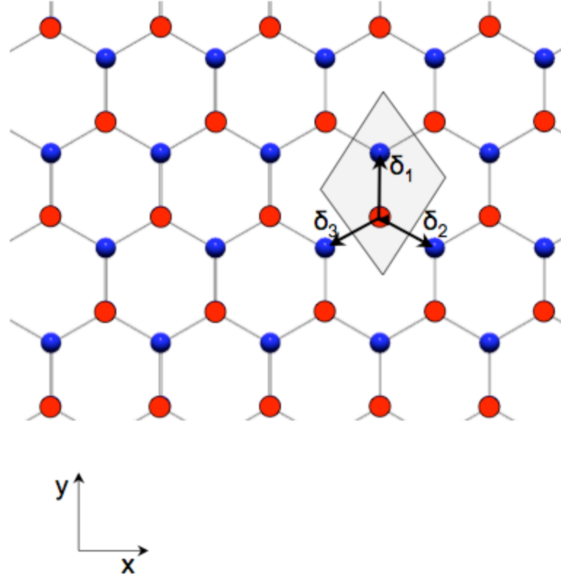

Fig 2.4: Nearest neighbor hopping. Real space lattice depicting hopping from an *A* atom to surrounding *B* atoms. $\delta_{1\text{-}3}$ represents the hopping terms.

The off-diagonal terms are acquired similarly. Physically, they describe the hopping between *A* and *B* sublattices.

$$H_{AB} = \frac{1}{N}\sum_{i=1}^{N}\sum_{j=1}^{N} e^{ik\cdot(R_{Bj}-R_{Ai})}\langle \phi_A(r-R_{Ai})|H|\phi_B(r-R_{Bj})\rangle \quad (2.16)$$

Keeping only nearest neighbor terms and fixing ourselves on an *A* site we see in fig. 2.4 that there are three neighboring *B* atoms, thus

$$H_{AB} = \frac{1}{N}\sum_{i=1}^{N}\sum_{l=1}^{3} e^{ik\cdot(R_{Bl}-R_{Ai})}\langle \phi_A(r-R_{Ai})|H|\phi_B(r-R_{Bl})\rangle \quad (2.17)$$

The coupling between each nearest neighbor *B* atom and the center *A* atom are the same, hence the term $\langle \phi_A(r-R_{Ai})|H|\phi_B(r-R_{Bl})\rangle$ can be set equal to a constant γ_0. The position of the nearest neighbor to the *A* atom is $\delta_l = R_{Bl} - R_{Ai}$, which leads to a transfer matrix element of,

$$H_{AB} \approx -\frac{1}{N}\sum_{i=1}^{N}\sum_{l=1}^{3} e^{ik\cdot\delta_l}\gamma_0 \equiv -\gamma_0 f(k)$$
$$f(k) = \sum_{l=1}^{3} e^{ik\cdot\delta_l} \qquad (2.18)$$

The nearest neighbor coordinates with respect to the *A* atom are given below and implementing them into the nearest neighbor hopping term we get,

$$\delta_1 = (0, \frac{a}{\sqrt{3}}), \quad \delta_2 = (\frac{a}{2}, -\frac{a}{2\sqrt{3}}), \quad \delta_3 = (-\frac{a}{2}, -\frac{a}{2\sqrt{3}}) \qquad (2.19)$$

$$\begin{aligned} f(k) &= e^{ik_y a/\sqrt{3}} + e^{ik_x a/2} e^{-ik_y a/2\sqrt{3}} + e^{-ik_x a/2} e^{-ik_y a/2\sqrt{3}} \\ &= e^{ik_y a/\sqrt{3}} + 2e^{-ik_y a/2\sqrt{3}} \cos(k_x a/2) \end{aligned} \qquad (2.20)$$

A similar procedure is employed to determine the off-diagonal overlap term,

$$\begin{aligned} S_{AB} &= \frac{1}{N}\sum_{i=1}^{N}\sum_{j=1}^{N} e^{ik\cdot(R_{Bj}-R_{Ai})} \langle \phi_A(r-R_{Ai}) | \phi_B(r-R_{Bj}) \rangle \\ &\approx \frac{1}{N}\sum_{i=1}^{N}\sum_{l=1}^{3} e^{ik\cdot(R_{Bl}-R_{Ai})} \langle \phi_A(r-R_{Ai}) | \phi_B(r-R_{Bl}) \rangle \\ &= s_o f(k) \end{aligned} \qquad (2.21)$$

where $s_o = \langle \phi_A(r-R_{Ai}) | \phi_B(r-R_{Bl}) \rangle$ is a constant because it is the same between all of the nearest neighbors and the center *A* atom. Physically, this parameter accounts for orbitals on adjacent atomic sites that are not strictly orthogonal. Using Hermitian conjugates to determine the remaining elements $H_{ab} = H_{ab}^*$ the transfer and overlap matrices are,

$$H_1 = \begin{pmatrix} \varepsilon_{2p} & -\gamma_o f(k) \\ -\gamma_o f(k) & \varepsilon_{2p} \end{pmatrix} \quad S_1 = \begin{pmatrix} 1 & s_o f(k) \\ s_o f(k) & 1 \end{pmatrix} \qquad (2.22)$$

Next, we use the secular equation to solve for the eigenvalues,

$$\det\begin{pmatrix} \varepsilon_{2p} - E & -(\gamma_o + Es_o)f(k) \\ -(\gamma_o + Es_o)f^*(k) & \varepsilon_{2p} - E \end{pmatrix} = 0$$

$$\Rightarrow (E - \varepsilon_{2p})^2 - ([E - \varepsilon_{2p}]s_o + \varepsilon_{2p}s_o + \gamma_o)^2 \, | f(k) |^2 = 0 \qquad (2.23)$$

$$E_{\pm} = \frac{\varepsilon_{2p} \pm \gamma_o \, | f(k) |}{1 \mp s_o \, | f(k) |}$$

The resultant band structure for these energies, where E_+ and E_- correspond to the conduction and valence bands, respectively, is shown in fig 2.5.

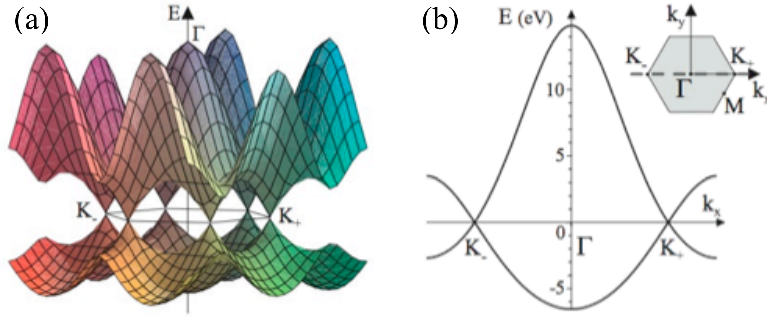

Fig 2.5: Band structure of SLG. a. Full tight binding calculation for the band structure of SLG, with γ_o = 3.033eV, s_o=0.129. b. Cross section from a. at k_y=0, note E is degenerate at the K_+ and K_- points, and valence and conduction bands meet at and touch at these points. Image from[8]

2.3 Low energy spectrum of SLG

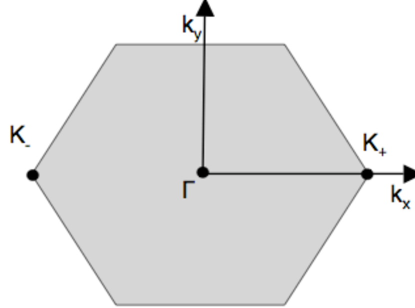

Fig 2.6: First Brillouin zone. The first Brillouin zone is shown, and it has six corners. Reciprocal lattice vectors connect K_+ and K_- to corners above and below but not to each other. K_+ and K_- are in equivalent.

The low energy spectrum of SLG calculated from the tight binding model exhibits intriguing features at the six corners of the Brillouin zone. To investigate this we will perform a low energy expansion of the hopping term in this region. First, as shown in fig. 2.5, the primitive reciprocal lattice vectors can connect K_+ and K_- to the two other corners in the Brillouin zone, but not to each other. This reduces the six corners of the first Brillouin zone to two inequivalent K points, K_+ and K_-, which are often referred to as valleys, fig. 2.6. These two distinct points, with respect to the previously defined primitive reciprocal lattice vectors, are

$$K_\xi = \xi(\frac{4\pi}{3a},0) \qquad (2.24)$$

where ξ denotes the two distinct valleys as + and -. At K_+ and K_- the hopping term reduces to zero leading to a two-fold degeneracy in the energy spectrum at these K-points. More interestingly, at slightly larger momentum this degeneracy ceases to exist.

To explore this we define a momentum $p = \hbar k - \hbar K_\xi$, which modifies the coupling between the sublattices to,

$$
\begin{aligned}
f(k) &= e^{ip_y a/\sqrt{3}\hbar} + 2e^{-ip_y a/2\sqrt{3}\hbar}\cos(\frac{2\pi\xi}{3} + \frac{p_x a}{2\hbar}) \\
&= (1 + \frac{ip_y a}{\sqrt{3}\hbar}) + 2(1 - \frac{ip_y a}{2\sqrt{3}\hbar})(-\frac{1}{2} - \frac{\xi\sqrt{3}p_x a}{4\hbar}) \qquad (2.25) \\
&= -\frac{\sqrt{3}a}{2\hbar}(\xi p_x - ip_y)
\end{aligned}
$$

where only linear terms in p were kept under the auspice that $pa/\hbar << 1$. The transfer integral matrix in the vicinity of the K points thus becomes,

$$
H_{1,\xi} = v\begin{pmatrix} 0 & \xi p_x - ip_y \\ \xi p_x + ip_y & 0 \end{pmatrix} \qquad (2.26)
$$

where ε_{2p} =0 and $v = \sqrt{3}a\gamma_o/2\hbar$ is the Fermi velocity. Substituting for each constant and using 3.033eV for γ_o we get ~10^6 m/s, which is two orders of magnitude less than the speed of light. The S_{AB} matrix contributes nonlinear p terms, and because of this it is ignored. The secular equation simplifies to $H_1\psi = E\psi$, where H_1 can be considered an effective Hamiltonian yielding,

$$
E_\pm = \pm vp, \quad \psi_\pm = \frac{1}{\sqrt{2}}\begin{pmatrix} 1 \\ \pm\xi e^{i\xi\varphi} \end{pmatrix} e^{ip\cdot r/\hbar}, \qquad (2.27)
$$

the ± sign refers to the conduction and valence band, respectively and φ is the polar angle in the graphene plane.

The above eigenvalues and eigenfunctions reveal the fantastic properties of graphene that set off a revolution: 1) Graphene possesses a linear energy dispersion with carriers that travel at an effective speed of light and 2) Graphene possesses a new

quantum number referred to as pseudo-spin. The consequence of a linear energy dispersion is quite clear, the electrons are massless and whiz by without regard for Newton or Schrödinger's prescriptions. In fact eq. 2.26 can be massaged[8] to resemble the Dirac equation by using the Pauli spin matrices in the *A* and *B* sublattice space,

$$\begin{aligned} H_{1\xi} &= v(\xi\sigma_x p_x + \sigma_y p_y) \\ &= vp\overline{\sigma}\cdot\hat{n}_1 \end{aligned} \tag{2.28}$$

In this expression for SLG, $\sigma = (\sigma_x, \sigma_y, \sigma_z)$ and represents the new quantum number pseudo-spin, and $\hat{n}_1 = (\xi\cos\varphi, \sin\varphi, 0)$ is a unit vector. The spin analogue is appropriate because in this representation σ resembles spin from the original Dirac equation. Yet, I stress it is only a provocative construct, because physically this degree of freedom is from the two different sublattices not spin.

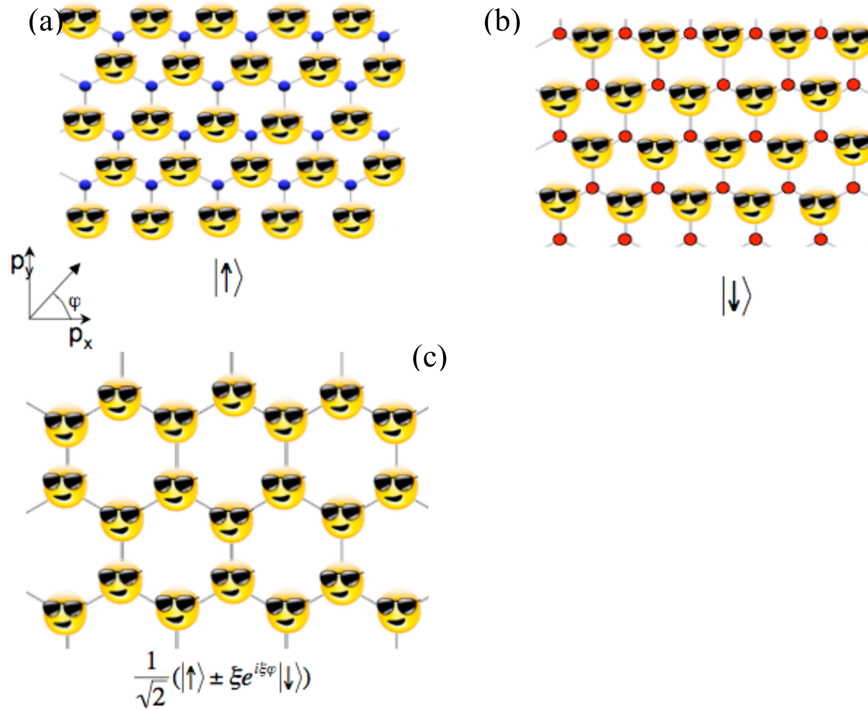

Fig 2.7: Sublattice of SLG. The sublattice degree of freedom cast as pseudospin. In a. and b. occupation of only one sublattice corresponds to an up or down pseudospin state. In c. occupation of both sublattices is a superposition of both states.

Pseudo-spin in SLG is represented in fig. 2.7 with the confident emoticons representing charge carriers. The carriers can reside on the *A* sublattice only, which we deem in an arbitrary fashion as “up” pseudospin. Alternatively they can reside on the *B* sublattice, subsequently named “down”. Usually, however, the electron density will be a superposition of “up” and “down” states similar to a gas of electrons with no constraint on their spin degree of freedom.

In addition to this new quantum number pseudo-spin, the electrons in graphene are chiral, which means that the direction of the pseudospin is related to the direction of

the momentum. Chirality arises from the simple fact that the amplitudes of the eigenstates depend on the polar angle φ between the pseudospin and $\boldsymbol{p}$. This imparts charge carriers with momentum and pseudo spin orientation that is depended on valley and carrier type as depicted in fig. 2.8. As a result, the conservation of pseudospin endows graphene with immunity to scattering within a valley, leading to large mean free paths. This physical phenomenon was discussed previously in single walled carbon nanotubes by Ando[9] and McEuen[10], and was used to explain the long mean free paths in that system.

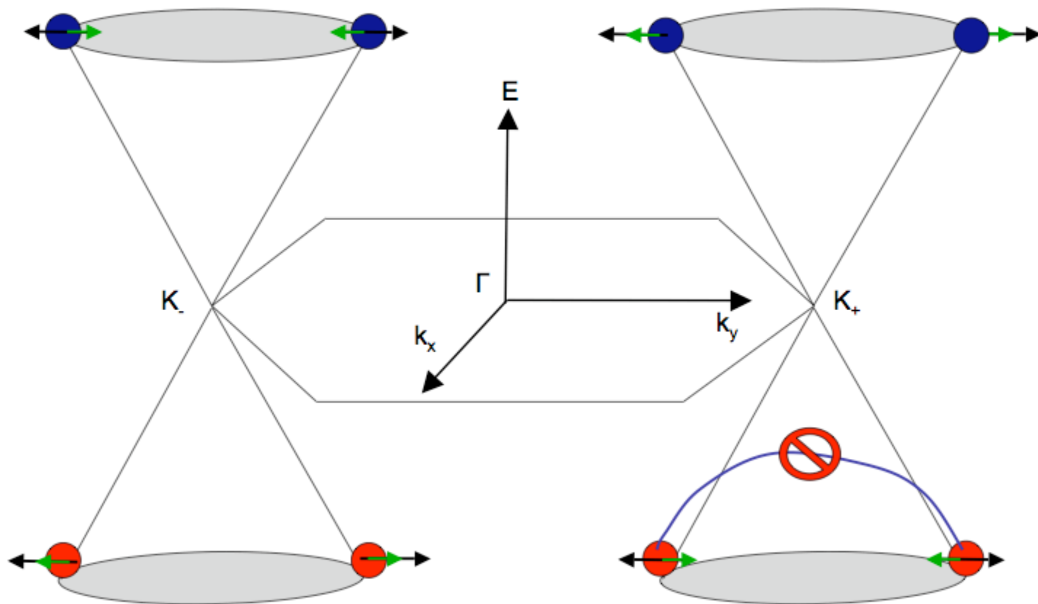

Fig 2.8: Pseudospin in SLG. The pseudospin is depicted as a green arrow and momentum as a black arrow. Chirality is the relation of the direction of pseudospin with the direction of the momentum. Due to pseudospin conservation backscattering is not permitted within a valley.

2.4 Crystal Structure and energy spectrum of bilayer graphene (BLG)

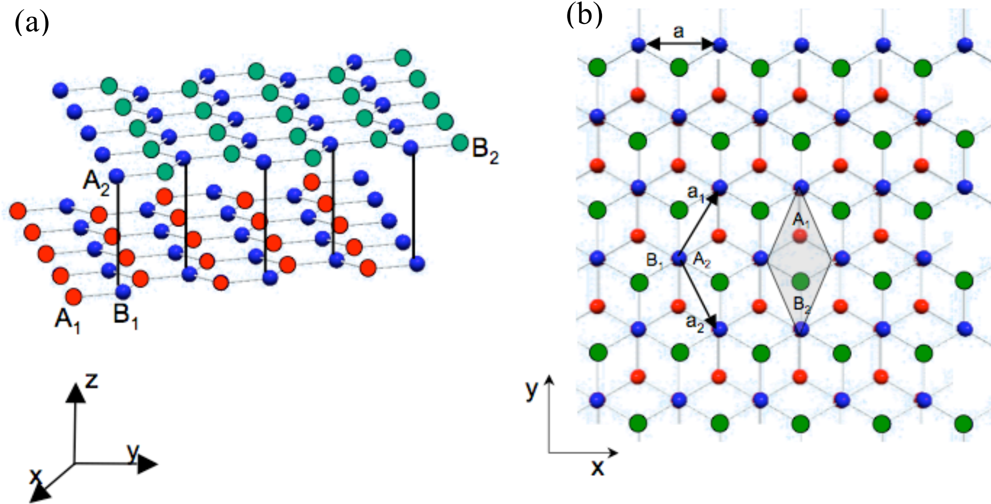

Fig 2.9: BLG in real space. In a. the three dimensional view of BLG is rendered depicting A_1(red), B_1(blue) atoms on bottom layer and A_2(blue), B_2(green) atoms on top layer. In b. the top view of BLG is shown. Shaded region is the unit cell comprised of all four atomic orbitals.

Before performing the tight binding calculation for BLG the crystal structure for this system must be well defined. BLG consists of two sheets of SLG stacked on top of one another, with relative shift such that one atom in the bottom layer is directly below one atom in the top layer. The stacked pair is often referenced to as a dimer. This stacking is named Bernal, after the scientist that resolved the stacking in graphite. It is also known as *AB* stacking, which is the same as in BLG. Fig. 2.9a depicts a three dimensional rendering of *AB* stacked BLG with solid black lines denoting the dimer pair A_2-B_1. The carbon-to-carbon bond length in each layer is the same as in SLG and the intralayer spacing is 3.39A. Fig. 2.9b is a top view of BLG with labels for the primitive lattice vectors, unit cell and the four different types of atomic orbitals. The primitive

lattice vectors are the same as the SLG case. They allow us to travel from unit cell to unit cell in a translationally invariant fashion. Interestingly, the shaded region denoting the unit cell is different. For BLG there are four distinct atomic orbitals labeled A_1(red), B_1(blue), which belong to the bottom layer and A_2(blue), B_2(green), which belong to the top layer. A_2 and B_1 comprise a dimer pair; hence from this view only A_2 is visible, while the other pair is offset from one another. Once again the playground is defined, so onto the tight binding calculation to see how these charge carriers behave!

Following the procedure detailed above for SLG, we will only consider nearest neighbor intralayer and interlayer hoppings, and noting that low energy excitations are the most relevant for transport studies. Applying these considerations within a four atomic orbital basis the transfer and overlap matrices for BLG are,

$$H = \begin{pmatrix} & A_1 & B_1 & A_2 & B_2 \\ A_1 & \varepsilon_{2p} & -\gamma_o f(k) & 0 & 0 \\ B_1 & -\gamma_o f(k) & \varepsilon_{2p} & \gamma_1 & 0 \\ A_2 & 0 & \gamma_1 & \varepsilon_{2p} & -\gamma_o f(k) \\ B_2 & 0 & 0 & -\gamma_o f(k) & \varepsilon_{2p} \end{pmatrix} \tag{2.29}$$

$$S = \begin{pmatrix} & A_1 & B_1 & A_2 & B_2 \\ A_1 & 1 & -s_o f(k) & 0 & 0 \\ B_1 & -s_o f(k) & 1 & 0 & 0 \\ A_2 & 0 & 0 & 1 & -s_o f(k) \\ B_2 & 0 & 0 & -s_o f(k) & 1 \end{pmatrix} \tag{2.30}$$

where $\gamma_1 = \langle \phi_{A2}(r - R_{A2}) | H | \phi_{B1}(r - R_{B1}) \rangle$ is a new term that describes the hopping between A_2-B_1 atomic sites each on different layers above one another. This four orbital basis

beautifully displays SLG blocks in the upper left and lower right corners of the overlap and transfer matrices, and between these two familiar blocks the coupling between layers is present.

The band structure is determined by solving the secular equation, det *(H-E$_j$S)=0,* but first a few judicious approximations can be made focusing on the low energy regions, which are the most relevant for transport. The transfer and overlap matrices can be simplified by setting the orbital energy $\varepsilon_{2p} = 0$, which is equivalent to defining the zero of the energy axis to the orbital energy, and by ignoring terms s_o**f(k)* because these terms are irrelevant at low energies. As a result the overlap matrix becomes a unit matrix and the transfer matrix is,

$$H = \begin{pmatrix} 0 & -\gamma_o f(k) & 0 & 0 \\ -\gamma_o f(k) & 0 & \gamma_1 & 0 \\ 0 & \gamma_1 & 0 & -\gamma_o f(k) \\ 0 & 0 & -\gamma_o f(k) & 0 \end{pmatrix} \qquad (2.31)$$

The subsequent eigenvalues are,

$$E_{\pm}^{(\alpha)} = \pm \frac{\gamma_1}{2}(\sqrt{1 + \frac{4\gamma_o^2 |f(k)|^2}{\gamma_1}} + \alpha \qquad (2.32)$$

with α=±1 indicating that there are four bands for BLG in agreement with the four orbitals used for the calculation. For most of the Brillouin zone $4\gamma_o^2 |f(k)|^2 >> \gamma_1^2$, hence $E_{\pm}^{(1)} \approx \pm\gamma_o |f(k)| + \alpha\gamma_1/2$ resulting in two bands that are similar to the SLG result. One striking difference, however, is visible at *f(k=K$_\pm$),* where the hopping function is zero, thus leaving a gap equivalent to $2\gamma_1$ between the valence and conduction band. Physically

these higher energy bands, which are depicted in fig 2.10, arise from the coupling between A_2 and B_1 orbitals, the dimer pair.

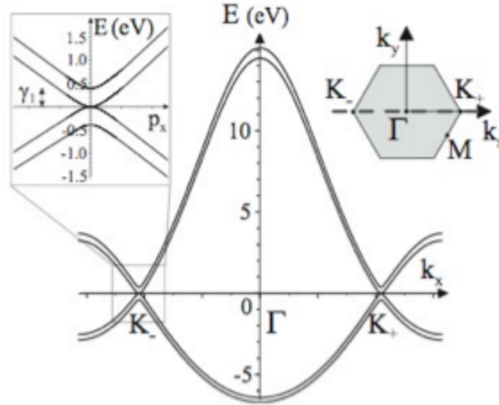

Fig 2.10: Band structure of BLG. Tight binding calculation for the band structure of BLG, with $\gamma_o = 3.033$eV, s_o=0.129, and $\gamma_1 = 0.39$eV at k_y=0. Note E is degenerate at the K_+ and K_- points, and valence and conduction bands meet at and touch, image from[8, 11]

2.4.1 Low energy spectrum of Bilayer graphene

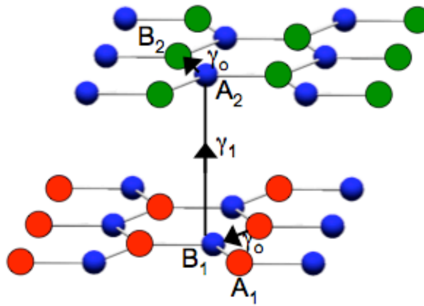

Fig 2.11: Hopping. Hopping is depicted between nearest neighbor intralayer and interlayer atoms represented by γ_o and γ_1 respectively.

The lower energy bands, which are depicted in fig 2.10, are near the K-points and are comprised of a hopping function, $f(k) = vp$. These bands arise from the indirect coupling of the non-dimer pair A_1-B_2 where the hopping is depicted in fig. 2.11. First, an intralayer hopping, on the bottom sheet, occurs from A_1 to B_1, and then an interlayer hopping from B_1 to A_2 followed by the last intralayer hopping, on the top sheet, from A_2 to B_2. A two component Hamiltonian that resembles the low energy SLG calculation can be used to represent this indirect coupling. Beginning with the secular equation from the previous section

$$\det\begin{pmatrix} -E & -\gamma_o f(k) & 0 & 0 \\ -\gamma_o f(k) & -E & \gamma_1 & 0 \\ 0 & \gamma_1 & -E & -\gamma_o f(k) \\ 0 & 0 & -\gamma_o f(k) & -E \end{pmatrix} = 0 \qquad (2.33)$$

which can be arranged as four separate equations[11],

$$\begin{aligned} &1) EC_{A_1} + \gamma_o f(k) C_{B_1} = 0 \\ &2) \gamma_o f(k) C_{A_1} + EC_{B_1} - \gamma_1 C_{A_2} = 0 \\ &3) -\gamma_1 C_{B_1} + EC_{A_2} + \gamma_o f(k) C_{B_2} = 0 \\ &4) \gamma_o f(k) C_{A_2} + EC_{B_2} = 0 \end{aligned} \qquad (2.34)$$

Eqs. 34.2 and 34.3 above can be solved for C_{B_1} *and* C_{A_2} separately

$$C_{B_1} = \frac{\gamma_o f(k)}{\gamma_1 d} C_{B_2} + \frac{E\gamma_o f^*(k)}{\gamma_1^2 d} C_{A_1} \qquad (2.35)$$

$$C_{A_2} = \frac{\gamma_o f^*(k)}{\gamma_1 d} C_{A_1} + \frac{E\gamma_o f(k)}{\gamma_1^2 d} C_{B_2} \qquad (2.36)$$

where $d = 1 - E^2/\gamma_1^2$. Then substituting these relationships into eqs 2.34.1 and 2.34.4 results in two new expressions containing only the non-dimer orbitals. At $|E| << |\gamma_1|$ and

$|\gamma_o * f(k)| << |\gamma_1|$ the approximations $d \approx 1$ and terms with order higher than $1/\gamma_1$ can be dropped,

$$EC_{A_1} + \frac{\gamma_o^2 f^2(k)}{\gamma_1} C_{B_2} = 0$$
$$EC_{B_2} + \frac{\gamma_o^2 f^2(k)}{\gamma_1} C_{A_1} = 0 \qquad (2.37)$$

Now the effective Hamiltonian, at low energy, can be arranged into a 2 X 2 matrix comprised of a basis with only the indirectly coupled orbitals. To that end we use eq. 2.20

$$H_{2\xi} = -\frac{1}{2m}\begin{pmatrix} 0 & (\xi p_x - ip_y)^2 \\ (\xi p_x + ip_y)^2 & 0 \end{pmatrix} \qquad (2.38)$$

with $m = \gamma_1/(2v^2)$ is the effective mass of charge carriers in BLG, and v is the Fermi velocity. By substituting 0.39eV for γ_1 and the value calculated for v from the previous section on SLG we get $m = 0.035 m_e$. This value is consistent with measurements of the cyclotron mass of the carriers in BLG[12, 13]. The low energy Hamiltonian in eq. 2.38 results in eignevalues and eigen functions,

$$E_\pm = \pm\frac{p^2}{2m}, \qquad \psi_\pm = \frac{1}{\sqrt{2}}\binom{1}{\mp e^{i2\xi\varphi}} e^{ip\cdot r/\hbar} \qquad (2.39)$$

The low energy two component Hamilitonian, comprised of the indirectly coupled atomic orbtitals A_1 and B_2, which are each on different layers, also possesses psuedospin. Interestingly, for BLG this sublattice degree of freedom can also be seen as a layer degree of freedom, which is depicted in fig. 2.12. The charge carriers can reside on the bottom layer only, corresponding to “up” pseudospin or on the top layer, deemed “down” pseudospin. Normally the charge carriers will reside on both layers shown in fig 2.12c,

yet with aid of an additional gate one can convince the charges to reside in one layer. This functions as an effective control of the psuedospin, which will be discussed later in the thesis in the experimental section on BLG. Upon inspection of the eigen-functions for BLG we see that these charge carriers also possess chirality. Motivated by the existence of pseudospin and chirality in BLG we rearrange the effective Hamilitonian using the Pauli spin matrices in the A_1-B_2 sublatttice space,

$$H_{2\xi} = -\frac{1}{2m}[\sigma_x(p_x^2 - p_y^2) + 2\xi\sigma_y p_x p_y] \qquad (2.40)$$

$$= (p^2/2m)\vec{\sigma}\cdot\vec{n}_2 \qquad (2.41)$$

where $\boldsymbol{n}$=-($cos2\varphi$, ξ sin2φ, 0) is a unit vector and $\boldsymbol{\sigma}$ =(σ_x, σ_y, σ_z) is the pseudospin matrix. This representations reveals that the pseudospin will rotate 2φ while the **p** rotates φ. Physically, the consequence is the absence of the robust pseudo-spin backscattering protection mechanism within a valley that was seen in SLG. Hence, in BLG pseudo-spin control is gained but at a cost.

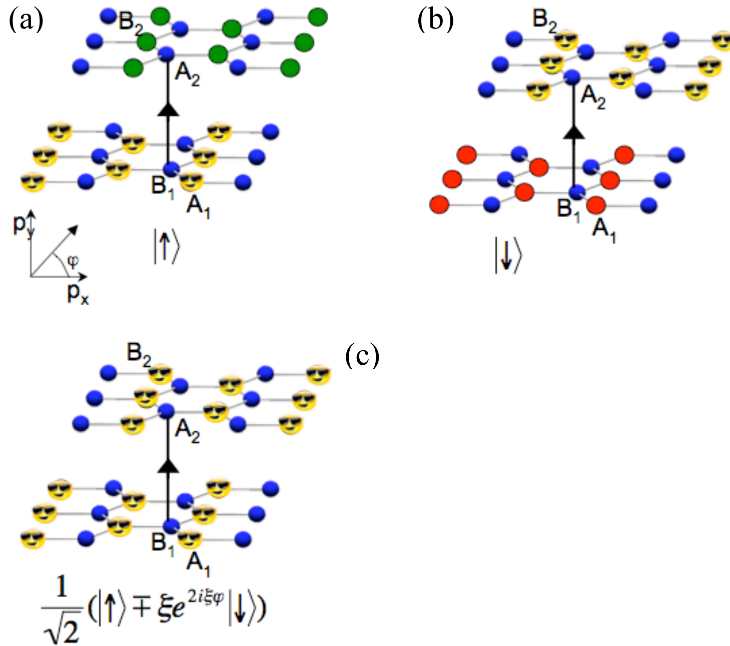

Fig 2.12: Sublattice for BLG. The sublattice degree of freedom in BLG is cast as pseudospin. Note it can also be viewed as a layer degree of freedom. In a. and b. occupation of only one sublattice corresponds to an up or down pseudospin state. In c occupation of both sublattices is a superposition of both states.

2.4.2 Induced Band Gap in BLG

Why would anyone want to gap the beautiful spectrums of SLG and BLG that were discussed above? The motivation comes from an applications point of view. For these carbon sheets to be implemented into a digital electronics setting, which is an attractive route because of their atomic dimensions, there must exist a mechanism to turn current off, i.e. a band gap. As discussed in section 2.4.1 the symmetry between *A*-*B* sublattices in SLG ensures a gapless spectrum. Creating a difference in energy between the sublattices, however, could break this symmetry. A promising proposal is to

implement a local periodic potential[14], but such a feat is currently experimentally unfeasible. There is another option: inducing a band gap by breaking sublattice symmetry is easily accomplished in BLG because the sublattices exist on different layers. Hence, doping or gating one of the layers preferentially induces a band gap in BLG[11].

Below I briefly discuss this sublattice symmetry breaking effect using the tight binding model. The induced gap from this single particle model is relevant for the results on BLG *pnp* junction in chapter five and many body interactions in ultra-clean BLG samples in chapters six and seven.

Introducing an asymmetry between the sublattices in each layer $\Delta=\varepsilon_2-\varepsilon_1$ and noting that each onsite energies are $\varepsilon_{A2}=\varepsilon_{B2}=\frac{1}{2}\Delta$ and $\varepsilon_{A1}=\varepsilon_{B1}=-\frac{1}{2}\Delta$ the transfer integral matrix is,

$$H=\begin{pmatrix} -\frac{1}{2}\Delta & -\gamma_o f(k) & 0 & 0 \\ -\gamma_o f(k) & -\frac{1}{2}\Delta & \gamma_1 & 0 \\ 0 & \gamma_1 & \frac{1}{2}\Delta & -\gamma_o f(k) \\ 0 & 0 & -\gamma_o f(k) & \frac{1}{2}\Delta \end{pmatrix} \tag{2.42}$$

As was done in section 2.3, the band structure can be determined by solving eq 2.10, and the result is plotted in fig 2.14. An analytic expression is obtained by focusing on the low energy, and neglecting non-orthogonality of the orbitals on adjacent sites, which simplifies the overlap matrix to unity. The subsequent eigenvalues are[11],

$$E_{\pm}^{(\alpha)}=\left[\frac{\Delta^2}{4}+v^2p^2+\frac{\gamma_1^2}{2}+\alpha\frac{\gamma_1^2}{2}\sqrt{1+\frac{4v^2p^2}{\gamma_1^2}+\frac{4\Delta^2v^2p^2}{\gamma_1^4}}\right]^{1/2} \tag{2.43}$$

The split bands are represented by α=1 and the low energy bands, which are of more interest to us, are denoted by α=-1. For an energy range within, $v\hbar k \ll \Delta \ll \gamma_1$ the gap reduces to[11],

$$\Delta_g = \frac{\gamma_1 eV}{\sqrt{\gamma_1^2 + eV^2}} \qquad (2.44)$$

where eV is the asymmetry between layers that can be tuned by an additional gate as was done in the experimental results discussed in chapters five through seven. Note, when eV $\gg \gamma_1$, Δ_g saturates at γ_1, which is 300-400 meV. Taken together, this tunable gap and the massive chiral charge carriers distinguished BLG as a system that can satisfy both technological and academic inquires. This motif will be explored in the proceeding chapters, first through the lens of an induced gap and then via the interaction gap.

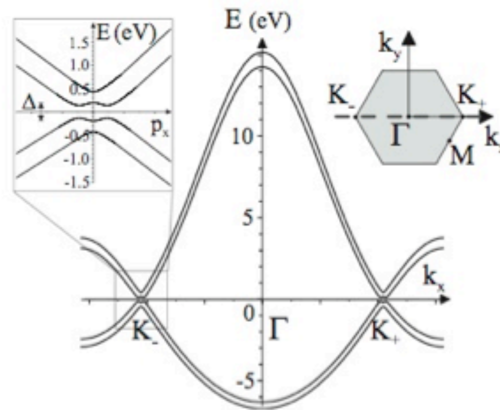

Fig 2.13: Band structure of gapped BLG. Tight binding calculation for the band structure of gapped BLG, with γ_o = 3.033eV, s_o=0.129, and $\Delta=\gamma_1$ = 0.39eV at k_y=0. Note Δ occurs at the K_+ and K_- points, image from[8]

2.5 Quantum Hall effect

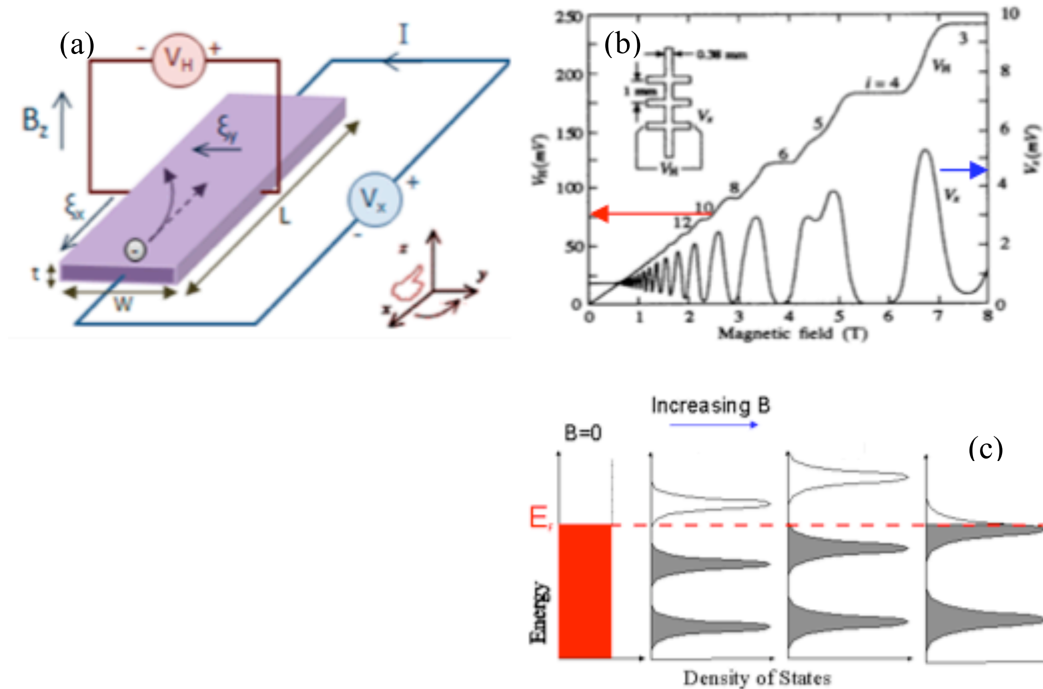

Fig 2.14: QHE in a conventional 2DEGS. a. Schematic of Hall and longitudinal voltage measurements for a conventional 2DEG in the presence of a perpendicular *B*. b. Hall voltage and longitudinal voltage plotted as a function of increasing *B* for a similar 2DEG. Notice plateau in Hall voltage and periodic behavior in the longitudinal voltage. c. Energy plotted as a function of density of states for a conventional 2DEGS as *B* increases. Note, energy becomes discrete as *B* is increased (Landau levels) images from wikipedia section on QHE.

For a two-dimensional gas of electrons, shown in fig 2.14a, the application of a perpendicular *B* persuades the electrons to follow cyclotron orbits, which results in a quantization of the allowed energies, shown in fig 2.14c. These quantized energy levels are called Landau levels (LL) after the great scientist Lev Landau who first solved this problem theoretically. Fig 2.14b plots the Hall and longitudinal voltage for a current

biased 2DEGS as B is increased. In the low B regime, LL give rise to quantum oscillations visible in a sample's measured longitudinal voltage, and are named Shubnikov-de Haas oscillations. In the high B regime, LL manifest in the sample's Hall voltage as quantized integer values of the quantum conductance e^2/h, hence the name quantum Hall effect (QHE).

For a conventional 2DEG, without any Berry's phase effects, the energies are equally spaced apart by $\hbar\omega_c$ where $\omega_c = eB/m$ and the lowest state is $E_o = \hbar\omega_c/2$. Both the discrete energy states and the conductance G at a finite B are plotted in fig 2.15 for several 2DEG systems[15]. When a discrete energy level is full there are no available states for the charge carriers to scatter to, hence the longitudinal resistance is zero and the Hall G will remain a constant integer related to the number of occupied states. Once a subsequent LL is reached available states are available for the scattered electrons, thus the longitudinal resistance becomes finite and the Hall G changes with density. This benchmark two-dimensional measurement will be discussed for graphene. In particular we will find how the addition of Berry's phase greatly influences its nature.

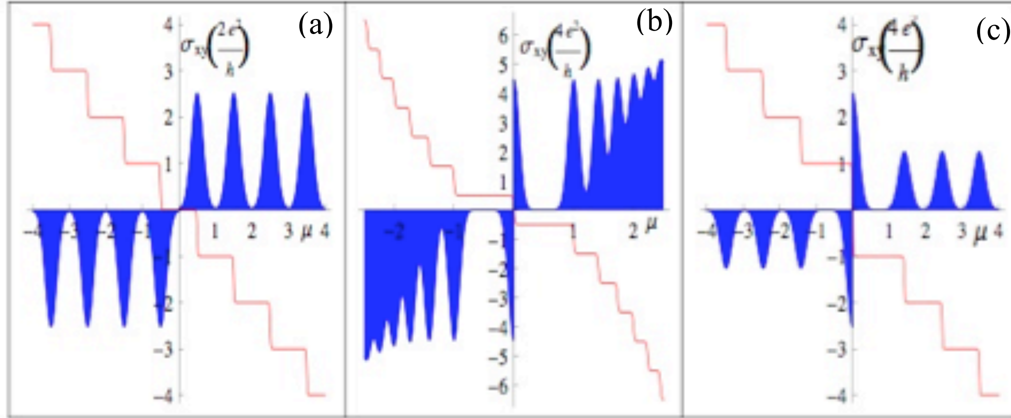

Fig 2.15: Hall conductance and energy plotted as a function of density in the QH regime for various 2DEG systems[15]. a. The Hall *G* and energy spectrum as a function of density for a conventional 2DEG. Note, the equal spacing among states, and the absences of a state at zero density. b. The Hall *G* and energy spectrum as a function of density for SLG. Unique to SLG, a state is present at zero density, and it is shared between holes and electrons. Also, the spacing between states changes as a function of density. The Hall *G* and energy spectrum as a function of density for BLG, which contains characteristics from both a. and b. Finite density states are equally spaced apart, but the zero density state is shared by both holes and electrons, and possess twice the degeneracy of the lowest LL in SLG.

2.5.1 Energy spectrum and QHE for SLG

For graphene, the quintessential 2DEG, the QHE was first studied as a mere toy model[1] fifty years ago. Its experimental isolation in 2004[16] and the subsequent observation of QHE[17, 18] was groundbreaking. This observation demonstrated that graphene was truly a two-dimensional system that is rather uniquely characterized by a Berry's phase of π, and ignited much interest. Below, we discuss, in a general fashion, and starting from the tight binding considerations in section 2.2, the uniqueness of the QHE in SLG.

Following fig 2.15a a SLG sample is arranged so that it experiences a perpendicular B in the z direction. The resultant Hamiltonian, focusing on the low energy regime in the vicinity of the K-points, can be written as,

$$H_{1,K_+} = v\begin{pmatrix} 0 & \pi^* \\ \pi & 0 \end{pmatrix}, \quad H_{1,K_-} = -v\begin{pmatrix} 0 & \pi \\ \pi^* & 0 \end{pmatrix} \qquad (2.45)$$

with π operators defined as,

$$\begin{aligned} \pi &= p_x + ip_y \\ \pi^* &= p_x - ip_y \end{aligned} \qquad (2.46)$$

In the presence of a B the operator $\boldsymbol{p} = (p_x, p_y) \equiv -i\hbar\nabla + e\vec{A}$, where **A** is the vector potential. Using the Landau gauge, **A**=(0, -Bx, 0) the Hamiltonian becomes,

$$\begin{aligned} \pi &= -i\hbar\partial_x + \hbar\partial_y - ieBx \\ \pi^* &= i\hbar\partial_x - \hbar\partial_y + ieBx \end{aligned} \qquad (2.47)$$

We note for the above Hamiltonian translational invariance is preserved in the y direction; hence, plane waves are suitable solutions for this component of the wave function. In the x direction the presence of the $\boldsymbol{x}$ operator is accommodated by harmonic oscillator solutions. Thus the complete wave function is,

$$\phi_l = A_l H_l\left(\frac{x}{\lambda_B} - \frac{p_y\lambda_B}{\hbar}\right)\exp\left[-\frac{1}{2}\left(\frac{x}{\lambda_B} - \frac{p_y\lambda_B}{\hbar}\right)^2 + \frac{ip_y y}{\hbar}\right] \qquad (2.48)$$

Where H_l are Hermite polynomials of order l, and l is an integer with $l \geq 0$, and $A_l = 1\big/\sqrt{2^l\, l!\sqrt{\pi}}$. The constant $\lambda_B = \sqrt{\hbar/eB}$, is the magnetic length.

By acting on the harmonic oscillator component of the solutions above with π and π^* we observe,

$$\pi\phi_l = -\frac{\sqrt{2}i\hbar}{\lambda_B}\sqrt{l}\phi_{l-1} \qquad (2.49)$$

$$\pi^*\phi_l = \frac{\sqrt{2}i\hbar}{\lambda_B}\sqrt{l+1}\phi_{l+1} \qquad (2.50)$$

This indicates π and π^* are the lowering and raising operators of the ladder method, respectively, which is discussed in[19] for a harmonic oscillator potential. Here we can utilize that machinery to help us acquire all of the solutions. The Landau level spectrum for the K_+ valley is,

$$K_+, l \geq l: \quad E_{l,\pm} = \pm\sqrt{2\hbar v^2 eBl}, \quad \psi_{l,\pm} = \frac{1}{\sqrt{2}}\begin{pmatrix} \phi_l \\ \mp\phi_{l-1} \end{pmatrix} \qquad (2.51)$$

$$K_+, l = 0: \quad E_0 = 0, \quad \psi_o = \begin{pmatrix} 0 \\ \phi_o \end{pmatrix} \qquad (2.52)$$

where $\pm$ refers to conduction and valence bands respectively. Notably the $E_l \propto \sqrt{B}$, which is different for the linear dependence in 2DEGS. For the K_- valley we have,

$$K_-, l \geq l: \quad E_{l,\pm} = \pm\sqrt{2\hbar v^2 eBl}, \quad \psi_{l,\pm} = \frac{1}{\sqrt{2}}\begin{pmatrix} \mp\phi_{l-1} \\ \phi_l \end{pmatrix} \qquad (2.53)$$

$$K_-, l = 0: \quad E_0 = 0, \quad \psi_o = \begin{pmatrix} 0 \\ \phi_o \end{pmatrix}. \qquad (2.54)$$

Interestingly, the ψ_o eigenfunction of the zeroth level is valley degenerate, since it has amplitude on each different sublattice for each distinct valley. When a two-fold spin degeneracy is included this leads to a total four-fold degeneracy in the LL spectrum of SLG.

The resulting QHE from the energy spectrum discussed above is shown in fig 2.15b and is described by,

$$\sigma_{xy} = \frac{1}{2}(2N+1)\left(\frac{4e^2}{h}\right) \qquad (2.55)$$

where N is an integer. This unique G spectrum is due to the four-fold degeneracy of the zeroth LL. The maximum carrier per density of a LL is gB/φ_o, where g is system's degeneracy and φ_o is the flux quantum h/e. From the single particle picture described in the last section we gather that the LL and thus the G plateau are separated in density by NgB/φ_o. Taken together, the fourfold degeneracy, and the degenracy's occurrence at E_o and at the boundary between electrons and holes, produces the $4e^2/h$ step size that straddles the zero density point. Unlike the traditional 2DEGS with zero G at zero density in graphene both electrons and holes share the lowest LL. This is the famous anomalous QHE of SLG.

2.6 Energy spectrum and Quantum Hall effect for BLG

Although BLG is not atomically thin as SLG, it is electronically a 2DEG as was discussed in chapter one. Therefore, when a BLG sample experiences a perpendicular B its electrons will follow cyclotron orbits, and LL will arise. Interestingly, these charge carriers share similarities with both SLG and the traditional 2DEGS. On one hand, they are massive and follow the more conventional parabolic energy dispersion. On the other hand, these massive charge carriers are chiral with a Berry phase of 2π, as shown in section 2.4. Hence, we expect their QHE to possess qualities of both systems. Below we examine this expectation.

In the presence of B applied in the z direction the resultant Hamiltonian is,

$$H_{2,K_+} = -\frac{1}{2m}\begin{pmatrix} 0 & (\pi^*)^2 \\ \pi^2 & 0 \end{pmatrix}, \quad H_{2,K_-} = -\frac{1}{2m}\begin{pmatrix} 0 & \pi^2 \\ (\pi^*)^2 & 0 \end{pmatrix} \qquad (2.56)$$

for the low energy regime in the vicinity of the K-points. Using the ladder method from the previous section we consider the result of the action of π, and then π^* on the previously discussed harmonic oscillator solutions. The LL energies and eigenstates for the K_+ are,

$$K_{+,} \, l \geq 2: \quad E_{l,\pm} = \pm \frac{\hbar eB}{m}\sqrt{l(l-1)}, \quad \psi_{l,\pm} = \frac{1}{\sqrt{2}}\begin{pmatrix} \phi_l \\ \phi_{l-2} \end{pmatrix} \qquad (2.57)$$

$$K_+, l = 1: \quad E_1 = 0, \quad \psi_{l,\pm} = \begin{pmatrix} \phi_1 \\ 0 \end{pmatrix} \qquad (2.58)$$

$$K_+, l = 0: \quad E_o = 0, \quad \psi_{l,\pm} = \begin{pmatrix} \phi_0 \\ 0 \end{pmatrix} \qquad (2.59)$$

and for the K_-

$$K_{-,} \, l \geq 2: \quad E_{l,\pm} = \pm \frac{\hbar eB}{m}\sqrt{l(l-1)}, \quad \psi_{l,\pm} = \frac{1}{\sqrt{2}}\begin{pmatrix} \phi_{l-2} \\ \phi_l \end{pmatrix} \qquad (2.60)$$

$$K_-, l = 1: \quad E_1 = 0, \quad \psi_{1,\pm} = \begin{pmatrix} 0 \\ \phi_1 \end{pmatrix} \qquad (2.61)$$

$$K_-, l = 0: \quad E_o = 0, \quad \psi_{o,\pm} = \begin{pmatrix} 0 \\ \phi_o \end{pmatrix} \qquad (2.62)$$

Fig 2.15c displays the Hall conductivity for BLG and its LL energy spectrum, it contains two main features; 1) At higher densities quantized conductance plateau are seen at integer values of $4e^2/h$, and equally spaced apart similar to the conventional 2DEG case; and 2) Across zero density there is an increment of $8e^2/h$. The first observation arises from the combination of 2-fold spin and 2-fold valley degeneracies present in

BLG. The second observation is similar to the SLG case in that it is shared by both holes and electrons, but with twice the degeneracy due to the enhanced degeneracy of the l=0 and l=1 LL shown in eq. 2.58 and 2.59.

To summarize, these carbon sheets of one and two layers represent a new QH playground. Their quintessential two-dimensional nature is perfectly suited for QH studies, and the chirality of the SLG and BLG carriers, which possess a berry phase of π and 2π, respectively, adds a fascinating new twist to the well-established QHE.

The single particle picture discussed in this section explains the existence of these zero density anomalies, where the lowest LL coexists between holes and electrons. To further explore the physics of these highly degenerate energy levels a more technical approach that includes electron-electron interactions is required. For a technical discussion on this topic the reader is referred to[15]. Experimentally, we will encounter this topic briefly first in chapter five with BLG *pnp* junctions, and then more extensively in chapters six and seven with our dual gated suspended BLG samples. The high quality attained by these latter samples is perfectly suited for unraveling the degenracies of the lowest LL in BLG as will be demonstrated.

Conclusion

This concludes the theoretical background for the basic electronic properties of SLG and BLG. The main points are: 1) SLG has a linear dispersion relation at energies relevant to transport, whereas BLG has a parabolic dispersion relation in the same energy regime, 2) Conservation of pseudo-spin protects carriers from backscattering within a

valley in SLG, while in BLG such a conservation law is not applicable, and 3) Pseudo-spin at low energies for BLG is essentially a matter of charge layer polarization unlike the case for SLG, and 4) Berry's phase effects in SLG and BLG result in a unique QH experience. The third point will be explored in the thesis during the discussion of experimental results in BLG studies. Interestingly, this tunable parameter will play an important role in both the non-interactive picture, which was drawn in this chapter, and for the correlated-electron picture, which is not mentioned in this chapter but is discussed in chapters six and seven experimentally. Quantum Hall physics of both SLG and BLG will also be discussed in chapters four and five in the experimental results for *pnp* junctions. As a young experimental physicist this was a wonderful time to engage in QH studies because each day was an opportunity to discover some new state. I often compared this to the plight of an astronomer during the advent of the telescope, or a biologist suddenly immersed in a new ecosystem teeming with unknown creatures.

References

1. P. R. Wallace, Physical Review **71** (9), 622-634 (1947).
2. E. McCann and V. I. Fal'ko, Phys. Rev. Lett. **96** (8), 086805 (2006).
3. F. Zhang, H. Min, M. Polini and A. H. MacDonald, Phys. Rev. B **81** (4), 041402 (R) (2010).
4. F. Zhang, J. Jung, G. A. Fiete, Q. A. Niu and A. H. MacDonald, Phys. Rev. Lett. **106** (15), 156801 (2011).
5. O. Vafek and K. Yang, Phys. Rev. B **81** (4), 041401 (2010).
6. R. Nandkishore and L. Levitov, preprint, arXiv:1002.1966v1001 (2010).
7. Y. Lemonik, I. L. Aleiner, C. Toke and V. I. Fal'ko, Phys. Rev. B **82** (20), 201408 (2010).
8. E. McCann, preprint, arXiv:1205.4849v1201.
9. T. Ando, T. Nakanishi and R. Saito, Journal of the Physical Society of Japan **67** (8), 2857-2862 (1998).
10. P. L. McEuen, M. Bockrath, D. H. Cobden, Y. G. Yoon and S. G. Louie, Physical Review Letters **83** (24), 5098-5101 (1999).
11. E. McCann, Phys. Rev. B **74**, 161403 (2006).
12. E. A. Henriksen, Z. Jiang, L.-C. Tung, M. E. Schwartz, M. Takita, Y.-J. Wang, P. Kim and H. L. Stormer, Phys. Rev. Lett. **100**, 087403 (2008).
13. S. Cho and M. S. Fuhrer, Nano Res. **4**, 385 (2011).
14. G. Giovannetti, P. A. Khomyakov, G. Brocks, P. J. Kelly and J. van den Brink, Physical Review B **76** (7), 073103 (2007).
15. B. Yafis, Y. Kun and A. H. MacDonald, Nanotechnology **23** (5), 052001 (2012).
16. K. S. Novoselov, A. K. Geim, S. V. Morozov, D. Jiang, Y. Zhang, S. V. Dubonos, I. V. Grigorieva and A. A. Firsov, Science **306** (5296), 666-669 (2004).
17. K. S. Novoselov, A. K. Geim, S. V. Morozov, D. Jiang, M. I. Katsnelson, I. V. Grigorieva, S. V. Dubonos and A. A. Firsov, Nature **438** (7065), 197-200 (2005).

18. Y. B. Zhang, Y. W. Tan, H. L. Stormer and P. Kim, Nature **438** (7065), 201-204 (2005).

19. D. J. Griffiths, *Introduction to Quantum Mechanics*, 1st ed. (Addison Wesley, 2004).

Chapter 3: Fabrication

Introduction

In this chapter I will discuss fabrication techniques for graphene and Bi_2Se_3 based samples that I developed or helped to develop. These techniques focused on suspended structures with the aim to achieve high sample quality. The suspended structures include: 1) Dual gated graphene on substrate with variations on the contactless top gate; 2) Acid free suspension of thin crystals, and 3) Dual gated suspended graphene.

Fabrication is a vital component in the experimental inquiry of electron transport because working samples are the first requirement for this enterprise. As samples improve and disorder is reduced the intrinsic physics within in a particular system is revealed. This was evident in the 2DEGS studies in the 1980's. When sufficiently clean Si-MOSFET samples became available, integer quantum Hall effect was discovered; after the even cleaner GaAs-InGaAs samples were fabricated, fractional quantum Hall effect was discovered, which is the archetype correlated electron phenomena. In graphene the situation was no different.

High quality suspended graphene structures with only one gate were first introduced by [1], [2] and then followed by [3], [4] with BLG based samples, both samples are shown in fig 3.1a-b. The first contactless dual gated graphene on substrate samples were made by [5, 6], fig 3.1c and were followed by[7] with a BLG analogue. These two device types were then combined first by[8] , and shortly after by[9] where the quality attained in the latter was much higher, fig 3.1d.

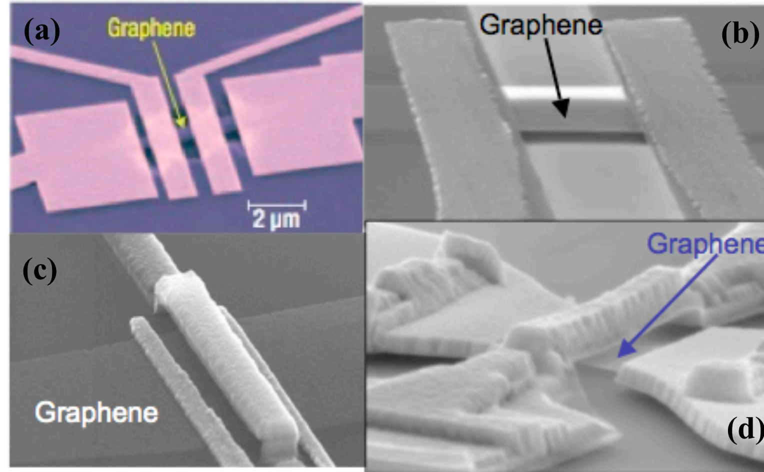

Fig 3.1 Suspended structures. a. A suspended graphene sample held up by four contacting electrodes made by [1]. This method uses a PMMA mask to only remove the oxide beneath the graphene while leaving the surrounding oxide intact. b. A suspended BLG sample clamped on by two contacting electrodes made by [4]. This method employs exfoliation onto pre-deifned trenches to suspend graphene, and a shadow mask to selectively deposit metal onto graphene for electrodes. c. A suspended top gate straddles from above a substrate supported graphene flake, made by [6]. This method utilizes a multi-level lithography technique to fabricate contactless top gates. d. A suspended top gate straddles from above a suspended graphene flake made by [9]. This method combines a variation on the technique from fig 3.1a and 3.1c.

There are several advantages, from a device fabrication perspective, for the contactless dual gated device on substrate, and these advantages also apply to the suspended dual gated device. The superiority of freestanding samples, from a scientific point of view is most salient in

$$\alpha \propto \frac{n^{-(p-1)/2}}{\varepsilon_r} \qquad (3.1)$$

Here α is a ratio of the kinetic and potential energy of the charge carriers known as the interaction parameter. It depends on *n* carrier density, *p* the power of the dispersion relation, which is related to number of layers for rhombohedral stacked multilayer graphene and ε_r the dielectric constant of the surrounding environment. Evidently, interactions are largest when the system is at low carrier densities, is rhombohedrally stacked and comprised of several layers, and is unfettered by any material. Hence, the suspended dual gated device is a superb structure to achieve a highly interacting graphene based system.

Finally, in addition to the physics-related reasons, personally, I find successful structures to be rewarding and aesthetically pleasing. The feat of suspending materials at the nanoscale is comparable to successfully executing a convoluted cooking recipe. Throughout the procedure, because of the scale of things, it is difficult to see the detailed microscopic ongoings. Instead, one can only look at their creation at specific stages much like a cook takes a taste test with their wooden spoon. At the end, if the recipe is executed correctly, the reward is the sight of the structure perched proudly above the substrate, the equivalent of a most delicious meal. Yet, as with the meal, a fortuitous anomaly does not suffice. Instead, the aim is a robust procedure where the success can always be repeated. To achieve this many hours and trials are required with an acute eye to details dovetailed with a shrewd intuition and an unabated tenacity. During these long nights a notion, which is captured elegantly by the renaissance sculptor Michelangelo, kept me motivated,

"Every block of stone has a statue inside of it and it is the task of the sculptor to discover it"

3.1: Fabrication of contactless topgates

3.1.1: Conventional dual gated devices

A remarkable electronic property of graphene is that both carrier type and density can be controlled electrostatically. Via the employment of a local gate and a global back gate, this feature also enables in situ creation and control of *p-n* junctions in graphene [10-13], which have been demonstrated or predicted to give rise to quantum Hall plateaus with fractional values due to mode mixing of edge states [10, 11, 13] this will be discussed in chapters four for SLG and five for BLG, Veselago lensing[14, 15] and Klein tunneling[16-18]. In the first generation of experiments, either an organic or a metal oxide layer has been used as the local gate dielectric, yet its deposition on a single atomic layer remains a delicate process that may lead to additional dopants and/or scattering sites. These devices are shown in fig 3.2a-d, where each structure is similar in the use of a dielectric between top gate and graphene, but different in the type of dielectric employed. Moreover, dramatically enhanced mobility has been observed in suspended graphene devices [1, 2], but fabrication of suspended graphene p-n junctions using conventional techniques could prove difficult, since direct deposition of local gate dielectrics may considerably stress or even collapse the atomic layer.

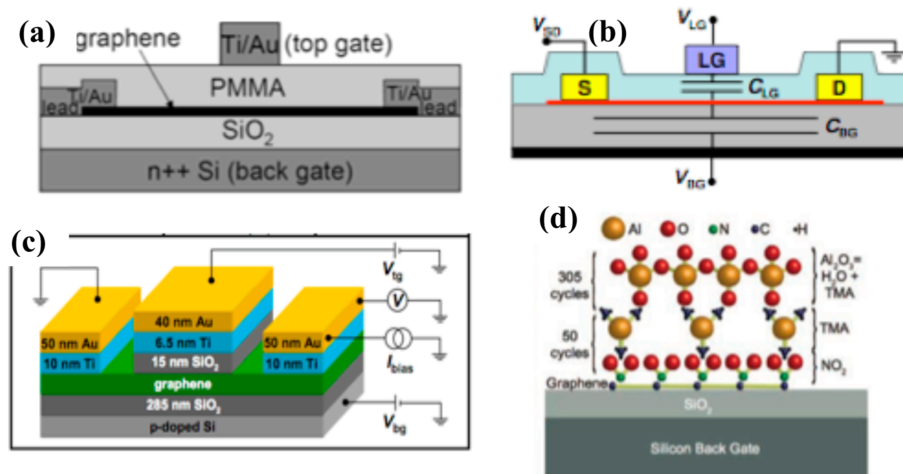

Fig 3.2: Dual gated graphene structures with. a. Substrate supported graphene sample is contacted by two metallic leads and a layer of PMMA rests on top of graphene supporting the metallic top gate. The PMMA is stiffened by procedure called cross-linking, which is simply a large exposure of 30,000 Kv, image from[12]. b. Substrate supported graphene sample is contacted by two metallic leads, and a 20 nm layer of HSQ(a negative resist) and 15 nm of HfO_2 that rests on top of graphene supporting the metallic top gate. The HSQ was spun onto the chip while the HfO_2 was grown by atomic layer deposition, image from[13] c. Substrate supported graphene sample is contacted by two metallic leads, and a 15 nm layer of SiO_2 rests on top of graphene supporting the metallic top gate. The SiO_2 was deposited via electron beam evaporation, image from[19]. d. Substrate supported graphene sample is contacted by two metallic leads, and a NCFL (non-covalent functionalized layer) and a 30 nm layer of Al_2 O_3 that rests on top of graphene supporting the metallic top gate. Both layers were grown by atomic layer deposition, image from[10].

3.1.2: A novel trick

We developed an innovative multi-level lithography technique to fabricate contactless top gates that are suspended ~100 nm above the graphene layers, which are only exposed to conventional electron-beam resists and developers, thus minimizing the damage to the atomic layer. The vacuum insulated gap between the "air bridge"-styled top gate and the device is not susceptible to pinholes, dielectric breakdown and leakage current. Unlike the standard graphene *p-n* junctions, devices fabricated using this technique are still amiable to annealing procedures that have been shown to be effective in improving device mobility and contact resistance [20, 21], hence this technique is powerful when combined when suspended graphene. Using this technique, we demonstrate the fabrication of a graphene *p-n-p* junction, and its quality is established by the presence of the $2e^2/h$ conductance plateau at high magnetic fields and by the presence of distinct resistance oscillations in the bipolar region that arise from Fabry–Perot interference, both of which will be discussed in the next chapter. Later in this chapter, the role of this method in the fabrication of the dual gated suspended graphene architecture will be discussed.

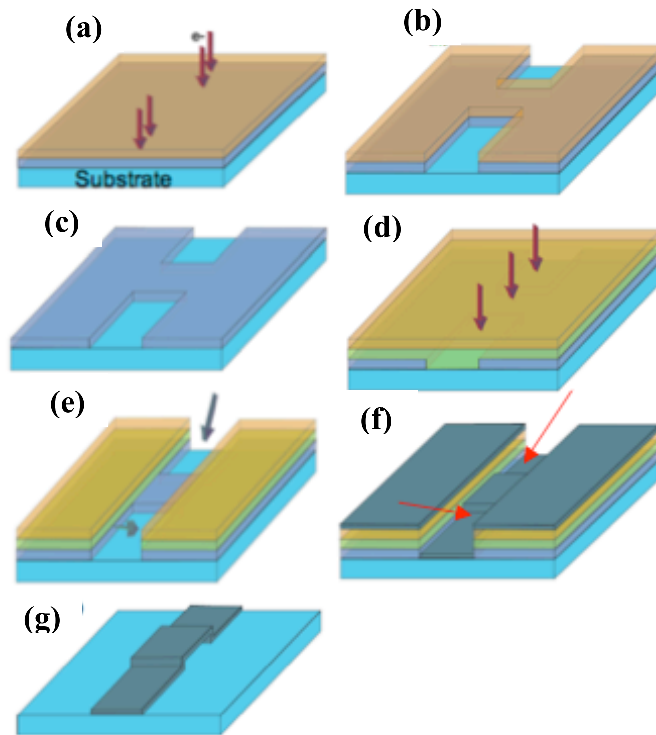

Fig 3.3: Schematics of fabrication process. a. LOR blue and PMMA brown are deposited onto the substrate and exposed to electron beams arrows. b. Developing in MIBK and MIF319 solutions opens windows for the electrodes. c. Lift-off in acetone removes PMMA but leaves LOR layer intact. d. MMA green and PMMA brown are deposited, and exposed to e beam arrows. e. Developing in MIBK opens windows for the electrodes and the suspended structure. f. Metals are evaporated at 45° and −45° in directions indicated by arrows in e. In g. Resists are lifted off in PG remover, leaving an air bridge contacted to electrodes.

This fabrication process of suspended structures takes advantage of the different exposure, developing and lift-off properties of different resists. fig 3.3 illustrates the fabrication process, which consists of two lithography steps and a several metal deposition steps. The goal of the first lithography step is two-fold: (1) to deposit a resist layer that will act as an initial mechanical support for the suspended portion of the air

bridge, and will be removed at the end of the fabrication; and (2) to create windows for the electrical leads that contact the suspended structure. To achieve these goals, LOR/PMMA bilayer resists are spun and baked on Si/SiO_2 substrates (fig. 3.3a). We then use an electron beam to expose the patterns for the electrical leads. The chips are developed twice – first in MIBK/IPA with a ratio of 3:1 for 60 seconds to dissolve the exposed PMMA, then in MF319 to dissolve portions of LOR via the PMMA windows (fig 3.3b). The duration for the latter development depends on the thickness of the LOR and type. These values can be found in the appendix. Subsequently, a 10-minute acetone bath is used to lift off the top PMMA layer while leaving the LOR intact (fig 3.3c). The final outcome of the first lithography step is an LOR layer with windows for electrical contacts for the air bridge.

During the second lithography step, MMA/PMMA bilayer resists are spun and baked on top of the LOR layer, followed by electron beam exposure of patterns for both the air bridge and the electrical leads (fig 3.3d). The chips are developed in MIBK for 60 seconds that removes exposed MMA and PMMA, leaving windows in MMA/PMMA bilayer for the air bridge, and windows in all three resist layers for the leads (fig 3.3e). Lastly, the device is completed by two metal depositions at 45° and -45°(fig 3.3f), where this is accomplished by placing the sample on an inclined bracket that is mounted on the center of the bell jar as shown in fig 3.4. The aim is to deposit metals onto the side-walls of the windows and ensure contact between the suspended structure and the electrical leads. For the final lift-off process, the three resist layers are removed by a warm PG remover bath for two hours, and then light agitation from a pipet full of the PG remover

from the bath to promote unwanted metal detachment. Finally, the chips are rinsed in isopropyl alcohol and dried in nitrogen gas.

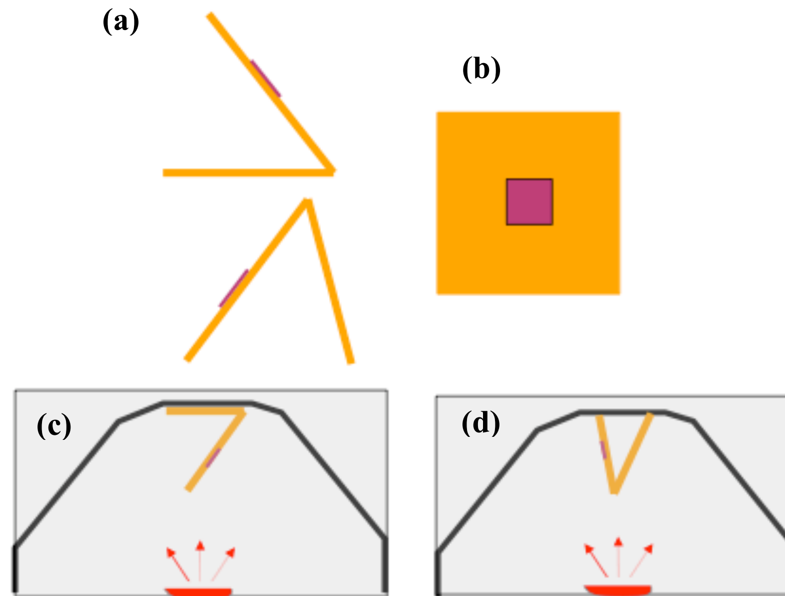

Fig 3.4 Schematics of angle evaporation at 45° and -45°. a. Front view of metal bracket (orange) with a sample(purple) secured onto it in the two evaporation orientations. b. Top view of a. In c-d bracket is secured on the top part of bell-jar(black line), which is in the evaporator(gray box) directly perpendicular to the metal source in the two different orientations.

Examples of completed suspended structures are shown in fig 3.5. The fabrication procedure is quite robust; by controlling the lithography conditions, we are able to fabricate suspended air bridges with considerable ranges in dimensions, including span (l), width (w) and height above the substrate (h). For our purpose of using a suspended bridge as a local top gate, the important parameters are l and h: the former directly limits the width of the graphene strip that can be used, the latter determines the gate efficiency.

The height of the bridge is determined by the thickness of the LOR resist layer, which may range from 50 nm to 3 μm. Fig 3.5a and 3.5b display two bridges that are suspended 300 nm and 100 nm above the substrates, respectively. On the other hand, we find that l increases with w and the material's strength. We note that we are able to create titanium air bridges ~ 7 μm long without critical point drying.

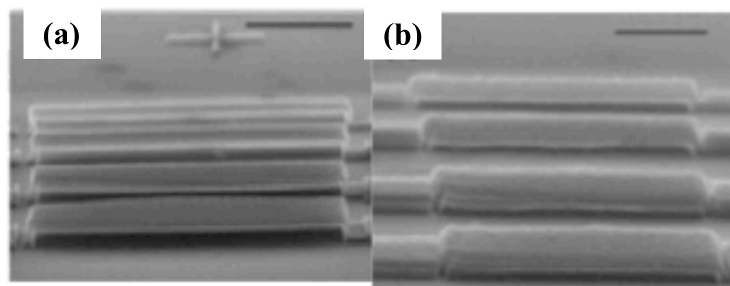

Fig 3.5: Finished top gates. SEM images of suspended air bridges with different spans, widths, and heights. Scale bars: 2 μm.

3.1.3 Stronger top gates

A high resolution and high magnification scanning electron micrograph (fig 3.6a) of a successfully completed top gate sample reveals rather thin sidewalls. To address this drawback in the device we added a third step in the metal deposition step at 0°. Fig. 3.6b-c schematically details the mounting of the sample on the bell jar for this step. The additional vertically directed metallic deposition increases the amount of metal in the joints leading to thicker sidewalls. As desired, fig 3.6d depicts the strengthening of these joints with the third step evaporation recipe versus the two-step method.

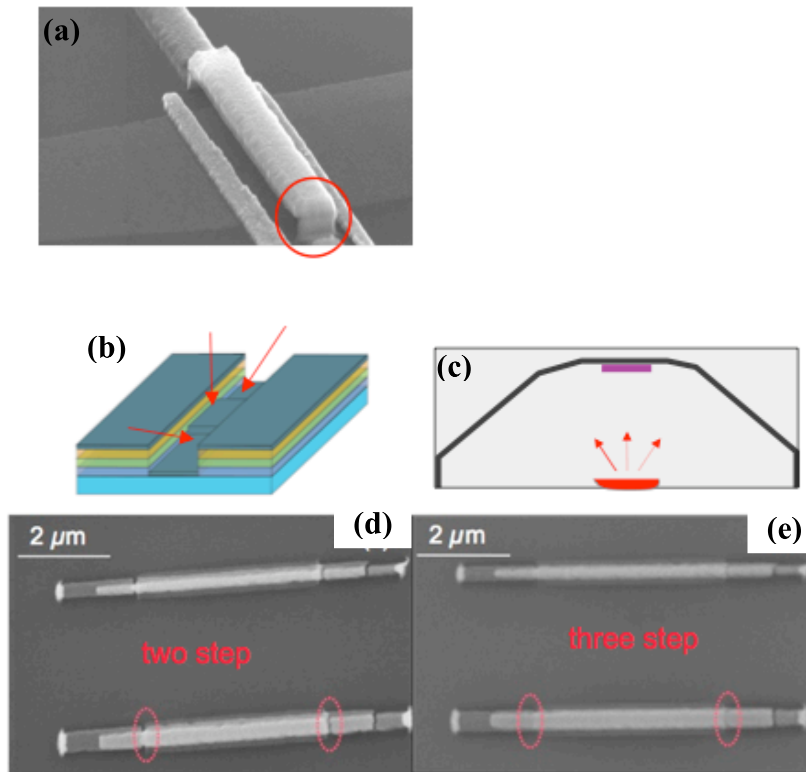

Fig 3.6: Schematics of third step evaporation. a. SEM image of a completed top gate, using two step method, showing thin side walls. b. Schematic representation of third step evaporation with red arrow symbolizing metallization. c. Schematic representation of sample mounted on bell jar in evaporator. d-e two step and three step evaporation results of top gates. Third step displays seemingly stronger joints.

To further strengthen the structural integrity of the bridge we utilized a critical point dryer after the liftoff step. Examples of the increased structural figures of merit are shown in fig 3.7. The first dimension that was improved was *h*, which was reduced to ~50nm as shown by fig 3.7a. This result is desirable because such a structure would have a greater coupling with the material beneath. The length was also improved significantly. Using a *h*~300nm, Al or Ti/Al for deposited metals and the modified recipe, arrays of

bridges with l between 15 to 30μm were achieved regularly as shown in fig 3.7b. To achieve the longest bridges, which were 40μm(fig 3.7c), we implemented an overnight liftoff in a warm PG remover bath with a slight agitation at the end, similar to what was mentioned before, but with care to direct this agitation away from the chip. By using this last recipe top gates of l~12μm were also achieved with Cr, Au and Cr/Au. The quantities of metal for the individual deposition step depend on the supporting LOR thickness and are listed accordingly in the table below.

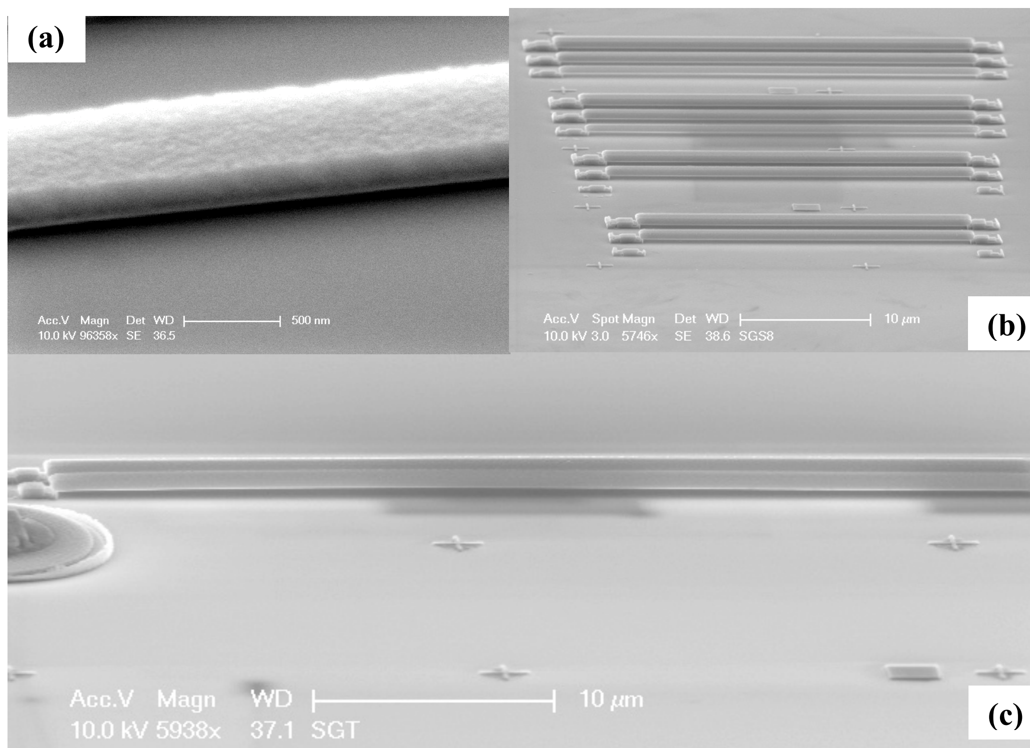

Fig 3.7 Top gate dried with critical point dryer. a. Angled SEM image of a titanium top gate ~50nm above the substrate. b. Aluminum top gates with a suspended portion that is between 15~30µm and a height of 300nm. c. Aluminum top gate with a height of 300nm and suspension length of 40 µm, record for Lau group.

3.1.4 Substrate supported SLG and dual gated devices

Graphene based devices, with a contactless gate, were fabricated using the earlier form of the recipe and the proceeding modified versions. For the remainder of this thesis I will focus on samples fabricated using the modified version of the recipe, which included a three-step evaporation and use of the critical point dryer.

Once the robust top gate was fabricated over a selected exfoliated graphene flake we performed oxygen annealing in our quartz tube furnace at 300°C and a flow of .4 Scc for one hour to remove resist residue. Then we spun a bilayer of resist comprised of MMA/PMMA at a slow centripetal acceleration of 300 rpm/s followed by standard electron beam lithography to define contact electrodes onto the graphene. After the exposure and developing (see appendix) we deposit metal, consisting of 10 nm of Ti and 80 nm of Al, on graphene and perform liftoff in a warm acetone bath for two hours. The drying is performed by a critical point dryer to ensure structural integrity. Fig. 3.8a displays a schematic indicating all of the components of the device and a completed device as well, respectively.

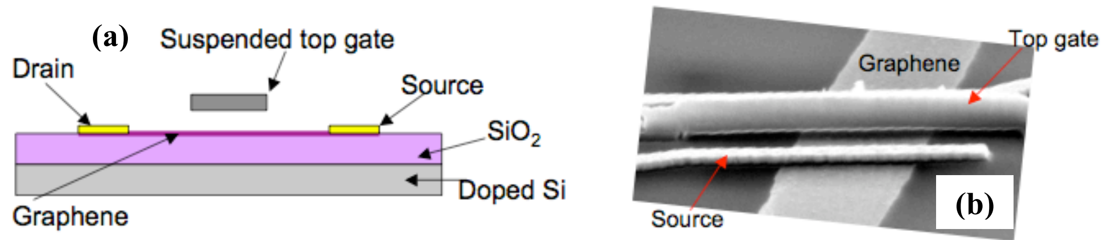

Fig 3.8: Graphene based dual gated device. a. Detailed schematic of a device, graphene (pink) resting on SiO_2 substrate(lavender) is coupled with Ti/Al electrodes(yellow), while titanium contactless top gate (grey) straddles graphene flake. b. SEM image similar to schematic.

The suspended gates can also be fabricated at nonzero angles with respect to the source– drain electrodes (fig 3.9 b-c), by careful control of the direction of metal evaporations. This is achieved by placing the sample with the top gate parallel to a line carved into the angled bracket for metallization. The carved line is made at an angle that matches the angle the top gate makes with a chosen line of reference from the design, as shown in fig. 3.9a. Such graphene devices with angled top gates were first proposed as an experimental platform to observe Klein tunneling, in which the transmission coefficient of charges across high potential barriers strongly depends on the incident angle[16].

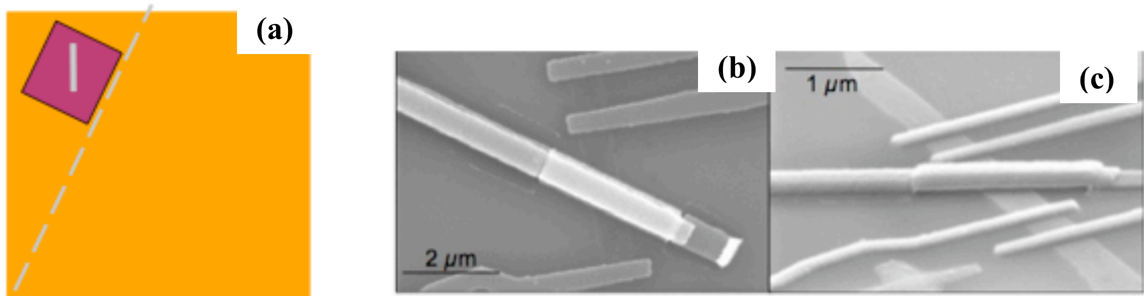

Fig 3.9: Angled top gate devices. a. Schematic of a chip(purple) containing a device(grey and not to drawn scale) mounted onto angled bracket(gold), which is seen from top view. Chip is tilted along dashed line, which aligns device with the dashed line. SEM images of an angled top gate device where the metallization was performed with procedure demonstrated in schematic.

Finally, to directly verify the mechanical robustness of these structures, we perform in-situ scanning electron microscope (SEM) imaging, while applying voltages to the top gate. As shown by the images in fig. 3.10a-c, the air bridge remains suspended and undeformed under voltages of 70 and 100V, and ultimately fails at 110V. This surprisingly high critical voltage demonstrates significant improvement over the previous top gate structures.

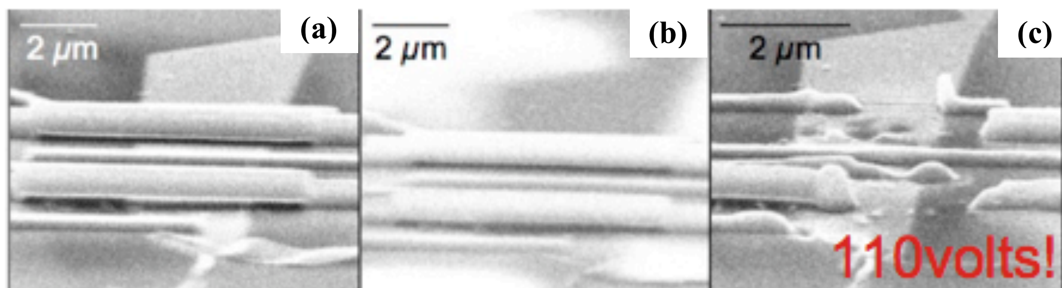

Fig 3.10: SEM images of top gates under applied voltage. SEM images of a suspended topgate under applied voltages of 70, 100 and 110V,respectively.

3.2: Suspension and Measurement of Graphene and Bi_2Se_3 Atomic Membranes

3.2.1: Fabricating in my dreams

Before diving into the meat of this work a brief anecdote. This work was developed between the end of the dual gated graphene devices on substrate and the start of the suspended graphene version. To make the latter it is required to use a buffered oxide etch solution to remove the supporting SiO_2, such a solution is comprised of an extremely dangerous acid named hydrofluoric acid (HF). Because HF interferes with nerve function, meaning that burns may not initially be painful, accidental exposures can go unnoticed, delaying treatment and increasing the extent and seriousness of the injury. In those early days my hands would shake when I handled this dangerous material and I would have reoccurring nightmares. This motivated me to develop an alternative to the BOE method for producing suspended samples, which my lab mates Adam and Hang became a part of because of the mutual interest for their projects on suspended Josephson junctions and effects of strain on transport. Despite my discomfort with the BOE method I continued making those samples in parallel and eventually nice results were attained with the BOE method first. Regardless of the outcome, this recipe can be used for exploration of physical phenomena in suspended graphene not accessible with gold electrodes.

Besides having the ability to boast that we can suspend any thin crystal, and couple it to any metal, which most likely elicits a resounding “so what!”, the fabrication method presented in this section paves the way for the exploration of many new and exciting physical phenomena, as was already shown by[22], which used a similar method to study

the effects of confinement in suspended SLG. In the following section, we will first briefly discuss the potential applications of this acid free substrate release method, and then describe the procedure in detail. Finally, we fabricate suspended SLG and Bi_2Se_3 samples coupled to superconducting electrodes Ti/Al to demonstrate the viability of our technique.

3.2.2: Atomic membranes and special electrodes

Recently, atomic membranes (AM) that are extracted from layered materials have become popular platforms for investigation of novel physical phenomena[23]. Some of the most studied materials are thin sheets of graphite[24], Bi_2Se_3 and Bi_2Te_3, which provide platforms for investigating massless Dirac fermions[25],[26] and topological insulators[27-29]. Due to their two-dimensionality, they display a number of desirable characteristics such as gate tunable charge density and/or type, enhanced Coulomb interaction and coupling between local morphology and electronic properties [30],[31]. As surface 2D electron systems, these membranes also enable optical and scanned probe measurements that are not possible in traditional semiconductor heterostructure devices.

Another significant advantage of these systems is that they can be easily coupled to special electrodes, such as superconductors or ferromagnets, potentially enabling experimental realization of some of the most fascinating predictions for these systems, such as specular Andreev Relfection[32], Majorana fermions[33] and spin Hall effect. Yet, interaction between AM and the substrate is known to be a significant impediment for the observation of such phenomena, since the substrate can locally dope the membranes, induce local corrugations and strains, and introduce scatterers such as charged impurities

and surface phonons. Thus far, removing the substrate has proven to yield exceedingly high-quality devices [1,2] yielding novel phenomena such as Wigner crystallization and Mott insulating states in carbon nanotubes [34,35] and fractional quantum Hall effect in graphene [36,37].

To remove substrates, the most commonly adopted technique is acid etching, which dissolves the oxide layer underneath the device. However, this technique suffers from several drawbacks, including limitation of membrane and electrode materials to those that are stable in acid, and substrate to those that are not. For instance, superconducting and ferromagnetic materials cannot survive such a procedure and many of the much sought-after topological insulator materials, including Bi_2Se_3 and Bi_2Te_3, are also partially soluble in hydrofluoric acid that etches SiO_2.

3.2.3: The same novel trick but different order

Below we discuss an innovative multilevel lithography technique to fabricate devices with freestanding thin crystals extracted from layered materials. Employing only standard resists and developers for liftoff lithography, this technique can be applied to the vast majority of commonly used substrate, membrane and electrode materials, while imparting minimal damage to the device, which does not undergo any acid or reactive ion etching. Moreover, since the device is suspended above the substrate, the risk of gate leakage is minimized. Using this technique, we demonstrate the fabrication of freestanding graphene coupled to Ti/Al electrodes, with a number of widths and source-drain separations. We also report, for the first time, fabrication and measurement of

suspended thin Bi_2Se_3 thin crystals (TC), with estimated mobility of ~500 cm^2/Vs. In the future, this versatile technique can be used to explore, for instance, superconductivity and spintronics in high mobility graphene and Bi_2Se_3 samples, as well as in other layered materials.

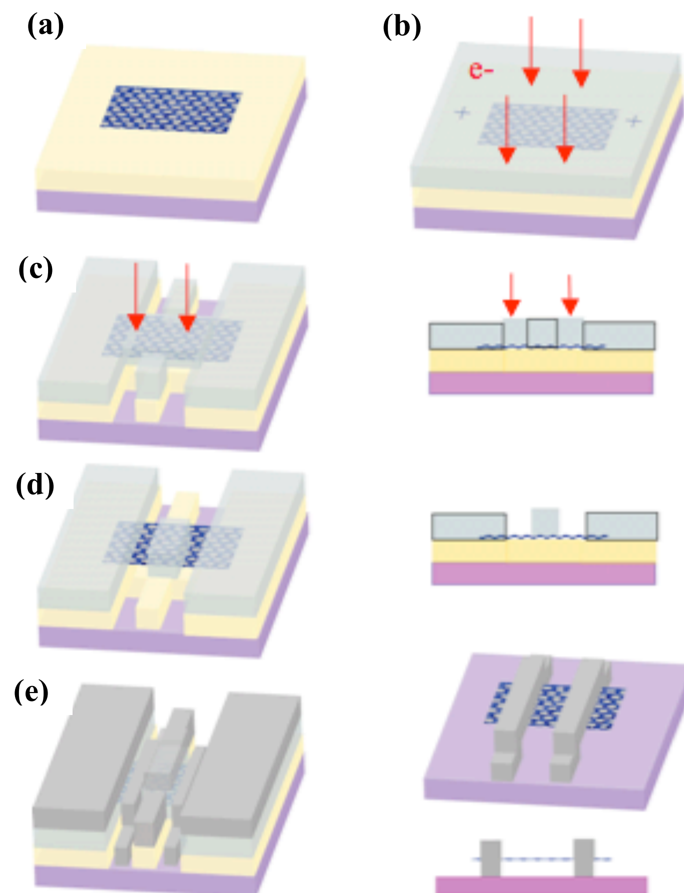

Fig 3.11: Schematics of fabrication process. a. TC is exfoliated onto LOR (yellow) which rests on SiO_2/Si substrate (purple). b. Bilayer MMA/PMMA (light gray) resists are deposited onto sample, and alignment cross marks are patterned by EBL. A second EBL is performed to expose regions indicated by the red arrows. c. Developing in MIBK and MF319 removes both LOR and MMA/PMMA bilayer in the exposed regions. The final EBL step is performed to expose regions indicated by the red arrows. d. Developing in MIBK removes only the MMA/PMMA resist bilayer in the exposed regions. e. Metal deposition is performed at +45°, - 45° and 0° using Ti/Al

(dark gray). Samples are then immersed in warm PG remover and dried using a critical point dryer, leaving suspended electrodes that "hold" TC above the substrate.

This fabrication process is based on a method developed by us[6] to suspend local gates above graphene, which was discussed in the previous sections. The procedure, which consists of three electron beam lithography (EBL) steps, utilizes different exposure, developing and lifting off properties of different resists. Fig 3.11 illustrates the entire procedure to create two suspended electrodes that contact a freestanding membrane. In the first step, we deposit and bake a layer of Lift-Off (LOR) resist onto a p-doped Si chip that is covered with a 310 nm-thick SiO2 layer. TC sheets are directly exfoliated onto the LOR layer, and can be identified using atomic force microscope or color interference under an optical microscope (fig 3.11a). Subsequently, a bilayer of electron beam resists, MMA/PMMA, are spun and baked onto the sample, followed by exposure of alignment mark patterns and development in MIBK. These alignment marks are used for locating and aligning electrode patterns to the TC in the subsequent steps. We note that no metal deposition is necessary, as openings in the PMMA/MMA layer are sufficiently visible in the scanning electron microscope (SEM) for alignment, thus greatly simplifying the fabrication procedure.

In the next step, we use EBL to expose areas adjacent to the TC, and develop in MIBK/isopropyl alcohol (IPA) solution that dissolves only the exposed regions of the MMA/PMMA bilayer, but not LOR, so that two windows in the resist bilayer are created on either side of the TC. The exposed LOR within the windows is removed by developing in MF319, while the rest of the LOR layer remains intact (fig 3.11c). The end

result of this step are four windows on the LOR/MMA/PMMA resist, which, after metallization, will form anchors on the substrate to connect to and support the two suspended electrodes.

In the third and final step of fabrication, we fabricate two suspended electrodes to contact the TC. To this end, we expose two long rectangular windows that lie directly on top of the TC and connect to the openings created in step 2 (fig 3.11d). The chip is developed in MIBK/IPA to remove the exposed MMA/PMMA. We then perform metal deposition at 3 different angles (+45°, -45° and 0°) to ensure good contact at the sidewalls that attach the anchors to the suspended electrodes[38]. Finally, the samples are immersed in warm PG remover to remove all resist layers, and dried using a critical point dryer to prevent structural instability during the drying process. The end result is a sheet of atomic membrane "held up" by two partially suspended electrodes.

This powerful fabrication technique is versatile and robust. By tuning lithography parameters, we can produce freestanding electrodes that suspend layered materials with varying widths, lengths and heights. Using graphene as an example of TC, we fabricate a number of suspended devices with electrode separations ranging from 700 nm to 4 μm (fig 3.12), with a total suspended length as long as 40 *μm* (fig 3.12a inset). The graphene sheets usually exhibit no discernible structural deformation, though strain-induced ripples[39] have been occasionally observed (fig 3.12d). In these examples, graphene sheets are suspended at ~300 nm above the SiO2 substrate, though this height can be easily adjusted from 50 nm to 3 μm by selecting different LOR solutions.

This acid-free fabrication technique is capable of producing devices with both long

and short electrode separations. The latter geometry is particularly interesting for, e.g. realization of a ballistic graphene-based Josephson junction. Such a system has been predicted to exhibit several novel phenomena, such as specular andreev relection[32], chargeless transfer of spins[40] and thermopower[41], but has yet to be experimentally realized.

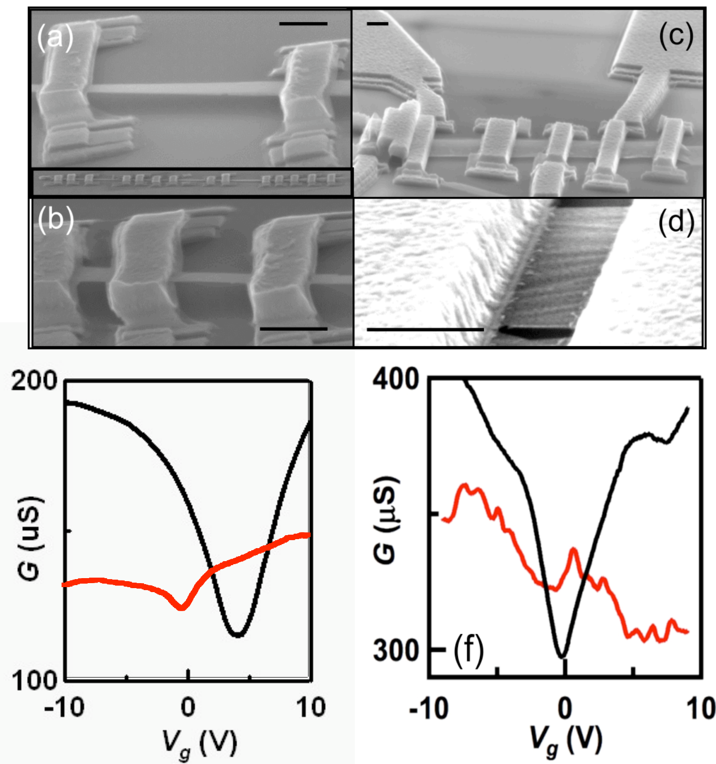

Fig 3.12: SEM images and transport data of suspended graphene devices. a-d. SEM images of suspended graphene sheets with different widths and lengths. Scale bars: 1 µm. Inset: a 40-µm long graphene sheet suspended by several electrodes. e-f. Device conductance as a function of gate voltage for two different suspended graphene devices. Red and black traces are for as- fabricated and current-annealed devices, respectively.

3.2.4: Suspended graphene and superconducting electrodes

To demonstrate the viability of this fabrication procedure, we fabricate freestanding

graphene devices with Ti/Al electrodes, and measure their transport characteristics using standard lock-in techniques at low temperature. In fig 3.12e-f we plot the conductance G as a function of gate voltage V_g for two different devices similar to the ones shown in fig 3.12c-d. Data displayed in fig 3.12e is obtained from a device with a source-drain separation of 1.7 μm, and graphene width 3.5 μm. The red trace shows the device's initial $G(V_g)$ behavior immediately after fabrication. The relatively large conductance indicates small contact resistance; however, the poor response to gate and the absence of a Dirac point suggests that the device is highly doped.

Such behavior is not uncommon for as-fabricated suspended graphene devices. After current annealing [1,2,20] at ~1.2 mA for 10 minutes, the device's behavior is significantly improved. As shown by the black trace, the Dirac point appears at V_g~0, and the $G(Vg)$ is symmetric with respect to the electron and hole branches. The device mobility is estimated to be ~3000 cm^2/Vs, which is reasonable and can be further optimized. The reproducibility of the results is demonstrated by similar behavior from a second device, with a mobility of 5500 cm^2/Vs (fig 3.12f). We also note that up to 80V in V_g can be applied (or equivalently, up to $1.1x10^{12}$ cm-2 in induced charge density) without collapsing graphene, which is significantly higher than that applied to free-standing graphene devices fabricated via acid-release of SiO_2 [1,2] thus allowing access to regimes of high carrier density with rich many-body effects.

3.2.5: Suspended Bi_2Se_3 and superconducting electrodes

As a further demonstration of the versatility of this procedure, we fabricate

suspended Bi_2Se_3 thin crystals, which is also a layered material. This topological insulator material is predicted to host a vast plethora of fascinating physical phenomena[28,42]. Experimentally, the most illuminating results to date arise from data obtained from ARPES and STM measurements [43,44,45], while transport measurements have been limited [46,47]. Here we demonstrate fabrication and measurement of suspended Bi_2Se_3 membranes, which have not been reported previously. The bulk samples are synthesized via Ca doping of single crystal Bi_2S_3 crystals [48]. Fig. 3.13a-b display SEM images of a completed Bi_2Se_3 device, which was measured by atomic force microscopy to be ~65 nm thick. The current-voltage (I-V) characteristics of this device at 300K and 4K are both linear, with a resistance of 142 and 117 Ω, respectively (fig. 3.13c). The linear I-V curves, in addition to the relatively small resistance that decreases with temperature, indicate low contact resistance and metallic conduction. Additionally, we also observed a small gate dependence: application of ΔV_g=5V induces ~10 μS change in conductance (5% change), suggesting that while much of the current is transported through the bulk, there could be some surface conduction.

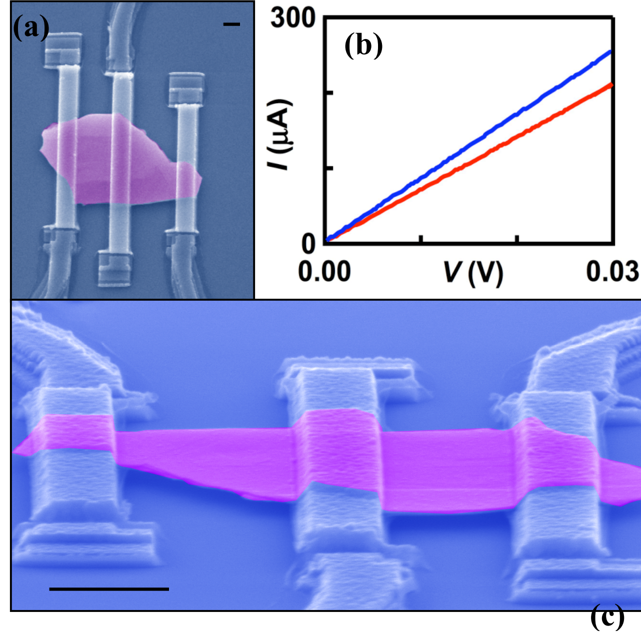

Fig 3.13: SEM images and transport data of a suspended Bi2Se3 device. a-b. Top and angled view of a suspended Bi_2Se_3 device. Scale bar: 1 μm. The images are false-colored. c. Current measured as a function of voltage bias at 300K (red) and 4K (blue).

Assuming parallel conduction through the surface states and the bulk [36], and that the charge density of the bulk is not affected by V_g, we estimate the field effect mobility μ_s of the device's surface state by $G = (W/L)n_s e\mu_s = \alpha(W/L)V_g e\mu_s$, where $\alpha = 1.5 \times 10$ cm^{-2} is the gate coupling efficiency, W/L the device's aspect ratio, and e the electron charge. Using ΔV_g=5V, W/L=0.7 and ΔG=10μS, we obtain μ_s~ 580cm^2 V^{-1}s^{-1}. This simple calculation ignores the possible difference in gate response for the top and bottom surface states, but could serve as an order-of-magnitude benchmark for sample quality. In the future, we expect that the device can be further optimized via improvement in material quality and reduction in membrane thickness.

In conclusion, we have developed a gentle and versatile multilevel lithography

process to fabricate freestanding atomic membranes that are extracted from layered materials. Using this technique, we successfully suspended and performed measurements on atomically thin graphite and Bi_2Se_3 films that were coupled to Ti/Al electrodes. This technique provides a viable path towards the investigation of superconductivity and spintronics in high mobility graphene and Bi_2Se_3 samples, as well as in other layered materials.

3.3: Fabrication of dual gates with suspended graphene

The recipe for the contactless gate discussed in the earlier sections produced reasonably high quality samples, but disorder was still strong enough to obscure most correlated electron phenomena. Because of the contactless nature of the second gate a promising next step was to remove the supporting substrate SiO_2 beneath the graphene. At the time after our first contacless gate publication[6], suspended graphene samples fabricated by Du and Bolotin had exhibited mobility an order of magnitude greater than the best substrate supported sample.

During our group dinner at APS 2008 in New Orleans Jeanie, Gang, Feng, Wenzhong and myself discussed how a dual gated device could be coupled with suspended graphene. We did not produce a working solution at the time. Yet, it was clear to us all that such a device would provide rich physics to explore leading to many exciting projects. Two years later the device was successfully realized. Though not the first group to fabricate these types of samples, we are able to achieve an unprecedented sample quality that allowed to the first resolution of an interaction-induced gap in BLG.

In this section I will discuss the recipe for this device architecture. The development of this recipe was a fun period in my studies.

Graphene sheets are exfoliated onto SiO_2 wafers and identified using optical contrast. Special attention is taken to select flakes that are 3-10 μm in length and 1-2 μm in width. Suspended top gates are first fabricated across selected graphene sheets, using the multi-level lithography technique that was described in previous sections with subtle changes. The key differences are: (1). Instead of titanium, chromium is used to ensure the suspended top gate survives the etching treatment; (2) The height of the top gate is designed to be ~300nm and the thicknesses of the 3 angled depositions are 150, 200 and 100 nm, respectively, to ensure structural integrity; (3) Chromium clamps are fabricated in the same step as the top gate and with the same orientation to ensure the flake will not roll up. After liftoff in a warm PG remover bath the device is placed in high purity IPA bath seven times so as to dilute the PG remover in preparation for drying in the critical point dryer. Most importantly, the liquid carbon dioxide used for the drying must be at least of grade four, so called laser spectroscopic grade.

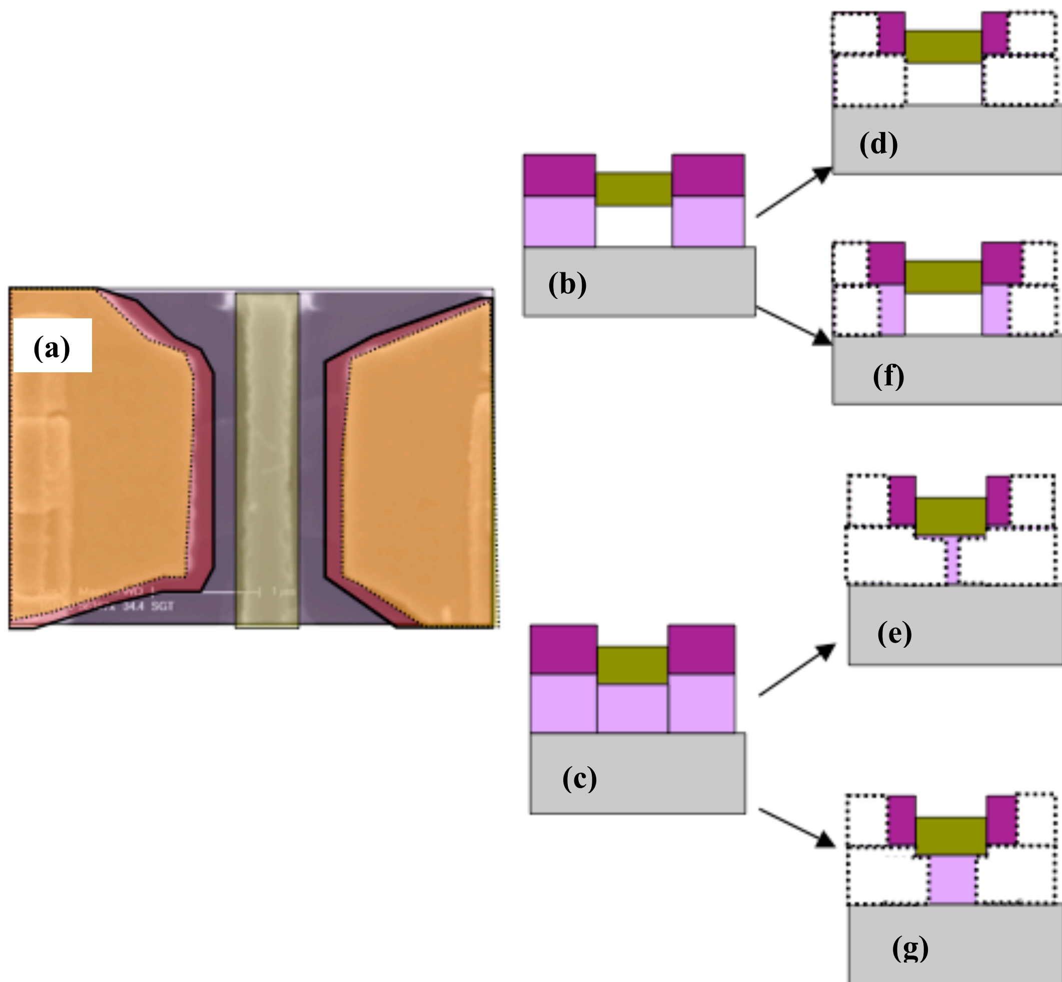

Fig 3.14 Schematics depicting the importance of undercut. a. Schematic overlaid on SEM image of a device. Yellow(dotted line border) and red polygon (solid line border) represents the windows opened in PMMA and MMA after exposure and development, respectively. Light purple regions depict resist that is intact and the brown rectangle is the already present top gate. Note it is of paramount importance that the red polygons are separated from the top gate by MMA. b-g. Schematic cross section view of already present top gate (brown), MMA(lavender) and PMMA)(purple) resists. The group of schematics b,d,f and c,e,g, respectively, represent a possible arrangement for resists and top gate. Schematics b and c are each arrangement before exposure and development. Schematics d,f and e,g are each distinct arrangement after exposure, and the white region with dotted line borders represent the removed resist after exposure and development. For the first and second case d and e, respectively, depicts the unwanted out come

where no resist surrounds the top gate, and solvent can enter and compromise the structure. For the first and second case f and g, respectively, depicts the desired outcome where resist surrounds the top gate, and solvent can not enter, hence the structure remains in tact.

After the top gate fabrication, the final step is to couple the graphene sheets to electrodes. Standard electron beam lithography is employed on a MMA/PMMA bilayer of resist, where MMA plays the crucial role of providing an undercut to aid the removal of the stubborn Cr/Au. This undercut must be carefully controlled because the junction between source and drain electrode is narrow (~1.3 μm), which is done to minimize unwanted structural anomalies of the suspended graphene. Fig 3.14 schematically shows the bilayer of resist after exposure and development overlaid on an SEM image of a device. A window is opened through the PMMA and MMA, but because of the differences in molecular weight MMA will disassociate more quickly. This is depicted by the gold and blue polygons in fig 3.14, which represent PMMA and MMA, respectively.

For the structural integrity of the top gate the opening in the MMA windows cannot be too close and certainly must not overlap with one another. Fig. 3.14b-g represents the two possible arrangements for this bilayer of resist from a cross sectional view through the fabrication. Essentially the resist either flows beneath the top gate or surrounds it. In both cases, it is crucial that there remains an MMA wall between each electrode window and the top gate. If this MMA barrier is absent then solvent will enter the region beneath the bridge, and compromise the structural integrity. If instead the MMA barrier is maintained the top gate suspension will remain intact during the

fabrication. Subsequently, 10 nm of Cr and 120 nm of Au are deposited to ensure the electrodes survive the etching treatment. To acquire good contact it is recommended that the rate of deposition be 4 A/s for the chromium layer. After metal deposition an overnight liftoff in warm acetone is employed. The Cr/Au adheres quite well; hence some agitation with a pipet in the acetone bath is usually needed to ensure the unwanted metal is removed. Once this metal has departed the devices are immersed in IPA, and then a buffered oxide etch(BOE 6:1), while using a Teflon boat to ensure the sample is always in liquid, for 70 seconds, so as to release the BLG sheets from the SiO_2 substrates, and immediately placed in DI water baths seven times, so as to dilute the BOE, and similarly in high purity IPA baths in preparation for drying in the critical point dryer, fig 3.15.

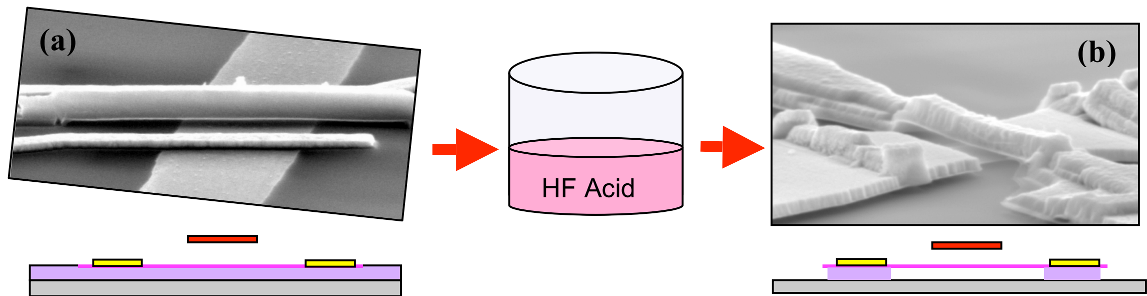

Fig 3.15: SEM images and schematics of device fabrication. a. Graphene (pink) resting on SiO_2 substrate(lavender) is coupled with Cr/Au electrodes(yellow), while chrome contactless top gate (red) straddles graphene flake. b. Red arrow illustrates completed device in a is immersed in hydrofluoric acid and then dried with critical point dryer (not shown). c. Using the same color scheme as in a., graphene is freestanding and clamped at the ends by Cr/Au electrodes and remaining SiO_2 substrate, while the chrome contactless top gate straddles graphene flake.

3.3: Post fabrication treatment of dual gates with suspended graphene

Structurally successful devices, which are determined by a visible difference in focus between the top gate and electrodes, are measured in our He3 cyrostat using a standard lock-in technique. As-fabricated suspended graphene samples require current annealing to improve their quality [20,1,2]. This is performed in our cyrostat under vacuum at base temperature $T \sim 240mK$ because the line resistance will cause the temperature to rise during the annealing. Usually the device is annealed in several stages as shown in fig 3.16 for a TLG sample, with the final stage determined by device mobility, minimum conductivity value, and proximity of the Dirac point to zero gate voltage. Fig 3.16a shows the response in the current as the voltage bias is increased and the corresponding status, which is characterized by measuring its conductance as function of V_{bg}. The slight non-linearity seen in the last run is an indicator that the device has reached its optimal state. This confirmed on the right with the TLG device reaching a highly desired insulating state[9,49].

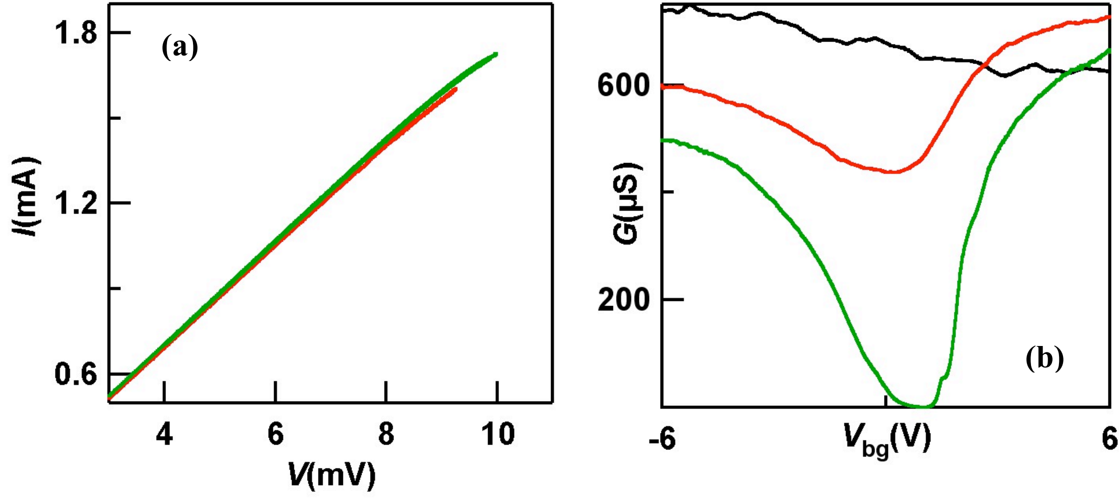

Fig 3.16: Current annealing. a. Voltage bias is applied on source-drain electrode top gate is floated and V_{bg}=0 and current is monitored. b. $G(V_{bg})$ measurements after each current annealing session, black is before any annealing, red is after the first session and green is after the last attempt.

The result of another successful annealing sequence is shown in fig 3.17a-b for a BLG sample. This device is characterized by measuring its resistance and top gate voltage V_{tg} in addition to the $R(V_{bg})$ response. The gate voltages are related to induced charge density n by

$$n_{bg} = \alpha(V_{bg}-V'_{bg})$$

$$n_{tg} = \beta (V_{tg}-V'_{tg})$$

where α and β are the gate coupling efficiencies for back and top gates, respectively, and V'_{tg} and V'_{bg} represent the dirac point for each gate. From Landau fan diagrams as well as from geometrical considerations, we estimate α ~ 1.83x10^{10} and β~3.14x10^{10} cm^{-2}V^{-1}. Close to zero gate voltage, both curves show a dramatic decrease in conductance, which

is symmetric across the $n = 0$ point and reaches maximum resistance values of approximately 50 kΩ.

Much can be learned of the sample quality from a careful study of the line traces in fig 3.17a-b. Their sharp rise over a small carrier density range denotes high mobility, ~ 60,000 V/cm^2*s, though values twice this number have been attained. These substantial mobility values suggest quasi-ballistic transport of the charge carriers in the BLG from source to drain electrode. The symmetric nature of the curve and close proximity to zero density indicates that the sample suffers from minute charge impurity doping[50]. This is further corroborated by a Dirac point, which is not shown here, that is within a hundredth of a volt. These attributes are superior in comparison to previous work in the literature for suspended bilayer graphene with a single gate [3,4] and exceptional with that of dual gated studies[8].

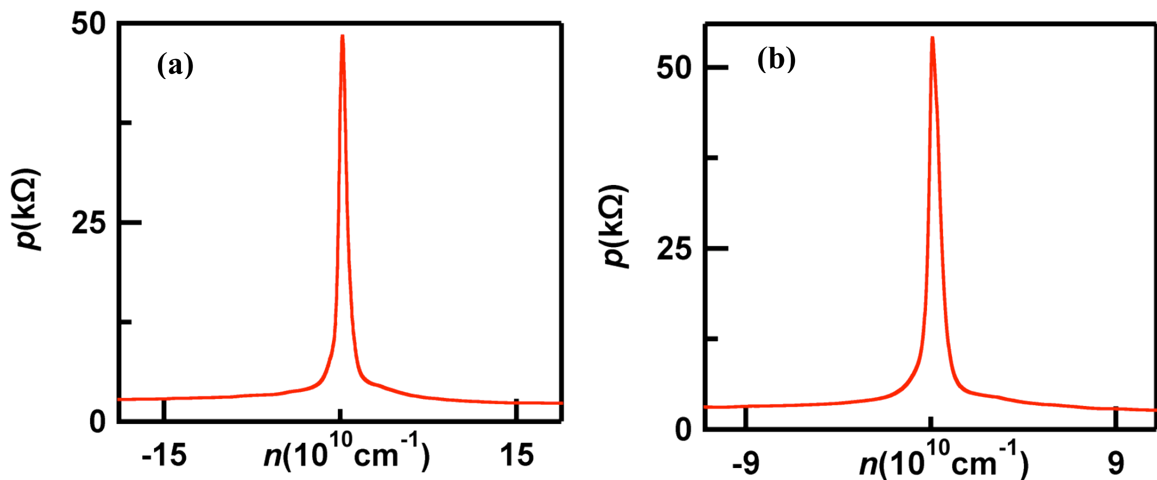

Fig 3.17: Single gate transport data at B=0 and T=300mK a. Resistivity plotted as a function of charge carrier density that is modulated by V_{bg}. b. Resistivity plotted as a function of charge carrier density that is modulated by V_{tg}. Both exhibit minute CNP offset suggesting minimal charge impurity doping.

Conclusion

This concludes the fabrication section of the thesis and for the remainder of the thesis I will focus on the physics behind the data acquired from dual gated samples with substrate supported and suspended graphene. For specific details on fabrication procedures the reader is directed to the appendix.

References

1. X. Du, I. Skachko, A. Barker and E. Y. Andrei, Nat. Nanotechnol. **3** (8), 491-495 (2008).

2. K. I. Bolotin, K. J. Sikes, Z. Jiang, M. Klima, G. Fudenberg, J. Hone, P. Kim and H. L. Stormer, Solid State Communications **146** (9-10), 351-355 (2008).

3. B. E. Feldman, J. Martin and A. Yacoby, Nat. Phys. **5** (12), 889-893 (2009).

4. W. Z. Bao, Z. Zhao, H. Zhang, G. Liu, P. Kratz, L. Jing, J. Velasco, D. Smirnov and C. N. Lau, Physical Review Letters **105** (24), 246601 (2010).

5. R. V. Gorbachev, A. S. Mayorov, A. K. Savchenko, D. W. Horsell and F. Guinea, Nano Letters **8** (7), 1995-1999 (2008).

6. G. Liu, J. Velasco, W. Z. Bao and C. N. Lau, Applied Physics Letters **92** (20), 203103 (2008).

7. L. Jing, J. Velasco Jr., P. Kratz, G. Liu, W. Bao, M. Bockrath and C. N. Lau, Nano Letters **10**, 4000-4004 (2010).

8. R. T. Weitz, M. T. Allen, B. E. Feldman, J. Martin and A. Yacoby, Science **330** (6005), 812-816 (2010).

9. J. Velasco, L. Jing, W. Bao, Y. Lee, P. Kratz, V. Aji, M. Bockrath, C. N. Lau, C. Varma, R. Stillwell, D. Smirnov, F. Zhang, J. Jung and A. H. MacDonald, Nature Nanotechnol. **7**, 156 (2012).

10. J. R. Williams, L. DiCarlo and C. M. Marcus, Science **317**, 638-641 (2007).

11. D. A. Abanin and L. S. Levitov, Science **317**, 641-643 (2007).

12. B. Huard, J. A. Sulpizio, N. Stander, K. Todd, B. Yang and D. Goldhaber-Gordon, Physical Review Letters **98**, 236803 (2007).

13. B. Ozyilmaz, P. Jarillo-Herrero, D. Efetov, D. A. Abanin, L. S. Levitov and P. Kim, Physical Review Letters **99**, 166804 (2007).

14. V. V. Cheianov, V. Fal'ko and B. L. Altshuler, Science **315** (5816), 1252-1255 (2007).

15. V. V. Cheianov and V. I. Fal'ko, Physical Review B **74** (4), 041403 (2006).

16. M. I. Katsnelson, K. S. Novoselov and A. K. Geim, Nat. Phys. **2** (9), 620-625 (2006).

17. A. F. Young and P. Kim, Nat. Phys. **5** (3), 222-226 (2009).

18. A. V. Shytov, M. S. Rudner and L. S. Levitov, Phys. Rev. Lett. **101**, 156804 (2008).

19. J. B. Oostinga, H. B. Heersche, X. L. Liu, A. F. Morpurgo and L. M. K. Vandersypen, Nat. Mater. **7** (2), 151-157 (2008).

20. J. Moser, A. Barreiro and A. Bachtold, Appl. Phys. Lett. **91**, 163513 (2007).

21. J. H. Chen, C. Jang, S. Adam, M. S. Fuhrer, E. D. Williams and M. Ishigami, Nat. Phys. **4** (5), 377-381 (2008).

22. N. Tombros, A. Veligura, J. Junesch, M. H. D. Guimaraes, I. J. Vera-Marun, H. T. Jonkman and B. J. van Wees, Nat. Phys. **7** (9), 697-700 (2011).

23. K. S. Novoselov, D. Jiang, F. Schedin, T. J. Booth, V. V. Khotkevich, S. V. Morozov and A. K. Geim, Proc. Natl. Acad. Sci. **102** (30), 10451-10453 (2005).

24. A. K. Geim and K. S. Novoselov, Nat. Mater. **6** (3), 183-191 (2007).

25. K. S. Novoselov, A. K. Geim, S. V. Morozov, D. Jiang, M. I. Katsnelson, I. V. Grigorieva, S. V. Dubonos and A. A. Firsov, Nature **438** (7065), 197-200 (2005).

26. Y. B. Zhang, Y. W. Tan, H. L. Stormer and P. Kim, Nature **438** (7065), 201-204 (2005).

27. C. L. Kane and E. J. Mele, Physical Review Letters **95** (22), 226801 (2005).

28. J. E. Moore and L. Balents, Physical Review B **75** (12), 121306 (2007).

29. B. A. Bernevig and S.-C. Zhang, Physical Review Letters **96** (10), 106802 (2006).

30. A. H. Castro Neto, F. Guinea, N. M. R. Peres, K. S. Novoselov and A. K. Geim, Rev. Mod. Phys. **81** (1), 109-162 (2009).

31. M. Z. Hasan and C. L. Kane, Reviews of Modern Physics **82** (4), 3045-3067 (2010).

32. C. W. J. Beenakker, Phys. Rev. Lett. **97** (6), 067007 (2006).

33. L. Fu and C. L. Kane, Physical Review Letters **100** (9), 096407 (2008).

34. V. V. Deshpande and M. Bockrath, Nat. Phys. **4**, 314 (2008).

35. V. V. Deshpande, B. Chandra, R. Caldwell, D. S. Novikov, J. Hone and M. Bockrath, Science **323** (5910), 106-110 (2009).

36. X. Du, I. Skachko, F. Duerr, A. Luican and E. Y. Andrei, Nature **462** (7270), 192-195 (2009).

37. K. I. Bolotin, F. Ghahari, M. D. Shulman, H. L. Stormer and P. Kim, Nature **462** (7270), 196-199 (2009).

38. J. Velasco, G. Liu, W. Z. Bao and C. N. Lau, New Journal of Physics **11**, 095008 (2009).

39. W. Z. Bao, F. Miao, Z. Chen, H. Zhang, W. Y. Jang, C. Dames and C. N. Lau, Nat. Nanotechnol. **4** (9), 562-566 (2009).

40. D. Greenbaum, S. Das, G. Schwiete and P. G. Silvestrov, Physical Review B **75** (19), 195437 (2007).

41. M. Titov, A. Ossipov and C. W. J. Beenakker, Phys. Rev. B **75** (4), 045417 (2007).

42. H. C. Manoharan, Nat. Nanotechnol. **5** (7), 477-479 (2010).

43. D. Hsieh, D. Qian, L. Wray, Y. Xia, Y. S. Hor, R. J. Cava and M. Z. Hasan, Nature **452** (7190), 970-U975 (2008).

44. P. Roushan, J. Seo, C. V. Parker, Y. S. Hor, D. Hsieh, D. Qian, A. Richardella, M. Z. Hasan, R. J. Cava and A. Yazdani, Nature **460** (7259), 1106-U1164 (2009).

45. H. Lin, R. S. Markiewicz, L. A. Wray, L. Fu, M. Z. Hasan and A. Bansil, Physical Review Letters **105** (3), 036404 (2010).

46. D. Teweldebrhan, V. Goyal, M. Rahman and A. A. Balandin, Appl. Phys. Lett. **96** (5) (2010).

47. J. G. Checkelsky, Y. S. Hor, M. H. Liu, D. X. Qu, R. J. Cava and N. P. Ong, Physical Review Letters **103** (24), 246601 (2009).

48. Z. Wang, T. Lin, P. Wei, X. Liu, R. Dumas, K. Liu and J. Shi, Appl. Phys. Lett. **97** (4), 125120 (2010).

49. W. Bao, J. V. Jr., F. Zhang, L. Jing, B. Standley, D. Smirnov, M. Bockrath, A. MacDonald and C. N. Lau, Proc. Natl. Acad. Sci., to appear (2012).

50. Y. W. Tan, Y. Zhang, K. Bolotin, Y. Zhao, S. Adam, E. H. Hwang, S. D. Sarma, H. L. Stormer and P. Kim, Phys. Rev. Lett. **99**, 246803 (2007).

Chapter 4: Quantum Hall effect in graphene *pnp* junctions

Introduction:

In this chapter I will discuss conductance measurements of high quality substrate supported graphene *pnp* junctions[1-7] with suspended top gates, and mostly in the QH regime. The top gate fabrication for these samples is the same from the discussion in the previous chapter; hence our samples are exceedingly clean. In magnetic fields B>3T, the device display well-developed conductance plateaus at uniform charge density n, with up to 15 discernible plateaus. Furthermore, within the QH regime, and by using a recently available theory for rectangular device geometry [8], we can satisfactorily account for the two-terminal device conductance at uniform charge densities. At high magnetic fields and by engaging both gates in our sample simultaneously, we find device conductance displays quantum Hall plateaus at fractional values of e^2/h. These features can be explained by an edge state equilibration model, which will be discussed in detail.

Interestingly, upon closer inspection of our quantum Hall data in our *pnp* junctions we observe reproducible conductance fluctuations (CF) between quantum Hall plateaus when the charge density of the top-gated region n_{tg} is modulated. In the n_{tg}-B plane, slopes of these fluctuations are parallel to those of the center of the adjacent plateaus with integer filling factors. We attribute such QH fluctuations to Coulomb-induced charging of localized states in the bulk of the device [9-11], which are estimated to be 80-130 nm in diameter. Notably, for the zeroth Landau level (LL), both positive and negative slopes in the n_{tg}-B plane are observed, indicating the evolution of both hole-and electron-doped states. Moreover, with increasing temperature, the conductance peaks of the fluctuations

remain constant, while the conductance valleys increase, in agreement with the behavior of a Coulomb-blockaded quantum dot. Our results reflect the importance of electronic interaction in QH regime for substrate-supported graphene, and demonstrate that electrical transport in *pnp* junctions uniquely reveals both local and global properties of the devices.

4.1 Device Characterization

4.1.1 Sample improvement through annealing

A multi- level lithography process [12, 13], which was discussed in the previous chapter, was used to fabricate a suspended top gate that straddles the center portion of graphene (fig 4.1a). Since no dielectric material directly contacts the single atomic layer, these graphene devices are exceedingly clean[13]. The air-gap between the top gate and graphene also allows surface absorbents, including those directly under the top gate, to be removed via annealing [14]. As a demonstration, we measure the two-terminal conductance G of a graphene device as a function of applied back gate voltage V_{bg} both before and after annealing in vacuum at 120°C (fig 4.1b). The $G(V_{bg})$ characteristics is considerably improved upon annealing, with a sharper Dirac point that is closer to zero, indicating the removal of undesirable adsorbates and resist residue.

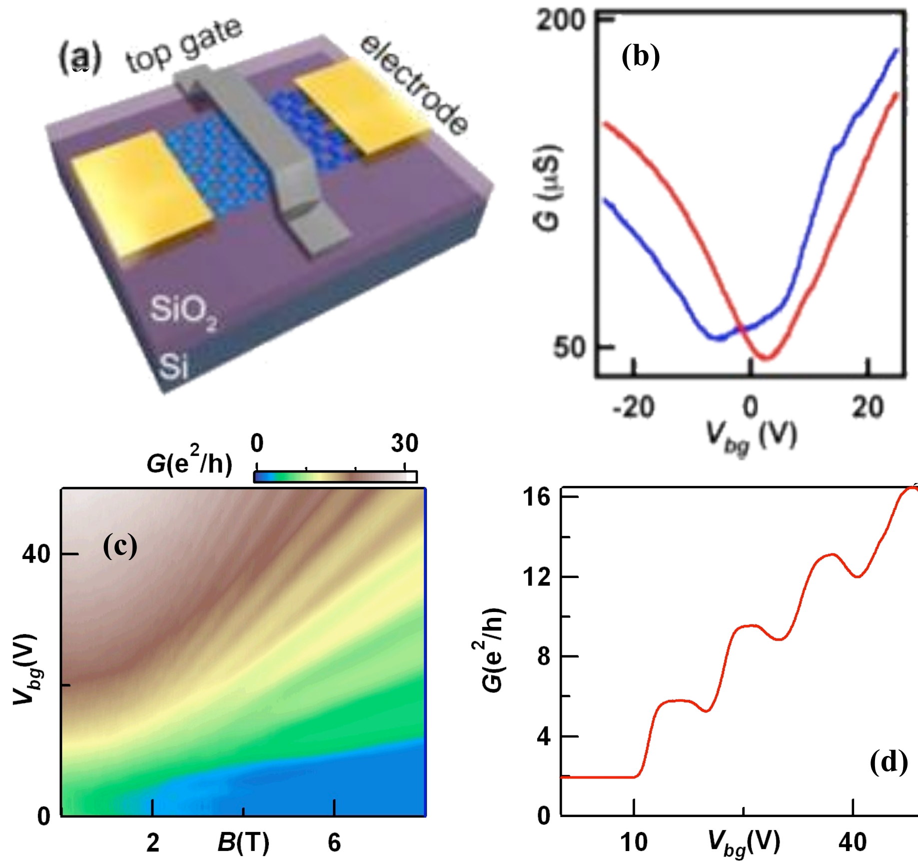

Fig 4.1: Device schematic and characterization. a. Device schematic with each component labeled: graphene (blue honeycomb lattice), electrodes(gold), top gate(silver), SiO_2(purple), Si(blue). b. Local heater anneal, blue line represents before annealing and red line after annealing. c. Transport measurements at 300mK, $G(V_{bg},B)$ with color scale denoting conductance. d. Line trace $G(V_{bg})$ from c. at 8T.

4.1.2 Single gate quantum Hall response

We now characterize the same device at 260mK using standard lock-in techniques, in a B to study its quantum Hall effect. The device's source-drain separation is 3.5 μm, with a top gate that covers a ~0.5 μm-long segment in the center and is suspended ~100 nm above the substrate. Besides mobility and CNP offset, discussed in the previous section, another metric for sample quality is the robustness of quantum Hall conductance plateau. As discussed in chapter two, it is expected that in high magnetic fields the cyclotron orbits of charge carriers in graphene coalesce to form Landau levels (*LLs*) with energies

$$E_{SLG} = \pm\sqrt{2\hbar v_F^2 eB|N|} \qquad (4.1)$$

Between the *LLs*, the two-teminal device conductance is quantized at

$$G = 4(N+\frac{1}{2})\frac{e^2}{h} \equiv \upsilon\frac{e^2}{h} \qquad (4.2)$$

where h is Planck's constant, v_F is the Fermi velocity, $N=...-1, 0, 1,...$ is an integer indicating the LL index, and $\nu=nh/Be$ is the filling factor. As mentioned in chapter 2, the factor of 4 denotes a degeneracy from spin and sublattice degrees of freedom. Disorder will broaden the LL, hence smearing the distinct energy levels and precluding observation of quantum Hall plateau.

In the absence of disorder, however, the unique energy spectrum of graphene is indeed reflected in transport measurements in finite B. The standard "fan diagram" of QH plateaus is shown in fig 4.1c, for B ranges from 0 to 8T and V_{bg} from 0 to 50V. A total of 15 QH plateaus are discernible (though conductance for plateaus for ν >20 are not exactly

quantized), and the $2e^2/h$ plateau is quantized at magnetic field as low as 2.5T. An impressive feat in light of the multiple processing steps required in fabricating the contactless gate. Fig 4.1d plots G in units of e^2/h vs. V_{bg} at B=8T with the top gate disconnected. Clear plateaus at ν = 2,6,10, 14 and 18 with almost perfectly quantized conductances are observed. All of these features underscore the high quality of the device.

Before moving on we can use the evolution of the quantum Hall states to acquire geometric information about the sample. For instance, from the fan diagram, the plateaus' centers have slopes in the V_{bg}-B plane given by

$$b_{bg}=\nu e/h\alpha_{bg} \quad (4.3)$$

where $\alpha_{bg}=n/V_{bg}$ is the coupling efficiencies for the back and top gates, respectively. In Fig. 4.1c, for the N=0, 1 and 2 plateaus, the slopes are measured to be b_{bg}=0.74, 2.0, and 3.4, respectively, yielding α_{bg} ~7.5x10^{10} cm^{-2} V^{-1}, in good agreement with that estimated from geometric considerations. This method allows us to determine the coupling ratio of any gate to graphene, its employment is prevalent in the latter QH studies performed by the group [15-17].

4.2 SLG *pnp* junctions: *B*=0T

4.2.1 The *pnp* Conductance map

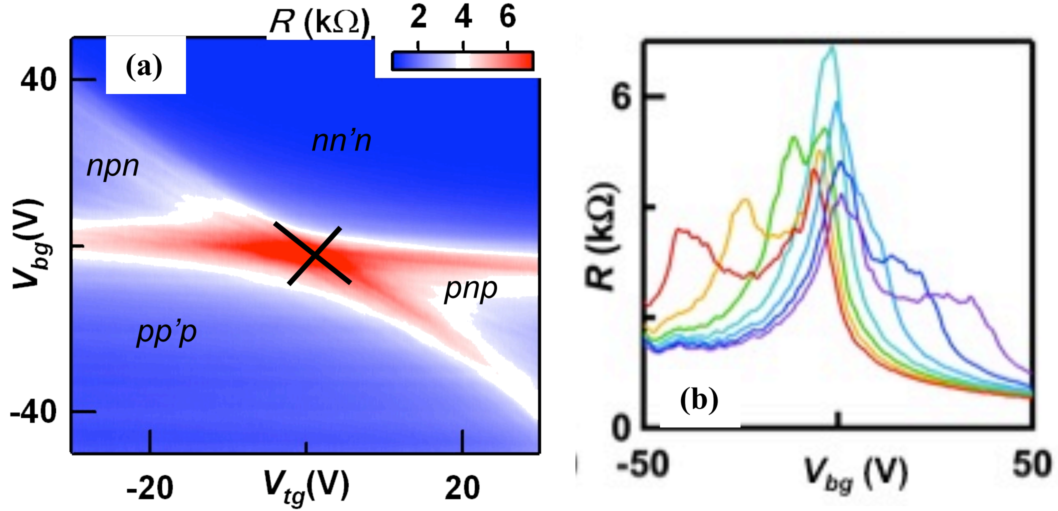

Fig 4.2: SLG transport data at *B=0*. a. $R(V_{bg}, V_{tg})$ of a double-gated SLG device. b. Line traces of a. from purple to red, V_{tg}=-30, -20, -10, 0, 10, 20, 29.5V, respectively.

By modulating voltages applied to both gates, one creates regions with different dopant levels and types that are adjacent to one another in a single graphene device, thus realizing *pnp* junctions with tunable junction polarity. This characteristic of graphene, which is due to its gapless energy spectrum, is highly attractive when compared to standard 2DEGS that require chemical doping to access different carrier types.

We now focus on dual gated transport measurements for the substrate-supported sample discussed in the previous section. In fig 4.2a, *R*(color) is plotted as functions of V_{bg} (vertical axis) and V_{tg}(horizontal axis). By symmetry, the "x" is the device's global

charge neutrality point, and it reaches a global resistance maximum R_{max}~$7k\Omega$. To investigate this further we plot $R(V_{bg})$ at different V_{tg} values in fig 4.2b. With increasing $|V_{tg}|$, R_{max} decreases to ~ 4 $k\Omega$, and a prominent side peak develops; the portion of the $R(V_{bg})$ curves between the 2 peaks corresponds to the behavior of a bipolar (*pnp or npn)* junction. This bipolar behavior manifests in the two-dimensional dataset as the horizontal and diagonal red lines, and indicates local resistance maxima, and corresponds to the CNP of the global gated and locally gated regions, respectively. Taken together, these two lines partition the plot into four regions with different dopant combinations– *pnp, pp'p, npn* and *nn'n*, thus demonstrating a graphene *pnp* junction with tunable junction polarity.

More information about the device can be acquired from further study of the striking features in fig 4.2a. For instance, the slope of the red line in fig 4.2a yields the ratio of the coupling efficiencies η of the two gates to graphene, and is determined by $\eta_{bg}/\eta_{tg}=\Delta V_{tg}/\Delta V_{bg}=1.27$. From a simple geometric consideration, η is given by the gate-device capacitance per unit area, $C=\varepsilon\varepsilon_o/d$, where ε is the dielectric constant of the gate dielectric (3.9 for SiO_2), ε_o is the permittivity of free space, and d is the gate-device separation. Hence, the coupling ratio is $C_{bg}/C_{tg}= (\varepsilon_{bg}/\varepsilon_{tg})*(d_{tg}/d_{bg})\approx(3.9)(100/300)\approx1.3$, in excellent agreement with the data.

4.2.2 Fabry Perot oscillations at a *pn* interface

We now focus on the $R(V_{bg},V_{tg})$ response of another device, with similar characteristics and quality shown in fig 4.3, specifically in the upper left region of fig

4.3a, i.e. when the junction is in the *npn* regime. Compared with the neighboring unipolar (*pp'p* or *nn'n*) regions, the junction resistance is significantly higher, as expected at the boundary of a *pn* junction. More interestingly, we observe resistance oscillations as a function of both V_{bg} and V_{tg}, as indicated by the arrows in fig 4.3a. Notably, these oscillations are not found in the unipolar regions. Such oscillations were first reported by [18], and arise from Fabry-Perot interference of the charges between the two *p-n* interfaces. Thus, the holes in the top-gated region are multiply reflected between the two interfaces, interfering to give rise to standing waves, similar to those observed in carbon nanotubes[19] or standard graphene devices[20]. Modulations in n_2 changes the Fermi wavelength of the charge carriers, hence altering the interference patterns and giving rise to the resistance oscillations.

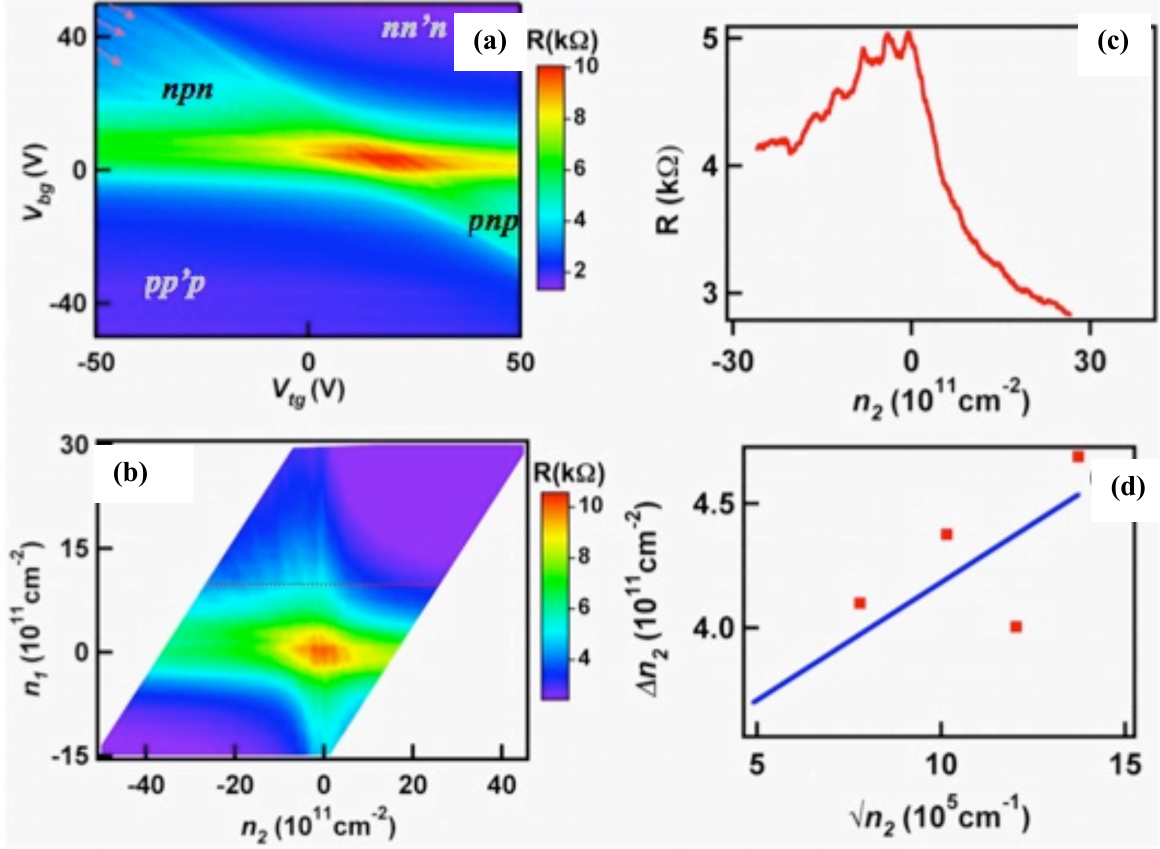

Fig 4.3: Transport data in B=0T. a. Four-terminal device resistance as functions of V_{bg} and V_{tg}. The arrows indicate oscillations in the *npn* region. b. Same data as a, but plotted against n_2 and n_1. c. Line trace along the dotted line in b, showing resistance oscillation as a function of n_2. d. The peak spacing Δn_2 vs. $\sqrt{n_2}$. The line represents a linear fit to the data.

To analyze these oscillations in detail, we replot the data in fig 4.3a in terms of n_1 and n_2, the induced charge by global and local gates, respectively. Utilizing a $C_{bg}/e \approx$ 6.51 x 10^{10} cm^{-2}, which was acquired from quantum Hall measurements, as mentioned at the end of section 4.1. We have,

$$n_1 = 6.5 \times 10^{10} (V_{bg} - V_{D,bg}) \text{cm}^{-2} \quad (4.4)$$

n_2=6.5 x10^{10} [(V_{bg}-$V_{D,bg}$)+ η(V_{tg}-$V_{D,tg}$)]cm $^{-2}$. (4.5)

The new plot is shown in fig 4.3b. The color scale is adjusted to accentuate the resistance oscillations, which appear as fringes fanning out from the Dirac point at n_1=n_2=0. Fig 4. 3c shows the device resistance vs. n_2 at n_1=1.3 x 10^{12} cm^{-2}, displaying clear oscillations.

Within the Fabry-Perot model, the resistance peaks correspond to minima in the overall transmission coefficient; the peak separation can be approximated by the condition k_F(2L)=2π, i.e. a charge accumulates a phase shift of 2π after completing a roundtrip 2L_c in the cavity. Here k_F is the Fermi wave vector of the charges, and L_c is the length of the Fabry Perot cavity. Under the top gate, $k_{f2} = \sqrt{\pi n_2}$, so the spacing between successive peaks is estimated to be

$$\Delta n_2 \approx \frac{4\sqrt{\pi n_2}}{L_c} \qquad (4.6)$$

In fig 4.3d, we plot the measured peak spacing for the curve shown in fig 4.3c against n_2. The data points fall approximately on a straight line. The best linear fit yields a line with a slope 0.95 x10^5/cm, corresponding to L_c=740 *nm* from Eq. (4.6). This agrees with the value estimated from electrostatics, L_c=L_{tg}+2*d*, as the electric field induced by the top gate on the device is expected to extend by a distance ~*d* away from either edge.

Finally, we note that the device in [18] had extremely narrow gates L_{tg}<~20 *nm*. In comparison, our top gate spans a much larger distance, L_{tg}~500*nm*. Thus, the observation of clear Fabry-Perot interference patterns underscores the high quality of our *pnp* graphene devices.

4.3 SLG *pnp* junctions: *B*=8T

4.3.1 Equilibration of edge states in SLG *pnp* junctions

As mentioned in the previous section a local dual gated device allows in-situio tuning of regions with different doping and polarities adjacent to one another. As a result, its quantum Hall conductance is not necessarily quantized at integer values of e^2/h, as discussed in section 4.2. Instead, G depends on the relative values of V_{bg} and V_{tg}, and can have fractional values of e^2/h.

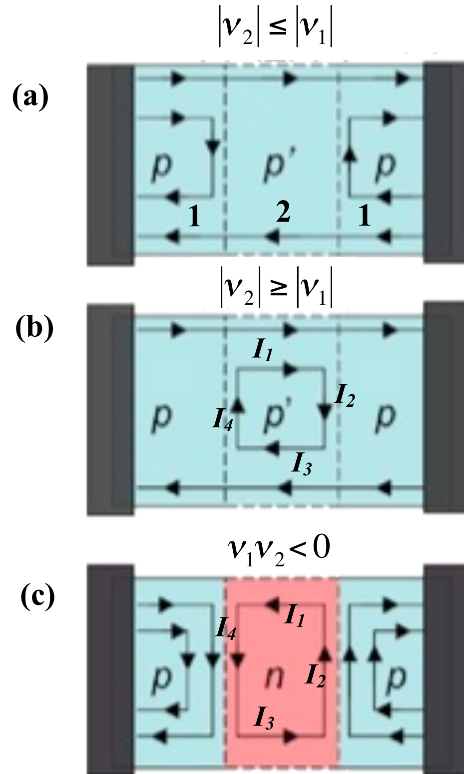

Fig 4.4: Schematics of edge state propagation. Edge state transport in the quantum Hall regime for different values of ν_1 and ν_2. Region 1 denotes back gate controlled only and both V_{bg} and V_{tg} control region 2.

A simple model was proposed by [2, 5], and is shown in fig 4.4, assuming perfect edge state equilibration at the interfaces between different regions: for a unipolar junction ($V_{bg}V_{tg}>0$) with $|\nu_1|\geq|\nu_2|$, the non-top-gated regions act as reflection-less contacts to the center region, yielding a device conductance

$$G=e^2/h|\nu_1|, \qquad (4.7)$$

where ν_1 and ν_2 are the filling factors in regions 1 and 2, respectively. Physically, in this configuration only the modes shared by both regions can traverse the junction. Another scenario occurs when $|\nu_2| > |\nu_1|$, the conductance is,

$$G= e^2/h\ (1/|\nu_1| - 1/|\nu_2| + 1/|\nu_1|)^{-1} \qquad (4.8)$$

The physical picture for this configuration is partial equilibration where the modes in the center couple to some of the exterior modes. By using current conservation eqs: $I_{in}+I_4=I_1$, $I_{out}+I_2=I_1$, $I_2=I_3$ and $I_2=rI_1$, $I_4=rI_3$, where $r=1-(\nu_1/\nu_2)$, the above relation is attained. For a bipolar junction ($V_{bg}V_{tg}<0$), the physical picture is different, and is simply three resistors in series,

$$G= e^2/h\ (1/|\nu_1| +1/|\nu_2| + 1/|\nu_1|)^{-1} \qquad (4.9)$$

By using current conservation eqs: $I_{in}+I_1=I_4$, $I_2=I_3$, $I_{out}+I_2=I_1$ and $I_1=rI_2$, $I_3=rI_4$, where $r=|\nu_2|/(|\nu_1|+|\nu_2|)$ the above relation is attained. This configuration is truly an unprecedented case since the well studied 2DEGS did not possess electron hole symmetry as found in graphene's gapless energy spectrum. With the three distinct relations for conductance a full map detailing the conductance plateau is produced fig 4.5a.

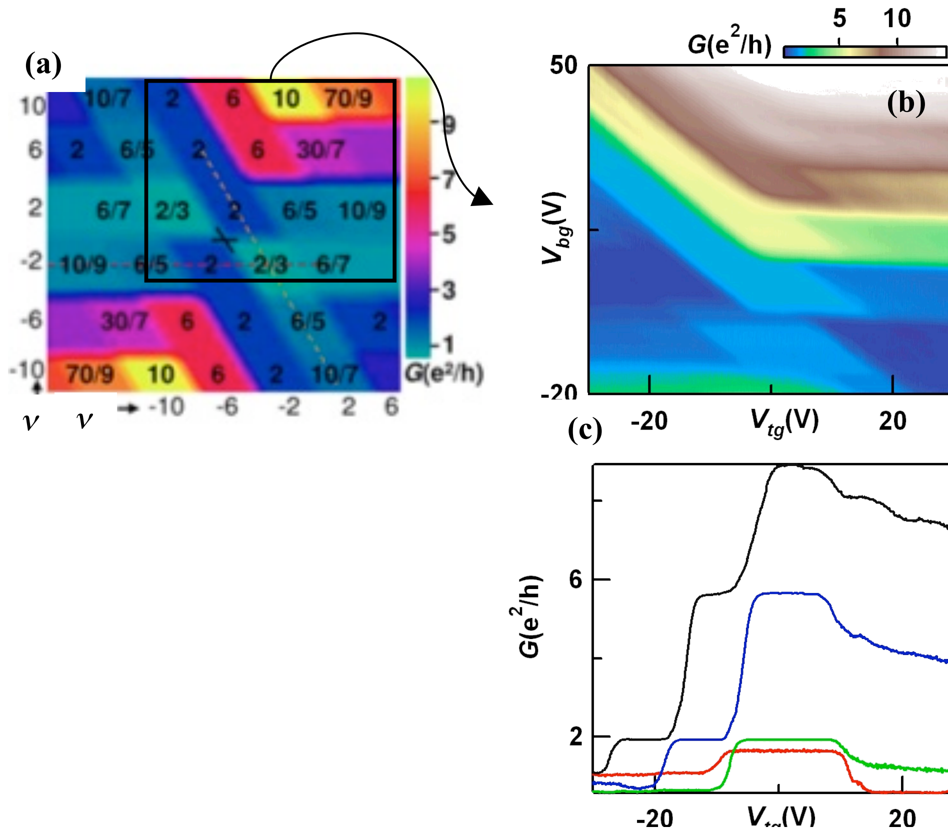

Fig 4.5: Theory and experiment for QHE of graphene *pnp* junctions. a. G(ν_1,ν_2) theoretical map displaying conductance plateau for different combinations of ν_1 and ν_2^2. b. G(V_{bg},V_{tg}) experimental map depicting conductance plateau. Note data reproduces right quadrant of a. c. G(V_{tg}) line traces from b. Note several plateau reproduce those predicted from a.

As shown in fig 4.5b, a typical dataset where $G(V_{bg},V_{tg})$ is plotted at B=8T, appears as a plaque of adjoined parallelograms with different colors, representing QH plateaus at different combination of ν_1 and ν_2. The slope of the diagonal lines, which is measured to be ~0.8, yields the ratio of the coupling efficiencies between the two gates. This agrees with the estimate made using geometric arguments in section 4.2. Thus, the top gate efficiency $\alpha_{tg}=n/V_{tg}$ is estimated to be 6x10^{10} cm^{-2} V^{-1}. Three line traces $G(V_{tg})$ at ν_1=2, 6 and 10 are displayed in the lower panel of fig 4.5c. The measured conductance

values of the plateaus are in excellent agreement with that obtained from eq. (4.7-4.9). The robust appearance of the various conductance plateau up to an orbital level of N=2 underscores the high quality of this sample. Moreover, our data reproduces the right quadrant of the theoretical map fig 4.5a. For instance, for ν_1=2, G =0.67 at ν_2=-2, G=2 at ν_2=2, and G=1.2 at ν_2=6. Thus, our data demonstrate partial and full equilibration of co- and counter-propagating edge states.

4.3.2 Aspect ratio and SLG QHE

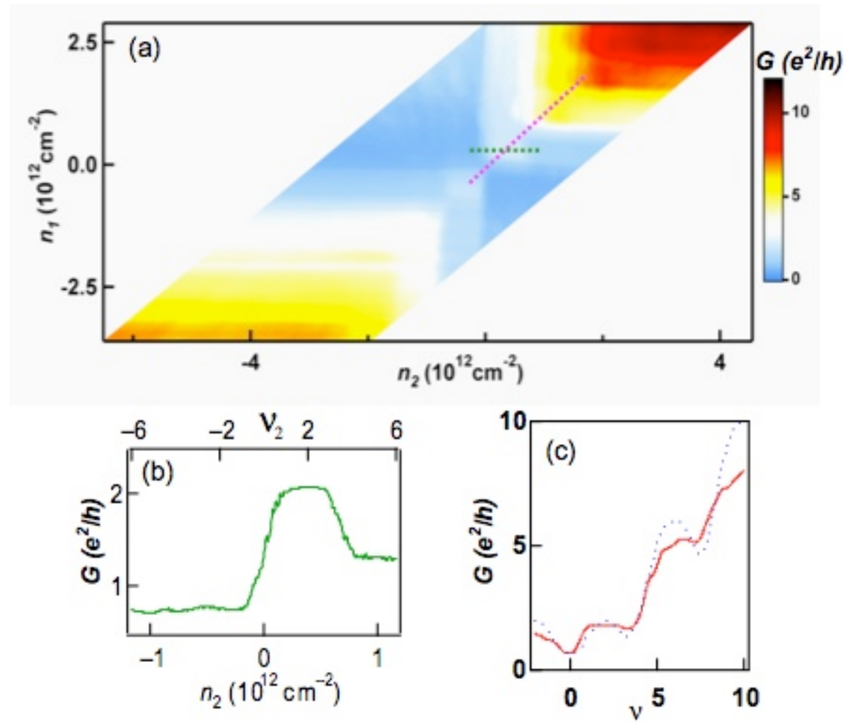

Fig 4.6: Transport data at *B* =8*T*. a. Two-terminal device conductance G versus n_1 and n_2. b. Line trace along the green dotted line ν_1 =2 in a. c. The solid red curve is a line trace taken along the magenta dotted line $n_2 = n_1$ in a. The dotted line is a theoretical curve calculated using the expressions in [20], L/W=3.5 and of the longitudinal resistivity in density.

The data in fig 4.6 is taken from another sample of similar quality as that in fig 4.5 but replotted as a $G(n_1,n_2)$ using eqs: 4.4-4.5. A line trace of G (n_2) at ν_1 =2 is shown in fig 4.6b, with equivalent values of ν_2 labeled on the top axis. The solid line in fig 4.6c plots G(ν) for uniform charge densities over the entire graphene sheet, i.e. along the diagonal dotted line $n_2 = n_1$ in fig 4.6a. The $\nu = 2$ plateau is well developed, indicating relatively small amount of disorder.

We now focus on the small conductance dips in fig 4.6c at $\nu \sim 3$ and 7, which are not expected to be present for a square device with L=W. Indeed, the two-terminal conductance of a conducting square includes both longitudinal and Hall conductivity signals, $G = \sqrt{\sigma_{xx}^2 + \sigma_{xy}^2}$, so $G(\nu)$ appears as stepwise plateaus that increases monotonously for ν > 0. However, for other device geometries the behaviors are more complicated. Depending on the aspect ratio of the device, the device conductance displays local conductance peaks or dips between the plateaus; if the device has significant LL broadening, the conductance will no longer be quantized at integer values of 2, 6, 10, ... e^2/h . This was studied in detail in [8], using an effective medium approach that yields a semicircle relation between σ_{xx} and σ_{xy}. To quantitatively examine the agreement between the data and the theory, we model the longitudinal conductivity as a Gaussian centered at an LL, $\delta_N \sigma_{xx}(\nu) = 2e^{-[\nu - 1/2(\nu_N + \nu_{N+1})]^2/\Gamma}$ in units of e^2/h. Here Γ describes the width of the Gaussian distribution. Following the procedures outlined in [8], and using a fitting parameter Γ= 0.67, we calculate $G(\nu)$ for our rectangular device with aspect ratio L/W = 3.5. The resultant curve is shown as the dotted line in fig 4.6c. The agreement with data is satisfactory at smaller values of ν, but deviates for $\nu > 6$. This is

quite reasonable, since the energetic difference between LL decreases for higher levels, a unique feature of LLs in SLG. Moreover, the value of = 0.67 obtained from the fitting is relatively small, again underscoring the high junction quality.

4.4 Observation of conductance fluctuations on transitions between QH plateaus

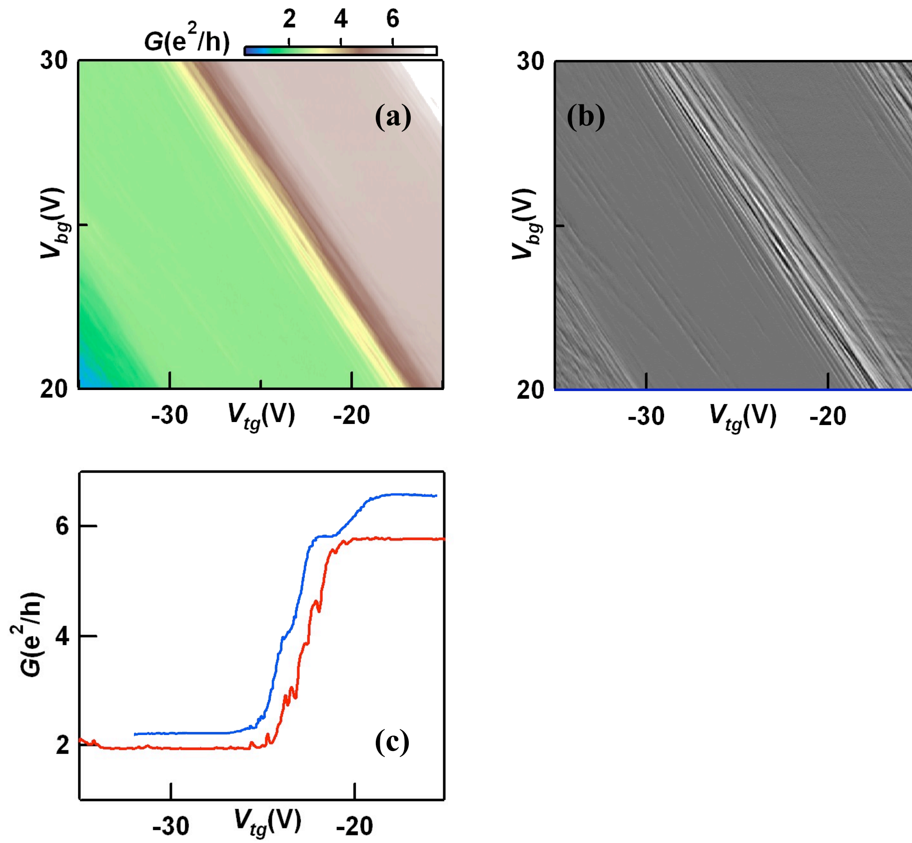

Fig 4.7: High resolution scans between conductance plateau. a. $G(V_{bg},V_{tg})$ with high resolution in gate voltage. b. $dG/dV_{tg}(V_{bg},V_{tg})$ by differentiating data in a. c. red line trace along the dotted line in a .the blue curve taken with medium V_{tg} resolution and offset for clarity.

Interestingly, though the transitions between QH plateaus appear to be smooth in fig 4.5b, more complicated structures develop upon high resolution $G(V_{bg},V_{tg})$ scans. Fig 4.7a presents data over a smaller range of that in fig 4.5b, but taken with 20 times higher gate voltage resolution at 5mV/pixel in V_{bg} and 50mV/pixel in V_{tg}. Instead of smooth

steps, the transitions between different QH plateaus now display pronounced fluctuations. A line trace of the transition between G=$2e^2/h$ to $6e^2/h$ plateaus is shown in the lower panel (red curve). To identify the movement of such fluctuations more clearly, we plot dG/dV_{tg} in the right panel of fig 4.7b. Evidently, these fluctuations are observed on all the transitions between different plateaus. Moreover, even though similar conductance fluctuations are observed in high resolution $G(V_{bg})$ plots when the device has uniform charge density (i.e. with the top gate disconnected) as shown in fig 4.8, the amplitudes are significantly smaller, indicating the local nature of these fluctuations.

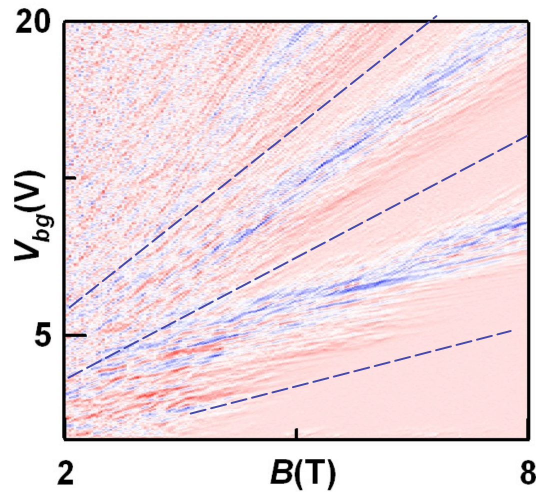

Fig 4.8: Differentiated Fan Diagram. $\mathrm{d}G/\mathrm{d}V_{bg}(V_{bg},B)$ taken from a fan diagram not shown. Smooth areas correspond to conductance plateau rough areas are the transitions between different plateau. Dotted lines indicate the trajectory of QH plateau: 2,6 and 10 e^2/h. There are Lines parallel to these plateau but they are lesser in magnitude than $\mathrm{d}G/\mathrm{d}V_{tg}(V_{tg},B)$ scans.

We note that with medium resolution scans (at 25mV/pixel in V_{bg}), these fluctuations appear as kinks or small plateaus on the transition, as shown by the blue curve in fig 4.7c, and may resemble that of spin- or valley-resolved LLs. To elucidate the origin of these fluctuations, we study their evolution with V_{tg} and B at constant V_{bg}. Fig 4.9 plots the differentiated conductance $dG/dV_{tg}(V_{tg}, B)$ at V_{bg}= 2.5V, or equivalently, at v_1=2. At B=8T, the conductance changes from 0.67e^2/h at V_{tg} =-13V (or v_2~ -1.7) to 2e^2/h at V_{tg}=-7V (or v_2~0.2). Fig 4.9b plots another data set $dG/dV_{tg}(V_{tg}, B)$, taken at V_{bg}=14V, or v_1=6. At B=8T, the conductance increases from 2e^2/h at V_{tg} =-20V (or v_2~0.5) to 2e^2/h at V_{tg}=-7V (or v_2~4.6). In both graphs, two pronounced features become evident: "smooth" sections that increase in area with increasing magnetic field, separated by strips of "rough areas" that stay approximately constant in size. In the smooth regions, dG/dV_{tg}=0, so they correspond to QH plateaus in the locally gated area; as the energetic spacing between *LL*s increases with magnetic fields, the width of a given smooth region grows accordingly. The red dotted lines plots the slopes of the plateaus in the V_{tg}-B plane, given by b_{bg}/η, which are calculated using values of b_{bg} measured from fig 4.4c, and η =0.8 from fig 4.5b.

We now focus on the "rough" areas separating the QH plateaus in fig 4.5. They consist of criss-crossing bright and dark lines, corresponding to extrema values in conductance fluctuations between QH transitions. Noticeably, trajectories of these ridges are parallel to the dotted lines, or to the adjacent QH plateaus. For instance, in fig 4.9b, the rough area separating the 2 e^2/h and 6 e^2/h plateaus consist of lines with the same slopes as the v_2=2 and v_2=6 plateaus; in fig 4.9a, the lines are parallel to the v_2=-2 and 2

plateaus, respectively. In the low-*B* (lower left) corner of fig 4.9b, several short lines parallel to the ν_2=2 plateau are visible, but abruptly stop as the device conductance become quantized at higher fields.

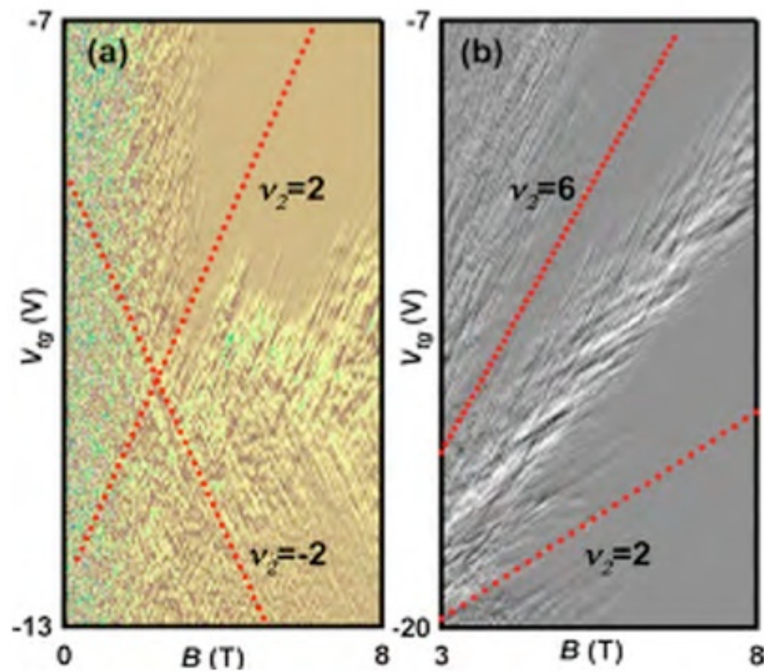

Fig 4.9: Conductance fluctuations (CF). a. d*G*/d*Vtg*(V_{tg}, *B*) at V_{tg},=2.5, or ν_1= 2. b. d*G*/d*Vtg* (V_{tg}, *B*) at V_{tg}, =14 or ν_1 =6. The dotted lines indicate the trajectory of the QH plateaus in the locally gated area.

4.4.1: Coulomb-induced charging of electron or hole-doped localized states

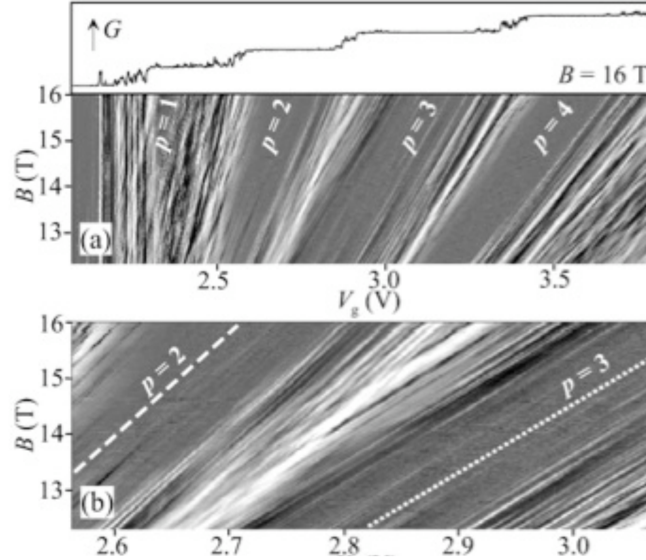

Fig 4.10: CF in the QH regime for Si-MOSFETS. a. $G(V_g)$ displays CF at transitions between plateaus, similar to fig 4.5 in SLG. a-b. $dG/dV_g(B,V_g)$ displays both rough and smooth regions similar to fig 4.7.

Such conductance fluctuations between QH transitions have been observed in Si-MOSFET devices[9] , though only with positive slopes fig 4.10. In the single-particle picture, conductance fluctuations may arise from resonant tunneling between the edge states on opposite sides of the device through states located in the bulk [21]. However, trajectories of these fluctuations are expected to be parallel to that of half-integer values of filling factors [9]. Thus, we attribute these fluctuations to charging and localization induced by electronic interactions. Assuming a general disorder potential induced by, e.g. impurities on the substrate or graphene, the electron density in graphene develop local valleys and hills as depicted in fig 4.11. At high magnetic fields, the edge channels in a 2D electron system form compressible and incompressible strips, with contours that

generally follow the local potential landscapes (fig 4.11a). Thus, when an incompressible (insulating) strip completely surrounds a compressible (metallic) region, this effectively creates a quantum dot with quantized charges as shown in fig 4.11b. The conductance fluctuations then arise from charging of and transport across one or multiple such quantum dots, and should only depend on the geometry of the dots. Since the filling factor v within an incompressible strip takes on integer values, which only depends on the ratio n/B, the size of the dot (and hence the fluctuations) should remain constant for the same n/B value, as observed experimentally. We note that in contrast to MOSFET devices [9], fluctuations with both positive and negative slopes in the V_{tg}-B plane are observed, indicating the presence of both electron- and hole- doped incompressible strips at the N=0 LL, once again a manifestation of graphene's unique band structure.

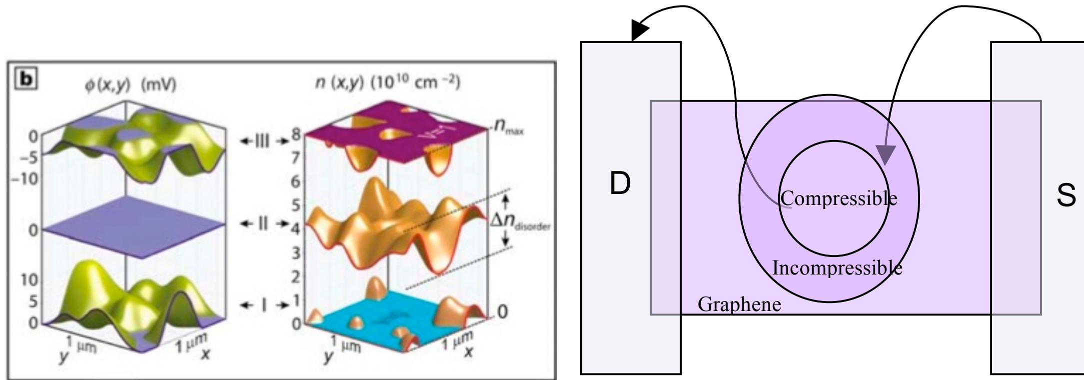

Fig 4.11: Visualization of disorder potential and formation of quantum dots. a. The density profile $n(x,y)$ and electrostatic potential profile $\phi(x,y)$, calculated self-consistently within the Thomas-Fermi scheme, for an almost empty (I), half full(II) and almost full(III) Landau level(ref). At high magnetic fields, the edge channels in a 2D electron system form compressible and incompressible strips, with contours that generally follow the local potential landscapes[11]. b. Schematic representation of formation of a quantum dot in a SLG sample. When a incompressible strip surrounds a compressible region a quantum dot is formed. Charging of the quantum dot is independent of B since it arises from disorder potential.

Our data shown in fig 4.9b, i.e., the parallel lines with slope given by eq. 4.1 for ν =-2, 2, 6..., bear striking resemblance with that of local inverse electronic compressibility of graphene[10]and GaAs/AlGaAs [11] devices using scanned single electron transistors (SET), albeit with one important difference: in the SET measurements, the line appear on the QH plateaus, at which the bulk of the device consists of incompressible states; in our experiment, the lines appear at the transitions, or equivalently, at the center of the Laudau Levels, when states in the bulk of the graphene are metallic and delocalized.

More supporting evidence is given by the quasi-periodic nature of some of the conductance fluctuations, with a typical separation in V_{tg} of ΔV_{tg}~0.1 – 0.35 V. In the

Coulomb blockade scenario, this represents the charging of a compressible quantum dot that dominates transport (fig 4.11b). Addition of one electron requires $\Delta V_{tg} = e/(\varepsilon_0 A/t)$, where ε_0 is the permittivity of vacuum and A is the area of the metallic region. This yields a typical metallic area with a diameter of ~80 –135nm, consistent with SET measurements [10,22]. Moreover, when a *LL* is almost completely filled, an incompressible strip percolates through the metallic regions, marking the onset of QH conductance plateaus. This corresponds to the short parallel lines that abruptly terminate just before the onset of QH conductance plateaus, as seen in the lower left corner of fig 4.9b.

4.4.2: Temperature dependence of Conductance Fluctuations

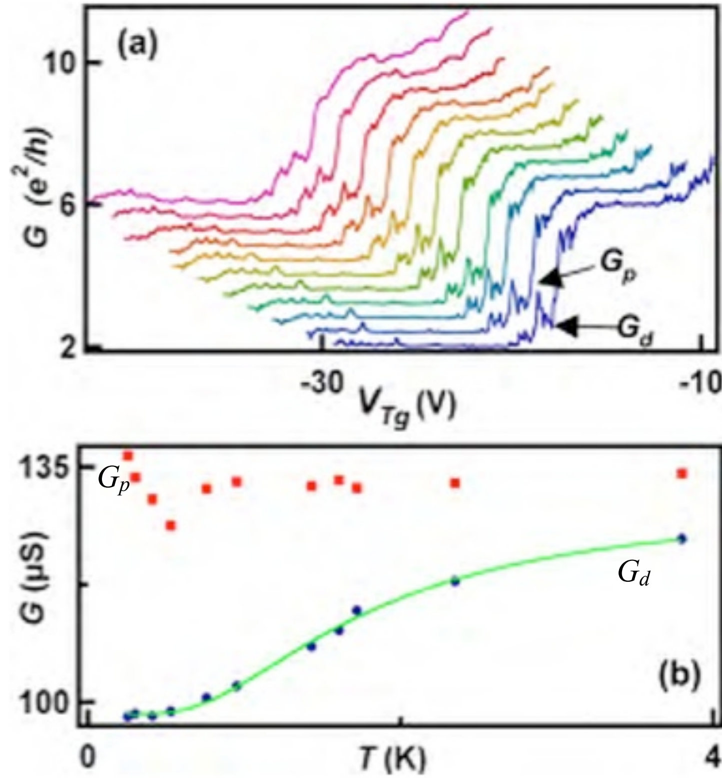

Fig 4.12: CF temperature dependence measurement. a. $G(V_{tg})$ for a transition between the v_2=2 and v_2=6 plateaus. From right to left, T=0.26, 0.31, 0.42, 0.53, 0.76, 0.95, 1.43, 1.61, 1.72, 2.35 and 3.8 K. The traces are offset for clarity. b. T-dependence of G_p (red squares) and G_d (blue dots). The green line is a fit using eq 4.3.

Finally, we study the temperature dependence of these fluctuations. We focus on the transition between v_2=2 and v_2=6 plateaus, whereas the non-top-gated regions are kept at v_1=6. The data are taken at B=8T and 10 different temperatures T between 0.26K and 3.8K(fig 4.12a). In particular, we follow the evolution of the group of fluctuations near the center of the transition, as marked by the arrows on fig 4.12a. Interestingly, with

increasing T, the conductance of the peak of these fluctuations G_p remains approximately constant, while that of the dips G_d increases (fig 4.12b). This is exactly what is expected for a Coulomb-blockaded classical quantum dot [23]: the dot's maximum conductance is temperature independent, as it is simply determined by the ohmic addition of the barrier resistances; the minimum conductance of the dot, however, is thermally activated. Thus, our data suggest that a single quantum dot dominates the conductance fluctuations. Modeling the conductance between the QH transitions by that of a single dot in parallel with other metallic paths, we write G_d as [23]

$$G_d(T) = \frac{A/k_B T}{\sinh(\delta/k_B T)} + C$$

where δ is the energy detuning from the resonant level, and k_B is the Boltzmann constant. Using A=123k_B, δ=4.0k_B, and C=98 μS, we plot the resultant curve as the green line in fig 4.12b, which is in excellent agreement with the data.

Conclusion:

In a broader context, one result of this work was the ability to track and distinguish QH features in n-B maps using dG/dn as the color scale, as seen in figs 4.9. Line traces, as shown in fig 4.7c, can be misleading by exhibiting plateau like features when in fact they are related to charging. By coupling the $dG/dn(n,B)$ maps with high resolution scans this misconception is avoided. Another take home point from this chapter is that our contactless gate produces exceedingly clean samples. This is supported by excellent single gate and local gate QH effect shown in figs 4.1 and 4.3. With this in

hand, and because of their contactless nature, suspended samples were the next logical step.

Yet, we took a slightly different approach. During the submission and review of this work I measured BLG substrate supported samples with a contactless local gate fabricated by Lei Jing, while also developing the dual gated suspended graphene recipe. It is a testament to our fruitful collaborative effort that we attained results as previous projects were wrapping up, and in the end both projects yielded excellent science.

The next section will be on substrate supported BLG *pnp* junctions. This study was performed during the nascent period of electron-electron interactions in BLG. In a certain sense the observation of *E-B* induced insulating states in those substrate-supported devices, prepared us for our study of correlated electron insulating states in the suspended dual gated device.

References

1. J. R. Williams, L. DiCarlo and C. M. Marcus, Science **317**, 638-641 (2007).

2. B. Ozyilmaz, P. Jarillo-Herrero, D. Efetov, D. A. Abanin, L. S. Levitov and P. Kim, Physical Review Letters **99**, 166804 (2007).

3. B. Huard, J. A. Sulpizio, N. Stander, K. Todd, B. Yang and D. Goldhaber-Gordon, Physical Review Letters **98**, 236803 (2007).

4. R. V. Gorbachev, A. S. Mayorov, A. K. Savchenko, D. W. Horsell and F. Guinea, Nano Letters **8** (7), 1995-1999 (2008).

5. D. A. Abanin and L. S. Levitov, Science **317**, 641-643 (2007).

6. V. V. Cheianov, V. Fal'ko and B. L. Altshuler, Science **315** (5816), 1252-1255 (2007).

7. V. V. Cheianov and V. I. Fal'ko, Physical Review B **74** (4), 041403 (2006).

8. D. A. Abanin and L. S. Levitov, Physical Review B **78** (3), 035416 (2008).

9. D. H. Cobden, C. H. W. Barnes and C. J. B. Ford, Physical Review Letters **82** (23), 4695-4698 (1999).

10. J. Martin, N. Akerman, G. Ulbricht, T. Lohmann, K. von Klitzing, J. H. Smet and A. Yacoby, Nature Physics **5** (9), 669-674 (2009).

11. S. Ilani, J. Martin, E. Teitelbaum, J. H. Smet, D. Mahalu, V. Umansky and A. Yacoby, Nature **427** (6972), 328-332 (2004).

12. G. Liu, J. Velasco, W. Z. Bao and C. N. Lau, Applied Physics Letters **92** (20), 203103 (2008).

13. J. Velasco, G. Liu, W. Z. Bao and C. N. Lau, New Journal of Physics **11**, 095008 (2009).

14. J. H. Chen, C. Jang, S. Adam, M. S. Fuhrer, E. D. Williams and M. Ishigami, Nature Physics **4** (5), 377-381 (2008).

15. W. Z. Bao, Z. Zhao, H. Zhang, G. Liu, P. Kratz, L. Jing, J. Velasco, D. Smirnov and C. N. Lau, Physical Review Letters **105** (24), 246601 (2010).

16. W. Bao, L. Jing, Y. Lee, J. V. Jr., P. Kratz, D. Tran, B. Standley, M. Aykol, S. B. Cronin, D. Smirnov, M. Koshino, E. McCann, M. Bockrath and C. N. Lau, Nature Physics **7**, 948-952 (2011).

17. L. Jing, J. Velasco Jr., P. Kratz, G. Liu, W. Bao, M. Bockrath and C. N. Lau, Nano Letters **10**, 4000-4004 (2010).

18. A. F. Young and P. Kim, Nature Physics **5** (3), 222-226 (2009).

19. W. J. Liang, M. Bockrath, D. Bozovic, J. H. Hafner, M. Tinkham and H. Park, Nature **411** (6838), 665-669 (2001).

20. F. Miao, S. Wijeratne, Y. Zhang, U. Coskun, W. Bao and C. N. Lau, Science **317**, 1530-1533 (2007).

21. J. K. Jain and S. A. Kivelson, Physical Review Letters **60** (15), 1542-1545 (1988).

22. J. Martin, N. Akerman, G. Ulbricht, T. Lohmann, J. H. Smet, K. v. Klitzing and A. Yacoby, Nat. Phys. **4**, 144-148 (2008).

23. L. P. Kouwenhoven, C. M. Marcus, P. L. McEuen, S. Tarucha, R. M. Westervelt and S. Wingreen, in *Mesoscopic Electron Transport*, edited by L. L. Sohn, L. P. Kouwenhoven and G. Schon (Springer, Kluwer, 1997).

Chapter 5: Quantum Hall effect in Bilayer *pnp* junction

Introduction:

In this chapter I will discuss our experimental investigation of BLG *pnp* junctions on substrate, which have mobility up to 10,000 cm^2/Vs, in zero and high magnetic fields. Using a combination of the Si back gate and a suspended top gate, which was fabricated with the methods discussed in chapter three, these dual-gated structures offer *in situ* control of the dopant density n and type of different regions, as well as independent tuning of n_2 and applied electric field E_2 for the region under the top gate. The effect of an E_2 is not significant in the dual gated SLG devices studied in the previous chapter. This difference between SLG and BLG, arises from the additional layer, which allows for a charge imbalance between the two layers in BLG, creates a tunable band gap. Increasing this E_2 drastically affects transport properties as discussed in chapter two. At the charge neutrality point, the device exhibits a sharp drop in conductance, which decreases exponentially as E_2 is increased. These data do not fit a thermal activation model, but instead can be satisfactorily accounted for by variable range hopping (VRH) in 2D, suggesting the opening of an electric field induced band gap that contains localized states. Interestingly, these localized states appear to be similar in nature to those discussed for SLG samples in section 4.7.

In high magnetic field B, we observe fractional-valued QH plateaus, which arise from edge state equilibration at the interface of differentially doped regions, in agreement with the same model used in the previous chapter for SLG *pnp* junctions, but by using the BLG filling factors instead. Also, we observe an insulating state that develops at filling

factor ν=0, whose conductance is exponentially dependent on applied B. Thus, the work presented in this chapter demonstrates that competing symmetries and insulating states in bilayer graphene can be tuned by electric and magnetic fields. This notion, which is absent in SLG, places BLG in a class of its own because it is relevant for both technological applications and fundamental study of 2D systems.

5.1: Device Characterization

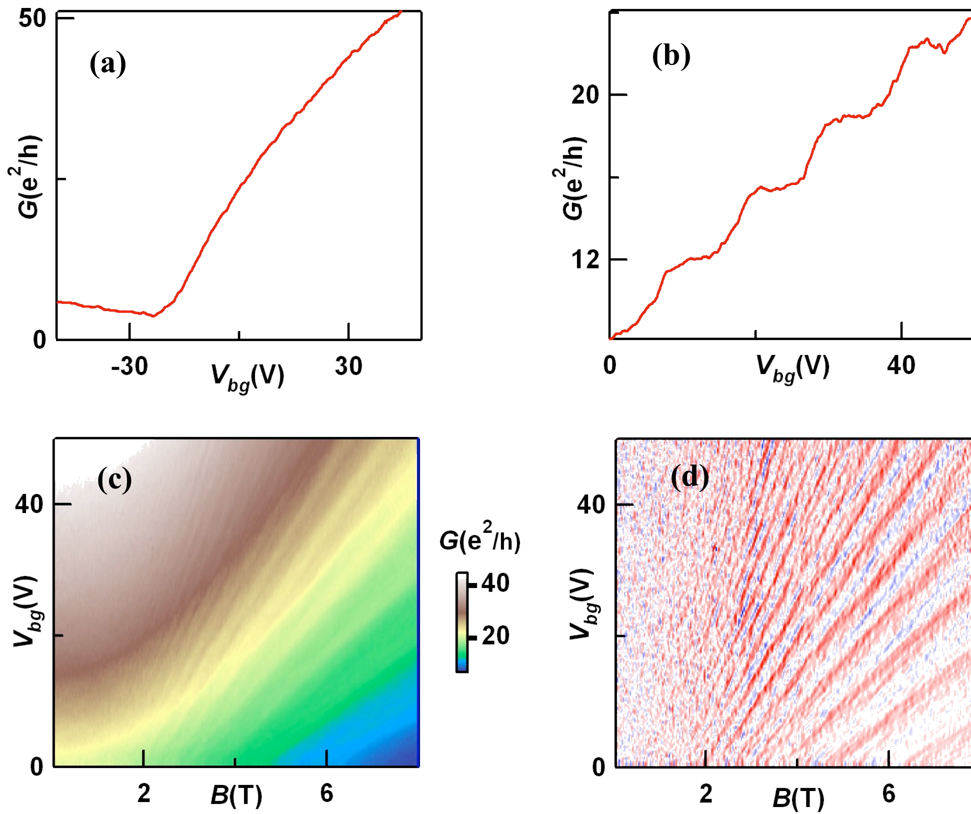

Fig 5.1: Transport measurements with a single gate at B=0~8T. a. $G(V_{bg})$ for a bilayer graphene device at T=260 mK and B=0. b. $G(V_{bg})$ of the device at B=8T. c. LL fan diagram $G(V_{bg},B)$ of the device. d. $dG/dV_{bg}(V_{bg},B)$ from c.

BLG sheets are exfoliated from bulk graphene onto piranha-treated Si/SiO_2 wafers. The Ti/Al electrodes and Ti suspended top gates[1, 2] are fabricated by electron beam lithography similar to the SLG device procedure. One crucial difference is the use of resist alignment marks where the alignment feature is an exposed and developed cross grid. This eliminates one step from the entire fabrication procedure, hence cleaner samples are attained. Unless specified otherwise, the substrate-supported devices are measured at 260 mK in a He^3 refrigerator using standard lock in techniques. In this chapter we focus on data from a single substrate supported device with width W=1.2 μm, and source-drain separation L= 2.3 μm. The top gate, straddling the center of the device, is 550 nm wide and suspended at d~50 nm above the substrate.

We first examine the device's behavior as a function of V_{bg}. Fig 5.1a plots the differential conductance G of the device *vs.* V_{bg} at B=0, with the Dirac point $V_{bg}^0 \approx -28$V. The electron mobility is ~ 10,000 cm^2/Vs, while the hole mobility is significantly lower. For the rest of this chapter we will focus on the electron-doped regimes for this substrate supported sample.

In fig 5.1b, clear plateaus that are quantized at G=8, 12, 16… e^2/h are observed, in agreement with eq 2.60 from chapter two on the QH conductance spectrum of BLG. Fig 5.1c shows the standard LL "fan diagram", *i.e.* the evolution of the conductance plateaus with B and V_{bg}. Impressively, a total of 15 QH states are visible for B>2T, demonstrating the high quality of this device. Such features are more apparent as blue regions in fig 5.1d, where the $dG/dV_{bg}(V_{bg},B)$ is plotted, as was discussed in the previous chapter four. Furthermore, since the trajectory of the center of a plateau has a slope

$\nu e/h\alpha_{bg}$ in the V_{bg}-B plane, where $\alpha_{bg}=n/V_{bg}$ is the back gate coupling efficiency, we extract $\alpha_{bg}\approx 7.4\times 10^{10}$ cm^{-2}V^{-1} from Fig. 1c or fig 5.1d.

5.2 Comparison with suspended BLG devices

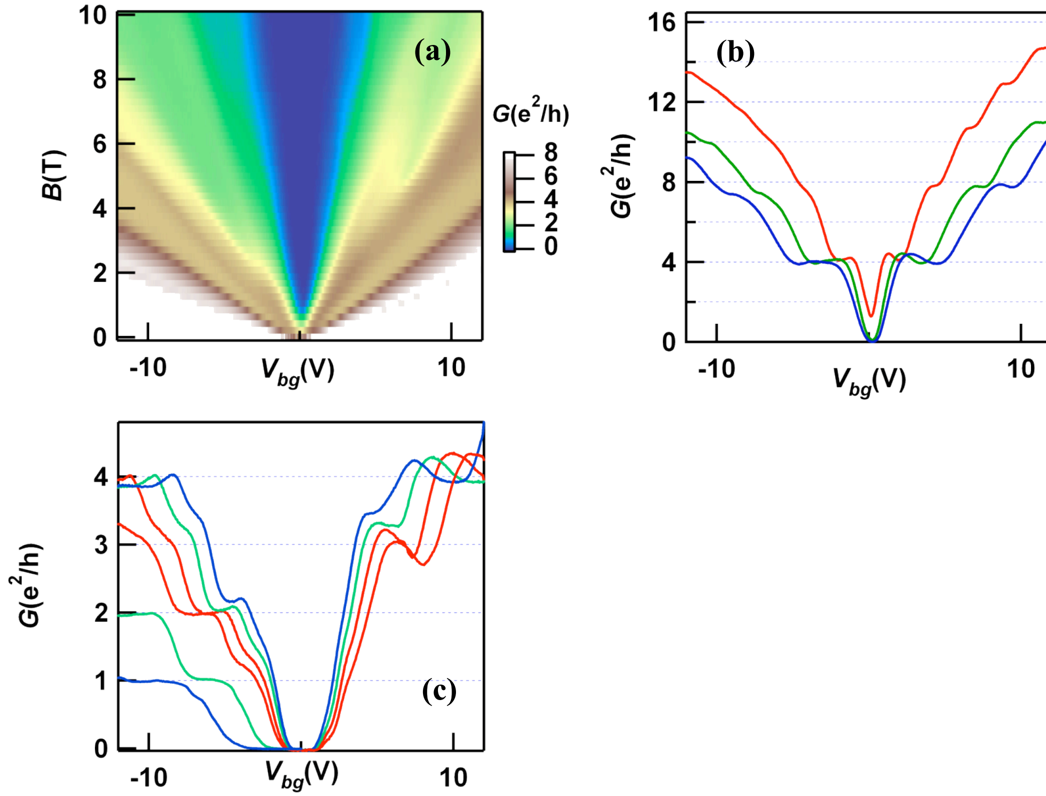

Fig 5.2: Transport measurements of a suspended BLG sample with one gate in finite *B*. a. $G(B,V_{bg})$ of the device. b. $G(V_{bg})$ from a. at B=0.6, 1.2, 1.6T, note single particle QH states are visible. c. $G(V_{bg})$ from a. at B=4, 4.6, 6.4, 11, 18T, note new integer QH states are seen not present in fig 5.1.

In recent years the innovations of suspended samples[3,4] and sample on hexagonal boron nitride (BN)[5] have significantly advanced the exploration of the QHE in SLG and

BLG. During the course of the work presented in this chapter results on suspended graphene samples with one gate were just published. Above, (and shortly below) we demonstrated the high quality of our substrate supported samples by the observation of the expected single particle quantum Hall states in spite of the lengthy top gate fabrication. Nonetheless, sample on SiO_2 has its limitations and simply cannot compete with suspended or BN based devices with regards to sample quality. This unfortunately limits the scope of physical phenomena that can be explored with SiO_2 supported samples.

The latter fact is most salient when comparing the observed conductance plateau in the lowest LL of dual gated suspended and substrate supported samples. Fig 5.2a shows the LL fan diagram for a suspended BLG sample after the current annealing procedure shown in chapter 3. The data displays fewer bands than fig 5.1, but most importantly they are: 1. Closely centered at a CNP of V'_{bg}~0, which is evidence of minute charge impurity doping; and 2. Display integer conductance plateau that cannot be accounted for by eq 2.60, which is the single particle picture. These features are more apparent in Figs 2b-c, which are horizontal line cuts from fig 2a at constant *B.* In fig 5.2b the $G(V_{bg})$ plots, which are taken at low B, reveal 0,4 and $8e^2/h$, also seen in fig 5.1 for the substrate supported sample. Interestingly, in fig 5.2c the $G(V_{bg})$ line traces show conductance plateau values 0,1,2, a budding 3 and 4 e^2/h, which were not seen in fig 5.1. These plateaus indicate that the 8-fold degeneracy of the lowest LL, which was intact for the substrate-supported samples, is broken in suspended samples, in agreement with theoretical predictions [6] and previous experiments[7-9]. Such phenomena are attributed to a

many body effect called quantum Hall ferromagnetism. Thus, when one is on the hunt for correlated electron phenomena, the cleaner sample quality afforded by suspended or BN device architectures are seemingly the only way.

One advantage the more disorder prone substrate supported samples have on the suspended devices is greater structural integrity. The ranges of accessible gate voltages are quite different for these devices (figs 5.1-5.2). Gate voltages applied to suspended samples are limited to <20V, to avoid collapsing the membranes under electrostatic pressure. This limits our experiments to the first, and occasionally the second, LL. In contrast, for the substrate supported samples, conductance plateaus for up to LL=7 are observed, which will be discussed in the following sections. When employing two gates this difference in structural integrity becomes even more important, since it limits the applied E, which has a significant effect on transport properties in BLG. Subsequent sections in this chapter and the next will cover this point. In this regime of high density or large E the BN samples appear to be the best option to take for the young fabricator. However, as was discussed in the introduction of chapter two, and will be covered in the next chapter, the physics around the CNP for an exceedingly clean BLG is extremely interesting. As of the writing of this thesis such samples are only attainable through the suspended method.

5.3 Two gates are better than one: B=0

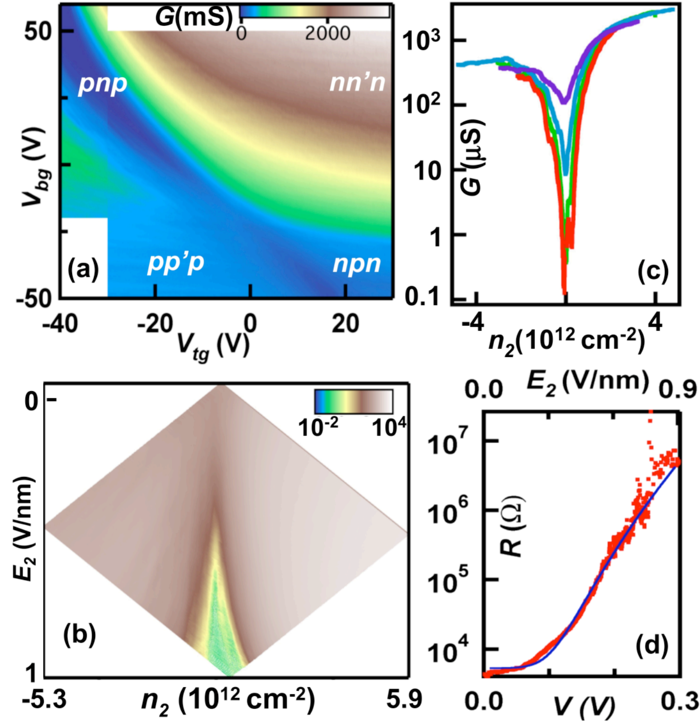

Fig 5.3: Transport measurements with two gates at *B*=0T. a. $G(V_{bg},V_{tg})$ of the device at B=0. The junction polarities are indicated on the graph. b. Data in a. plotted in terms of E_2 and n_2. Note the logarithmic color scale. c. (Top to bottom) Line traces $G(n_2)$ at E_2=0.21, 0.49, 0.65 and 0.73 V/nm. d. $R(E_2)$ at n_2=0. The line is a fit of the data to the VRH model, $R=R_0+A\exp[-((4\pi e)/(k_B)aV_2)^{1/3}]$

By applying voltages to both top and back gates, we can create *pnp* junctions with *in situ* modulation of junction polarity and dopant levels. Fig. 5.3a shows the conductance plot of G (color) *vs.* V_{bg} (vertical axis) and V_{tg} (horizontal axis) at B=0 for a substrate supported device. The plot can be partitioned into 4 regions with different combinations of dopant types, with the CNP occurring at (V_{tg}^0, V_{bg}^0)=(-2.6V, -18V). In particular, the blue diagonal features correspond to the conductance of the region that is controlled by

both V_{tg} and V_{bg}, *i.e.*, the area under the top gate. From the slope of the diagonal features near the CNPs, which corresponds to the ratio of the coupling efficiencies between the top gate and the back gate, we extract the top gate coupling efficiency $\alpha_{tg} \approx 1.2 \times 10^{11}$ cm^{-2}V^{-1}. At high V_{tg} and V_{bg} values, the dark blue regions exhibit noticeable curvature, which arises from the deflection of the top gate under the electrostatic pressure.

This *in situ* creation of *pnp* or *npn* junctions in double gated junctions has been extensively studied in single layer graphene (SLG) devices[1, 10-12], and enabled observation of phenomena such as Klein tunneling[13], equilibration of counter-propagating edge modes[1, 10-12], conductance fluctuations induced by charge localization in the quantum Hall regime[12]. These last two phenomena were discussed in the previous chapter and their manifestation in substrate supported BLG device will be discussed here. For BLG, a unique aspect not found in SLG, is the possibility for independent control of the charge density n_2 and the electric field E_2 applied across the bilayer[14, 15 16-19]. Here the subscript 2 denotes the top-gated region. Quantitatively, V_{bg} induces an electric field below graphene $E_b = \varepsilon_{SiO}(V_{bg} - V_{bg}^0)/t$, where $\varepsilon_{SiO} \approx 3.9$ and t=300nm are the dielectric constant and thickness of the SiO_2 layer, respectively. Similarly, V_{tg} induces $E_t = -(V_{tg} - V_{tg}^0)/d$ above graphene. The difference of the fields yields the total charge density under the top gate, $n_2 = (E_b - E_t)e$, whereas their average $E_2 = (E_b + E_t)/2$ breaks the inversion symmetry and yields a potential difference $V_2 = E_2$ (3.3 Å) across the bilayer. For the data shown in fig 5.3a, E_2 ranges from 0 to 0.96 V/nm, a number that was never reached in the suspended samples.

To better explore this unique aspect of BLG, we replot part of the data shown in fig. 5.3a in terms of n_2 (horizontal axis) and E_2 (vertical axis), as shown in fig 5.3b (note the logarithmic color scale that spans 6 orders of magnitude). To account for the deflection of the top gate under applied voltages, we self-consistently solve for the deflection and E_t by considering the electrostatically induced bending of a beam, which adopts a parabolic profile and in turn modifies the electrostatic pressure. As demonstrated by fig 5.3b, this procedure successfully accounts for much of the curvature in fig 5.3a.

A striking feature in fig 5.3b is the vertical dark brown band at $n_2 \sim 0$, which, with increasing E_2, develops into a triangular green region. This indicates a very low conductance state at high electric field and charge neutrality point. Fig 5.3c plots several line traces $G(n_2)$ at different E_2 values ranging from 0.21 to 0.73 V/nm. Each curve displays a minimum at $n_2 \approx 0$. For small values of E_2, the minimum is rather shallow, and the device's on/off ratio η, defined as the ratio between the maximum and minimum conductance values at a given E_2, is about 10. As E_2 increases, the device conductance at $n_2 \approx 0$ decreases dramatically, while that for large n_2 remains almost constant, resulting in a rapidly increasing η. For E_2=0.73 V/nm, η>20,000.

Fig 3d plots the device resistance $R=1/G$ at n_2=0 *vs.* E_2 (top axis) and V_2 (bottom axis); the exponential increase in R with increasing V_2 over nearly 3 decade suggests a field-induced opening of a band gap in the top gated region. Though the data presented was obtained at T=260mK, we observe little temperature dependence of conductance for T<1K. From tight binding calculations [14, 15, 20, 21] as was discussed in chapter two, BLG's

band structure adopts a “Mexican-hat” shape under an applied potential V_2, with a dispersion relation

$$E^{\pm -} \approx \pm \frac{eV_2}{2} \mp \frac{eV_2 v_F^2 \hbar^2 k^2}{t_\perp^2} \pm \frac{v_F^4 \hbar^4 k^4}{t_\perp^2 eV_2} \qquad (5.1)$$

which is valid for, $v_f \hbar k \ll V \ll t_\perp$ and a band gap

$$\Delta = \frac{t_\perp eV_2}{\sqrt{t_\perp^2 + eV_2^2}} \qquad (5.2)$$

Here $t_\perp$ ~ 0.2-0.4 eV is the inter-layer hopping energy, and k is the electron wave vector. From (2), Δ scales almost linearly with V_2 until it saturates at $t_\perp$; if screening is taken into account, it can be reduced by a factor of 2. In our devices, Δ ~ 0-0.1 eV [19,15]. If electrons are thermally activated to transverse the gapped region, we expect $R \sim exp(-eV_2/2k_BT)$, with an exponent $b \sim e/2k_BT$ ~19000, where k_B is Boltzmann’s constant and T=.3K. However, from fig 5.3d, the slope of the semi-log plot is ~36, or 2-3 orders of magnitude smaller than expected. This suggests that transport across the top gated region is not thermally activated. Indeed, we observe little temperature dependence of conductance for T<1K.

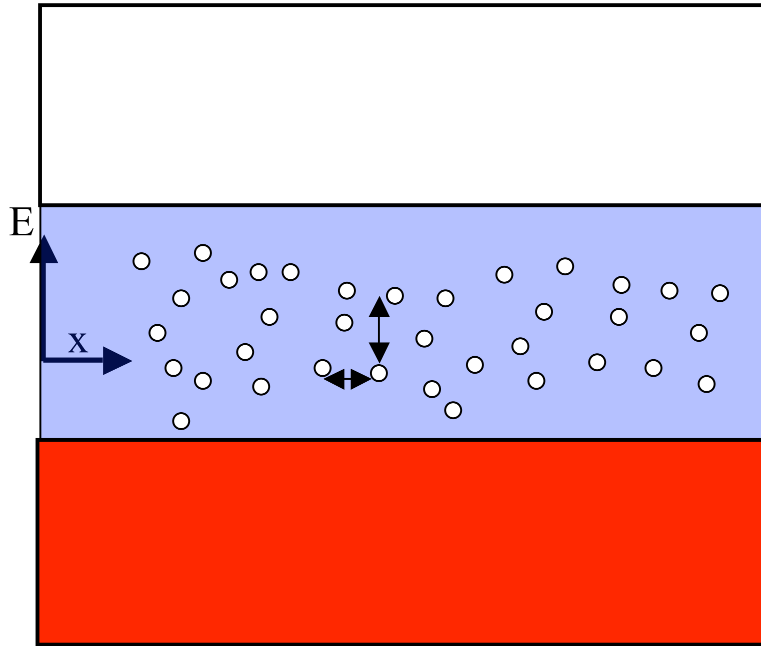

Fig 5.4: Schematic for variable range hopping. Vertical axis is energy and horizontal axis is position. White and red rectangles represent empty conduction and filled valence bands, respectively. Blue region depicts energy gap between bands and white dots are charge trap sites. In the absence of charge traps a pure gap exists. When charge traps are present electrons from valence band can traverse the gap by hopping through charge traps. This hopping depends on the distance and energetic spacing between the charge traps. At small separations or energetic differences hopping is facilitated.

Another transport mechanism is variable range hopping (VRH)[22], in which charge carriers are thermally activated to hop between localized states. This hopping depends on both the distance and difference in energy between the localized states (fig 5.4). For VRH in 2D, one expects $G \sim \exp[-(T_o/T)^{1/3}]$ where $k_BT_0=4a\kappa^2/\rho_0$, a is a dimensional less constant of order unity, κ the coefficient of the exponential decay of the localized state, and ρ_0 is the density of states at the Fermi level[22]. Using the WKB approximation, we

expect $\kappa \sim (2m^* V_2)^{1/2}/\hbar$, where m^* is the effective mass of charge carriers. From eq (5.2), $\rho_0 = \frac{2k}{\pi}\frac{\partial k}{\partial E}$ and $m^* = \hbar^2 / \frac{\partial^2 E}{\partial k^2}$, and ignoring the quadratic term in $v_F \hbar k / V_2$, we obtain $k_B T_0 \approx 4\pi a e V_2$.

To see if VRH can quantitatively account for the data, we fit the data in fig 5.3d to the expression $R = R_0 + A\exp\left[-\left(\frac{4\pi e}{k_B} a V_2\right)^{1/3}\right]$, where R_0 is the series resistance to account for the resistance of the non-top-gated region. Here we use $T_0/T=T_0$ because of our data's temperature independence below 1K. Satisfactory fit can be obtained by using the parameters R_0=5.3 kΩ, A=1.85x10^{-4} Ω, and a=0.32, in agreement with the expectation that a is a constant of order unity. This excellent agreement between VRH model and our data strongly suggests a successful band gap opening in BLG, and transport via variable range hopping between localized states that lie within the gap or are formed from disorder-induced charge puddles. Also, as shown in the next section, we observe the localized states in B, similar to those in SLG discussed in chapter 4. These charge traps appear to be the nefarious elements that reduce the electric field-induced band gap in substrate supported BLG device.

5.4 Two gates are better than one: *B*=8T

5.4.1 Edge state equilibration in BLG *pnp* junctions: *B*=8T

We now focus on the device behavior in high magnetic fields. In the QH regime, the non-uniform charge density gives rise to regions of different filling factors, and, for bi-polar (i.e. *pnp* or *npn*) junctions, conductance plateaus at fractional values of e^2/h. This was discussed for SLG *pnp* junctions in the previous chapter and were attributed to the mixing of edge states at the interfaces. Naively, one would hope these simple relations will continue to hold for BLG, with ν_1, ν_2=..-8, -4, 4, 8… instead of the SLG filling factors.

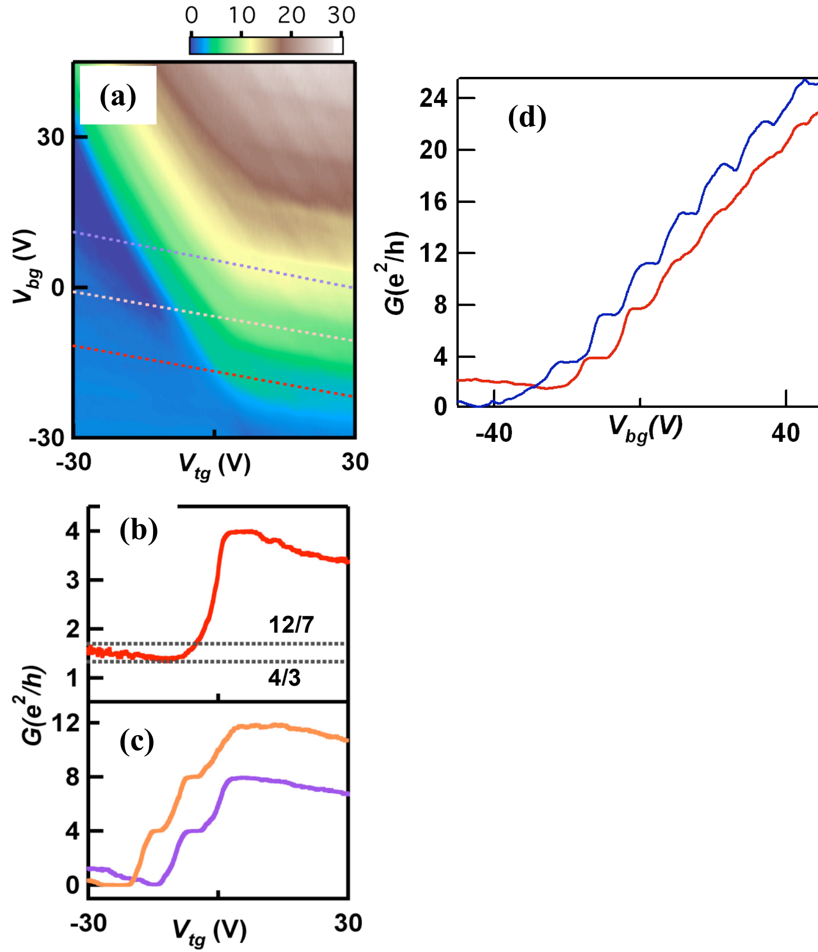

Fig 5.5: Transport measurements with two gates at *B*=8T. a.$G(V_{bg},V_{tg})$ of the device at B=8T. b. Line trace at ν_1=4, i.e., along the red dotted line in a. c. Line traces $G(V_{tg})$ at ν_1=8 (yellow) and ν_1=12 (purple). d.$G(V_{bg})$ with V_{tg}=0(red) and V_{tg}= (blue). Latter measurement displays resolution of several plateau that start to appear in first measurement.

Fig. 5.5a displays a typical data set $G(V_{tg},V_{bg})$ measured at B=8T. The conductance map appears as a plaque of adjoined parallelograms, corresponding to different ν_1 and ν_2 combinations, similar at first glance to that observed in SLG devices. First, the quality of the sample can be further accessed by focusing on fig 5.5b where two

line traces $G(V_{bg})$ are plotted in units of e^2/h at constant V_{tg}=0(red) and V'_{tg}~15(blue), respectively. Notably, quantum Hall states are better resolved or stabilized upon the application of additional V_{tg}, and an insulating state appears. This suggests the coordinate V'_{tg}~11V is the top gate dirac point. Impressively, robust conductance plateau quantization up to N=7 orbital levels are seen underscoring the high quality of our junctions.

Now focusing on $G(V_{tg})$ line traces in fig 5.5b, as V_{tg} increases from -30 or ν_2=~-15, G decreases from 1.6, reaching a minimum of 1.35 at ν_2=-4, then increases to a maximum plateau of 4 at ν_2=4, before decreasing again. From eq 4.8 and using the BLG single particle filling factors, the conductance values are predicted to be 12/7, 8/5, 4/3 and 4, for ν_2=-12, -8, -4 and 4, respectively, in good agreement with the data. Similarly, line traces at $\nu_1=8$ and 12 are shown in fig 5.5c, with conductance values reasonably accounted for by eq 5.1. We emphasize that this was the first time that the edge state equilibration was observed in bilayer *pnp* junctions, again underscoring the high quality of our junctions.

5.4.2 Two insulating states in BLG *pnp* junctions

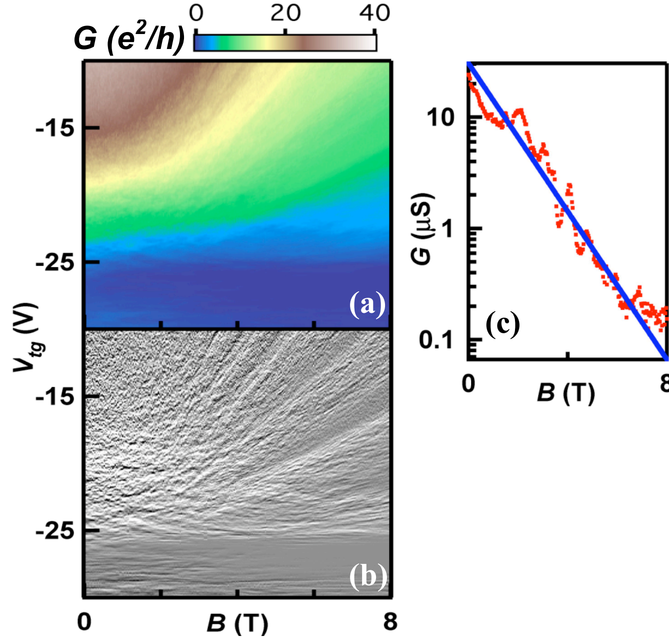

Fig 5.6: Insulating state induced by B. a. $G(V_{tg},B)$ at V_{bg}=19V. b. Data in a differentiated with respect to V_{tg}. c. Line trace $G(B)$ taken at V_{bg}=19V and V_{tg}=-27V. The blue line is a fit to an exponential function.

There is, however, one important discrepancy between eq 5.4 and our data – in fig 5.5c-d, G reaches a minimum of <10^{-7} S, or an insulating state, which cannot be obtained from (5.4) using ν_1, ν_2=…-8, -4, 4, 8…. This zero conductance state corresponds to ν_2=0, indicating opening of a band gap in the top gated region and lifting of the orbital LL degeneracy in this substrate supported device. A discussion on this state in a suspended device is provided in the next section. To further investigate this insulating state in this substrate supported device we measure the device conductance as a function of V_{tg} and B, at fixed V_{bg}=19V, shown in fig 5.6a. Significant fluctuations are visible, with same slopes in the V_{tg} –B plane as those of the adjacent plateaus fig 5.6b. As discussed in the last

chapter, these fluctuations arise from charging and localization from quantum dots in the bulk of the device, which consist of compressible regions that are surrounded by incompressible regions[12, 23]. Notably, fluctuations with zero slopes have been observed, again indicating the presence of the ν_2=0 state, which is not observed for SLG devices on substrate. These fluctuations also suggest significant spatial variations in density (up to $\pm\nu$) in the BLG sheet, and confirm the presence of electron and hole puddles near the charge neutrality point, that could give rise to localized states within the gap, as discussed above.

We now focus on the insulating ν_2=0 state. Fig 5.6c plots $R(B)$ at $V_{tg}=-27V$ and V_{bg}=19V, or equivalently, $n_2=10^{11}$ cm^{-2} and E=0.24 V/nm. At B=0, G~25 μS; with increasing B, G decreases exponentially with an exponent $c\approx$0.70, reaching 0.12μS at B=8T. Such exponential dependence of G on B has been observed in suspended bilayer devices[8], and is discussed in the next section in more detail.

Thus far we have observed two different insulating states in BLG. The first is induced by an external electric field at B=0, and the conductance decreases exponentially with E_2. The second insulating state occurs at finite electric *and* magnetic fields, and the conductance decreases exponentially with B. These two insulating states arise from the competition between the E and B. In principle, a transition between the layer polarized insulator and the QH ferromagnet insulator is expected to be observable[24] in low-disordered devices, with a slope E/B~10^7 V/m/T. In these devices, the relatively large number of disorder-induced impurity states smears any such transition. Hence, though the SiO_2 supported device with contactless topgate exhibits fantastic integer QH, the

correlated electron physics, especially phenomena at the CNP, requires a higher regime of sample quality.

Conclusion

By using bilayer graphene *pnp* junctions, we have demonstrated equilibration of QH edge states, insulating states induced by electric and/or magnetic fields, and transport via VRH in the gapped regime. Yet, to probe the fascinating correlated electron phenomena in BLG a new device architecture is needed.

Here I would like to make another comparison between dual gated substrate supported and suspended BLG devices. Differences between these two sample types were observed in section 5.1.1 for the finite carrier density regime. I will now focus on the distinctions between the two in the zero density regime. In fact, in this regime the suspended devices significantly outshine both the SiO_2 and BN sample types. This is due to the larger interaction parameter afforded by the suspended sample as seen in eq 3.1 from chapter two. Striking consequences of this are the intriguing ν=0 quantum Hall state, and the insulating states arising from the competition between E and B both manifest in a richer fashion.

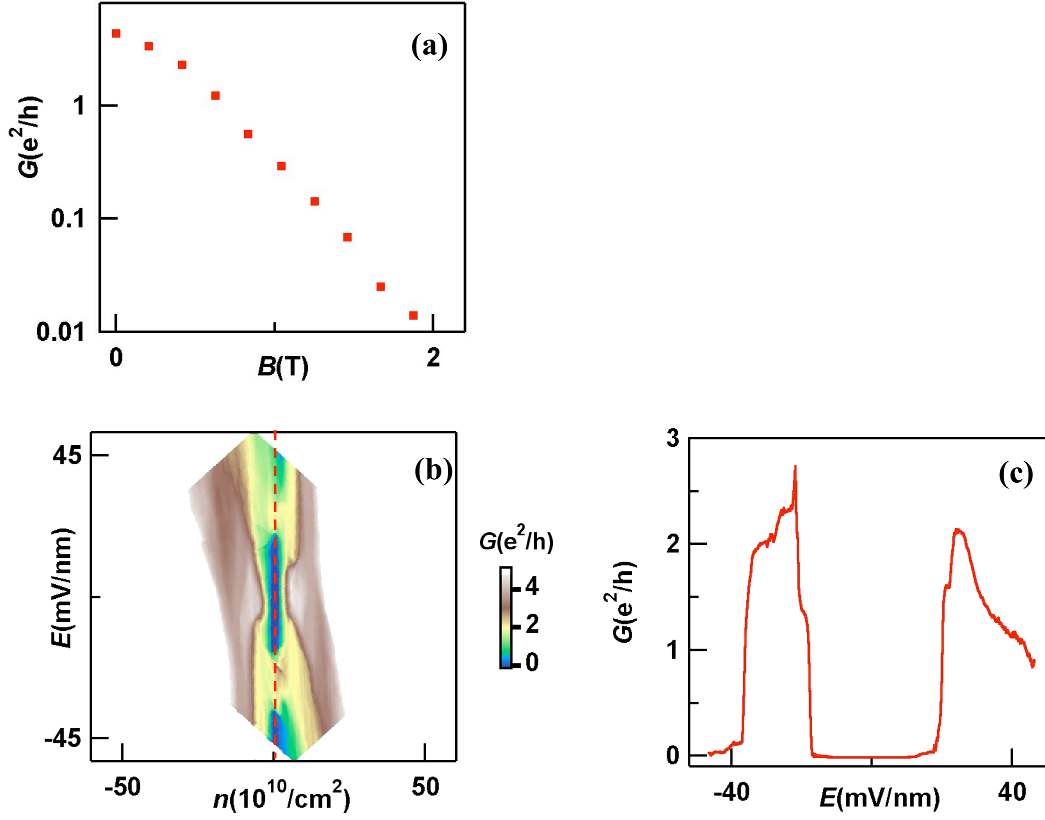

Fig 5.7: Transport measurements of a suspended BLG sample in finite *B*. a. $G(B)$ of the device at CNP. b. $G(E,n)$ at B=1.3T c. $G(E,n=0)$ from a. note two distinct insulating states not seen in fig 5.5a.

Figs 5.7a-c are data sets from a dual gated suspended device that display both of these phenomena. First, in fig 5.7a, which was taken at V'_{bg}~0 from the fan diagram in fig 5.2a , we see that the $G(B)$ decays much more quickly than that in fig 5.6b for the substrate supported sample. This correspondence between a sharper drop and improved quality reaffirms the many body nature of the observed behavior, and is consistent with previous experimental studies[7-9]. In fig 5.7b we utilize the additional gate in another clean

suspended sample to explore the effect of an $E_{\perp}$ in the QH regime, similar to the data shown in figs 5.6a and 5.5a for the substrate-supported sample. Focusing on the zero carrier density portion in fig 5.7a, we see two blue regions in the center separated by a yellow region as $E_{\perp}$ is increased from negative values to zero. These two blue features correspond to two distinct insulating states that arise at zero carrier density in the QH regime with an applied $E_{\perp}$. Fig 5.7c is a vertical line trace from fig 5.7b that plots $G(E)$ at n=0 that clearly depicts the two insulating states. This corresponds to a transition, likely between the layer polarized insulator and the QH ferromagnet insulator, which is smeared by disorder. Evidently, our suspended samples are clean enough allowing us to observe these physical phenomena. In light of this I conclude the section on dual gated substrate supported samples. In the next chapter we will focus on the correlated electron phenomena seen with the dual gated suspended samples. Specifically we will continue the discussion on competing symmetries, which is accessible in most of these samples, and describe the main result of the thesis, the observation of a spontaneous gap, which was only seen in the best samples, and is the culmination of the experimental work presented in the thesis.

References

1. G. Liu, J. Velasco, W. Z. Bao and C. N. Lau, Applied Physics Letters **92** (20), 203103 (2008).

2. J. Velasco, G. Liu, W. Z. Bao and C. N. Lau, New Journal of Physics **11**, 095008 (2009).

3. K. I. Bolotin, K. J. Sikes, Z. Jiang, M. Klima, G. Fudenberg, J. Hone, P. Kim and H. L. Stormer, Solid State Communications **146** (9-10), 351-355 (2008).

4. X. Du, I. Skachko, A. Barker and E. Y. Andrei, Nat. Nanotechnol. **3** (8), 491-495 (2008).

5. C. R. Dean, A. F. Young, MericI, LeeC, WangL, SorgenfreiS, WatanabeK, TaniguchiT, KimP, K. L. Shepard and HoneJ, Nature Nanotechnology **5** (10), 722-726 (2010).

6. Y. Barlas, R. Cote, K. Nomura and A. H. MacDonald, Phys. Rev. Lett. **101** (9), 097601 (2008).

7. Y. Zhao, P. Cadden-Zimansky, Z. Jiang and P. Kim, Phys. Rev. Lett. **104** (6), 066801 (2010).

8. B. E. Feldman, J. Martin and A. Yacoby, Nat. Phys. **5** (12), 889-893 (2009).

9. W. Z. Bao, Z. Zhao, H. Zhang, G. Liu, P. Kratz, L. Jing, J. Velasco, D. Smirnov and C. N. Lau, Physical Review Letters **105** (24), 246601 (2010).

10. B. Ozyilmaz, P. Jarillo-Herrero, D. Efetov, D. A. Abanin, L. S. Levitov and P. Kim, Physical Review Letters **99**, 166804 (2007).

11. J. R. Williams, L. DiCarlo and C. M. Marcus, Science **317**, 638-641 (2007).

12. J. Velasco, G. Liu, L. Jing, P. Kratz, H. Zhang, W. Z. Bao, M. Bockrath and C. N. Lau, Phys. Rev. B **81** (12), R121407 (2010).

13. A. F. Young and P. Kim, Nature Physics **5** (3), 222-226 (2009).

14. E. V. Castro, K. S. Novoselov, S. V. Morozov, N. M. R. Peres, J. Dos Santos, J. Nilsson, F. Guinea, A. K. Geim and A. H. Castro Neto, Phys. Rev. Lett. **99** (21), 216802 (2007).

15. E. McCann, Phys. Rev. B **74**, 161403 (2006).

16. J. B. Oostinga, H. B. Heersche, X. L. Liu, A. F. Morpurgo and L. M. K. Vandersypen, Nat. Mater. **7** (2), 151-157 (2008).

17. F. N. Xia, D. B. Farmer, Y. M. Lin and P. Avouris, Nano Lett. **10** (2), 715-718 (2010).

18. B. N. Szafranek, D. Schall, M. Otto, D. Neumaier and H. Kurz, Appl. Phys. Lett. **96** (11), 112103 (2010).

19. Y. B. Zhang, T. T. Tang, C. Girit, Z. Hao, M. C. Martin, A. Zettl, M. F. Crommie, Y. R. Shen and F. Wang, Nature **459** (7248), 820-823 (2009).

20. K. S. Novoselov, E. McCann, S. V. Morozov, V. I. Fal'ko, M. I. Katsnelson, U. Zeitler, D. Jiang, F. Schedin and A. K. Geim, Nat. Phys. **2** (3), 177-180 (2006).

21. E. McCann and V. I. Fal'ko, Phys. Rev. Lett. **96** (8), 086805 (2006).

22. V. Ambegaokar, B. I. Halperin and J. S. Langer, Physical Review B **4** (8), 2612 (1971).

23. S. Branchaud, A. Kam, P. Zawadzki, F. M. Peeters and A. S. Sachrajda, Physical Review B **81** (12), R121406 (2010).

24. R. Nandkishore and L. Levitov, preprint, arXiv:1002.1966v1001 (2010).

Chapter 6: BLG has an intrinsic gap at the CNP

Introduction:

In this chapter I will discuss our transport measurements on ultra-clean double-gated BLG. These studies utilized fabrication and current annealing methods discussed at the end of chapter three to produce unprecedented high quality dual gated samples. The first sets of measurements were in high *B*, similar to those described in the previous chapter on substrate supported BLG *pnp* junctions. However, this chapter will deal mainly with devices where the top gate is global. A new element in this study was the source-drain bias as a spectroscopic tool, which was used to resolve a gap of ~2 meV at the CNP. Implementing this measurement tool with a simultaneous dual gate sweep we found the gap can be closed by an electric field $E_{\perp}$~ 15 mV/nm but increases monotonically with a magnetic field *B*, with an apparent particle-hole asymmetry above the gap. These data sets were the first spectroscopic mapping of the ground states in BLG in the presence of both applied electric and magnetic fields.

In the first experimental reports [1,2], which hinted at an ordered state in BLG, the minimum conductivity σ_{min} was a non-monotonic function of $E_{\perp}$, with a value ~60 μS at $n= E_{\perp}=0$, though the experimental evidence for spontaneous gaps in this work was not conclusive. Following works using single-gated samples report either a very high minimum conductivity σ_{min} ~$7e^2/h$, which is attributed to the presence of a gapless nematic phase [3], or low σ_{min}, which hinted at a gapped state[4]. Our work unequivocally established the presence of a gap at the CNP, and was the first to investigate its broken symmetries.

6.1: A second look at the band structure of BLG

Table 6.1. Attributes of possible ordered states in BLG at n=$E_{\perp}$=0.

	Nematic Order	QAH	QSH	LAF	CLP (QVH)
Gapped?	No	Yes	Yes	Yes	Yes
2- terminal σ_{min}	finite	$4e^2/h$	$4e^2/h$	0	0
Broken Symmetries	in-plane rotation	time reversal; Ising Valley	spin rotational; Ising Valley	time reversal; spin rotation	inversion

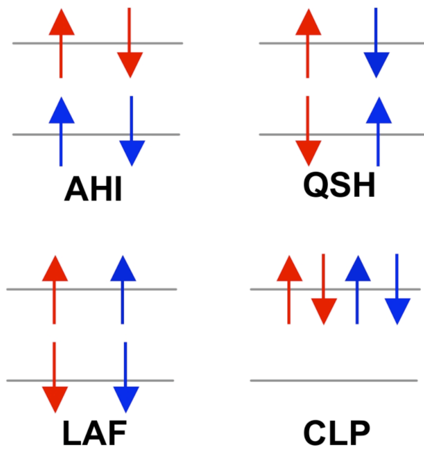

Fig 6.1: Spin-valley configurations of the electrons in BLG for several possible phases. Here red (blue) arrows indicate electrons from the *K* (*K'*) valley.

As discussed in chapter two the single-particle band structure of bilayer graphene resembles that of a gapless semi-conductor, with parabolic valence and conduction bands touching at the highly symmetric *K* and *K'* Dirac points. When weak remote hopping processes are included (γ_3), the momentum space band-touching point splits in four[5] and Liftshitz transitions occur at low carrier densities[6](supplementary information). As was discussed in chapter two theoretically, and shown in the previous chapter with our BLG

pnp junctions, a perpendicular electric field $E_\perp$ will induce a band gap that increases with increasing $E_\perp$, saturating at ~0.3 eV,[5, 7, 8] and the conduction band will adopt a "Mexican hat" shape. When electron-electron interactions are included bilayer graphene is expected to be unstable to broken-symmetry states that can be viewed as layer-pseudospin ferromagnets.[9]

Under these considerations bilayer graphene near the charge neutrality point has been a discussed using a two-band model[10], with the broken-symmetry state quasiparticle Hamiltonian

$$H = -\left(\frac{p^2}{2m^*}\right)\left[\cos(2\phi_{\mathbf{p}})\sigma_x \pm \sin(2\phi_{\mathbf{p}})\sigma_y\right] - \mathbf{\Delta}\cdot\boldsymbol{\sigma} \ . \quad (6.1)$$

The first term in eq.(6.1) is the quadratic band Hamiltonian, where $\tan\phi_{\boldsymbol{p}}=p_y/p_x$, $\boldsymbol{p}$ is the angular momentum, m^* is the effective mass of the carriers, σ is a Pauli matrix vector that acts on the layer degree of freedom, Δ represents the order parameter of the broken symmetry state, and the ± signs refers to the K and K' valleys, respectively. It has been variously predicted[9-13] to be oriented in the $\pm z$ direction, yielding gapped isotropic states with large momentum-space Berry curvature[10], or in the xy plane, yielding gapless anisotropic (nematic) states[14, 15] with vanishing Berry curvatures. A variety of distinct but related massive states occur, depending on the relation of the sign of Δ_z to spin and valley[10]. The broken symmetries and two terminal σ_{min} of some theoretically proposed bilayer graphene states are summarized in Table 6.1 and their configuration in terms of the available degrees of freedom, spin, valley and layer are depicted in fig 6.1. Their

relationship between Δ and quasiparticle electronic properties is discussed in technical detail in[6](supplementary information).

6.2 Device characterization – A tale of two device mobilities

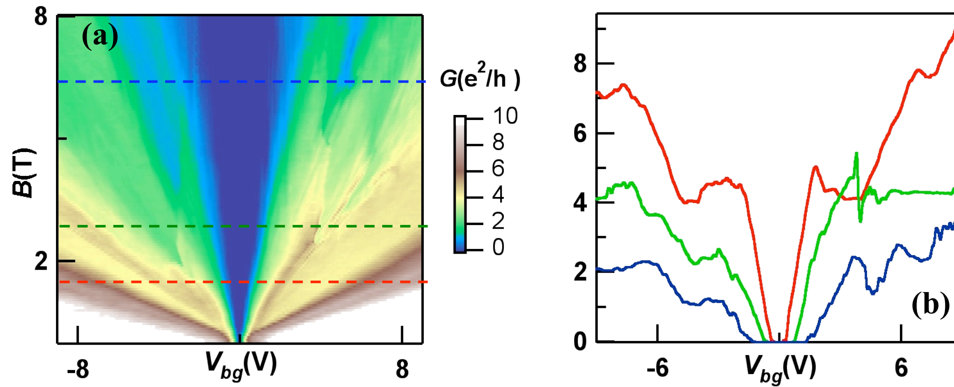

Fig 6.2: Transport measurements in finite B and at 260mK. a. Differential conductance G=dI/dV vs. B and V_{bg} showing the Landau fan diagram. b. Line traces $G(V_{bg})$ along the dotted line in c. at B=1.3, 2.8 and 6T, respectively.

Our devices consist of exfoliated bilayer graphene sheets with Cr/Au electrodes suspended between Si/SiO_2 back gates and metal top gates, which follow the procedures outlined at the end of chapter three. The devices' field effect mobility $\mu_{FE}=1/e(d\sigma/dn)$, typically calculated by taking the slope of the $\sigma(V_{bg})$ curves between $n=0$ and $n\sim4x10^{10}$ cm^{-2}, is ~80,000 – 100,000 cm^2/Vs after the current annealing procedure detailed in chapter three. Here σ is the device conductivity, and e is electron charge. By tuning voltages applied to the back gate V_{bg} and top gate V_{tg}, we can independently control $E_\perp$ and the charge density n induced in the bilayer as discussed in the previous chapter. Notably, we find that this capability is of utter importance, since even a small amount of

$E_{\perp}$ or n, which may be inadvertently present in single-gated devices, can obscure the insulating state and significantly elevate σ_{min}. This will be discussed in detail in the next chapter.

Fig 6.2a plots the two-terminal differential conductance $G=dI/dV$ at $V=0$ (color) *vs.* V_{bg} and B and reveals Landau levels as colored bands radiating from the charge neutrality point and $B=0$. Line traces of $G(V_{bg})$ at constant B exhibit conductance plateaus with values near 0, 1, 2, 3, 4 and 8 e^2/h (fig 6.2b), indicating that the 8-fold degeneracy of the lowest Landau level (LL)[16-19] is broken. Observation of these plateaus at relatively low B underscores the high quality of the device. This data set is from a dual gated suspended BLG device that we focus on for the rest of this chapter.

Close inspection of fig 6.2b reveals that the $\nu=0$ gap appears to persist down to $B=0$. Indeed, at $B=0$, the $G(E_{\perp},n)$ plot shows a local minimum at $n=E_{\perp}=0$ (fig 6.3b). This contradicts the single-particle picture, which predicts a gap that is roughly linear in $E_{\perp}$, hence a monotonically decreasing $G(|E_{\perp}|)$ with a local maximum at $n=E_{\perp}=0$, as shown in fig 6.3a. The latter data set is from another dual gated suspended BLG sample that has lower mobility and larger CNP offset. These two factors and their effects on the transport properties of BLG samples will be discussed in greater detail in the next chapter. The dramatic differences between the two devices suggest a breakdown of the non-interacting electron picture.

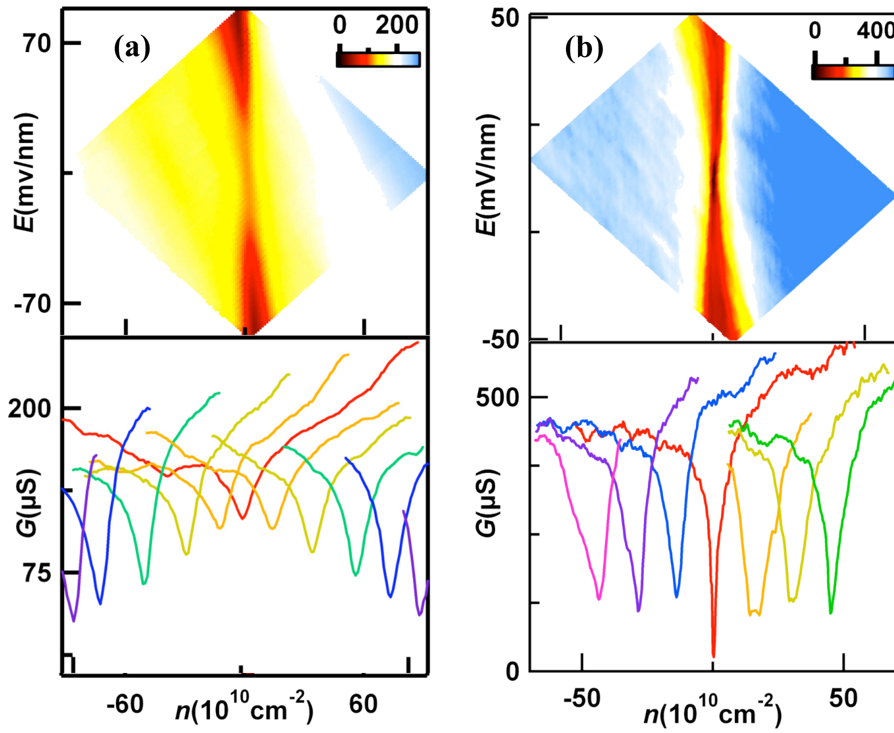

Fig 6.3:Dual gate transport data at *B*=0 and *T*=300mK for two different devices. a**.** *G(n, E)* and line traces *G(n)* at *E*=85, 71, 57, 42, 28, 14, 0, -14, -28, -42, -57, -71, -85 mV/nm, respectively (left to right). The line traces are laterally offset for clarity. b. *G(n, E)* and line traces *G(n)* at *E*=-37.5, -25, -12.5, 0, 12.5, 25 and 37.5 mV/nm, respectively (left to right). The line traces are laterally offset for clarity.

6.3 Bias-dependent measurements

6.3.1 Bias-dependent measurements at B=0T

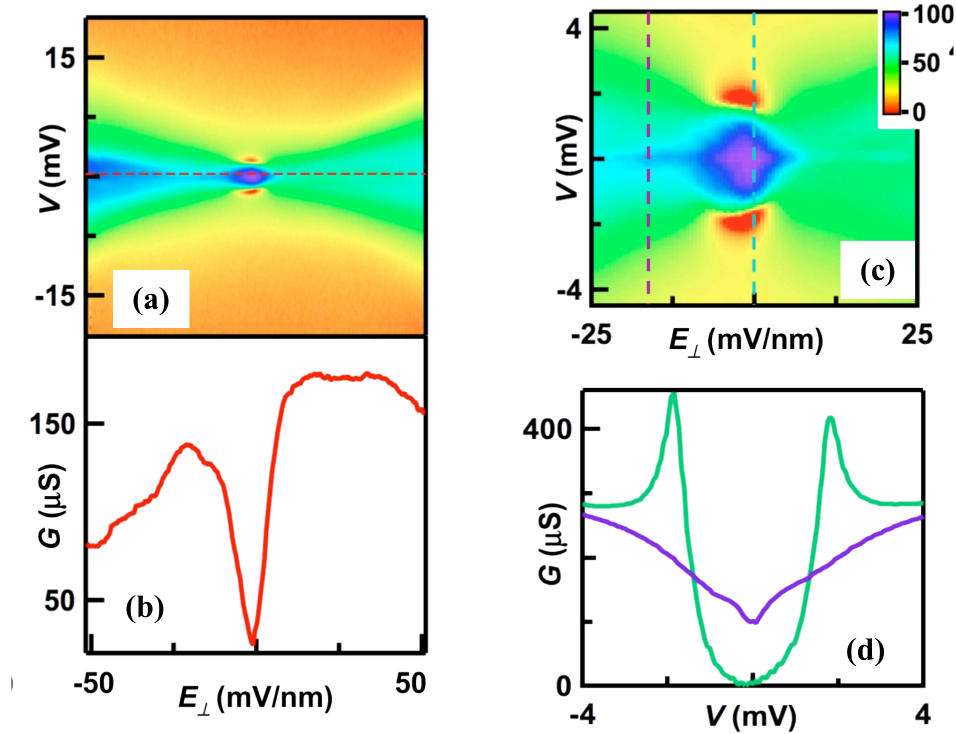

Fig 6.4: Bias measurement at *B*=0 and *T*=300mK with two gates. a-b. Large range $G(V, E_{\perp})$ and line trace $G(E_{\perp})$ at n=0. b. High resolution $G(V, E_{\perp})$ for small bias range at n=0. d. Line traces $G(V)$ along the dotted lines in b at $E_{\perp}$ =0 and -15 mV/nm, respectively.

To investigate the resistive state at the charge neutrality point spectroscopically, we measure G as a function of source-drain bias V and $E_{\perp}$ while keeping n=0. This measurement technique is a departure from the studies performed in chapters four and five on the substrate supported devices. Typical spectroscopic transport measurements are performed using tunnel probes, whereas our devices have highly transparent contacts.

Because they are in the quasi-ballistic limit, we nevertheless anticipate spectroscopic resolution. Our non-linear transport data is summarized in fig 6.4a-d. The most striking feature is the region of dark blue/purple at the center of the plots, corresponding to the highly resistive state at small $E_{\perp}$. At $n=E_{\perp}=V=0$, the device is *insulating*, with G_{min}<~0.5 μS (fig 6.4d, green curve). We note that this insulating state is observed only in high mobility samples realized after current annealing, and then only at low sweeping rates, and after careful optimization of the measurement setup to eliminate spurious voltage noise. These additional factors will be discussed in section 6.5. As V increases, G remains approximately 0 until it increases abruptly at V~±1.9 mV, reaching sharp peaks before it decreases again to ~300 μS.

The $G(V)$ curve bears a striking resemblance to the tunneling density of states of a gapped insulator, and strongly suggests the formation of an ordered phase with an energy gap E_{gap}~1.9 meV. This value is further corroborated by temperature dependent measurements of σ_{min} for a sample in the gapped regime, and by the n-dependence of the gap, both subjects that will be discussed in greater detail in the next chapter. Importantly, this gap can be closed by application of $E_{\perp}$ of *either* polarity: G increases with $|E_{\perp}|$ (fig 6.4c); upon application of moderate $E_{\perp}$ >~ 15 mV/nm, the gap-like structure completely vanishes and the $G(V)$ curve becomes approximately V-shaped, with a finite conductance minimum of ~100 μS at $n=0$ (fig 6.4d, purple curve). Finally, for sufficiently large $E_{\perp}$, $G(V=0)$ start to decrease with increasing $E_{\perp}$ (fig 6.4c), reverting to single-particle behavior.

6.3.2 Bias measurements at finite B

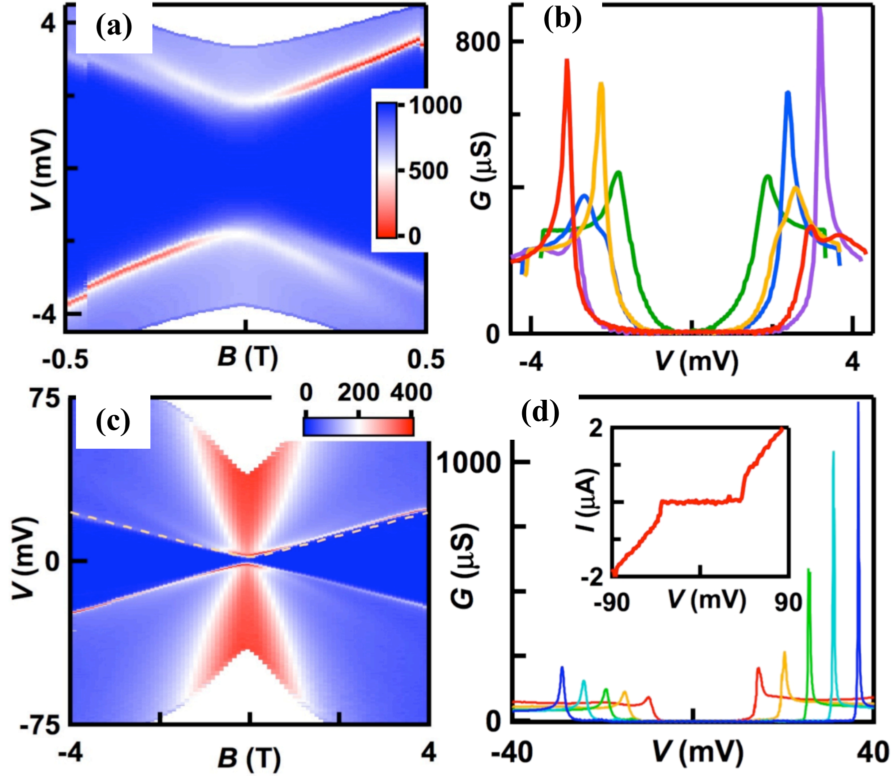

Fig 6.5: Transport data in magnetic field at *n*=0 and $E_{\perp}$=0. a-b. $G(V,B)$ and line traces $G(V)$ at B=-0.4 (red), -0.2 (orange), 0 (green), 0.2 (blue) and 0.4 T (purple), respectively. c. Large range $G(V,B)$. The dotted line plots Eq. (2) with Δ_o=1 meV, and a=5.5 meV/T. d. Line traces $G(V)$ at B=2 (red), 3 (orange), 4 (green), 5(cyan) and 6T (blue). Inset : Current-voltage characteristics at B=8T.

Such an insulating state, which is the most salient experimental feature, is only observed in devices with the highest mobility. To gain further insight, we study its evolution with B (fig 6.5a-d). When B increases from 0, the gapped phase continuously evolves into a bilayer insulating state at filling factor ν=0 similar in nature to the

insulating state studied in chapter 5 for substrate supported BLG *pnp* junctions, with the sharp peaks in G becoming sharper and more dramatic. The magnitude of the gap, as measured from the bias values of the sharp peaks in G, is well-described by,

$$E_{gap} = \Delta_o + \sqrt{a^2 B^2 + \Delta_o^2} \qquad (6.2)$$

where $|\Delta_0|$ ~1 meV obtained from Fig. 5a, and a=5.5 mV/T. For B>0.5T, E_{gap} ~ 5.5 B (meV/T) which is much larger than the single-particle gap induced by Zeeman splitting, ~0.1 meV/T. We note that our observation of a linear dependence of $\Delta_{\nu=0}$ on B is consistent with previous reports[11, 18], but with a significantly larger magnitude, due to the superior quality of our device. Another noteworthy feature of fig 6.5 is that the conductance peaks at positive and negative bias voltages, which we associate with conduction and valence band edges, are highly asymmetric. Because the device's current-voltage characteristics are symmetric in V outside the gapped region, this observed asymmetry, which increases with increasing B, and reverses when B changes sign, does not arise from contact asymmetry, nor can it be accounted for by the Onsager relation since the measurements are done in the non-linear regime. Rather, it suggests particle-hole asymmetry in the device.

6.4 Sensitive gap measurements

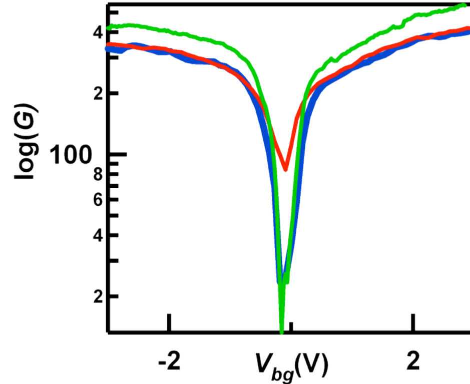

Fig 6.6: G (V_{bg}) with different measurement configurations. Red curve is at a sweeping rate of 0.1V/step in V_g before the correction of ~0.4 mV dc offset. Blue is after correcting for the offset but still at the same sweeping speed. Green is after dc-offset correction and with a sweeping rate of 0.03 V/step.

We find that the conductance of the insulating state at $n=E_{\perp}=0$ is highly sensitive to noise, circuit optimization and sweeping rate. For instance, there is typically a small dc offset (~0.3-1 mV) in our voltage bias. Generally such a small offset has minimal effect on differential conductance measurements when the device is conductive; however, in the insulating regime, even a small offset induces considerable increase in G. The value of $G(n=E_{\perp}=0)$ is minimized after eliminating the dc offset, after careful grounding, and when the sweeping rate of parameters such as V_g is reduced.

These effects are illustrated in fig 6.6. The red curve shows the $G(V_g)$ behavior which is measured at a sweeping rate of 0.1V/s in V_g before the correction of ~0.4 mV dc offset. Here the minimum conductance G_{min} is ~76 μS. After correcting for the offset but

still at the same sweeping speed, G_{min} decreases to 26 μS (blue curve). With a decrease in the sweeping speed to 0.03 V/step, G_{min} decreases further to 12 μS (green curve). In all these measurements, the top gate voltage is kept at 0. When the top gate is tuned to the CNP, ~ -0.1V, and taking all the precautions, the minimum conductance measured is ~ 1 μS, as shown in fig 6.2 in the main text.

Using this optimized circuit and slower sweeping rates we have studied a number of single-gated and double-gated suspended BLG devices. At $n=E_{\perp}=0$, while almost all devices show a resistive state (defined as σ_{min}<50 mS), insulating states (σ_{min}<10 mS) are only observed in devices with very high mobility and $|V_g^D|<0.1$, where V_g^D is the gate voltage value at which G_{min} is observed.

Further insight into the ground state in charge neutral BLG is attained by comparing the $G(V)$ curves of these devices. Fig 6.7a plots $G(V)$ at different values of $E_{\perp}$ for device 1 with an insulating state. At $E_{\perp}=0$, the $G(V)$ curve is U-shaped and resembles the density of states of a gapped phase, with σ_{min}~0 and sharp conductance peaks at ±~2 mV. When $E_{\perp}$ is increased, the sharp peaks become less prominent and σ_{min} increases to 28 μS; finally, at sufficiently large $E_{\perp}$, the conductance peaks disappear, the $G(V)$ curve becomes V-shaped and the device is conductive.

In comparison, fig 6.7b-c displays the $G(V)$ curves for 2 additional devices with relatively low conductance (~5 and 36 μS) at the CNP. We note that the curves resemble those from device 1 at finite values of $E_{\perp}$. This observation strongly suggest that the insulating state is the intrinsic ground state of charge neutral BLG; in devices with moderate mobility or $|V_g^D|>0.1$, unintentional doping or electric fields may be introduced

by charged impurities, thus obscuring the insulating state and giving rise to a finite conductance. A thorough study on the insulating state's dependence on mobility and CNP offset is presented in the next chapter.

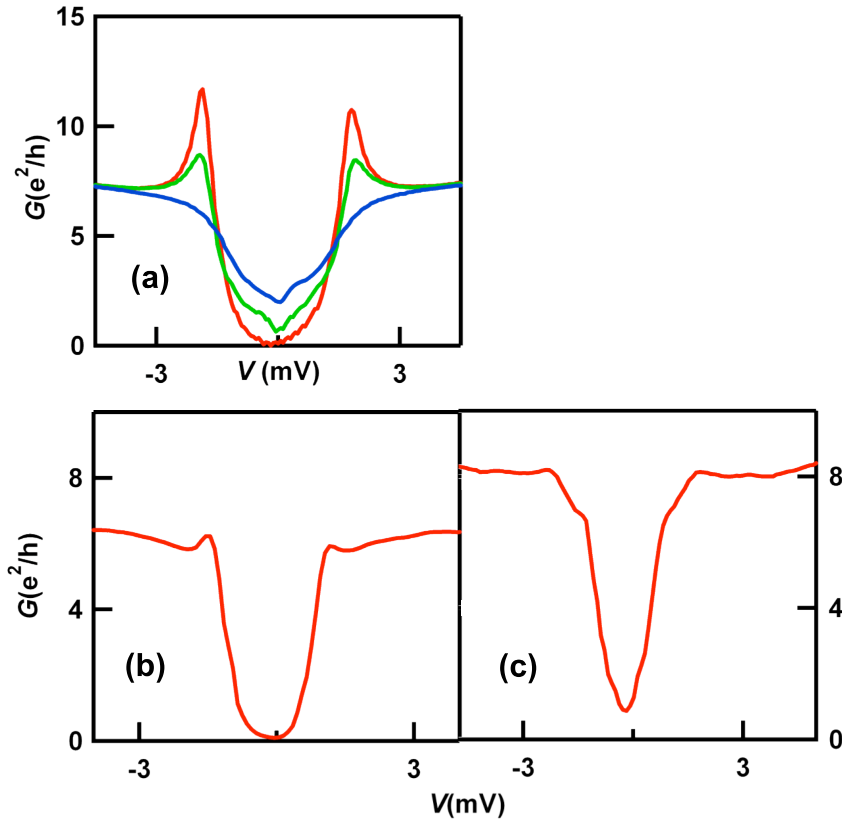

Fig 6.7: **Transport Data of BLG devices**. a $G(V)$ for the device of the main text at $E_{\perp}$=0 (red), $E_{\perp}$=-5mVnm (green) and $E_{\perp}$=-9mV/nm (blue), (b-c) $G(V)$ for two additional devices at CNP and $E_{\perp}$=0.

6.5 Discussion

To summarize our experimental findings: (A) ultra-clean bilayer graphene is insulating at $n=B=E_\perp=0$, with an energy gap $E_{gap} \sim 1.9$ meV that can be closed by $E_\perp$ of either sign; (B) the energy gap evolves in B following eq (6.2); and (C) this state is apparently particle-hole asymmetric. These observations provide much insight into the nature of bilayer graphene's symmetry-broken ground state. For instance, observation (A) rules out gapless ordered states[14, 15]. For the gapped states, the symmetric dependence on $E_\perp$ indicates that there is no net charge imbalance between the two layers, thus excluding states with net spontaneous layer polarization like the charge layer polarized (CLP) state depicted in fig 6.1. We note that the charge layer polarized phase, also called the quantum valley Hall state (QVH), is expected to be the ground state under sufficiently large $E_\perp$, as observed experimentally.

Thus, among the proposed states, we are left with the 3 gapped state candidates that have no overall layer polarization. Given the flavor (spin-valley) symmetries, electrons in each layer can be valley polarized and form a quantum anomalous Hall insulator (QAH)[10, 11, 20, 21], spin polarized to form a layer antiferromagnet (LAF)[10, 22], or neither to form a quantum spin Hall (QSH) insulator[10, 11, 23-25] (fig 6.1b). Mean-field calculations indicate that these states are comparable[12] in energy and that the charge layer polarized state is stabilized by electric fields $E_\perp \sim 5\text{-}20$ mV/nm[11, 12] , in agreement with the critical field value of ~ 15 mV/nm observed experimentally. For all three states, eq. (6.1) predicts a gap within each valley with a B-dependence described by eq. (6.2), with

parameters $\Delta_z = \Delta_0$ and $a = \sqrt{2}\hbar e/m^*$. From a=5.5 meV/T, we obtain $m^* = 0.03\ m_e$ where m_e is electron rest mass, in good agreement with other measurements[26, 27] of the interaction enhanced[28, 29] quasi-particle mass near the bilayer graphene charge neutrality point. Thus our observations demonstrate unequivocally the symmetry-broken gapped phase in charge neutral graphene.

Nailing down the exact phase of the ground state, however, is considerably more difficult. Eq. (6.2) applies to charges in a single valley. If we assume ideal coupling of both layers to electrodes, none of the candidate states can account for all aspects of our data. The LAF state would have a *B*-independent gap. Both quantum anomalous Hall and quantum spin Hall states are ruled out by their topologically protected edge states which are expected to yield two-terminal conductances ~ $4e^2/h$ or 154 μS. The quantum anomalous Hall state is also ruled out because the density position of its gap is expected to deviate from the charge neutrality point in a finite magnetic field, following lines with ν=4; yet it is the only state with particle-hole asymmetry and valley-indirect gaps that are in agreement with Eq. (6.2).

On the other hand, we note that since most of the metals are deposited on the top layer and contact the bottom layer only via the edges, the electrodes could couple preferentially to one layer (or equivalently, one valley). In this case, the LAF state, which is the only proposed insulating phase, can account for both observations (A) and (B). Since the absence of edge states is the most robust experimental signature, our observations are most consistent with the LAF state, though the particle-hole asymmetry in *B* is not explained within this picture. It is thus possible that a new ground state that

has not been theoretically proposed underlie our observations [30].

Further theoretical and experimental work will be necessary to ascertain the nature of the gapped state and achieve full understanding of our observations. Nonetheless, at the time of the writing of this thesis several transport studies have reproduced this gap with approximately the same size. One recent study performed a parallel B measurement and observed a reduction of the measured conductance with increasing parallel B[31]. This observation is consistent with the LAF state.

The spontaneous gap in ultra clean BLG represents inquiry on the frontier, and is an intriguing avenue for more investigation. A promising direction is the study of this gap using optical methods[32] or a local probe method such as STM.

6.6 Bias measurement of the ν=0 quantum Hall state

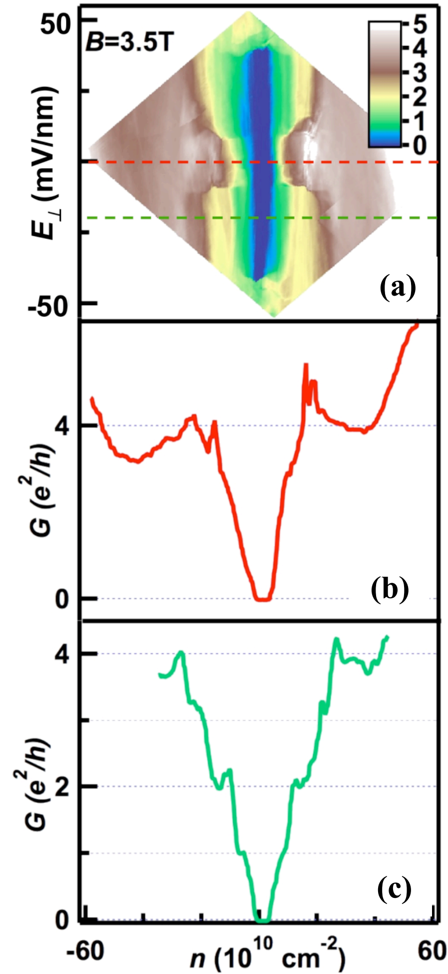

Fig 6.8: Transport data at constant B. a. $G(n, E)$ at B=3.5T. b-c, Line traces $G(n)$ along the dotted lines in a at E =0 and -20 mV/nm.

Lastly, we focus on the quantum Hall states in external electric and magnetic fields and further establish the bias-dependent measurement as a spectroscopic tool. This section focuses on bias measurements performed at the CNP in the presence of both E and B fields, in chapter nine we will discuss a similar measurement scheme at finite

densities, which is used to acquire the energy gaps of integer quantum Hall states. Fig 6.8a plots G vs. $E_\perp$ and n at constant B=3.5T. As shown by the line traces in fig 6.8b-c, at $E_\perp$=0, only the ν=0 and ν=4 quantum Hall plateaus are observed; at finite $E_\perp$, all integer quantum Hall states between 0 and 4 are resolved, demonstrating degeneracy-lifting by the perpendicular electric field.

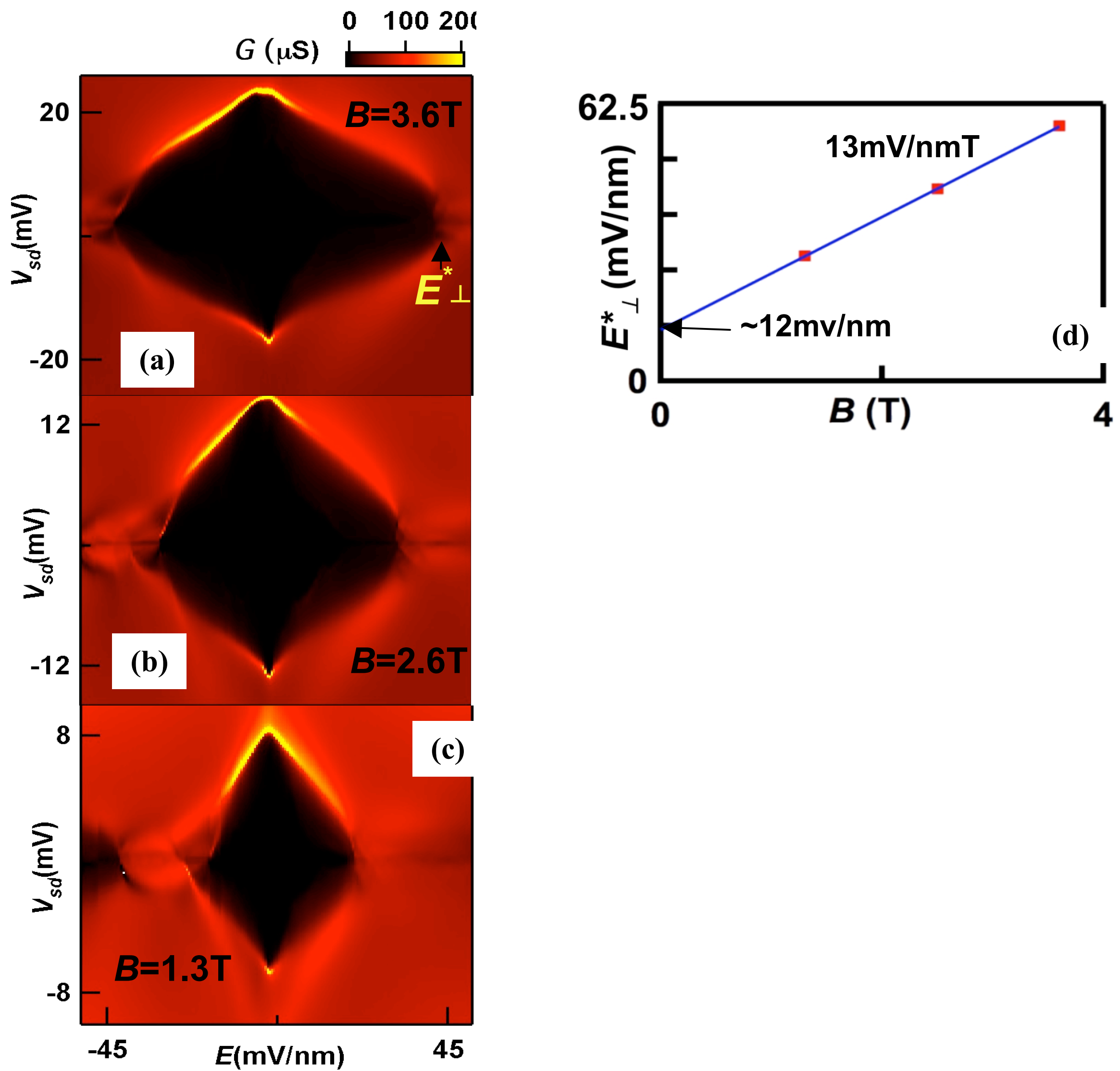

Fig 6.9: Bias measurements with applied fields. a-c. $G(V,E_\perp)$ at B=1.3T, 2.6T and 3.6T, respectively. d. Critical electric field $E^*_\perp$ vs. B. The blue line is a best-fit to data, with a slope of 12.7 mV/nm/T.

We now focus on bias measurements performed on the vertical contour where n=0 from fig. 6.8. The spectroscopic data $G(V,E_\perp)$ at constant B is plotted in fig 6.9(a-b), where the gap $\Delta_{\nu=0}$ is diamond-shaped: its magnitude decreases linearly with applied $E_\perp$ of either polarity, until it is completely closed at a critical field $E_\perp^*$. Fig 6.9c plots $E_\perp^*$ obtained at 3 different B values. The data points fall on a straight line, with a best-fit slope of ~ 12.7mV/nm/T. Extrapolation of the best-fit line to $B=0$ yields a finite $E_\perp^*$ intercept ~ 12.5 mV/nm, which agrees with the critical $E_\perp$ value estimated from the zero B field data in fig 6.4b. Both the slope and the finite $E_\perp^*$ intercept are consistent with those measured from the movement of the ν=4 plateau as functions of $E_\perp$ and B[1], also shown in fig 6.10. Taken together, our data confirms that the bias-dependent measurement provides a spectroscopic determination of the ν=0 gap, and indicates a transition between 2 different quantum Hall ferromagnetic phases[33, 34], similar bias dependent measurements for broken symmetry QH states will be discussed in chapter nine.

Finally, a recent theoretical analysis[33, 34] suggests the nature of these two phases is a canted antiferromagnetic and a charge layer-polarized state. Such a finding is consistent with our conclusion from section 6.4 of the observation of the LAF phase at $B= E_\perp=n=0$.

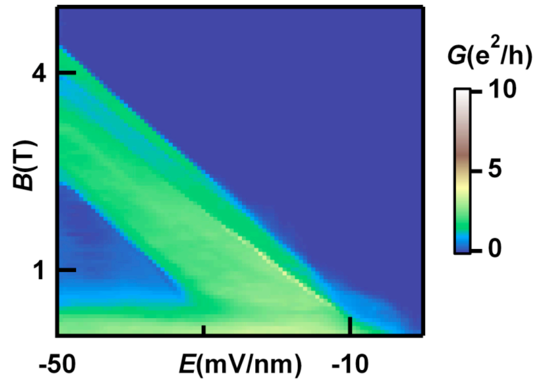

Fig 6.10: *G*($E_\perp$,*B*) at 250mK. The diagonal green band is a conductive segment that separates the 2 insulating (blue) regions, with a slope of ~10.5 mV/nm/T.

Conclusion:

In summary, we demonstrate the formation of a gapped, insulating phase in charge neutral bilayer graphene. The gap is closed by application of a perpendicular *E* field of either polarity and evolves into a ν=0 state in a magnetic field with a gap of ~5.5 meV/T, with an apparent particle-hole symmetry. Our work, together with prior and contemporary studies[1-4, 35], contribute towards understanding the rich interaction-driven physics in bilayer graphene. Further theoretical and experimental work, *e.g.*, scanning tunneling microscopy or optical Kerr effect measurements, is warranted to ascertain the nature of the gapped states.

Soon after this work Wenzhong Bao and I pooled our data sets together from several samples that we each fabricated. This combined data contains ~10 gapped insulating devices, hence further establishing the presence of an interaction gap at the

CNP in BLG. By investigating the temperature dependence of these insulating devices at the CNP we found evidence for a phase transition, from an insulating state to a conductive state. Subsequently, by utilizing our insulating samples with dual gates we discovered that disorder, E and n tune this transition. The next chapter will cover this nice study.

References

1. R. T. Weitz, M. T. Allen, B. E. Feldman, J. Martin and A. Yacoby, Science 330 (6005), 812-816 (2010).

2. J. Martin, B. E. Feldman, R. T. Weitz, M. T. Allen and A. Yacoby, Phys. Rev. Lett. 105 (25), 256806 (2010).

3. A. S. Mayorov, D. C. Elias, M. Mucha-Kruczynski, R. V. Gorbachev, T. Tudorovskiy, A. Zhukov, S. V. Morozov, M. I. Katsnelson, V. I. Fal'ko, A. K. Geim and K. S. Novoselov, Science 333 (6044), 860 (2011).

4. F. Freitag, j. Trbovic, M. Weiss and C. Schonenberger, Phys. Rev. Lett. 108, 076602 (2012).

5. E. McCann and V. I. Fal'ko, Phys. Rev. Lett. 96 (8), 086805 (2006).

6. J. Velasco, L. Jing, W. Bao, Y. Lee, P. Kratz, V. Aji, M. Bockrath, C. N. Lau, C. Varma, R. Stillwell, D. Smirnov, F. Zhang, J. Jung and A. H. MacDonald, Nature Nanotechnol. 7, 156 (2012).

7. H. K. Min, B. Sahu, S. K. Banerjee and A. H. MacDonald, Phys. Rev. B 75 (15), 155115 (2007).

8. T. Ohta, A. Bostwick, T. Seyller, K. Horn and E. Rotenberg, Science 313 (5789), 951-954 (2006).

9. H. Min, G. Borghi, M. Polini and A. H. MacDonald, Phys. Rev. B 77 (4), 041407 (2008).

10. F. Zhang, J. Jung, G. A. Fiete, Q. A. Niu and A. H. MacDonald, Phys. Rev. Lett. 106 (15), 156801 (2011).

11. R. Nandkishore and L. Levitov, preprint, arXiv:1002.1966v1001 (2010).

12. J. Jung, F. Zhang and A. H. MacDonald, Phys. Rev. B 83 (11), 115408 (2011).

13. F. Zhang, H. Min, M. Polini and A. H. MacDonald, Phys. Rev. B 81 (4), 041402 (R) (2010).

14. Y. Lemonik, I. L. Aleiner, C. Toke and V. I. Fal'ko, Phys. Rev. B 82 (20), 201408 (2010).

15. O. Vafek and K. Yang, Phys. Rev. B 81 (4), 041401 (2010).

16. Y. Barlas, R. Cote, K. Nomura and A. H. MacDonald, Phys. Rev. Lett. 101 (9), 097601 (2008).

17. Y. Zhao, P. Cadden-Zimansky, Z. Jiang and P. Kim, Phys. Rev. Lett. 104 (6), 066801 (2010).

18. B. E. Feldman, J. Martin and A. Yacoby, Nat. Phys. 5 (12), 889-893 (2009).

19. W. Z. Bao, Z. Zhao, H. Zhang, G. Liu, P. Kratz, L. Jing, J. Velasco, D. Smirnov and C. N. Lau, Physical Review Letters 105 (24), 246601 (2010).

20. F. D. M. Haldane, Physical Review Letters 61 (18), 2015-2018 (1988).

21. N. Nagaosa, J. Sinova, S. Onoda, A. H. MacDonald and N. P. Ong, Rev. Mod. Phys. 82 (2), 1539-1592 (2010).

22. O. Vafek, Phys. Rev. B 82 (20), 205106 (2010).

23. C. L. Kane and E. J. Mele, Physical Review Letters 95 (22), 226801 (2005).

24. M. Konig, S. Wiedmann, C. Brune, A. Roth, H. Buhmann, L. W. Molenkamp, X. L. Qi and S. C. Zhang, Science 318, 766-770 (2007).

25. S. Raghu, X. L. Qi, C. Honerkamp and S. C. Zhang, Physical Review Letters 100 (15), 156401 (2008).

26. S. Cho and M. S. Fuhrer, Nano Res. 4, 385 (2011).

27. E. A. Henriksen, Z. Jiang, L.-C. Tung, M. E. Schwartz, M. Takita, Y.-J. Wang, P. Kim and H. L. Stormer, Phys. Rev. Lett. 100, 087403 (2008).

28. E. V. Castro, N. M. R. Peres and J. M. B. L. d. Santos, Phys. Stat. Sol. B 244, 2311 (2007).

29. G. Borghi, M. Polini, R. Asgari and A. H. MacDonald, Solid State Commun. 149, 1117-1122 (2009).

30. L. Zhu, V. Aji and C. M. Varma, arXiv:1202.0821v1201 (2012).

31. A. Veligura, H. J. van Elferen, N. Tombros, J. C. Maan, U. Zeitler and B. J. van Wees, Phys. Rev. B 85 (15), 155412 (2012).

32. R. Nandkishore and L. Levitov, Phys. Rev. Lett. 107 (9), 097402 (2011).

33. M. Kharitonov, preprint, arXiv:1105.5386v1101 (2011).

34. M. Kharitonov, preprint, arXiv:1109.1553v1101 (2011).

35. W. Bao, L. Jing, Y. Lee, J. V. Jr., P. Kratz, D. Tran, B. Standley, M. Aykol, S. B. Cronin, D. Smirnov, M. Koshino, E. McCann, M. Bockrath and C. N. Lau, Nature Physics 7, 948-952 (2011).

Chapter 7: Phase transitions in ultra clean BLG

Introduction

In this chapter I will discuss a systematic study of the minimum conductivity σ_{min} in a large number of single-gated and double-gated BLG samples, with mobilities ranging from 500 to 2000 cm^2/Vs for substrate-supported samples, and 6000 to 350,000 for suspended samples. We find a surprisingly constant σ_{min} value ~ 2-3 e^2/h for the majority of devices, independent of device mobility and the presence or absence of substrates. However, in some of the devices with highest mobility and smallest CNP offset an insulating state with an energy gap ~ 2-3 meV manifests, which is similar to the insulating state discussed in the previous chapter. This bimodal distribution of σ_{min} suggests that transport in conducting devices either arise from single particle physics, or occurs along domain boundaries that separate regions with different spontaneous quantum Hall states. Interestingly, for insulating devices, a transition between conducting and insulating states can be driven by disorder, temperature, charge density n, and perpendicular electric field $E_{\perp}$.

7.1: The different ground states of BLG

Bilayer graphene (BLG) has provided a fascinating new platform for both post-silicon electronics and exotic many-body physics [1-15], as was discussed in the previous chapter. In this section we briefly contextualize the theoretical background for the experimental work that will be presented in the proceeding sections.

Because BLG's conduction and valence bands touch at two points in momentum space and have approximately quadratic dispersion accompanied by vorticity J=2 momentum-space pseudospin textures, charge neutral BLG is likely to have a broken symmetry ground state in the absence of disorder [6-13, 15-17]. Theoretical work on the character of the ground state in neutral bilayer graphene has examined a variety of distinct but related pseudospin ferromagnet states, including gapped anomalous Hall states [5,6,17] and layer antiferromagnetic states[6-8,13,14,20] that break time-reversal symmetry, and gapless nematic states which alter Dirac point structure and reduce rotational symmetry [6-13, 15-17]. Recent experiments, such as the work presented in the previous chapter, [18-22] have reported low-temperature conductivity σ_{min} values for neutral BLG that vary over a large range, from 0.05 to 250 μS. Because radically different transport characteristics are observed in samples that are apparently quite similar, it has been difficult to draw firm conclusions about the nature of the low-temperature electronic state.

7.2 Device Characterization:

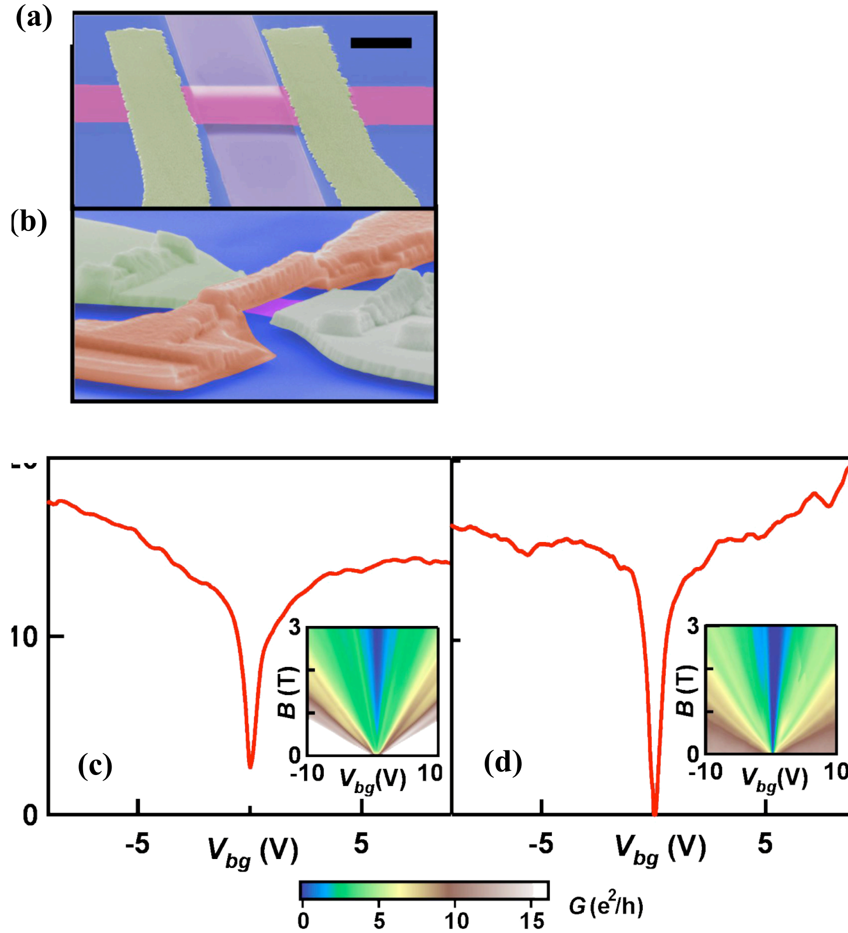

Fig 7.1: SEM images of devices and transport data. a. and b. False-color scanning electron micrograph of BLG device with and without top gate. Scale Bar: μm. c-d. Main panels and insets: σ (V_g) and $G(V_{bg},B)$ for two BLG devices with and without insulating state at CNP (T=1.5K). Both samples are single gated.

Wenzhong Bao fabricated and measured single-gated BLG devices using a lithography-free technique [23], and I fabricated and measured suspended double-gated BLG by combining acid etching with a multi-level lithographic technique[24, 25] which was

discussed in chapter three, and made devices with suspended top gates[21]. All as-fabricated suspended BLG devices have relatively low mobilities, presumably due to gas or water absorption on the surface of BLG when exposed to an ambient environment. Current annealing is performed in vacuum to improve device quality[26-28] as was shown in chapter three.

Fig 7.1c-d display the two terminal differential conductivity $\sigma=(L/W)dI/dV$ of two single gated suspended BLG devices *vs.* V_{bg} at T=1.5K after current annealing. Here L/W is the aspect ratio of the device. Both curves are steeply *V*-shaped, with CNPs (marked by conductivity minima) close to V_{bg}=0V. Surprisingly, the σ_{min} values of the devices are drastically different – 2.5 and 0.02 e^2/h, respectively. The insulating behavior of the latter device and other such samples has been confirmed by *I-V* curves. In a magnetic field B, both devices display quantum Hall plateaus with the 8-fold degeneracy [29, 30] of the zero energy Landau level (LL) fully lifted [31]. From the Landau fan diagram that plots the differential conductance G (color) *vs.* V_{bg} and B (Fig. 1d-e, insets), the n=0 state is visible for both devices at B>0.5T and persists down to B=0 for the device with very low σ_{min} [20, 32].

7.3 Bimodal distribution of devices

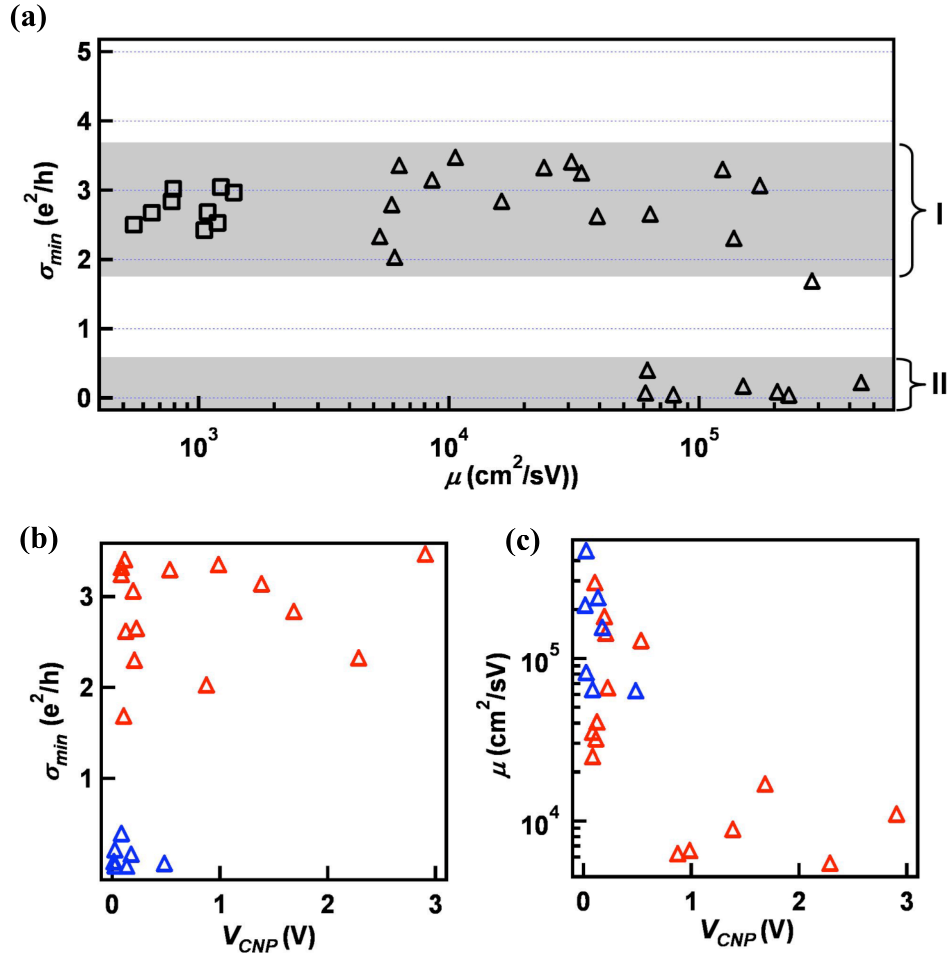

Fig 7.2: Characteristics of several substrate supported and suspended BLG devices. a. $\sigma_{min}(\mu)$ for 9 substrate supported BLG devices (square symbols) and 23 suspended BLG devices (triangular symbols). b-c. $\mu(V_{CNP})$ and $\sigma_{min}(V_{CNP})$ for suspended BLG devices. The blue symbols denote devices in region II.

With the goal of discovering the origin of the large range of σ_{min}, we investigated 9 substrate- supported BLG devices and 23 suspended BLG devices with aspect ratios between 0.5 and 2, and areas 1-18 μm^2. The results are summarized in fig 7.2a, which

plots σ_{min} as a function of field effect mobility $\mu = \frac{1}{e}\frac{d\sigma}{dn}$ for each device. Evidently, the data points separate into two groups. Most data points fall into group I, in which σ_{min} is almost independent of mobility and similar for suspended and supported devices. Within this class of devices the CNP conductivity ~ 100μS ~*2.8* e^2/h (*24-31*).

Very different behavior is found in the 8 devices that fall into group II – σ_{min} is at most 0.4 e^2/h, and as low as 1 μS. Notably, all 8 devices have very high mobility, and are suspended. To shed further light on the physical difference between the two groups, we also examine V_{CNP}, the devices' applied V_{bg} at the CNP, which indicates the overall doping level. Fig. 2b-c display σ_{min} and μ *vs.* V_{CNP} for all suspended samples with the insulating devices denoted by blue triangles. Two striking features are evident: (1) μ decreases with increasing V_{CNP} in agreement with previous reports in substrate supported graphene[33, 34], suggesting that charged impurities remain important scatterers even in these high mobility devices; (2) the insulating-BLG devices in fig 7.2b-c cluster around V_{CNP}=0. Thus, the insulating behavior in BLG at the CNP is only observed in devices with *both* high mobility and low charged impurity density. The insulating state, which is apparently masked by impurities in group I samples, occurs for devices with fewer scatterers and cannot be explained by single-particle physics.

7.4 Temperature dependence of single gated devices

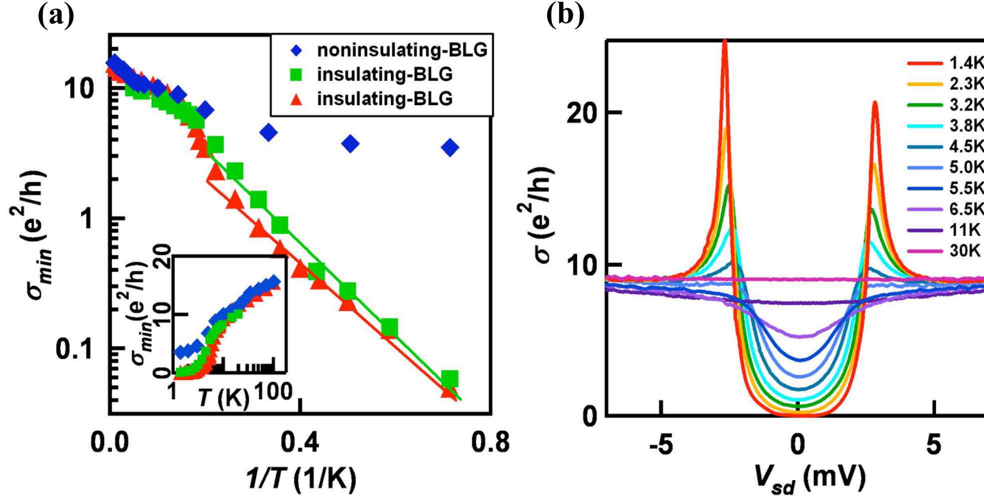

Fig 7.3: Temperature dependence measurements at CNP. a. $\sigma_{min}(1/T)$ for insulating and noninsulating single gated BLG devices. Inset: $\sigma_{min}(T)$ of data set. The solid lines are fits to data T<5K to Eq. (1). b. T-dependence of $\sigma(V_{sd})$ at CNP for an insulating-BLG device.

To obtain further insight we compare the temperature dependences of group I and group II devices, which are both suspended samples. Fig 7.3a displays σ_{min} on a logarithmic scale *vs* $1/T$ for $1.4 \leq T \leq 100$ K for one non-insulating device and two different insulating BLG devices. The inset plots the same data sets $\sigma_{min}(T)$ on linear-log scales. Amazingly, for $10 < T < 100$K, the $\sigma_{min}(T)$ curve of all 3 devices collapse into a single curve. This is in contrast with the previous work on single layer[35] and trilayer graphene[36, 37], which reported large sample-to-sample variation in $\sigma_{min}(T)$. Thus, the consistent behaviors among 3 devices for T>10K strongly suggest that we are indeed observing intrinsic attributes of BLG.

However, the behaviors of the two types of devices start to deviate at ~ 5-7 K – σ_{min} of the non-insulating device decreases only modestly; in contrast, the σ_{min} of both insulating ones exhibit an abrupt change in slope, or a kink, and drops precipitously for T<5K where the data are well-described by $\sigma_{min}(T)=A\ exp(-E_A/2k_BT)$ (here A is the pre-factor, E_A is the activation energy and k_B is the Boltzmann constant). The best fit is obtained by using A=17 e^2/h and E_A~18K, indicating thermally activated transport over a gap >~ 1.6 meV.

These data suggest the presence of a gap in insulating devices for T<5K. To investigate this further, we study σ *vs.* source drain bias V_{sd} at the CNP[20, 21](fig 7.3b), as was discussed in the previous chapter. At T=1.4K, σ increases precipitously when $|V_{sd}|$ increases from 0, forming a "U"-shaped profile and reaching two dramatic peaks at ±2.8 mV, and deceases again to ~ $8e^2$/h for $|V_{sd}|$>5mV. Such a $\sigma(V_{sd})$ curve, which was also discussed in the previous chapter, strongly resemble the density of states (DOS) for gapped phases, like superconductors, charge density waves, perhaps most pertinently the displacement field induced gapped BLG state [4, 38]. Since the device has symmetric coupling to both electrodes, we take the magnitude of the gap to be half of the separation between the two peaks, ~2.8 meV. This is larger than the value ~1.6 meV obtained from thermal activation measurements, but not surprising due to level broadening by, *e.g.,* impurities. Thus, the $\sigma(V_{sd})$ curves, together with the $\sigma_{min}(T)$ measurements, unequivocally establishes the presence of a low-temperature gap ~ 2-3 meV in group II BLG's spectrum.

7.5 Suppressing the gap

7.5.1 Suppressing the gap by turning up the heat

We now examine the $\sigma(V_{sd})$ curves of the insulating device with one gate at different temperatures (fig 7.3b). When T increases from 1.4 K, σ_{min} increases, $\sigma(V_{sd})$ adopts a "V"-shaped profile, and the magnitudes of the two peaks decrease and vanish entirely at ~5K (fig 7.3b). All these observations suggest the disappearance of the gap for T>5K. Our data thus provide strong evidence for a finite temperature phase transition to an insulating state with a critical temperature T_c~5K and a gap Δ_{kB} (~20-30K). Because the gap disappears with temperature, it cannot be of single-particle origin, and must arise from many-body interaction effects. The rough correspondence between the critical temperature and gap scales suggests that the broken symmetry is reasonably well described by mean-field theory[31].

Our data thus far suggests a T-dependent phase transition in charge-neutral BLG between a conducting state and an interaction-induced insulating state. The conducting state could be due to bulk two-dimensional metallic behavior, or alternatively due to transport along topologically protected edge states supported by domain walls separating regions with different spin and valley dependent Chern numbers. Future experiments will be necessary to ascertain the nature of the conducting electronic state at the CNP. In particular, to explore the notion of domains, local probes such as an STM would be the most promising approach.

7.5.2 Suppressing the gap by reducing sample quality

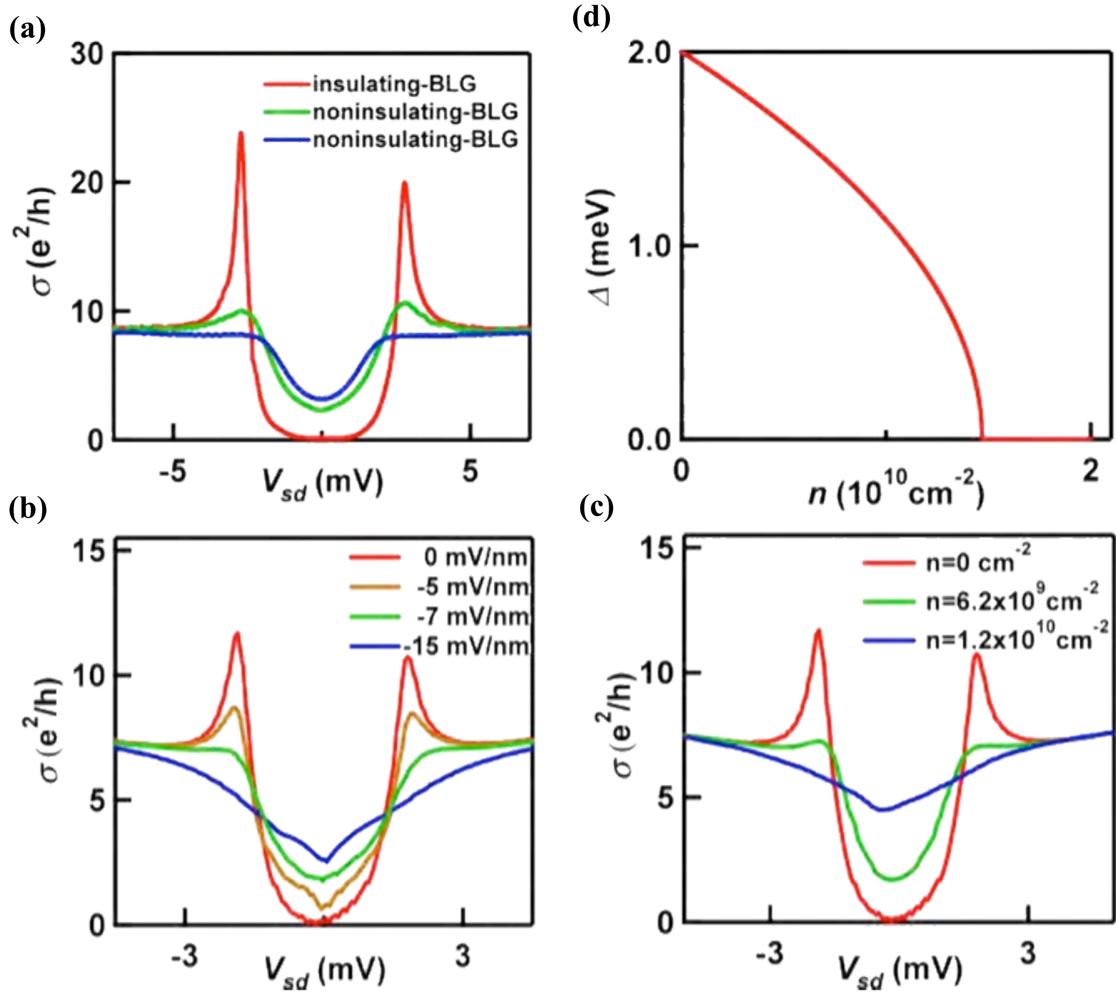

Fig 7.4: Suppression of gap by several parameters. a. $\sigma(V_{sd})$ for insulating and noninsulating-BLG devices at the CNP. b. $\sigma(V_{sd})$ at n=0 for a doubly gated BLG at $E_{\perp}$=0, -5, -7 and -15 mV/nm. c. $\sigma(V_{sd})$ at $E_{\perp}$=0 for a doubly gated BLG at different values of n. d. Magnitude of flavor gap vs. n calculated from MFT.

An intriguing possibility is that of a quantum phase transition, *i.e.* one that is tuned by parameters other than T such as disorder or electric field may take place at T=0.

To this end, we examine the $\sigma(V_{sd})$ curves of two single gated conducting devices, which have mobility 140,000 and 24,000 cm^2/Vs, respectively, at T=1.4K (fig 7.4a). Data from an insulating device is also plotted for comparison. Remarkably, $\sigma(V)$ of both conducting devices bears a striking resemblance to those of insulating BLG at higher temperatures. In particular, the device with μ=140,000 cm^2/Vs has a "V-shaped" profile at small V_{sd}, elevated σ_{min} and smaller peaks at $V_{sd} \sim \pm 2.5$ mV, and resembles the curve in fig 7.3b at T~4K. For the device with μ=24,000 cm^2/Vs, $\sigma(V)$ is flatter without the side peaks, thus resembling the curve from the insulating device at T~10K. Taken together, charge disorder and temperature have similar effects on the insulating state in BLG.

7.5.3 Suppressing the gap by tuning n and $E_\perp$

Finally we examine the effect of carrier density n and an applied $E_\perp$ that induces an interlayer potential difference as was described in chapter two for BLG. In our doubly gated BLG devices we can control n and $E_\perp$ independently. Several line traces of $\sigma(V_{sd})$ at $n=0$ for different values of $E_\perp$ are shown in fig 7.4b. As $E_\perp$ increases from 0 to -7mV/nm, the "U"-shaped $\sigma(V_{sd})$ curve becomes "V"-shaped, with less prominent side features and an elevated σ_{min}, *i.e.* the gap size appears to be diminished by $E_\perp$. For still larger fields the well-known single-particle gap [2,4,33] of unbalanced bilayers gradually emerges. This distinguishes $E_\perp$ as the only parameter to obscure, and then with continual increment induce another gapped state. On the other hand, the influence of total carrier density on the insulating state is extremely sharp. At $E_\perp$=0 (fig 7.4c) – a small density n ~

6.2×10^9 cm^{-2} is sufficient to significantly obscure the gapped correlated state; when n ~1.2×10^{10} cm^{-2}, the gapped feature completely vanishes and σ_{min} reaches ~ $5e^2/h$.

Our experimental results provide strong evidence for a quantum phase transition between insulating and conducting states that is tuned by $E_\perp$, n and charge disorder. The gapped state is susceptible to small variations in total carrier density, displacement field, and disorder, which could explain why it is not always seen in devices that appear to be of high quality.

7.6 Discussion

A family of gapped states in which each spin-valley flavor is spontaneously layer polarized, inducing large momentum-space berry curvatures, has been theoretically anticipated. States within the family are distinguished by their flavor-dependent configuration of layer polarizations. In these states each flavor supports a quantized anomalous Hall conductivity contribution whose sign changes with the sense of its layer polarization. Increasing carrier density works against broken symmetry order by Pauli blocking of layer polarization, which simply means further spin polarized charges cannot be introduced to a layer because of the Pauli exclusion principle. Incrementing carrier density will also increase screening, hence reducing the interactions between the carriers. MFT predicts that the spontaneous quantum Hall states disappear once the carrier density is larger than 1.47×10^{10} cm^{-2} [31], in excellent agreement with our experimental findings (fig 7.4d). The role of temperature in MFT is both similar to that in BCS theory of

superconductivity and in qualitative agreement with the experiment. Because for MFT there is no *Anderson Theorem* to mitigate the role of disorder, gapped states are expected only in the highest-quality samples.

Increasing $E_{\perp}$ favors configurations in which each flavor has the same polarization. Using a calculation of the band structure at each valley, a transition from a LAF state, which has $E_{\perp}=0$, to a layer-flavor polarization state is depicted in fig 7.5[39]. Increasing $E_{\perp}$ will cause the gap at one valley to open further, and close at the other valley. Continued increment of $E_{\perp}$ reopens the gap that was closed, and corresponds to a transition into a flavor-layer polarized state shown in chapter six, fig 6.1. Data from fig 6.3 demonstrates a non-monotonic behavior in conductance, and reflects this band structure morphology. Adding an external magnetic field favors configurations in which each flavor has the same sign of Hall conductivity and the carrier density at which the largest gap occurs is consequently proportional to field strength (eq 6.2). Future work that explores the combined influence of all experimentally adjustable parameters could enable the gapped state to be uniquely assigned.

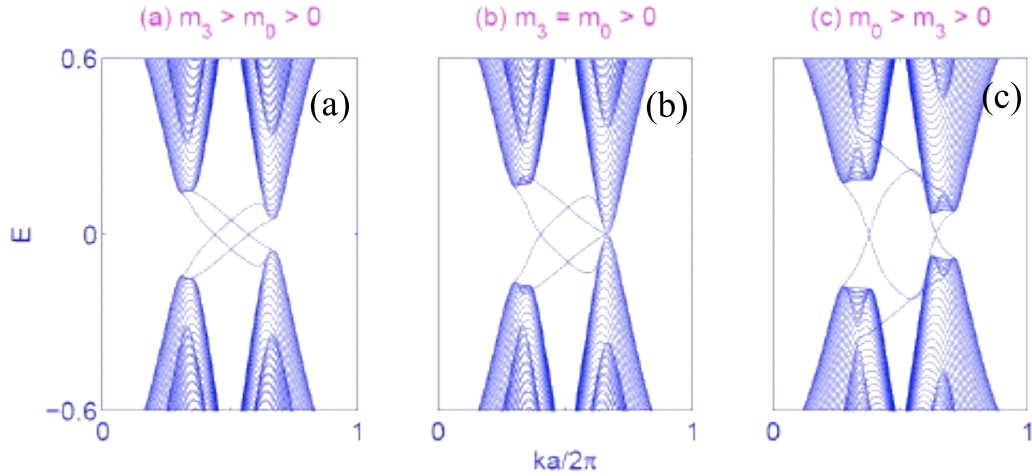

Fig 7.5: Band structure calculation shows gap suppression by increasing $E_{\perp}$. a. Small finite $E_{\perp}$, increases gap in one valley while diminishing it in the other. b. Further increase of $E_{\perp}$ closes gap in one valley completely. c. Continued increase of $E_{\perp}$ induces a transition into a flavor-layer polarized state that is also gapped. Band structures calculated using MFT by Fan Zhang.

Conclusion:

In summary, our systematic study of a large number of high quality BLG devices suggests that ultra-clean charge neutral BLG devices undergo a phase transition at T_c~ 5K, from a metallic state to an insulating state with an energy gap ~2-3 meV. The latter arises from electron correlation and is likely a spontaneous quantum Hall state *without* overall layer polarization, deemed the layer antiferromagnetic state and is depicted in the previous chapter fig 6.1b[21]. Interestingly, increasing *n* or disorder has similar effects on the insulating state as temperature, suggesting that these parameters can drive quantum phase transitions. Increasing $E_{\perp}$ with either polarity will also induce a transition into a

topologically different gapped state with layer polarization. We expect the rich physics that we have studied in BLG to also appear in the rhombrohedral-stacked multilayer relatives, such as ABC TLG. This will be discussed in the last chapter of the thesis.

References

1. K. S. Novoselov, E. McCann, S. V. Morozov, V. I. Fal'ko, M. I. Katsnelson, U. Zeitler, D. Jiang, F. Schedin and A. K. Geim, Nat. Phys. 2 (3), 177-180 (2006).
2. E. McCann, Phys. Rev. B 74, 161403 (2006).
3. A. H. Castro Neto, F. Guinea, N. M. R. Peres, K. S. Novoselov and A. K. Geim, Rev. Mod. Phys. 81 (1), 109-162 (2009).
4. H. K. Min, B. Sahu, S. K. Banerjee and A. H. MacDonald, Phys. Rev. B 75 (15), 155115 (2007).
5. R. Nandkishore and L. Levitov, Phys. Rev. B 82 (11), 115124 (2010).
6. F. Zhang, J. Jung, G. A. Fiete, Q. A. Niu and A. H. MacDonald, Phys. Rev. Lett. 106 (15), 156801 (2011).
7. J. Jung, F. Zhang and A. H. MacDonald, Phys. Rev. B 83 (11), 115408 (2011).
8. F. Zhang, H. Min, M. Polini and A. H. MacDonald, Phys. Rev. B 81 (4), 041402 (R) (2010).
9. Y. Lemonik, I. L. Aleiner, C. Toke and V. I. Fal'ko, Phys. Rev. B 82 (20), 201408 (2010).
10. O. Vafek and K. Yang, Phys. Rev. B 81 (4), 041401 (2010).
11. E. V. Castro, N. M. R. Peres, T. Stauber and N. A. P. Silva, Phys. Rev. Lett. 100 (18), 186803 (2008).
12. I. Martin, Y. M. Blanter and A. F. Morpurgo, Phys. Rev. Lett. 100 (3), 036804 (2008).
13. M. Kharitonov, preprint, arXiv:1105.5386v1101 (2011).
14. M. Kharitonov, preprint, arXiv:1109.1553v1101 (2011).
15. F. Zhang and A. H. MacDonald, preprint, arXiv:1107.4727v1101 (2011).
16. H. Min, G. Borghi, M. Polini and A. H. MacDonald, Phys. Rev. B 77 (4), 041407 (2008).
17. R. Nandkishore and L. Levitov, preprint, arXiv:1002.1966v1001 (2010).

18. R. T. Weitz, M. T. Allen, B. E. Feldman, J. Martin and A. Yacoby, Science 330 (6005), 812-816 (2010).

19. J. Martin, B. E. Feldman, R. T. Weitz, M. T. Allen and A. Yacoby, Phys. Rev. Lett. 105 (25), 256806 (2010).

20. F. Freitag, j. Trbovic, M. Weiss and C. Schonenberger, Phys. Rev. Lett. 108, 076602 (2012).

21. J. Velasco, L. Jing, W. Bao, Y. Lee, P. Kratz, V. Aji, M. Bockrath, C. N. Lau, C. Varma, R. Stillwell, D. Smirnov, F. Zhang, J. Jung and A. H. MacDonald, Nature Nanotechnol. 7, 156 (2012).

22. A. S. Mayorov, D. C. Elias, M. Mucha-Kruczynski, R. V. Gorbachev, T. Tudorovskiy, A. Zhukov, S. V. Morozov, M. I. Katsnelson, V. I. Fal'ko, A. K. Geim and K. S. Novoselov, Science 333 (6044), 860 (2011).

23. W. Z. Bao, G. Liu, Z. Zhao, H. Zhang, D. Yan, A. Deshpande, B. LeRoy and C. N. Lau, Nano Res. 3 (2), 98-102 (2010).

24. G. Liu, J. Velasco, W. Z. Bao and C. N. Lau, Applied Physics Letters 92 (20), 203103 (2008).

25. J. Velasco, G. Liu, W. Z. Bao and C. N. Lau, New Journal of Physics 11, 095008 (2009).

26. J. Moser, A. Barreiro and A. Bachtold, Appl. Phys. Lett. 91, 163513 (2007).

27. K. I. Bolotin, K. J. Sikes, Z. Jiang, M. Klima, G. Fudenberg, J. Hone, P. Kim and H. L. Stormer, Solid State Communications 146 (9-10), 351-355 (2008).

28. X. Du, I. Skachko, A. Barker and E. Y. Andrei, Nat. Nanotechnol. 3 (8), 491-495 (2008).

29. Y. Zhao, P. Cadden-Zimansky, Z. Jiang and P. Kim, Phys. Rev. Lett. 104 (6), 066801 (2010).

30. B. E. Feldman, J. Martin and A. Yacoby, Nat. Phys. 5 (12), 889-893 (2009).

31. W. Bao, J. V. Jr., F. Zhang, L. Jing, B. Standley, D. Smirnov, M. Bockrath, A. MacDonald and C. N. Lau, Proc. Natl. Acad. Sci., to appear (2012).

32. J. Velasco, Jr., Z. Zhao, H. Zhang, F. Wang, Z. Wang, P. Kratz, L. Jing, W. Bao, J. Shi and C. N. Lau, Nanotechnology 22 (28), 285305 (2011).

33. Y. W. Tan, Y. Zhang, K. Bolotin, Y. Zhao, S. Adam, E. H. Hwang, S. D. Sarma, H. L. Stormer and P. Kim, Phys. Rev. Lett. 99, 246803 (2007).

34. S. Adam, E. H. Hwang, V. M. Galitski and S. Das Sarma, Proceedings Of The National Academy Of Sciences Of The United States Of America 104 (47), 18392-18397 (2007).

35. K. I. Bolotin, K. J. Sikes, J. Hone, H. L. Stormer and P. Kim, Phys. Rev. Lett. 101 (9), 096802 (2008).

36. W. J. Zhu, V. Perebeinos, M. Freitag and P. Avouris, Phys. Rev. B 80 (23) (2009).

37. W. Bao, L. Jing, Y. Lee, J. V. Jr., P. Kratz, D. Tran, B. Standley, M. Aykol, S. B. Cronin, D. Smirnov, M. Koshino, E. McCann, M. Bockrath and C. N. Lau, Nature Physics 7, 948-952 (2011).

38. E. Rossi and S. Das Sarma, preprint, arXiv:1103.3012 (2011).

39. F. Zhang Private Communication.

Chapter 8: The Charge neutrality point in the QH regime

Introduction

In this chapter I will discuss our study of transport phenomena in our dual-gated suspended BLG samples at the CNP in the QH regime. In previous chapters, we demonstrated the spontaneous gap at the CNP in these samples, which is an example of interaction-driven physics in BLG. We found that upon an increasing perpendicular B, the gapped state transitioned smoothly to the filling factor $\nu=0$ QH state, with a gap size that increases monotonically according to eq 6.2 in chapter six. Our findings are consistent with the LAF state, which is depicted in fig 6.1, as the ground state of BLG at $B=0$.

The $\nu=0$ QH state in its own right is an interesting state that has no parallel in the conventional 2DEGS[1, 2]. Recent theory[3, 4], has focused on the transition between the LAF state at $B=0$ and the $\nu=0$ state in the QH regime as a function of B. This work concludes increasing B will drive the system from a LAF to a canted (tilted) LAF state, and application of a sufficiently large in plane magnetic field $B_{||}$ in the QH regime will drive the system into a ferromagnetic phase (FM).

In the following sections I will focus on our dc current-voltage (I-V) measurements at the CNP as a function of B, and in zero and at finite $E_{\perp}$. At large B, these I-V curves are hysteretic, and in many aspects, strongly reminiscent to those of Josephson junctions[5]. Such hysteresis is quenched by increasing temperature T and $E_{\perp}$. We tentatively propose a qualitative picture akin to the superconductor to normal

conductor transition in a Josephon junction to explain our experimental observations. Our study provides valuable insight into the rich phase space offered by BLG at the CNP.

8.1: The ν=0 QH state via a linear measurement

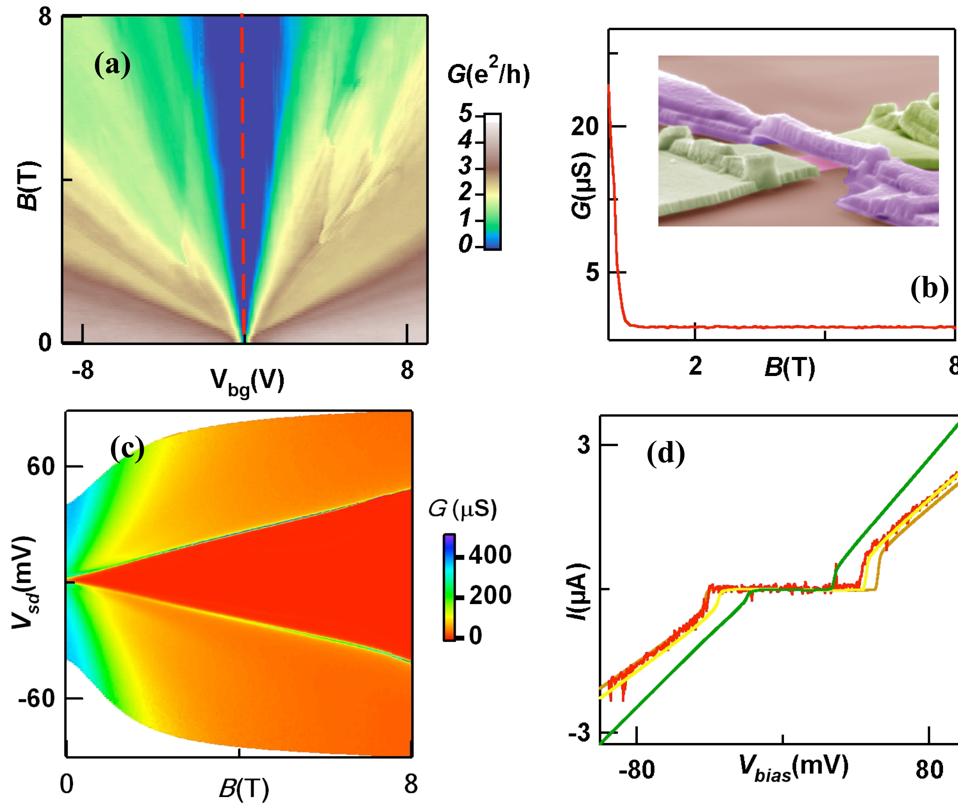

Fig 8.1: ν=0 and Δ measurement. a. $G(V_{bg,}B)$ fan diagram for suspended BLG device at T=260mK. b.$G(V_{bg})$ from a. at the CNP, device image inset. c. $G(V_{sd,}B)$ at the CNP and at T=260mK. d. IV traces at finite B. The red line trace is an actual IV measurement at 8T, while the orange line trace(8T), yellow line trace(7T), and green line trace (3T) are dI/dV measurements from c. that were integrated.

The Landau fan diagram of suspended BLG samples with dual gates is shown in fig 8.1a. Here we will focus on the center blue band (finite carrier densities adjacent to

this feature will be considered in the next chapter), which first manifests as the spontaneous gap at B=0, and then transitions to the ν=0 QH state as B is increased[6]. The $G(B)$ line trace at n=0 displays a dramatic drop as B is increased.

To further investigate the nature of the ν=0 QH state we position both gates at the CNP and measure differential conductance $G=dI/dV$ (using a lock-in amplifier) as a function of the source drain voltage bias V and B. This type of measurement, which is pioneered by us for graphene, enables direct measurement of the energy gaps. The $G(V)$ curves display an insulating (G=0) state at small bias; when V becomes larger than a critical value V_c, G exhibits a sharp peak before falling back to finite values ~ 1 e^2/h. I-V curves, which can be obtained by numerical integration or direct dc measurements, displays an insulating branch for $V<V_c$ and an abrupt jump to the conducting branch for $V>V_c$. As discussed in chapter six, we associate eV_c , which scales linearly with B, with the energy gap of the =0 state.

To demonstrate that these type of I-V curves are intrinsic to BLG and not arising from extrinsic effects such as heating or “training” and movement of domain walls, we maintain finite V across the device so that it stays at the conducting branch at B=7T. As B is increases towards 8T, V_c increases so that the device jumps back to the insulating state. Similarly, when the device is maintained at the insulating state at B=8T, decreasing B reduces V_c and the device jumps to the conducting state. Thus these peculiar I-V curves are indicative of a correlated state.

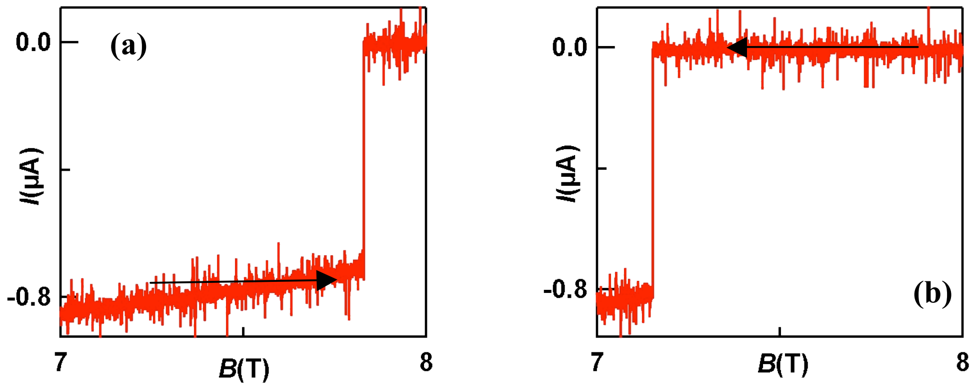

Fig 8.2: *B* induced switching between conducting and insulating state. a. *I*(*B*) with the device at CNP and at *V* corresponding to the conducting branch of *IV* profile in fig 1d. b. *I*(*B*) with the device at CNP and at *V* corresponding to the insulating branch of *IV* profile in fig 8.1d.

8.2: Hysteresis at the ν=0 QH state

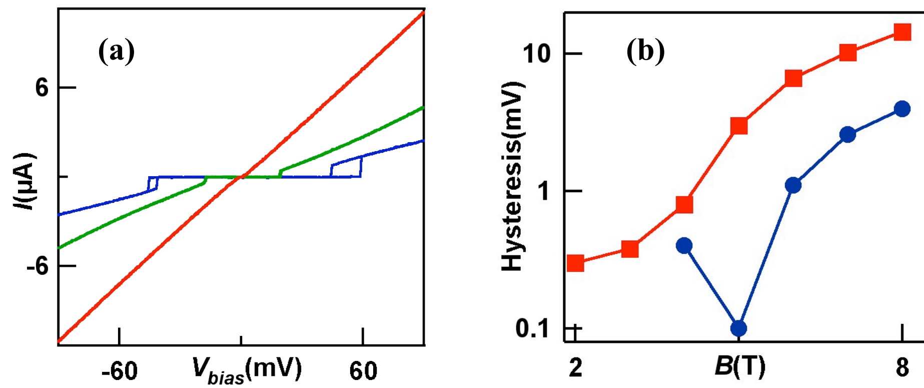

Fig 8.3: Hysteresis loops with increasing *B*. a. *I*(*V*) up and down sweeps at the CNP and at *B*=0T(red), *B*=1T(green) and *B*=8T(blue). At *B*>2T the hysteresis loops are visible. b. Plot of hystersis loop size as a function of increasing *B*, with loop size on log scale.

Thus far the I-V curves are only taken in the direction of increasing V. When data from both upsweep and downsweep directions are included, we find that the curves are hysteretic at large B, *i.e.* the device returns from the conducting to the insulating state at a bias voltage V_r, and $|V_r|<|V_c|$. Such hysteretic I-Vs are very similar to those of under-damped Josephson junctions, albeit with the I and V axes switched.

To investigate the hysteresis, we examine its behavior as a function of sample mobility, magnetic field, electric field and temperature. Typically hysteresis loops only appear in high mobility samples (80,000) in B>2T, or in moderate mobility samples (20,000) at B>12T. In one device the I-V curves were not hysteretic at B=8T after initial annealing, but upon further annealing hysteresis appears. The size of the hysteretic loops are strongly dependent on magnetic fields. As shown in fig 8.3a, the hysteresis is absent at B=0 (red), but appears at B=2T (green), and is quite prominent at B=8T (blue). The hystersis loop size, defined as $|V_c-V_r|$, increases exponentially with B (fig 9.3b). Similar data set have been seen in four different samples and using two different cryostats.

We now focus on the effect of $E_\perp$ on the hysteresis. Fig 8.4 plots the $I(V)$ in the negative V region at B=8T for three different $E_\perp$ values. The red line trace, which displays a prominent loop, corresponds to $E_\perp$=0, while the green and blue line traces are taken at $E_\perp$~0.1mV/nm and $E_\perp$~0.5mV/nm, respectively. Evidently, minute $E_\perp$~ 0.1mV/nm is sufficient to completely quench the hysteresis. Such sensitive dependence on $E_\perp$ suggests that the hysteresis phenomena have no net charge layer polarization. Further increasing $E_\perp$ (blue line trace) reduces V_c, *i.e.* suppresses the ν=0 gap, as discussed in Ch. 6, fig6.9.

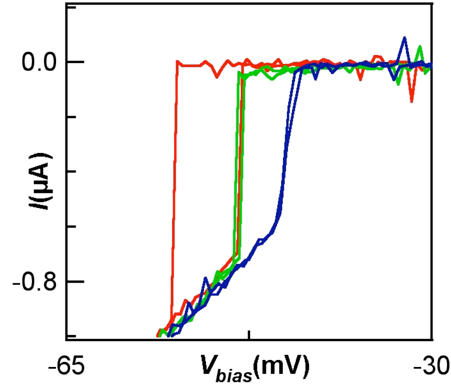

Fig 8.4: Suppression of Hysteresis loops with increasing $E_\perp$. ~ $I(V)$ up and down sweeps at the CNP and at B=8T. Different line traces correspond to increasing $E_\perp$, with $E_\perp$=0(red), $E_\perp$~0.1mV/nm(green), and $E_\perp$~0.5mV/nm(blue).

In fig 8.5a we plot *I-V* characteristics at different temperatures from another suspended BLG device with dual gates at B=18T (measurements performed in Tallahassee). The exponential dependence of the hystersis loop size on B allows us to achieve significantly larger loops than fig 8.3a. Different color traces in fig 8.5a correspond to different temperatures; the red line trace was performed at the base temperature ~300mK, green at ~20K and blue at ~60K. Clearly, increasing T suppresses the hysteresis loops, until the *I-V* curves are no longer hysteretic; upon further increase in T, the device is no longer insulating, but display a finite conductance ~ 30 μS.

To characterize the T dependence we plot the movement of V_c(red) and V_r (blue) as a function of T (fig 8.5b). Interestingly, V_c is relatively temperature independent for $0.3<T<5$K, then decreases almost linearly with T; in contrast, V_r remains almost constant until T~ 16K. At T~20K, $V_c \sim V_r$, *i.e.* the *I-V* curves are no longer hysteretic.

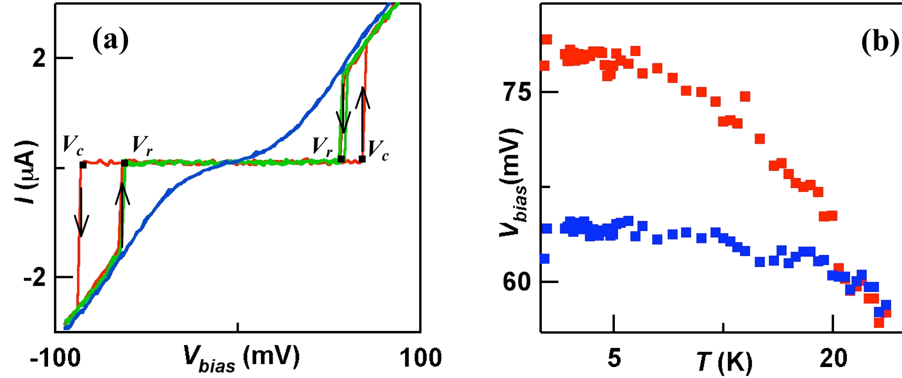

Fig 8.5: Suppression of hysteresis loops with increasing *T*. a. $I(V)$ up and down sweeps at the CNP and at B=18T. Direction of sweeps and inflection points are labeled. Different traces correspond to different T, with T=260mK(red), T=20K(green), and T=60K(blue). c. Movement of V_r(blue) and V_c(red) with increasing T.

To further study the behavior of V_c and V_r we perform 100 consecutive $I(V)$ measurements at B=8T and T=300 mK, and at the CNP, using another suspended BLG device that displayed hysteresis loops. All parameters such as $E_{\perp}$, T and B are maintained constant during the sweeps with T=260mK. We find that the V_c and V_r values are not exactly the same, but vary slightly for each sweep. This suggests that the switching between the insulating and conducting states is stochastic (fig 8.6), likely due to thermal fluctuations. The widths of the distribution of both V_c and V_r values are similar, which is consistent with the fact that both V_c and V_r have the same temperature dependence at this low temperature. If finite-width distribution of V_c and V_r is indeed induced by thermal activation, we then expect that, since V_c is more strongly T-dependent at, say, 10K, it will has a wider distribution than V_r.

Our experimental data may be summarized as follows: 1) Our I-V measurements at CNP display a transition between a conductive and an insulating state; 2) These curves

exhibit a hysteresis between up and down sweeps, and these hysteretic loops grow exponentially with B; and 3) These loops can be suppressed by small $E_{\perp}$ and increasing T. The former in point (3) suggests the loops at large B are not a layer-polarized phenomenon. To understand the data, below we develop a qualitative model that borrows from the framework of an underdamped Josephson junction[5].

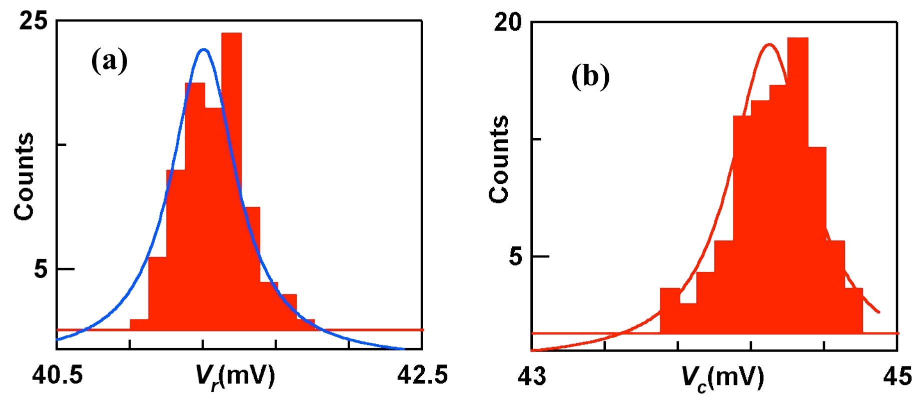

Fig 8.6: Distribution of V_r and V_c at 260mK. a. Distribution of V_r from 100 up and down sweeps performed in tandem at 260mK. b. Distribution of V_c from 100 up and down sweeps performed in tandem at 260mK. Sweeps are similar, and do not exhibit stochastic behavior, which is not surprising due to their apparent insensitivity to temperature from fig 5b at base T.

8.3: Discussion

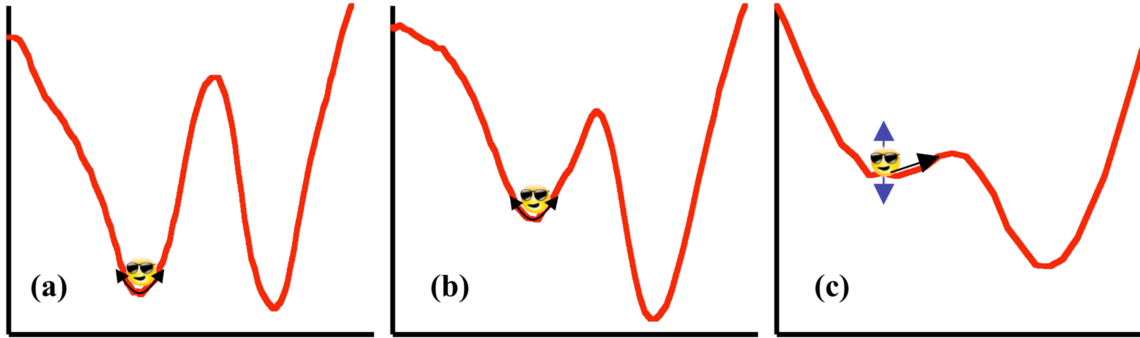

Fig 8.7: Tilted washboard potential. a. Washboard potential and ball with V=0. Minima represents the insulating state in our measurement, while slopped region represents the conducting state. b. Increasing V tilts the potential as shown, in this case $0<V<V_c$. c. $V_c<V$, hence ball moves freely. The double sided blue arrow represents thermal fluctuations, which modify V_c and V_r.

The qualitative model presented in this section is motivated by the similarities between our data and the *VI* curves of an underdamped Josephson junction (JJ) :(1). Both systems display sharp transitions between a conducting state and a zero resistance/conductance state. (2). The *I-V* curves are hysteretic (3). The hysteresis can be suppressed by increasing temperature. (4). The "critical" and "return" voltages/currents exhibit finite-width distributions upon repeated sweeps, suggesting stochastic switching.

The mechanical analogue that describes the dynamics of a JJ is a particle in a tilted washboard potential; in our system, the washboard can be tilted by increasing V. The qualitative picture is sketched in fig 8.7a-c with the potential changing as V is increased for the three cases shown. In the first case, the system is not biased, hence the

ball remains in the left minimum, which corresponds to the insulating state in our measurement. In the third case the applied V is larger than V_c, and the potential has been considerably tilted so that the particle is no longer confined to the left local minimum, and can roll to the other well, reflecting the transition to the conductive branch in our measurement.

To explain the hysteresis, we consider the effect of damping. As we reduce V, the particle will return to left minimum at a smaller V_r, *if* the friction of the right "well" is large or if the well is deeper. The finite distribution of V_c and V_r values reflects the role of thermal fluctuations, which may stochastically push the particle to the other minimum when V is close to the threshold. As in JJ, the ratio V_c/V_r can be related to dissipation (or perhaps relative depth of the 2 minima in our case).

This toy model is rather crude, but gives us certain insights into the system. Further theoretical studies will be necessary to fully understand this intriguing phenomenon.

Conclusion

In summary we have discussed *I-V* measurements at the CNP in the QH regime using our ultra clean suspended dual gated devices. We find that: (1) *IV* curves display sharp jumps between insulating and conducting branches, similar to the *VI* curves of an underdamped Josephson junction. (2). The IV curves of high mobility samples are hysteretic. (3). The size of the hysteresis increases with B, but decreases with T, and can be reduced by even minute $E_{\perp}$. (4). The threshold voltage values that underlie the

transitions display a finite-width distribution, likely due to stochastic switching induced by thermal fluctuations. The data strongly resemble those of an underdamped JJ, and lend us insight into the system, though a microscopic theory will be warranted to truly understand our results.

This chapter concludes our focus on the CNP in BLG and in the next chapter we will focus on bias spectroscopy measurements in QH regime at finite n. We expect bias dependent measurements will prove to be useful in unraveling the correlation physics in SLG and other multilayer graphene systems. For the multilayer systems it will be crucial to use a dual gated system since $E_{\perp}$ is likely to have a strong effect. Finally, more studies can be performed on BLG to further elucidate the nature of the hysteresis loops. For instance, the loops could be studied with increasing $B_{||}$ in the QH regime to determine if spin has an important role.

References

1. Y. Zhao, P. Cadden-Zimansky, Z. Jiang and P. Kim, Phys. Rev. Lett. **104** (6), 066801 (2010).

2. B. E. Feldman, J. Martin and A. Yacoby, Nat. Phys. **5** (12), 889-893 (2009).

3. M. Kharitonov, preprint, arXiv:1105.5386v1101 (2011).

4. F. Zhang and A. H. MacDonald, Physical Review Letters **108** (18), 186804 (2012).

5. M. Tinkham, *Introduction to Superconductivity*, Second Edition ed. (McGraw-Hill Book Co., 1996).

6. J. Velasco, L. Jing, W. Bao, Y. Lee, P. Kratz, V. Aji, M. Bockrath, C. N. Lau, C. Varma, R. Stillwell, D. Smirnov, F. Zhang, J. Jung and A. H. MacDonald, Nature Nanotechnol. **7**, 156 (2012).

Chapter 9: Bias spectroscopy at finite densities

Introduction

In this chapter I will discuss transport spectroscopy measurements of Landau level gaps in dual-gated suspended BLG, which is achieved by using source-drain bias voltage V as a spectroscopic tool in the quantum Hall regime. This measurement is similar to the studies presented in chapter six on the ν =0 state. The major difference is that in this chapter we will focus on the finite n regime. Specifically, plotting the device's two-terminal differential conductance $G=dI/dV$ as a function of V and n yields a series of distinct diamonds, which correspond to and evolve with QH plateaus. These diamonds arise from charge transport across graphene when the Fermi level is aligned to or detuned from Landau levels in the bulk of the device, and yield information on the bulk gap and edge channel transport. Using this technique, and exploiting our additional gate, we measure the evolution of ν=±4, -2 and -1 gaps as a function of magnetic field B(in the QH regime) in zero and finite $E_\perp$. We find the ν=±4 gap is independent of $E_\perp$ and scales linearly with B, yielding an effective mass of ~0.03 m_e, in agreement with prior theoretical and experimental results [1-4]; hence, establishing this technique as a viable alternative to thermal activation measurements for acquiring QH gaps. Additionally, we find In contrast to the ν=4 states, the ν=-2 and -1 gaps are strongly $E_\perp$-dependent. Our results demonstrate a new simple and direct transport measurement of Landau level gaps, and provide valuable insight into the QH ferromagnetism in BLG. Moreover, this technique can be extended onto SLG or other multilayer systems, which will be discussed in the last chapter of the thesis.

9.1: Broken Symmetry states in BLG

As discussed in previous chapters, bilayer graphene (BLG) hosts a plentitude of unusual QH phenomena, such as the Berry's phase of 2π[5], a unique state at filling factor ν=0 with diverging Hall *and* longitudinal resistance[6], quantum Hall ferromagnetism[7-9], and electric-field driven transitions between quantum Hall states[10, 11]. In particular, breaking the 8-fold degeneracy of the lowest Landau level has been a rich topic of study, since it is related to electronic interactions and competing symmetries. Though the complete lifting of the 8-fold degeneracy has been observed[6, 8], the exact nature of the symmetry-broken QH states (ν=0, 1, 2 and 3) remains under intense debate, partially due to the limited knowledge about the gap size Δ between the Landau levels.

The conventional technique of thermal activation measurement of $\rho_{xx}(T)$ [8] only yields the lower bound of Δ, due to smearing from disorders and other scatterers. Scanned probe studies such as scanning tunneling microscopy[12] or scanned single-electron transistor (SSET) measurements[13]often provide more accurate information, but they require specialized tools and are extremely difficult to perform on suspended devices (that afford the highest mobility to date) or double-gated devices (that allow simultaneous adjustment of out-of-plane electric field $E_{\perp}$ and charge density n). More importantly, the symmetry-broken QH states are expected to have layer polarization components, hence Δ should depend strongly on the out-of-plane electric field $E_{\perp}$. Yet, to date all measurements of Δ are performed on single-gated BLG devices [6, 8, 13], which, unlike dual

gated samples, cannot decouple modulation of n and $E_{\perp}$; thus study of the dependence of Δ with a *bona fide* control of $E_{\perp}$ has been lacking.

9.2: Bias spectroscopy measurements using a single gate

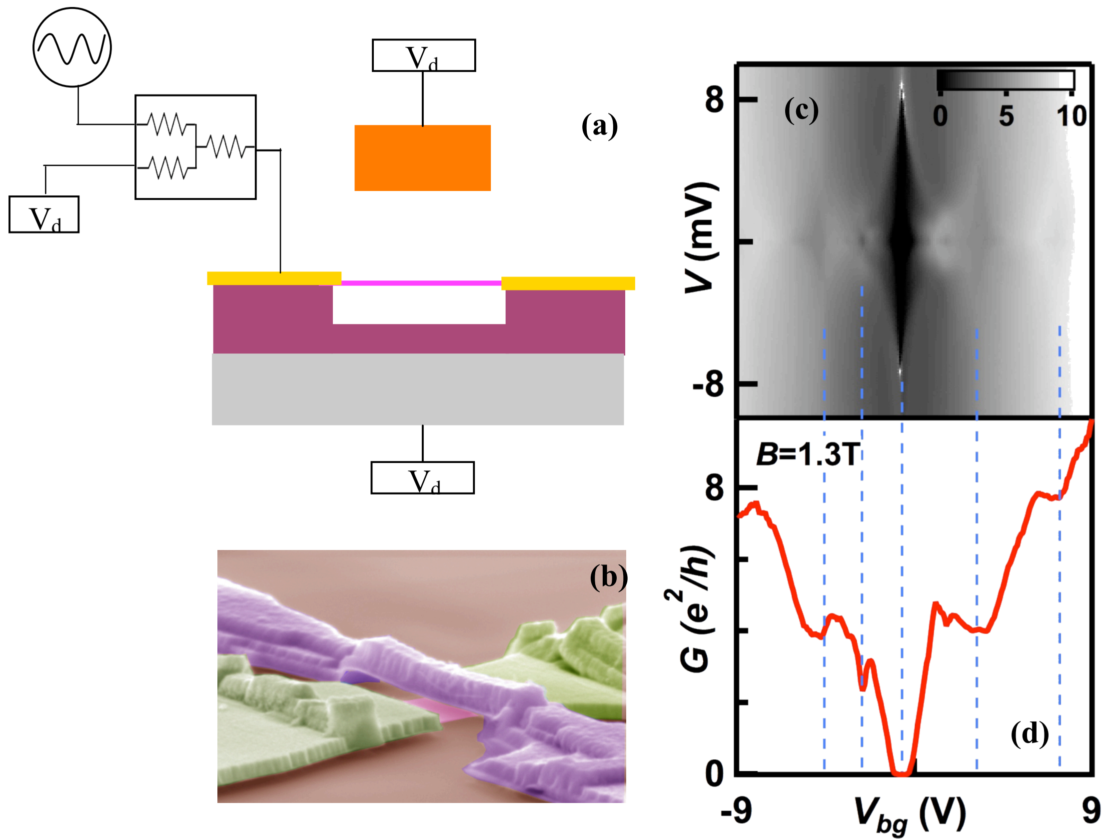

Fig 9.1: Measurement schematics and bias measurements with a single gate. a. Measurement schematic depicting suspended BLG(pink) clamped on at the ends by electrodes(gold), which are supported by remaining SiO_2 substrate(purple), and V_{bg} applied by Si below BLG, and V_{tg} applied by chrome air bridge above BLG. Source is biased by an AC and DC voltage simultaneously. b. False colored SEM image of device: electrodes are green, top gate is purple and graphene is pink. c. $G(V,V_b)$ measured at 250mK and B=1.3T. d. Line trace from $G(V_{bg},B)$ of fig 6.2 in chapter six with plateau that align in V_{bg} with diamonds in c.

The double-gated suspended BLG device depicted in fig 9.1b are fabricated using a multi-level lithographic technique, and released from the substrates by HF etching, as described in chapter three. The devices' field effect mobility values at T=260mK range from 20,000 to 150,000 cm^2/Vs. The presence of two gates allows independent adjustment of n and $E_\perp$. Here we focus on a BLG device with mobility ~ 80,000 cm^2/Vs (similar data were observed in more than 5 devices). Using the Landau fan diagram obtained by using only the back gate, similar to fig 6.2 of chapter six, we measure slopes of the plateaus, which yield the back gate coupling ratio (eq 4.1 from chapter four) of ~ 3.1×10^{10} $cm^{-2}V^{-1}$. The line trace $G(V_{bg})$ at B=1.3T is shown in fig 9.1d, displaying well-developed plateaus at ν=-2, ±4 and ±8. Interestingly, plot $G(V, V_{bg})$ at B=1.3T reveals a striking series of diamonds, whose centers line up with the conductance plateaus, as indicated by the dotted lines.

Such series of diamonds strongly resemble the Coulomb blockade data from a quantum dot, *i.e.* transport across a device with quantized energy levels. Combined with the perfect correspondence between the diamonds and QH plateaus, we thus attribute the quantized levels to Landau levels, which are energetically separated by Δ_ν.

9.3: Bias spectroscopy measurements using two gates

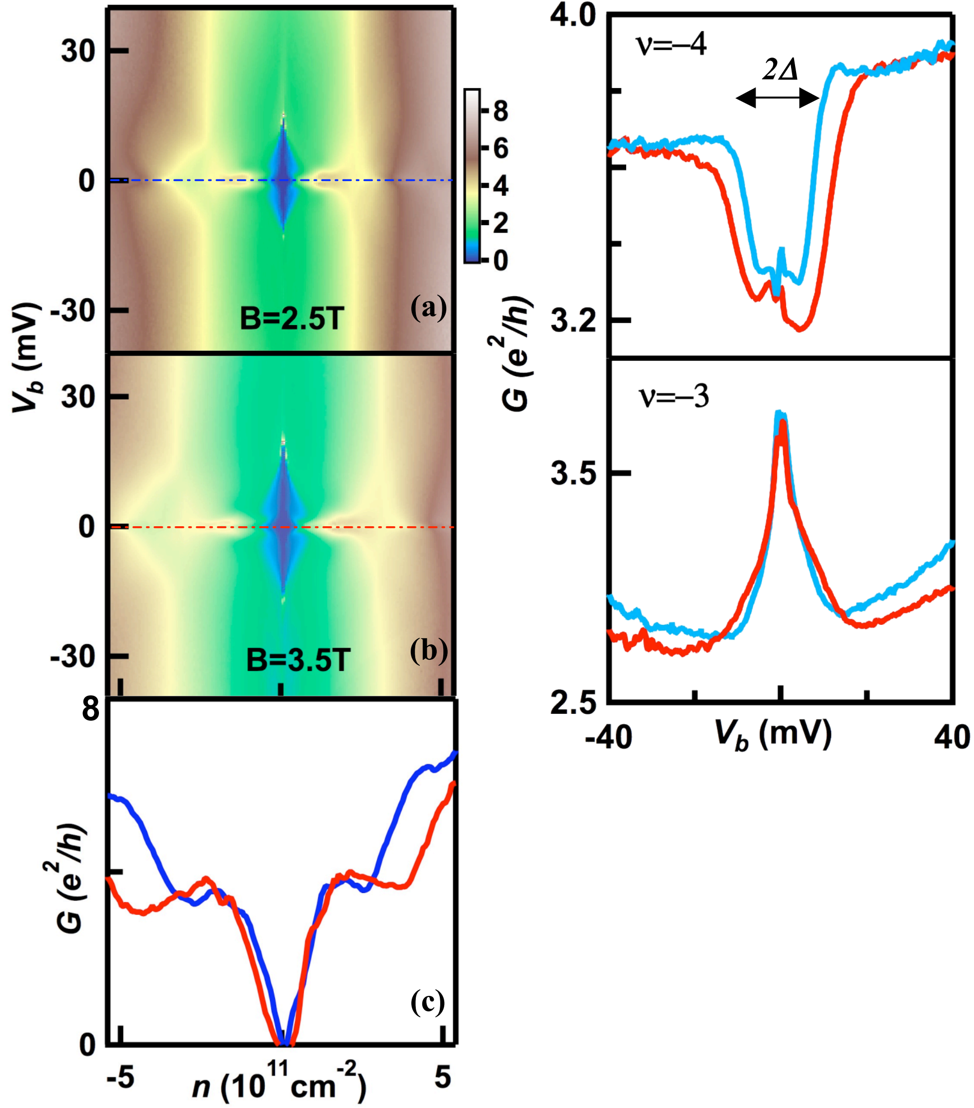

Fig 9.2: Bias measurements with dual gates at $E_\perp$=0, and in the QH regime. a. $G(V,n)$ at $E_\perp$=0 and B=2.5T and T=260mK. b. $G(V,n)$ at $E_\perp$=0 and B=3.5T and T=260mK. c. Line trace $G(V$=0, $n)$ from a. and b. d. Vertical line traces from a. and b. at n=-2.4x10^{11} and 3.5x10^{11} cm^{-2},respectively. e. Vertical line traces from a. and b. at n=-1.8x10^{11} and 2.63x10^{11} cm^{-2}, respectively.

Motivated by our observations from the previous section, and exploiting our additional gate, we examine $G(V,n)$ data at $E_{\perp}=0$,where, by using V we can spectroscopically resolve Δ, and systematically examine the effects on it from B, *n, and* $E_{\perp}$ by tuning each parameter independently. Fig 9.1a shows a schematic of such a measurement, where we apply a DC and AC signal simultaneously at the source while modulating both top and bottom gates. Fig 9.2a-b plot the resulting data sets at two different magnetic fields, B=2.5T and 3.5T, respectively. At zero bias, the ν=0 and ±4 plateaus in both data sets are well-developed (fig 9.2c). In fig 9.2a, the prominent diamond centered at n=-2.4x10^{11} cm^{-2} correspond to the center of ν=-4 plateau; a line trace $G(V)$ at this density displays a U-shaped conductance valley around zero bias (fig 9.2d, blue line). Similarly, at larger B=3.5T, the ν=-4 plateau corresponds to the diamond centered at 3.5x10^{11} cm^{-2}, at which $G(V)$ shows a *wider* conductance valley (fig 9.2d, red line). On the other hand, at ν~-3, zero bias conductance *peaks* appear in both data sets (fig 9.2e), which is consistent with the absence of a diamond feature at n=-1.8x10^{11} cm^{-2} and -2.63x10^{11} cm^{-2} the density corresponding to ν~ -3 at B=2.5T.

9.4: Model behind the measurement technique

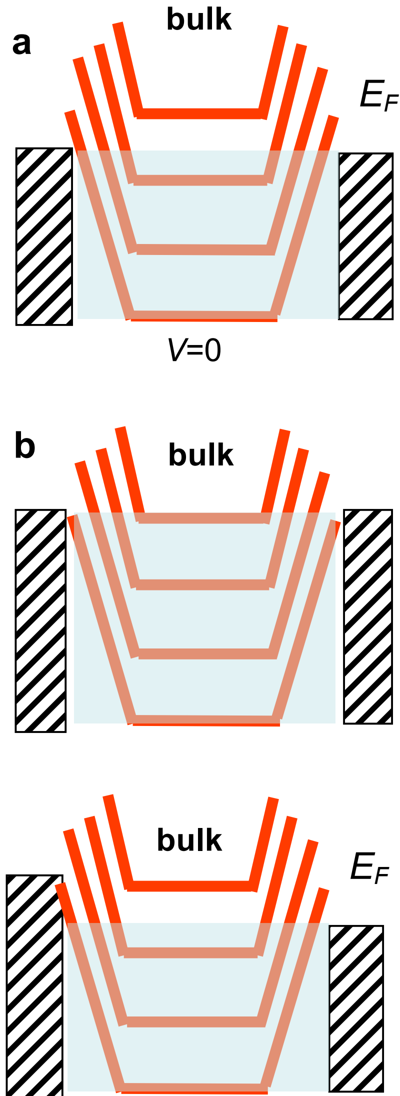

Fig 9.3: Model for bias spectroscopy. a. Red lines correspond to discrete energy bands (LL) plotted as a function of position, and the rectangle with dashed lines are the electrodes, light blue region is the Fermi energy E_f. Modulation of gates adjusts $E_\perp$ and E_f. When BLG E_f is tuned to above a LL transport is dominated by edge states. Adjusting bias allows access to the next unfilled LL, hence at zero bias there will be a dip. On the other hand, when E_f in BLG is tuned to an empty or partially filled LL transport is dominated by the bulk. Adjusting bias detunes BLG from the bulk transport, and results in a peak at zero bias.

Our experimental observations can be understood by considering ballistic transport of the device, where any applied bias induces voltage drop *only* at the two electrode-graphene interfaces, akin to that in tunneling spectroscopy measurements. In the QH regime, the measured conductance consists of contributions from both the bulk and the edge channels: when BLG's Fermi level is located between LLs, the bulk of the device is gapped, and charges are carried by edge states; conversely, when an integer number of LL is partially filled, transport occurs mainly via the gapless bulk. For simplicity, we assume zero conduction from the bulk when it is gapped and neglect any hopping conduction. Hence, when the zero-bias conductance is at the center of the QH plateau, the bulk of the device is gapped and the electrodes' Fermi level is pinned between the highest filled and the next unfilled LLs. Increasing bias raises the source's Fermi level, which eventually aligns with the next unfilled LL (fig 9.3b) that allows additional charge transport through the bulk, thereby leading to increased conductance. As a result, the device displays a conductance valley at V=0. On the other hand, when G is between the plateaus, the electrodes' Fermi level is aligned with the highest filled LL (denoted by the blue region in fig 9.3c), thus allowing transport through the bulk. Increasing bias detunes from the LL and disallows bulk transport, thus leading to lower current, and an overall conductance peak at V=0.

Based on this simple model, we can spectroscopically resolve LL gaps by examining the $G(V)$ curves at the center of a QH plateau. The conductance at V=0 yields the edge state contribution, whereas the full width of the conductance valley yields 2Δ, where Δ is the gap between the filled and unfilled LLs. As was noted in chapters six-

eight, the factor of 2 arises from the symmetric voltage drop at the two electrodes. We also note that a crucial component of the model is the ballistic transport of charges in the devices. Indeed, for devices with lower mobility, the diamond features are often smeared and difficult to resolve.

9.5: Bias spectroscopy measurements of $\Delta_{\nu=\pm 4}$

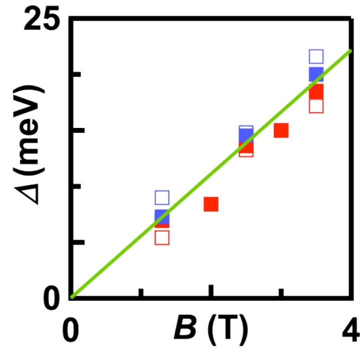

Fig 9.4: $\Delta_{\nu=-4}(B)$ at $E_\perp$=0 and finite $E_\perp$. The $\Delta_{\nu=-4}$ was acquired from $G(V,n)$ maps at finite and zero $E_\perp$. The gap size is linear with increasing B and independent of $E_\perp$.

To test this technique, we first apply it to the ν=±4 state that has a well-established gap. As shown in chapter two, the single particle LL spectrum of BLG is $E = \pm \frac{\hbar eB}{m^*}\sqrt{N(N-1)}$, where h is Planck's constant, e is electron charge, B is magnetic field, N=..-1, 0, 1… is an integer denoting the LL index, m^*~0.02 – 0.04m_e is the effective mass of the charge carriers, and m_e is electron's rest mass[14]. Hence $\Delta_{\upsilon=4} = \sqrt{2}\frac{\hbar eB}{m^*}$. To this end, we take $G(V)$ traces at ν=±4 and different magnetic fields between 1.3 and 3.5 T, and measure half-widths of the conductance dips. At each B, we

also measure $\Delta_{\nu=\pm 4}$ at zero and finite (-14.4 mV/nm) electric field $E_{\perp}$. The resultant data are shown in fig 9.4. All the data points fall on a single straight line, with a best-fit slope 5.5 mV/T, which corresponds to $m^{*}\approx 0.03 m_e$. Both the linear dependence on B and the effective mass are in excellent agreement with theoretical calculations[3, 4] as well as prior experiments [1, 2]. The independence of $\Delta_{\nu=\pm 4}$ of $E_{\perp}$ is also expected, since this is a single particle gap that does not involve layer polarization. Thus our results demonstrate bias spectroscopy as a powerful tool to determine LL gaps, which in this case are the single particle LL gaps. The gaps of the broken-symmetry states exhibit different behavior.

9.6: Bias spectroscopy measurements of the broken symmetry states

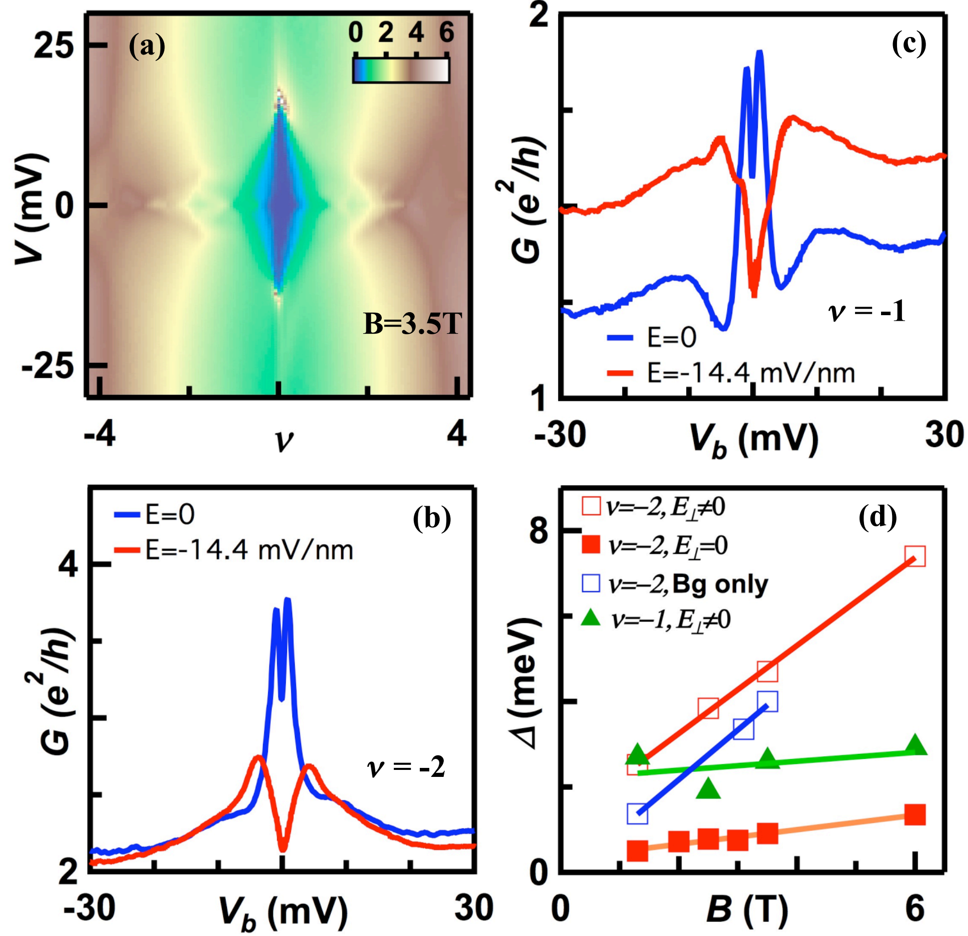

Fig 9.5: Bias spectroscopy measurements of broken symmetry states. a. $G(V,n)$ at B=3.5T and $E_\perp$=-14.4 mV/nm. b.-c. $G(V)$ at ν=-2 and -1, respectively, from a. d. $\Delta_{\nu=-2}$ and $\Delta_{\nu=-1}$ plotted as a function of increasing B, and at finite and zero $E_\perp$.

We now focus on the symmetry broken ν=-2 and ν=-1 states, which arise from electronic interactions. Previous works[10, 11] have shown that these states are resolved in the presence of $E_\perp$, suggesting a layer polarization component. Indeed, the effect of $E_\perp$ is borne out by comparing the two $G(V,n)$ data sets at B=3.5T in fig 9.2b and 9.5a, which

are taken at $E_\perp$=0 and -14.4 mV/nm, respectively. The diamonds at ν=-2 and ν=-1 in the latter plot are significantly larger, indicating the increase of the LL gaps at finite $E_\perp$. At $E_\perp$=0, the $G(V)$ traces display only small conductance dips at zero bias (blue lines in fig 9.5b-c), suggesting only partial resolution of the LLs. In contrast, prominent zero-bias valleys appear at $E_\perp$=-14.4 mV/nm (red traces), indicating these states become fully resolved.

Fig 9.4a displays $G(V, n)$ at B=3.5T and $E_\perp$=-14.4 mV/nm. Comparing with the data at $E_\perp$=0 (fig 9.2a), the diamonds at ν=-2 and -1 are noticeably larger. Interestingly, this data set is similar to that acquired using only V_{bg}. For both states, the $G(V)$ curve display a conductance peak around zero bias at $E_\perp$=0, but a conductance valley at finite $E_\perp$ (fig 9.5b-c). The measured values of $\Delta_{\nu=-2}$ and $\Delta_{\nu=-1}$ are shown in fig 9.5d. At $E_\perp$=0, $\Delta_{\nu=-2}$ ~ 0.17 mV/T, but increases by more than five-fold to ~1.0 mV/T at modest $E_\perp$=-14.4 mV/nm. For the ν=-1 state, $\Delta_{\nu=-1}$ ~ 0.1 mV/T at $E_\perp$=-14.4 mV/nm, but is too small (<0.02 mV/T) to be resolved in the absence of $E_\perp$. We note that our measured values of $\Delta_{\nu=-2}$ and $\Delta_{\nu=-1}$ at finite $E_\perp$ agree with previous measurements obtained via scanned SET on single-gated BLG[13] ,which is reasonable, since single-gated devices will posses a finite $E_\perp$, and this will be further explored in the next section. Thus our data unambiguously demonstrate the strong dependence of $\Delta_{\nu=-2}$ and $\Delta_{\nu=-1}$ on $E_\perp$, and the importance of decoupling the effects of $E_\perp$ and n.

Table 9.1: Broken symmetry states Δ sizes. The Δ size for ν=-1 and -2 for from previous studies using a single gate configuration and from this study with a dual gate configuration where $E'_{\perp}$=0 or -14.4mV/nm.

		$\Delta_{\nu=2}$	$\Delta_{\nu=1}$
single-gated[13]		0.05 mV/T	0.01mV/T
single-gated [8]		1 mV/T	0.1 mV/T
This work	Single-gated	1.1 mV/T	
	$E_{\perp}$=14.4 mV/nm	1 mV/T	0.17mV/T
	$E_{\perp}$=0	0.1 mV/T	<0.05mV/T

9.7: Comparison between dual gate and single gate measurement and E_c

The striking disparities in gap sizes of the broken symmetry states between our single gated and dual gated measurements at $E_{\perp}$=0 indicate there is an appreciable $E_{\perp}$ in the former. To investigate the value of this unintentionally applied electric field $E'_{\perp}$ we calculate the field induced by V_{bg} while setting V_{tg}=0. Using a simple electro-static model of parallel plate capacitors above and below BLG, and a V_{bg} = -2.5V, which corresponds to ν=-2 state at B=1.3T, we find $E'_{\perp}$ ~ -8mV/nm. This value is not negligible, and about half of the $E_{\perp}$ in fig 9.5a, thus underscoring the significance of the dual gated device to adequately control the desired applied $E_{\perp}$.

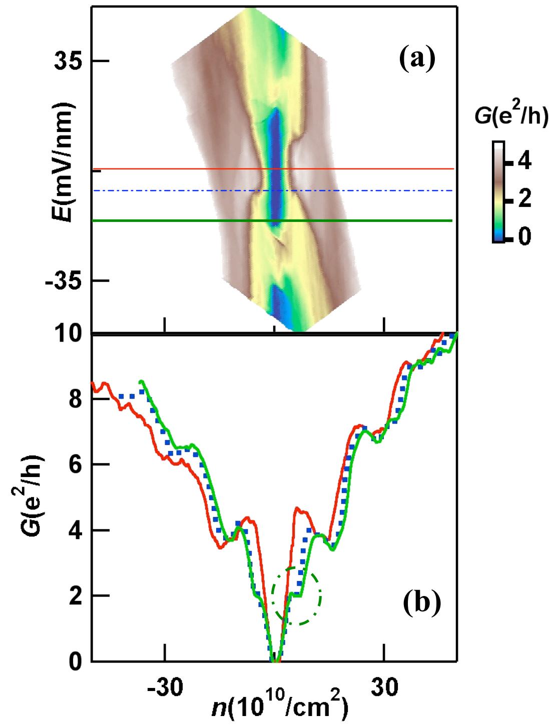

Fig 9.6: Dual gated transport measurements in the QH regime, and at 260mK. a. $G(E_{\perp},n)$ at B=1.3T. b. $G(n)$ at $E_{\perp}$=0(red), $E_{\perp}$=-8 mV/nm (green), and $E_{\perp}$=-14.4 mV/nm(dotted blue line). Note, ν=±2 states emerge at $E_{\perp}$=-8 mV/nm and are stabilized with increasing $E_{\perp}$.

To further understand the rich behavior of the broken symmetry states as a function of $E_{\perp}$ we plot, in fig 9.6, the G (color scale) as a function of $E_{\perp}$(vertical axis) and n(horizontal axis) at B=1.3T. In the center of the data set, *i.e.* at n=0 and small $E_{\perp}$, the blue region corresponds to the ν=0 QH state, and as discussed in previous chapters, its dependence on $|E_{\perp}|$ suggests the existence of two distinct insulating states arising from the competition between B and $E_{\perp}$. Now focusing on the finite density regime, the yellow and brown regions correspond to the ν=±2 and ±4 QH states, respectively. For large $E_{\perp}$,

these regions appear as vertical bands, indicating that they are independent of $E_\perp$. However, for small $E_\perp$, the yellow ν=±2 states are "interrupted" by the brown ν=±4 states, with an apparent critical value $|E_\perp|$>~ 7 mV/nm. In other words, the ν=±2 states are resolved for $E_\perp$>~ 7 mV/nm, but absent otherwise. This can be clearly seen in line traces. In fig 9.6b, the red line trace is taken at $E_\perp$=0, and only states ν =±4 and higher are seen; however, ν= -2 appears for the dotted blue and solid green lines, which are taken at $E_\perp$~ -8mV/nm and -14mV/nm. Interestingly, since single-gated BLG experience an $E_\perp$~ -8mV/nm at B=1.3T, ν= -2 state is resolved, as shown in fig 9.1. Hence, we conclude that, due to the strong dependence of the broken symmetry states on $E_\perp$, dual gated devices are critical for independent control of $E_\perp$ and n.

To further explore the $E_\perp$-dependence of the broken symmetry states in finite B we perform measurements at larger B. Fig 9.6c plots $G(n,E)$ B=6T. At this much large B, the vertical bands corresponding to QH states are more robust. The blue band, which is the ν= 0 QH state, spans the entire scan, while the green and yellow bands, which are the ν=1, and 2 states, respectively, abruptly end at small $E_\perp$ values. This behavior is more evident in vertical line cuts at finite n corresponding to each state, which is plotted on the right. For both states, the constant conductance at moderate $E_\perp$ abruptly jumps up to ~ 3-4 e^2/h, suggesting a first-order phase transition at critical $E_{\perp,c}$~6-8mV/nm. Interestingly, this critical $E_\perp$ value has no (or extremely weak) dependence on B.

In summary, the key points regarding the behavior of the broken symmetry QH states in $E_\perp$ are: 1) a relatively modest critical $E_\perp$, *e.g.* that induced by a single gate, is

sufficient to establish these states; and 2) the transition is exceedingly sharp and robust, and appears constant between 1~8T.

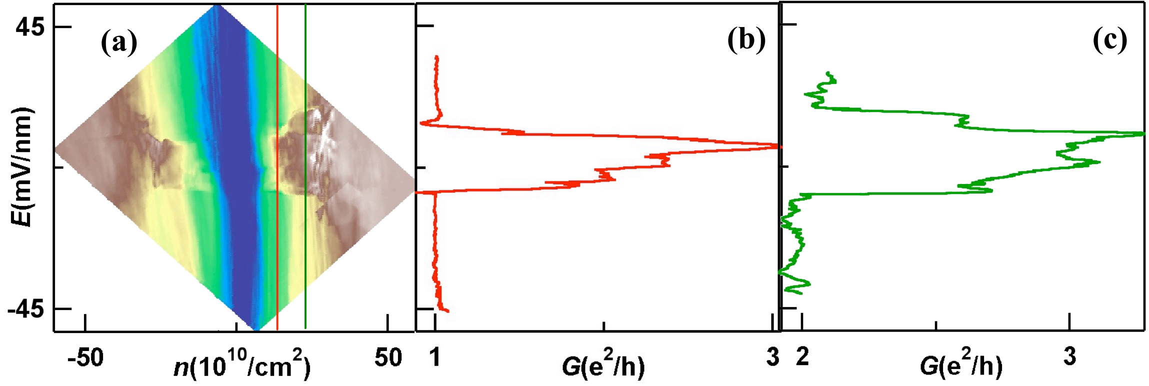

Fig 9.7: Dual gated transport measurements in the QH regime, and at 260mK. a. $G(E_\perp,n)$ at B=6T. b-c. $G(E_\perp)$ at ν=1(red) and ν=2(green). Note, ν=1 and 2 exhibit sharp transitions driven by $E_\perp$.

Conclusion

Taken together, our experimental observations indicate: 1) the ν=4 and the $\Delta_{\nu=\pm4}$ are not affected by a finite $E_\perp$, hence this state does not contain a layer polarization component; 2) broken symmetry states ν=±1, ±2,and their respective gaps are depended on $E_\perp$, thus these states have a layer polarized component; 3) single gate measurements, similar to fig 9.1 and[8, 13], suffers from an unintentional $E'_\perp$ component that scales with gate voltage, thus do not yield the intrinsic values of Δ; and 4). for relatively small B, the ν=±1 and ±2 states are resolved only when applied $E_\perp$ exceeds a certain critical value (we anticipate that at sufficiently large B, these states will be resolved even at $E_\perp$=0, but possibly with different broken symmetries). Our novel study provides the first

measurement of the intrinsic values of these gaps and their dependence on $E_{\perp}$, and can be used for the investigation of broken symmetries in other multilayer graphene systems

This concludes the experimental discussion on BLG in the thesis. We now move onto the final results on transport measurements of suspended dual gated ABA TLG in the QH regime.

References

1. S. Cho and M. S. Fuhrer, Nano Res. **4**, 385 (2011).

2. E. A. Henriksen, Z. Jiang, L.-C. Tung, M. E. Schwartz, M. Takita, Y.-J. Wang, P. Kim and H. L. Stormer, Phys. Rev. Lett. **100**, 087403 (2008).

3. E. V. Castro, N. M. R. Peres and J. M. B. L. d. Santos, Phys. Stat. Sol. B **244**, 2311 (2007).

4. G. Borghi, M. Polini, R. Asgari and A. H. MacDonald, Solid State Commun. **149**, 1117-1122 (2009).

5. K. S. Novoselov, E. McCann, S. V. Morozov, V. I. Fal'ko, M. I. Katsnelson, U. Zeitler, D. Jiang, F. Schedin and A. K. Geim, Nat. Phys. **2** (3), 177-180 (2006).

6. B. E. Feldman, J. Martin and A. Yacoby, Nat. Phys. **5** (12), 889-893 (2009).

7. Y. Barlas, R. Cote, K. Nomura and A. H. MacDonald, Phys. Rev. Lett. **101** (9), 097601 (2008).

8. Y. Zhao, P. Cadden-Zimansky, Z. Jiang and P. Kim, Phys. Rev. Lett. **104** (6), 066801 (2010).

9. W. Z. Bao, Z. Zhao, H. Zhang, G. Liu, P. Kratz, L. Jing, J. Velasco, D. Smirnov and C. N. Lau, Physical Review Letters **105** (24), 246601 (2010).

10. R. T. Weitz, M. T. Allen, B. E. Feldman, J. Martin and A. Yacoby, Science **330** (6005), 812-816 (2010).

11. J. Velasco, L. Jing, W. Bao, Y. Lee, P. Kratz, V. Aji, M. Bockrath, C. N. Lau, C. Varma, R. Stillwell, D. Smirnov, F. Zhang, J. Jung and A. H. MacDonald, Nature Nanotechnol. **7**, 156 (2012).

12. G. Li and E. Y. Andrei, Nature Physics **3** (9), 623-627 (2007).

13. J. Martin, B. E. Feldman, R. T. Weitz, M. T. Allen and A. Yacoby, Phys. Rev. Lett. **105** (25), 256806 (2010).

14. E. McCann and V. I. Fal'ko, Phys. Rev. Lett. **96** (8), 086805 (2006).

Chapter 10: Broken Symmetry States in dual gated ABA TLG

Introduction

In this chapter I will discuss transport measurements on high mobility dual-gated ABA TLG devices in the QH regime. These devices were fabricated and current annealed using the methods discussed in chapter three, and exhibit robust QH conductance plateau originating from different underlying mechanisms. At low magnetic field B<4T, we resolve single particle QH states at filling factors ν=-8, -2, 2, 6, and 10, which can be accounted for by the “2+1” tight-binding model that includes all hopping parameters[1]. At higher B, we observe additional states at ν=±1, ±3, -4 and -5, indicating almost complete lifting of the degeneracy of the lowest LL, which for TLG is an impressive 12-fold degenerate. At constant B, application of an out-of-plane electric field $E_\perp$ gives rise to degeneracy breaking and transitions between QH plateaus, suggesting the interplay of layer polarization and B-enhanced exchange interactions of these states. Finally, depending on its polarity, we find the $E_\perp$ *selectively* breaks the LL degeneracy in the electron-doped or hole-doped regimes.

This chapter is the last experimental results of the thesis, and its focus on ABA TLG indicates one direction for future work. Because of its band structure ABA TLG is not expected to host a spontaneous gap at the CNP as found in BLG (chapters six and seven) or rhombrohedral multilayer graphene[2, 3]. Nevertheless, ABA TLG is interesting in its own right, because of its rich QH conductance spectrum, as will be discussed below. Previous chapters five and nine demonstrated for BLG in the QH regime that: 1) Exceedingly clean suspended samples facilitate the observation of broken symmetry

states, and 2) The nature of these broken symmetry states is highly depended on $E_\perp$. In this chapter we benefit from those lessons learned in BLG, and focus on the QH regime for ABA-TLG with control of $E_\perp$. Our study demonstrates the suspended dual gated device architecture is a great tool to unravel this rich physics.

10.1: QHE in ABA Trilayer Grapehene, sibling rivalry

As a fascinating surface two-dimensional (2D) system with massless chiral charge carriers and spectacular electronic, mechanical and thermal properties, graphene and its multilayer relatives[4-6] have emerged as new platforms for investigation of QH physics. A number of novel phenomena have been observed, such as multicomponent fractional QH effect in single layer graphene(SLG)[7], insulating ν=0 states in SLG and BLG[8-11], which were studied in chapter six, electric-field driven transitions among symmetry-broken QH states in BLG[12-14], which were discussed in chapters six and seven, and chiral charge carriers with berry phase of 3π[15] and Lifshitz transition in ABC-stacked TLG[2].

Like SLG and BLG, TLG also offers an exciting platform with unique band structures. In particular, ABA-stacked TLG hosts a unique mirror symmetry (fig 10.2b), and its band structure can be viewed as a combination of the linear dispersion of SLG and parabolic dispersion of BLG, *i.e.* the so-called “2+1” model within tight-binding calculations[16-24] (fig 10.2a). Though TLG has attracted more attention in the past year[15, 25-31], the nature of broken symmetry QH states in TLG and their evolutions under electric and magnetic fields remain experimentally unexplored. In particular, studies with dual

gates on ABA TLG have been lacking, and the few that exist are relegated to single particle QH physics because of disorder.

10.2: Device characterization

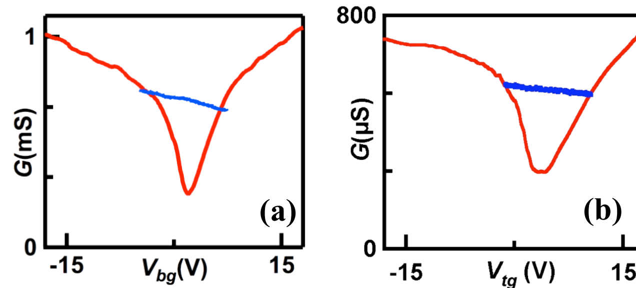

Fig 10.1:Before and after current annealing. a-b. $G(V_{bg})$ and $G(V_{tg})$ before(blue) and after(red) current annealing.

TLG sheets are isolated via mechanical exfoliation on Si/SiO_2 substrates, identified by optical contrast and Raman spectroscopy, and coupled to Cr/Au electrodes and Cr suspended top gates[32, 33], and completed by removal of SiO_2 under the graphene with HF etching, as was described in chapter three. All data presented in this chapter are taken at 300mK in He^3 refrigerators, and similar phenomena are observed in 3 devices.

As with SLG and BLG, the TLG devices dramatically improved after current annealing. Fig 10.1 displays the two-terminal conductance G as a function of back gate V_{bg} before (blue curve) and after (red curve) current annealing, a similar plot is shown for G as a function of top gate V_{tg}. After annealing, the curve becomes 'V'-shaped, with charge neutrality close to zero, drastically lower minimum conductance, and high field effect mobility of ~15,000 cm^2/Vs.

10.3: The band structure of ABA TLG

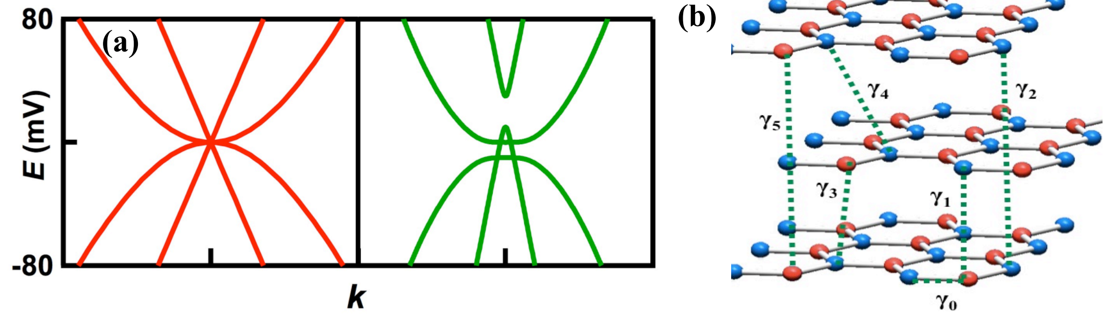

Fig 10.2: The band structure of ABA TLG. a. Low energy band structure of ABA-stacked TLG calculating (left panel) using only γ_0 and γ_1, (right panel) using $\gamma_0 - \gamma_5$. b. ABA-stacked TLG lattice with hopping parameters γ_1- γ_5.

In the simplest tight binding model that includes only the nearest neighbor in-plane and inter-plane hopping parameters γ_0 and γ_1, the band structure of ABA-stacked TLG consists of the SLG-like and BLG-like branches touching at a single point (fig 10.2a, left panel). In sufficiently large applied *B*, the charges' cyclotron orbits coalesce to form discrete LL, with energy given by[16, 34-36]:

$$E_{M,N} = \pm\sqrt{2\hbar v_F^2 eB|N|} \quad \text{and} \quad E_{B,N} = \pm\frac{\hbar eB}{m^*}\sqrt{N(N-1)} \qquad (10.1)$$

The lowest LL is 12-fold degenerate, giving rise to quantized plateaus at filling factors $\nu=nh/Be=$...-10, -6, 6, 10, 14…. Here *e* is electron charge, *n* the induced charge density, *h* Planck's constant, v_F~10^6 m/s the Fermi velocity, m^*=0.02-0.04 m_e, m_e the electron rest mass, and *N* is an integer denoting the LL index.

10.4: Single particle QH states in ABA TLG

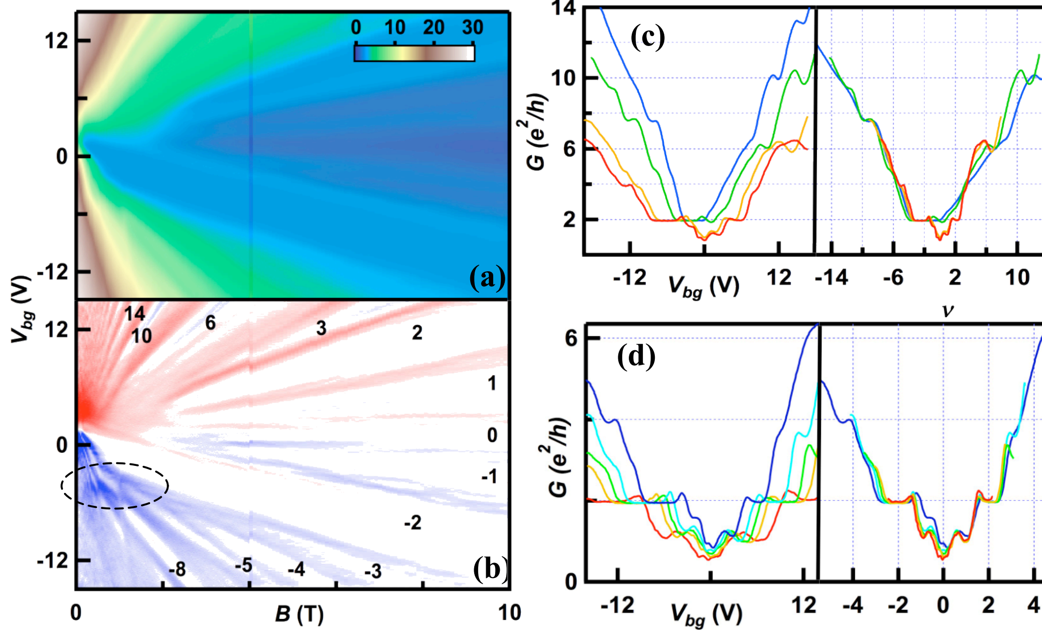

Fig 10.3: Transport measurements at 260mK and in the QH regime. a-b. $G(V_{bg},B)$ and dG/dV_{bg} of a TLG device. Numbers indicate filling factors. c. $G(V_{bg})$ and $G(n)$ at B=1.5, 2.2, 3.5 and 4.2 T, respectively. d. $G(V_{bg})$ and $G(n)$ at B=4.5, 6, 7, 8 and 10 T.

Fig 10.3a shows the standard LL "fan diagram" of the device, *i.e.* G (color scale) as a function of V_{bg} (horizontal axis) and B (vertical axis). The QH plateaus appear as the colored bands that diverge from B=0 and the CNP. From the fan diagram, the back gate's coupling efficiency is determined using the method outlined in chapter four by eq 4.1, and estimated to be α_{bg}~3.8x10^{10} cm^{-2}/V.

To accentuate the evolution of the QH plateaus with V_{bg} and B, we plot dG/dV_{bg} (V_{bg}, B) of the same data set in fig 10.3b, similar to our discussion with BLG of chapter five fig 5.1. The filling factor of each plateau, which appears as a white band,

$\nu = nh/Be = \alpha_{bg} V_{bg} h/Be$, is calculated from its slope in the V_{bg}-B plane and labeled in fig 10.3b. The most prominent feature is the very strong ν=-2 plateau in the hole-doped regime, which is resolved at B as small as 0.25T. (Here we define hole-doped and electron-doped regime to have negative and positive filling factors, respectively.) Line traces $G(V_{bg})$ at several B values for $B<4.2$T are shown in fig 10.3c. When replotted as a function of ν, the traces nearly collapse into a single curve, with properly quantized plateaus at ν=-2, 2, 6 and 10.

The appearance of robust ν=6 and 10 states agrees with Eq. (10.1), and agrees with prior reports[27, 29, 31]. On the other hand, our observation of the $\nu=2$ and in particular the exceedingly robust ν=-2 plateaus, is unexpected from Eq. (10.1). This can however be accounted for by the "2+1" model that takes remote hopping into account – instead of SLG-like and BLG-like bands both touching at a single point, including next-nearest hopping parameters (γ_2 and γ_5) leads to bands that are individually gapped, with a relative vertical offset between the SLG-like and BLG-like bands, whose tops of valence bands are located at $-\gamma_2/2$ and $\gamma_2/2$, respectively (fig 10.2a, right panel). Such a band structure is a departure from the flat bands found in BLG, which host the spontaneous gaps discussed in chapters six and seven. Yet, this difference in energy spectrum by no means diminishes the richness of physical phenomena in ABA TLG. Consequently, the LL spectrum of such a band structure is modified from Eq. (10.1) as follows: (1). the valley degeneracy of the lowest LL is broken[1], manifesting as $\nu=\pm 2$ plateaus, as observed experimentally; (2). the spectrum is particle-hole asymmetric, and (3). LLs originating from the SLG-like and BLG-like bands cross at energy $\sim -\gamma_2/2$.

All three features are observed in our experimental data. Apart from the robust $\nu=\pm 2$ plateaus, the particle-hole asymmetry is clearly reflected in the sequence of resolved plateaus -- the $\nu=6$ and 10 plateau is observed only in the electron doped regime, and $\nu=-8$ solely in the hole-doped regime. The dark blue feature at $V_{bg}\sim$ -5V, indicated by the dotted circle in fig 10.3b, corresponds to the crossings between LLs that belong to the SLG and BLG-like spectra. From the data, the crossings occur at ~1.9×10^{11} cm^{-2}, corresponding to ~8 meV. Thus our data suggest $\gamma_2\sim$-16 meV in TLG, in reasonable agreement with the value from bulk graphite, -20 meV[37].

10.5: Interaction induced QH states in ABA TLG

10.5.1: QH states resolved with one gate

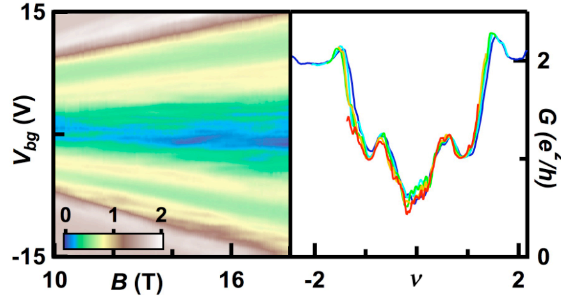

Fig 10.4: Transport measurements at 260mK and in the QH regime. e. $G(V_{bg},B)$ and $G(n)$ at B=10, 12, 14, 16 and 18T.

Thus far the ν=-2, 2, 6, and 10 plateaus are well accounted for by single particle tight binding calculations. At larger B, we also observe additional plateaus at ν=±1,±3,-4 and -5, which indicate almost complete lifting of spin, valley and orbital degeneracies. The ν=0 plateau, although resolved, is ~ 0.3 e^2/h at 18T. This lack of true insulating behavior is likely due to the presence of small amount of residual impurities, and can also be attributed to the crossing bands, which are shown in fig 10.2a-right panel, thus obscuring the insulating state. Fig 10.3c-d plots $G(V_{bg})$ and $G(\nu)$ at B=4.5, 6, 7, 8 and 10T, respectively, showing excellent conductance quantization. The ν=±1 plateaus are resolved at B as low as 4.5T, and persists to 18T (fig 10.4), the highest available field.

These additional plateaus cannot be accounted for by any tight binding model, and their appearance at high B values in samples with high mobility (≥10,000 cm^2/Vs) strongly suggests symmetry breaking arising from electronic interactions. In fact, they

can be qualitatively understood in terms of QH ferromagnetism and Hunds rule-like filling of the LLs[38]. Within this model, the LLs between ν=-6 and 6 are filled in the order of maximizing spin, chirality (BLG branch first), valley and orbital indices. At large *B*, the ν= -5, -4, -3, -2, 1, 2 and 3 states belong to the BLG-like branch, while the ν=−1, 0, +4 and +5 states to the SLG-like branch[38]. As observed experimentally, all the BLG-like states are fully resolved, whereas only the ν=−1 (and to some extent the ν=0) state in the SLG-like branches is observed. This is consistent with previous observations that the QH ferromagnetic states in BLG are more easily resolved, due to its enhanced density of states and stronger electronic interactions in BLG.

10.5.2: QH states resolved with dual gates, the role of $E_{\perp}$

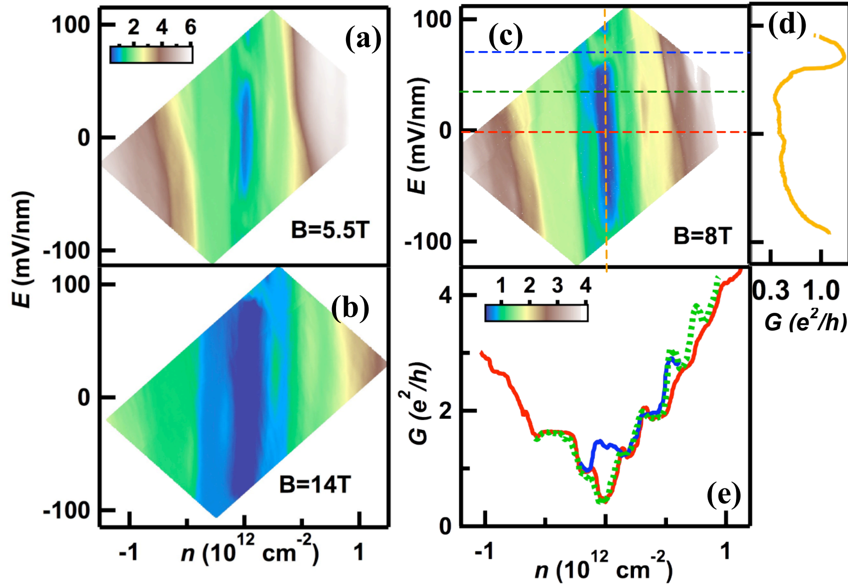

Fig 10.5: Transport measurements at 260mK, and in the QH regime with dual gates. a-c. $G(n,E_{\perp})$ at B=5.5, 14 and 8T. d. $G(E_{\perp})$ along the vertical line in c. at n=0. e. $G(n)$ along the horizontal lines in c. at $E_{\perp}$=0 (red), 43 (green dotted line) and 73 mV/nm (blue), respectively.

We now focus on the QH states in the presence of both top and back gates. Sweeping both top and back gate voltages enables independent modulation of the electric field $E_{\perp}$ and total charge carrier density n in TLG, which has emerged as a critical tool to study the broken symmetry states in bilayer graphene[12, 13] as was shown extensively in the previous chapter. For ABA-stacked TLG, $E_{\perp}$ breaks its mirror reflection symmetry, and is expected to give rise to otherwise unresolved plateaus or the stabilization of existing plateau with finite $E_{\perp}$.

In fig 10.5a-c G (color scale) is plotted as a function of $E_\perp$ (vertical axis) and n (horizontal axis) at B=5.5, 8 and 14T, respectively. The vertical color bands correspond to the conductance plateaus at different filling factors. Fig 10.5d plots $G(n)$ at B=8T and $E_\perp$=0, 43 and 73 mV/nm, respectively. At $E_\perp$=0, plateaus ν=0, 1, 2 and 3 are observed. At $E_\perp$=43 mV/nm, the first 3 plateaus remain almost unchanged, whereas the ν=3 plateau is better resolved, and the ν=4 plateau emerges. Thus, our data suggest that layer polarization is an important component in the ν=3 and 4 states.

Another striking feature in these $G(n, E_\perp)$ plots is the dependence of the ν=0 plateau on $E_\perp$: it abruptly increases from 0.3 to ~1 e^2/h at a critical $E_{\perp c}$ value, and decreases to 0.3 again for a larger $E_\perp$ (fig 10.5d). The $G(n)$ trace at $E_{\perp c}$ is characterized by the absence of the ν=0 plateau (fig 10.5e, blue line). Taken together, our data establish transitions between spin- to layer-polarized states driven by B and $E_\perp$, respectively, and is highly reminiscent of that in BLG[12, 13], (see fig 6.9 in chapter six).

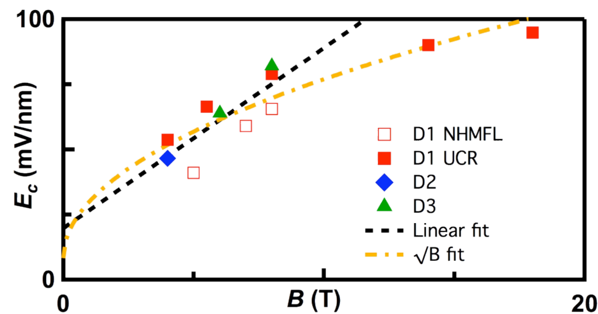

Fig 10.6: Critical electric field E_c plotted as a function of increasing B. $E_{\perp c}(B)$ from 3 different devices. The black and orange lines correspond to linear and $B^{1/2}$ fits, respectively.

To further investigate the transition between the LLs, we examine the dependence of $E_{\perp c}$ on B. In BLG, $E_{\perp c}$ is linearly dependent on B, with a slope ~ 13 mV/nm/T and extrapolates to a finite value ~ 12 mV/nm at B=0[12, 13], as was discussed in chapter six. Fig 10.6 plots $E_{\perp c}$ *vs.* B for 3 different devices (device D1 was measured at 2 separate locations). For B<8T, within the scatter in the data, $E_{\perp c}$ is approximately linear in B, with a best-fit equation $E_{\perp c}$ (mV/nm) = 19.7 + 6.9B. The finite intercept indicates the evolution of subband gaps at B=0 when mirror symmetry is broken by electric fields, or alternatively, a transition from spin-polarized to layer-polarized states that persists to zero magnetic field. Interestingly, when B is extended to 18T, the data points are no longer linear; instead, they can be adequately fitted to the equation $E_{\perp c} = 8.3 + 21.7\, B^{1/2}$, suggesting a $\sqrt{B}$ Coulomb interactions play an essential role at large B. There is little theoretical work on LL transitions in ABA-stacked TLG in the presence of electric and magnetic fields, and this phenomenon warrants further experimental and theoretical investigation.

Finally, we focus on a striking feature of the conductance in the presence of $E_{\perp}$ and B. Fig 10. 7 plots $G(E_{\perp},n)$ at B=7T. At finite E, the $G(n)$ traces are asymmetric with respect to electrons and holes. Interestingly, such asymmetry depends on the direction of the applied $E_{\perp}$, and reverses upon reversal of the sign of $E_{\perp}$. In Fig 10.7a, this asymmetry can be seen as the asymmetric appearance of the bright blue band to the right (left) of the charge neutrality point for positive (negative) $E_{\perp}$. Fig 10.7b plots the $G(n)$ curves at $E_{\perp}$=0, -17 and 13.6 mV/nm, respectively. The ν=-1 plateau was only resolved for $E_{\perp}$<0, whereas the ν=1 state was better resolved for $E_{\perp}$>0. Thus, $E_{\perp}$ appears to selectively break

the symmetry of LLs of the electron- or hole- doped regimes, depending on its polarity. We currently do not have explanation for this phenomenon. It may be related to the particle-hole asymmetry in TLG's band structure[39], or to more intriguing effects such as spin-orbit interactions or magneto-electric effects. Further experimental investigation will be necessary to fully elucidate its origin.

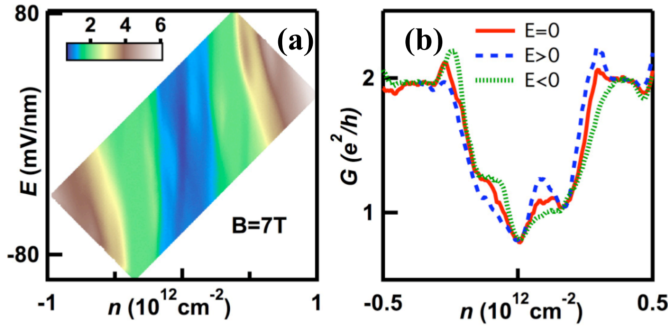

Fig 10.7: Transport measurements at 260mK, and in the QH regime with dual gates. a. $G(n,E_\perp)$ at B=7T. b. $G(n)$ at $E_\perp$=0 (red solid line), -17 (green dotted line) and13.6 mV/nm (blue dashed line).

Conclusion

In conclusion, using dual-gated high mobility samples, we observe several intriguing phenomena related to the broken symmetry QH states in ABA-stacked TLG, including almost complete lifting of the spin, valley and orbital degenerancies of the lowest LL, stabilization of some of these states by $E_\perp$, transition between LLs driven by $E_\perp$ and B, and a particle-hole asymmetry that depends on the polarity of $E_\perp$. Our study demonstrates the rich interaction physics in ABA TLG in the $E_\perp$-B phase space. A

number of unresolved questions, such as the dependence of $E_{\perp c}$ on B at large field, and dependence of the electron-hole asymmetry on $E_{\perp}$, await further studies.

Another promising future direction is to study the QH states using our bias spectroscopy technique, which was discussed in the previous chapter for BLG. Because study of the QH states in ABA TLG is in its infancy, there is much to be done. As of the writing of this thesis, there are no published studies on the gaps of single particle and broken symmetry states. Using our bias spectroscopy technique we could resolve these gaps, and with the aide of our additional gate study their dependence on $E_{\perp}$.

References

1. M. Koshino and E. McCann, Phys. Rev. B **83** (16), 165443 (2011).

2. W. Bao, L. Jing, Y. Lee, J. V. Jr., P. Kratz, D. Tran, B. Standley, M. Aykol, S. B. Cronin, D. Smirnov, M. Koshino, E. McCann, M. Bockrath and C. N. Lau, Nature Physics **7**, 948-952 (2011).

3. F. Zhang, J. Jung, G. A. Fiete, Q. A. Niu and A. H. MacDonald, Phys. Rev. Lett. **106** (15), 156801 (2011).

4. K. S. Novoselov, A. K. Geim, S. V. Morozov, D. Jiang, Y. Zhang, S. V. Dubonos, I. V. Grigorieva and A. A. Firsov, Science **306** (5296), 666-669 (2004).

5. M. S. Fuhrer, C. N. Lau and A. H. MacDonald, MRS Bulletin **35** (4), 289-295 (2010).

6. C. N. Lau, W. Bao and J. V. Jr., Materials Today **15**, 238-245 (2012).

7. C. R. Dean, A. F. Young, P. Cadden-Zimansky, L. Wang, H. Ren, K. Watanabe, T. Taniguchi, P. Kim, J. Hone and K. L. Shepard, Nature Phys. **7** (9), 693-696 (2011).

8. J. G. Checkelsky, L. Li and N. P. Ong, Phys. Rev. Lett. **100** (20), 206801 (2008).

9. J. G. Checkelsky, L. Li and N. P. Ong, Phys. Rev. B **79** (11), 115434 (2009).

10. Y. Zhao, P. Cadden-Zimansky, Z. Jiang and P. Kim, Phys. Rev. Lett. **104** (6), 066801 (2010).

11. B. E. Feldman, J. Martin and A. Yacoby, Nat. Phys. **5** (12), 889-893 (2009).

12. R. T. Weitz, M. T. Allen, B. E. Feldman, J. Martin and A. Yacoby, Science **330** (6005), 812-816 (2010).

13. J. Velasco, L. Jing, W. Bao, Y. Lee, P. Kratz, V. Aji, M. Bockrath, C. N. Lau, C. Varma, R. Stillwell, D. Smirnov, F. Zhang, J. Jung and A. H. MacDonald, Nature Nanotechnol. **7**, 156 (2012).

14. W. Bao, J. V. Jr., F. Zhang, L. Jing, B. Standley, D. Smirnov, M. Bockrath, A. MacDonald and C. N. Lau, Proc. Natl. Acad. Sci., to appear (2012).

15. L. Zhang, Y. Zhang, J. Camacho, M. Khodas and I. A. Zaliznyak, Nat. Phys. **7** (12), 953-957 (2011).

16. F. Guinea, A. H. Castro Neto and N. M. R. Peres, Phys. Rev. B **73** (24), 245426 (2006).

17. M. Aoki and H. Amawashi, Sol. State Commun. **142** (3), 123-127 (2007).

18. M. Koshino and E. McCann, Phys. Rev. B **79** (12), 125443 (2009).

19. F. Zhang, B. Sahu, H. K. Min and A. H. MacDonald, Phys. Rev. B **82** (3), 035409 (2010).

20. J. L. Manes, F. Guinea and M. A. H. Vozmediano, Phys. Rev. B **75**, 155424 (2007).

21. B. Partoens and F. M. Peeters, Phys. Rev. B **74** (7), 075404 (2006).

22. S. Latil and L. Henrard, Phys. Rev. Lett. **97** (3), 036803 (2006).

23. M. Koshino, Phys. Rev. B **81** (12), 125304 (2010).

24. Y. Shengjun, R. Roldaacuten and M. I. Katsnelson, Phys. Rev. B **84** (12), 125455 (2011).

25. M. F. Craciun, S. Russo, M. Yamamoto, J. B. Oostinga, A. F. Morpurgo and S. Thrucha, Nat. Nanotechnol. **4** (6), 383-388 (2009).

26. W. Z. Bao, Z. Zhao, H. Zhang, G. Liu, P. Kratz, L. Jing, J. Velasco, D. Smirnov and C. N. Lau, Physical Review Letters **105** (24), 246601 (2010).

27. T. Taychatanapat, K. Watanabe, T. Taniguchi and P. Jarillo-Herrero, Nat. Phys. **7**, 621 (2011).

28. C. H. Lui, Z. Li, K. F. Mak, E. Cappelluti and T. F. Heinz, Nat. Phys. **7**, 944 (2011).

29. E. A. Henriksen, D. Nandi and J. P. Eisenstein, Phys. Rev. X **2** (1), 011004 (2012).

30. S. H. Jhang, M. F. Craciun, S. Schmidmeier, S. Tokumitsu, S. Russo, M. Yamamoto, Y. Skourski, J. Wosnitza, S. Tarucha, J. Eroms and C. Strunk, Phys. Rev. B **84** (16), 161408 (2011).

31. T. Khodkov, F. Withers, D. C. Hudson, M. F. Craciun and S. Russo, Appl. Phys. Lett. **100** (1), 013114 (2012).

32. G. Liu, J. Velasco, W. Z. Bao and C. N. Lau, Applied Physics Letters **92** (20), 203103 (2008).

33. J. Velasco, G. Liu, W. Z. Bao and C. N. Lau, New Journal of Physics **11**, 095008 (2009).

34. J. W. McClure, Phys. Rev. **104** (3), 666-671 (1956).

35. E. McCann and V. I. Fal'ko, Phys. Rev. Lett. **96** (8), 086805 (2006).

36. M. Ezawa, J. Phys. Soc. Jpn. **76**, 094701 (2007).

37. M. S. Dresselhaus and G. Dresselhaus, Advances in Physics **51** (1), 1-186 (2002).

38. F. Zhang, D. Tilahun and A. H. MacDonald, Physical Review B **85** (16), 165139 (2012).

39. L. M. Zhang, M. M. Fogler and D. P. Arovas, Phys. Rev. B **84** (7), 075451 (2011).

Chapter 11 Conclusion and Outlook:

11.1 Conclusion:

The end of the thesis has arrived! In summary, the band structures of single-, bi- and tri-layer graphene differ dramatically, as was demonstrated in chapters two and ten, yet they are all similar in that they host competing symmetries (such as spin, valley and orbital) that may be broken spontaneously, as was seen in chapters six and seven or by an external field as was discussed in chapters five through ten. In this thesis we described and discussed our comprehensive transport studies on high quality double-gated single-, bi- and tri-layer graphene samples, which were enabled by our innovative fabrication techniques to reduce disorder. Our work has lead to further insight into single-particle and many-body physics in these fantastic 2D systems.

In the past few years there have been several exciting new developments in the quest for high quality graphene samples. The most important one is using hexagonal boron nitride as the substrate, as discussed below.

11.2: Boron-nitride based graphene samples

Sample on hexagonal Boron-Nitride (h-BN) is an alternative method to produce high quality devices[1]. h-BN is a suitable choice for a supporting substrate for the following reasons: 1) It has a crystal structure similar to graphene's, but since the sublattice symmetry is broken (boron and nitrogen atoms occupy different sublattices),it is a wide band gap material ~6eV, hence it is a good supporting dielectric, 2) Its Strong in-plane bonds minimizes dangling bonds, thus it is chemically inert and less susceptible

to charge traps than SiO_2, 3) As an atomically flat membrane BN should not induce ripples or other unwanted surface morphologies that promote momentum scattering[1].

Transferring exfoliated graphene onto exfoliated h-BN that is supported by a substrate, which is commonly SiO2, achieves a high quality device. This method was innovated by the Columbia group[1] and has been further developed by many transport groups[2, 3]. These samples are well supported, hence they are compatible with the standard Hall bar geometry, and were used successfully to resolve clear fractional *G* plateau[4]. Recent efforts have focused on vertical device architectures such as tunneling between graphene-BN-graphene layers, or Coulomb drag phenomena in BN-graphene-BN-graphene-BN bilayer structures[3,5]. These device structures are at the forefront of graphene transport research and should reveal many exciting phenomena.

11.3 Outlook:

The fabrication methods presented in Chapter 3 can be extended to realize many exciting graphene based nanostructures. For instance, other geometries such as split gates can be explored, and coupled to the high sample quality achieved to realize a ballistic quantum dot, or with careful design electron based interferometers. Another intriguing direction is to study electron transport in a single sample containing different layers and/or stacking domains. Dual gates will be crucial in these studies because, as was shown, transport properties can vary drastically under applied $E_{\perp}$ between different layers or stackings. One very interesting question is the transport across a layer or stacking

boundary where the equation of motion of the charge carrier may change[6, 7]. This is akin to stepping into another world where Newton's law is replaced by another law!

The scientific results presented in Chapters 6 through 10 mainly deal with 3 major questions: 1) Spontaneous gaps at B=0, the symmetries behind them and phase transitions between these states and a conducting state; 2) The ν=0 state in the QH regime, its E-B phase diagram, and 3) Broken symmetry states at finite densities, and their associated gap values and underlying symmetries.

For the future work, rhombrohederal-stacked multilayer graphene presents an exciting future direction for question (1). These graphene relatives are expected to have flatter bands that meet and touch at the CNP, hence they should host more robust spontaneous gaps, which may become useful for technological purposes. Investigating these spontaneous gaps in a dual gated device scheme will allow determination of the underlying symmetries, which is appealing academically.

The second question have been investigated quite extensively for SLG[8-11] and most recently using BN samples, which revealed signatures of spin skyrmions[12]. For multilayer systems, the requirement of an additional gate has a twofold effect: 1). Proper control of the $E_\perp$ so as to deconvolute it from n, and 2) Tuning $E_\perp$ is akin to modulating pseudospin, which cannot be manipulated presently in SLG. Previous studies on BLG did not possess sufficient sample quality[13] or an additional gate[14] to effectively address the above points. With the advent of better samples with dual gates much progress is expected in the near future on this system in this regard. Studies with thicker layers are

just beginning both experimentally[2, 15] and theoretically, hence from an exploratory perspective these systems may be the most exciting.

Similarly, for QH states at finite density in multilayer graphene, in particular broken symmetry states, the role of the $E_{\perp}$ cannot be overlooked. Its importance has been demonstrated in chapter 9 for BLG and chapter 10 for ABA-TLG, and should remain so for multilayer graphene in general. Another direction is the measurement of Landau level (LL) gaps in the multilayer systems, which is still at a nascent stage, while tuning $E_{\perp}$ and B. Since there have been limited both experimental[2, 16-18] and theoretical[19, 20] studies, this area should offer great opportunities for original work and exciting discoveries.

References

1. C. R. Dean, A. F. Young, MericI, LeeC, WangL, SorgenfreiS, WatanabeK, TaniguchiT, KimP, K. L. Shepard and HoneJ, Nat. Nanotechnol. 5 (10), 722-726 (2010).

2. T. Taychatanapat, K. Watanabe, T. Taniguchi and P. Jarillo-Herrero, Nat. Phys. 7, 621 (2011).

3. L. A. Ponomarenko, A. K. Geim, A. A. Zhukov, R. Jalil, S. V. Morozov, K. S. Novoselov, I. V. Grigorieva, E. H. Hill, V. V. Cheianov, V. I. Fal/'ko, K. Watanabe, T. Taniguchi and R. V. Gorbachev, Nat Phys 7 (12), 958-961 (2011).

4. C. R. Dean, A. F. Young, P. Cadden-Zimansky, L. Wang, H. Ren, K. Watanabe, T. Taniguchi, P. Kim, J. Hone and K. L. Shepard, Nature Phys. 7 (9), 693-696 (2011).

5. L. Britnell, R. V. Gorbachev, R. Jalil, B. D. Belle, F. Schedin, A. Mishchenko, T. Georgiou, M. I. Katsnelson, L. Eaves, S. V. Morozov, N. M. R. Peres, J. Leist, A. K. Geim, K. S. Novoselov and L. A. Ponomarenko, Science 335 (6071), 947-950 (2012).

6. A. W. Tsen, L. Brown, M. P. Levendorf, F. Ghahari, P. Y. Huang, R. W. Havener, C. S. Ruiz-Vargas, D. A. Muller, P. Kim and J. Park, Science 336 (6085), 1143-1146 (2012).

7. P. Kim, Nat. Mater. 9 (10), 792-793 (2010).

8. J. G. Checkelsky, L. Li and N. P. Ong, Phys. Rev. Lett. 100 (20), 206801 (2008).

9. J. G. Checkelsky, L. Li and N. P. Ong, Phys. Rev. B 79 (11), 115434 (2009).

10. Y. Zhang, Z. Jiang, J. P. Small, M. S. Purewal, Y. W. Tan, M. Fazlollahi, J. D. Chudow, J. A. Jaszczak, H. L. Stormer and P. Kim, Physical Review Letters 96 (13), 136806 (2006).

11. Z. Jiang, Y. Zhang, H. L. Stormer and P. Kim, Phys Rev Lett 99 (10), 106802 (2007).

12. A. F. Young, C. R. Dean, L. Wang, H. Ren, P. Cadden-Zimansky, K. Watanabe, T. Taniguchi, J. Hone, K. L. Shepard and P. Kim, Nat Phys 8 (7), 550-556 (2012).

13. Y. Zhao, P. Cadden-Zimansky, Z. Jiang and P. Kim, Phys. Rev. Lett. 104 (6), 066801 (2010).

14. B. E. Feldman, J. Martin and A. Yacoby, Nat. Phys. 5 (12), 889-893 (2009).

15. W. Bao, L. Jing, Y. Lee, J. V. Jr., P. Kratz, D. Tran, B. Standley, M. Aykol, S. B. Cronin, D. Smirnov, M. Koshino, E. McCann, M. Bockrath and C. N. Lau, Nat. Phys. 7, 948-952 (2011).

16. E. A. Henriksen, D. Nandi and J. P. Eisenstein, Phys. Rev. X 2 (1), 011004 (2012).

17. T. Khodkov, F. Withers, D. C. Hudson, M. F. Craciun and S. Russo, Appl. Phys. Lett. 100 (1), 013114 (2012).

18. L. Zhang, Y. Zhang, J. Camacho, M. Khodas and I. A. Zaliznyak, Nat. Phys. 7 (12), 953-957 (2011).

19. F. Zhang, D. Tilahun and A. H. MacDonald, Phys. Rev. B 85 (16), 165139 (2012).

20. M. Koshino and E. McCann, Phys. Rev. B 83 (16), 165443 (2011).

Appendix 1: Janis fridge and magnet operation

A.1.1 Janis VTI fridge cooling down procedure

1. Pumping the OVC (Outer Vacuum Chamber, only required if OVC vacuum is broken. This should only be done after consultation with Jeanie). To do this, a valve on the dewar that is in line with the liquid nitrogen (LN2) inlet and vent port is opened with a wrench. Then a turbo pump is attached that possesses a gauge so that the pressure may be monitored. The pressure of OVC should reach 10^{-6} torr. Upon reaching this value close OVC.

2. Pumping the IVC (Inner Vacuum Chamber which has a green valve). A turbo pump with a gauge should be attached to this valve and the pressure monitored. The pressure of the IVC should reach 10^{-6} torr. Upon reaching this value close the IVC.

3. Pumping the sample space. Attach a "T" to sample space inlet for mechanical pump and for He gas use. Pump the sample space to low pressure and then pump and flush sample space with He gas at least 3 times. Leave sample space over-pressurized with He gas. Magnet's resistance should be ~11ohm at room temperature, and ~0 at 4K.

4. Cooling the liquid helium reservoir with liquid nitrogen.

a) Note two dewars of liquid nitrogen are required for this procedure since one is used for cooling and the other for filling the nitrogen bath. The "T" from the previous step should still be in place. Vent liquid helium reservoir and open its inlet.

b) Attach rubber hose onto liquid nitrogen dewar and the other end with hose clamp to blow out tube (make a good seal to prevent leakage). Feed liquid nitrogen into the liquid helium reservoir inlet. While liquid helium reservoir is being filled the sample space should be pumped and the needle valve should be slightly opened and closed occasionally to prevent it from freezing shut, but do not leave this valve open because pumping on the liquid nitrogen is advised against by Janis.

c) Fill liquid helium reservoir with liquid nitrogen only a few inches into the belly (refer to drawing on wall). The goal in this step is to cool the magnet so one should monitor the resistance of the magnet during this step.

d) Once the liquid nitrogen has reached the right level close the needle valve and over-pressurize sample space with He gas. Close all ports and leave the system to cool with liquid nitrogen over an extended period of time (overnight works well). Note it takes a while for the Liquid nitrogen to collect in the liquid helium reservoir and one liquid nitrogen dewar may not be enough.

5. Preparations for introducing liquid helium into liquid helium reservoir.

Use the temperature controller to monitor the sample space, and use helium gas to over-pressurize any residual liquid nitrogen out of the sample space to the liquid helium reservoir, which is filled with liquid nitrogen.

Once the temperature reaches ~84K and pressure is zero in the sample space there should be no nitrogen in the sample space. Pump and flush the sample space with helium gas and leave this space over-pressurized.

6. Blow out liquid nitrogen from the liquid helium reservoir into the liquid nitrogen bath.

a. First attach the blow out tube, note this stainless steel tube should be long enough to reach the bottom of the liquid helium reservoir, with hose clamp on one side that will go into liquid helium inlet and rubber hose on the other end of the blowout tube. The other side of the rubber hose attaches to the liquid nitrogen port. Try to make a good seal here to prevent liquid nitrogen from leaking during transfer. See figure below.

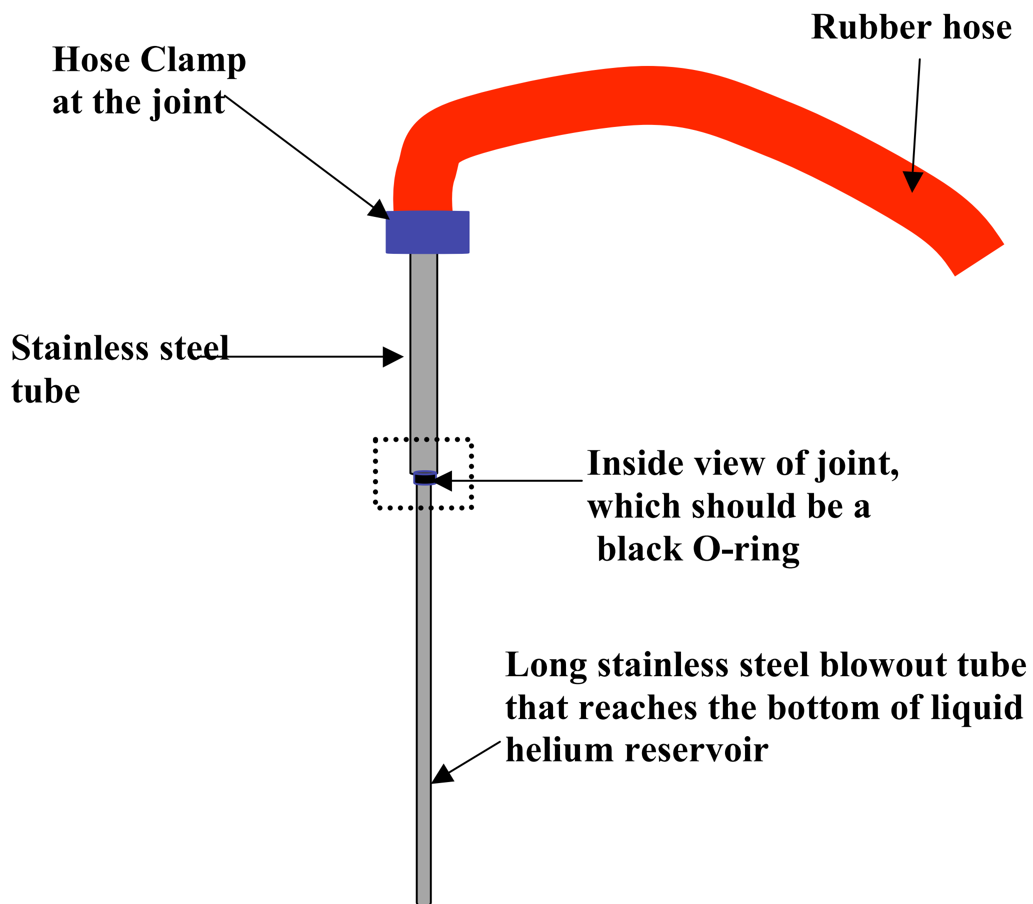

b. Once liquid nitrogen has been removed from liquid helium reservoir leave the blow out tube in place and block its end. Attach “T” with He gas and mechanical pump to liquid helium quench port, note sample space should be sealed. Next, pump and flush with mechanical pump and helium gas through quench port, and over-pressurize liquid helum reservoir with helium gas and take blocker off from other end of the blow out tube. This should allow unwanted LN2 to escape.

Indications of complete removal of liquid nitrogen from liquid helium reservoir:

a) Monitor the value of carbon resister to see if it displays a continued increase in resistance (this is a sign of cooling indicating nitrogen is still present). If it does, there may be more liquid nitrogen left in the liquid helium reservoir.

b) When pumping the liquid helium reservoir the gauge value may stay at a pressure of -25mm Hg. If this occurs, over-pressurize the liquid helium reservoir with helium gas to try to push liquid nitrogen out.

7. Filling the liquid helium reservoir with liquid helium.

a) Attach the liquid helium transfer line to the liquid helium dewar and liquid helium reservoir, while leaving the liquid helium reservoir quench port open. Transfer liquid helium until the meter indicates 32 inches. During this procedure open and close the needle valve to prevent it from freezing shut.

b) Once desired level is reached close liquid helium quench port after shutting all the other liquid helium vent ports. At this point the carbon resister’s value should be

~5.48kohm at 4K. Near liquid nitrogen temperature this resistor will indicate ~483ohm.

A.1.2 Sample loading and removal (please read all the text below before operating the fridge)

NOTE #1: If the fridge is cold the sample space should be prepared by heating it to room temperature and then over pressurizing. When removing the sample the sample space should be heated to room temperature and over pressurized to prevent condensation on the sample. The heating is performed with the temperature controller, which heats sample space to room temperature; it is best to use both vaporizer and sample heater. This will most likely reduce the condensation on sample insert when it is removed. This heating procedure should take no less than one hour.

NOTE #2: During this procedure a “T” should be attached with helium gas and a mechanical pump to the sample space. The Needle valve should be slightly open to maintain flow. Failure to do the latter may result in breaking the heater in the sample space.

A.1.3 Procedure to warming the fridge up.

1. Blow out all liquid nitrogen by running nitrogen gas through liquid nitrogen port
2. Blow out liquid helium with the blow out tube, which should reach the bottom of the liquid helium reservoir, and pressurize with helium gas.
3. After Liquid helium is blown out flow helium gas through liquid helium reservoir for an hour. While flowing helium gas crack the needle valve open, and warm up the sample

space. Pump the space if the pressure gets high.

A.1.4 Magnet operation

1. CHECK magnet Resistance at Liquid Helium temperature. It should be R~.12Ω. CHECK Helium Level is larger than 15 inches. This is a strict requirement.

3. Settings: **(Using panel Setup—Rates, Donot press Hi limit▲, Lo limit▼, Mag►)**

Current Range	Sweeping Rate
0-50Amps	0.08Amps/s
50-70Amps	0.054Amps/s
70-85Amps	0.027Amps/s
85-91.22Amps	0.027Amps/s

(Ref. Table5-1 on manual book)

4. Make sure the voltage limit is 5V, current limit (High sweep limit) is set to the magnetic field of your choice.**(Using panel Setup—limits, Do not press Hi limit▲, Lo limit▼, Mag►)**

5.**Press HTR ON** to turn on heater, note heater should only be turned on when current in the leads matches the current in the magnet.

6.Run current to the desired magnetic field value. **Press Hi limit▲**

7. Once the current reaches the desired value and is stable for ~1min press pause and wait for two minutes.

8. Turn off heater. **Press HTR OFF**

9. Zero the current. **Press ZERO,** once it reaches zero wait for two minutes. Magnet should be persistent mode

10. **Press Hi limit▲**, current in the leads will go to the previously defined current.

12. Once the current has reached the desired value and is stable for one minute **Press pause** and wait for two minutes then **Press HTR ON**. Current in the leads will match the current in the magnet, and persistent mode is disengaged.

13. To zero the current and bring the magnet to zero wait for two minutes and then **Press ZERO.** Magnet is now off.

Appendix 2

Exposure and development parameters:

A.2.1: Exposure parameters

The suspended dual gated device is comprised of three main electron beam lithography steps. Below I list the parameters I used for several runs with a measured beam current of 60-65 pA, and next to the respective pattern. Note these parameters depend on the

stability of the electron beam writer. Please perform a dosage test before writing critical patterns.

Step 1_e: Define top gate anchor (dark blue), connecting wire (dark blue) and graphene clamps(aqua blue).

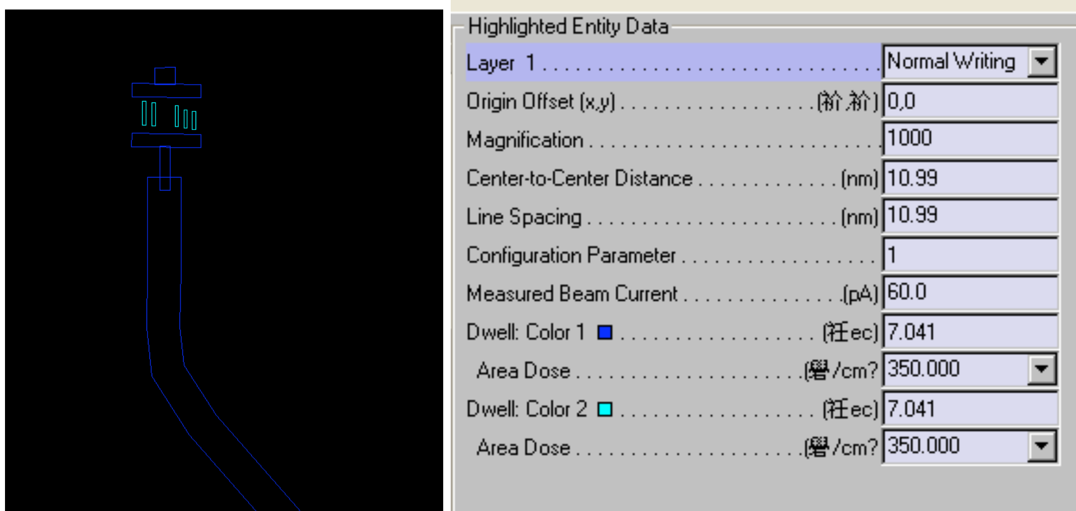

Step 2_e: Define top gate bridge (orange), connecting wire (dark blue) and graphene clamps (aqua blue).

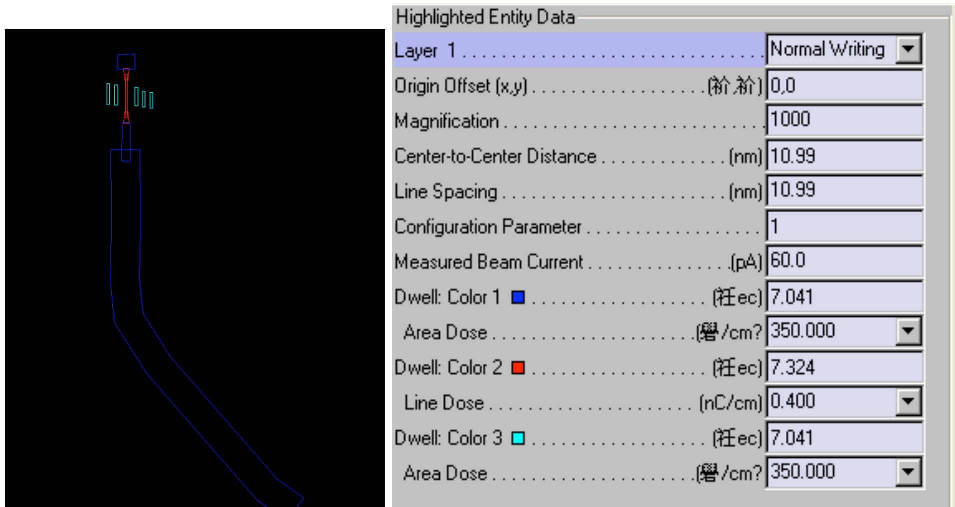

Step 3_e: Define source drain electrodes(red dashed line), connecting wire (dark blue).

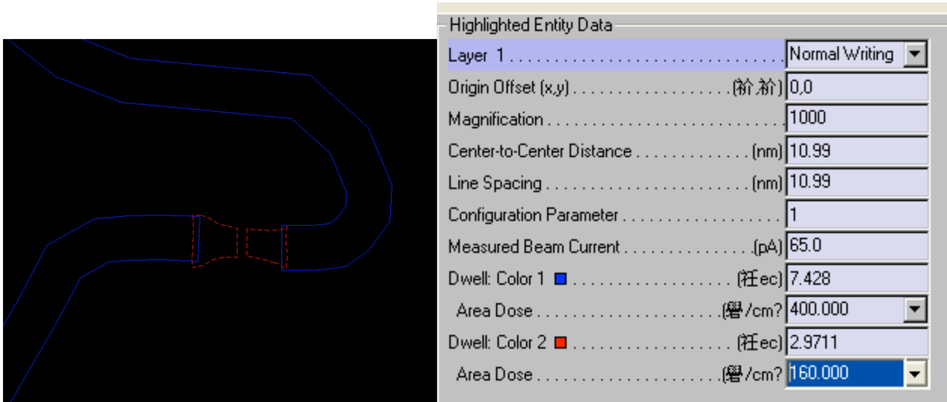

A.2.2 Developing parameters

	PMMA	**MMA**	**LOR3B**	**LOR1A**
Spin	4000 rpm	4000 rpm	4000 rpm	4000 rpm
Bake time	20 mins at 170°C	20 mins at 170°C	5 mins at 190°C	5 mins at 170°C
Develop time (seconds)	60 s	60 s	1-2 s	7-9 s
Rinse	IPA 60 s	IPA 60 s	DI water 60 s	DI water 60 s